



# Trajectory planning and tracking for autonomous vehicles navigation

Alia Chebly

## ► To cite this version:

Alia Chebly. Trajectory planning and tracking for autonomous vehicles navigation. Automatic Control Engineering. Université de Technologie de Compiègne, 2017. English. NNT : 2017COMP2392 . tel-01727720

HAL Id: tel-01727720

<https://tel.archives-ouvertes.fr/tel-01727720>

Submitted on 9 Mar 2018

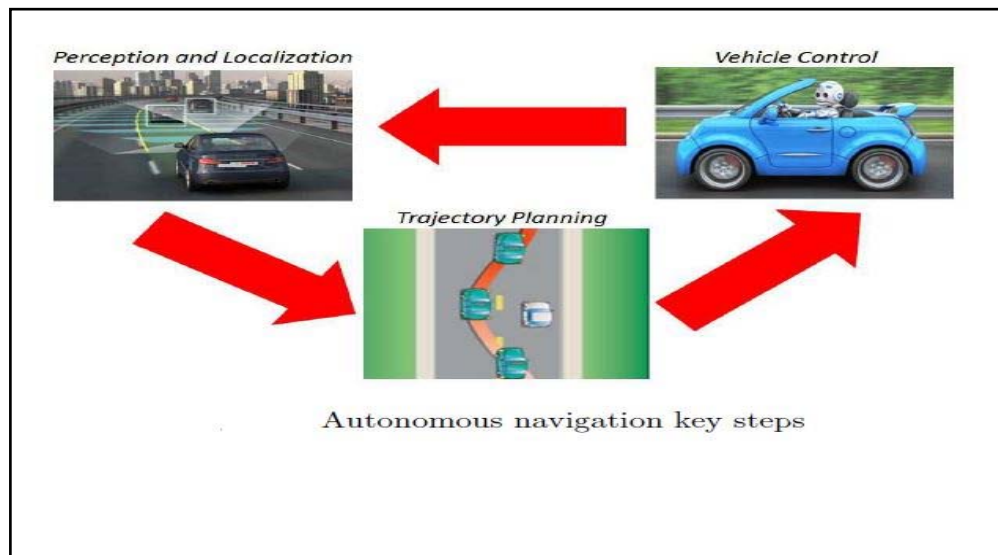
**HAL** is a multi-disciplinary open access archive for the deposit and dissemination of scientific research documents, whether they are published or not. The documents may come from teaching and research institutions in France or abroad, or from public or private research centers.

L'archive ouverte pluridisciplinaire **HAL**, est destinée au dépôt et à la diffusion de documents scientifiques de niveau recherche, publiés ou non, émanant des établissements d'enseignement et de recherche français ou étrangers, des laboratoires publics ou privés.

Par **Alia CHEBLY**

*Trajectory planning and tracking for autonomous vehicles navigation*

# Thèse présentée pour l'obtention du grade de Docteur de l'UTC



Soutenue le 5 décembre 2017  
**Spécialité** : Automatics : Unité de recherche Heudyasic  
(UMR-7253)

D2392

# **TRAJECTORY PLANNING AND TRACKING FOR AUTONOMOUS VEHICLES NAVIGATION**

**Alia Chebly**

**Specialty: Automatics**

Heudiasyc Laboratory,  
CNRS, Heudiasyc UMR 7253, CS 60 319 Compiègne France

Sorbonne universités, Université de Technologie de Compiègne

PHD defended on 5 december 2017 in front of the jury composed of :

**Rapporteurs :**

Ahmed El Hajjaji Professeur des Universités, UPJV  
Mariana Netto Chargée de Recherche IFSTTAR

**Examimators :**

Dominique Meizel Professeur Emérite, Université de Limoges  
Véronique Cherfaoui Professeur des Universités, UTC

**PHD Supervisors :**

Reine Talj Chargée de recherche CNRS, UTC  
Ali Charara Professeur des Universités, UTC



# **Planification et suivi de trajectoires pour la navigation des véhicules autonomes**

**Par Alia Chebly**

Soutenue le 5 décembre 2017 devant le jury composé de :

M<sup>me</sup> V. CHERFAOUI (Présidente)  
M<sup>me</sup> R. TALJ (Directrice de thèse)  
M. A. CHARARA (Directeur de thèse)  
M. A. EL HAJJAJI (Rapporteur)  
M<sup>me</sup> M. NETTO (Rapporteur)  
M. D. MEIZEL

# Abstract

In this thesis, the trajectory planning and the control of autonomous vehicles are addressed. As a first step, a multi-body modeling technique is used to develop a four wheeled vehicle planar model. This technique considers the vehicle as a robot consisting of articulated bodies. The geometric description of the vehicle system is derived using the modified Denavit Hartenberg parameterization and then the dynamic model of the vehicle is computed by applying a recursive method used in robotics, namely Newton-Euler based Algorithm. The validation of the developed vehicle model was then conducted using an automotive simulator developed by Oktal, the Scaner-Studio simulator.

The developed vehicle model is then used to derive coupled control laws for the lateral and the longitudinal vehicle dynamics. Two coupled controllers are proposed in this thesis: In the first controller, the control is designed using Lyapunov control techniques while in the second one an Immersion and Invariance approach is used. Both of the controllers aim to ensure a robust tracking of the reference trajectory and the desired speed while taking into account the strong coupling between the lateral and the longitudinal vehicle dynamics. In fact, the coupled controller is a key step for the vehicle safety handling, especially in coupled maneuvers such as lane-change maneuvers, obstacle avoidance maneuvers and combined maneuvers in critical driving situations. The developed controllers were validated in simulation under Matlab/Simulink using experimental data. Subsequently, an experimental validation of the proposed controllers was conducted using a robotized vehicle (Renault-ZOE) present in the Heudiasyc laboratory within the Equipex Robotex project. Concerning the trajectory planning, a local planning method based on the clothoid tentacles method is developed. Moreover, a maneuver planning strategy focusing on the overtaking maneuver is developed to improve and complete the local planning approach. The local and the maneuver planners are then combined in order to establish a complete navigation strategy. This strategy is then validated using the developed robotics vehicle model and the Lyapunov based controller under Matlab/Simulink.

**Keywords:** Autonomous vehicles, trajectory planning, tentacles method, coupled control, overtaking maneuver, robotics modeling.

# Résumé

Les travaux de cette thèse portent sur la navigation des véhicules autonomes, notamment la planification de trajectoires et le contrôle du véhicule.

En premier lieu, un modèle véhicule plan est développé en utilisant une technique de modélisation qui assimile le véhicule à un robot constitué de plusieurs corps articulés. La description géométrique du véhicule est basée sur la convention de Denavit-Hartenberg modifiée. Le modèle dynamique du véhicule est ensuite calculé en utilisant la méthode récursive de Newton-Euler, qui est souvent utilisée dans le domaine de robotique. La validation du modèle a été conduite sur le simulateur Scaner-Studio développé par Oktal pour les applications automobiles.

Le modèle du véhicule développé est ensuite utilisé pour la synthèse de lois de commande couplées pour les dynamiques longitudinale et latérale du véhicule. Deux correcteurs sont proposés dans ce travail : le premier est basé sur les techniques de commande par Lyapunov, le second utilise une approche "Immersion et Invariance". Ces deux contrôleurs ont pour objectifs de suivre une trajectoire de référence donnée avec un profil de vitesse désirée, tout en tenant compte du couplage existant entre les dynamiques longitudinale et latérale du véhicule. En effet, le contrôle couplé est nécessaire pour garantir la sécurité du véhicule autonome surtout lors de l'exécution des manœuvres couplées comme les manœuvres de changement de voie, les manœuvres d'évitement d'obstacles et les manœuvres exécutées dans les situations de conduite critiques. Les contrôleurs développés ont été validés en simulation sous Matlab/Simulink en utilisant des données expérimentales. Par la suite, ces contrôleurs ont été validés expérimentalement en utilisant le véhicule démonstrateur robotisé (Renault-Zoé) du laboratoire Heudiasyc financé par l'Equipex Robotex. En ce qui concerne la planification de trajectoires, une méthode de planification basée sur la méthode des tentacules sous forme de clothoides a été développée. En outre, une méthode de planification de manœuvres qui s'intéresse essentiellement à la manœuvre de dépassement a été mise en place, afin d'améliorer et de compléter la méthode locale des tentacules. Le planificateur local et le planificateur de manœuvres ont été ensuite combinés pour établir une stratégie de navigation complète. Cette stratégie a été validée par la suite sous Matlab/Simulink en utilisant le modèle de véhicule développé et le contrôleur basé sur Lyapunov.

**Mots clés:** Véhicules autonomes, planification de trajectoires, méthode des tentacules, contrôle couplé, manœuvres de dépassement, modélisation robotique.



# Acknowledgement

Firstly, I would like to express my sincere gratitude to my advisors, Mr Ali Charara and Ms Reine Talj, for the continuous support of my Ph.D study and related research, for their patience, motivation, and immense knowledge. Their guidance helped me in all the time of research and writing of this thesis.

Besides my advisor, I would like to thank the rest of my thesis committee: Mr Ahmad El Hajjaji, Ms Mariana Netto, Mr Dominique Meizel and Ms Veronique Cherfaoui , for their insightful comments and encouragement, but also for the hard questions which incited me to widen my research from various perspectives.

My sincere thanks also goes to Mr. Stéphane Bonnet and Mr. Thierry Monglon, who assisted me during the experimental tests that were conducted in this thesis. I would also like to thank Ms Chloé Lallich, the director of the Technology Park in Compiègne where some of the tests had place, for the time and the interest she has given to me. I am also grateful to the UTC staff for their unfailing support and assistance in all the administrative and technical issues.

I thank my fellow labmates in for the stimulating discussions, for the sleepless nights we were working together before deadlines, and for all the fun we have had in the last three years. Also I thank my friends I have met in Compiègne for all their support and the funny time we spent together.

Last but not the least, I would like to thank my family: my parents and my brothers and sisters for supporting me spiritually throughout writing this thesis and for being always in my side.

# Contents

<b>1</b>	<b>Introduction</b>	<b>1</b>
1.1	Context and Motivations . . . . .	1
1.2	Problem formulation . . . . .	3
1.3	Contributions . . . . .	3
1.4	Thesis Outline . . . . .	6
<b>2</b>	<b>Trajectory Planning</b>	<b>7</b>
2.1	Introduction . . . . .	7
2.2	Local Planning with Clothoid Tentacles Method . . . . .	8
2.2.1	Existing Local Planning Techniques . . . . .	8
2.2.1.1	Potential fields Method . . . . .	8
2.2.1.2	Dynamic Window . . . . .	9
2.2.1.3	Model Predictive Control . . . . .	10
2.2.1.4	Roadmap Methods . . . . .	11
2.2.1.5	Partial Motion Planning approach (PMP) . . . . .	12
2.2.1.6	State Lattices Planners . . . . .	13
2.2.1.7	Geometric Curves . . . . .	13
2.2.2	Tentacles Method with Clothoid Form . . . . .	17
2.2.2.1	Occupancy Grid . . . . .	18
2.2.2.2	Tentacles Generation . . . . .	19
2.2.2.3	Navigable Tentacles Selection . . . . .	22
2.2.2.4	Best Tentacle Choice . . . . .	23
2.2.3	Tentacles Method Validation . . . . .	25
2.2.3.1	Simulation Results . . . . .	25
2.2.3.2	Comparison with the circular tentacles method . . . . .	26
2.2.3.3	Preliminary Experimental Results . . . . .	29
2.2.3.3.1	Experimental tools and Evaluation method . . . . .	29
2.2.3.3.2	Evaluation Results . . . . .	32
2.3	Maneuver Planning: Overtaking Maneuver . . . . .	34
2.3.1	Existing Approaches for the Overtaking Maneuver Planning . . . . .	34
2.3.2	Developed Overtaking Maneuver . . . . .	36
2.3.2.1	Maneuver planning approach . . . . .	36
2.3.2.2	Overtaking Trajectory Generation . . . . .	37
2.3.2.2.1	Phase 1: Lane Changing Maneuver . . . . .	37
2.3.2.2.2	Phase 2: Navigating on the left lane . . . . .	41
2.3.2.2.3	Phase 3: Returning to the right lane . . . . .	42
2.3.3	Validation of the maneuver planning algorithm . . . . .	45
2.3.3.1	Scenario 1 . . . . .	46

2.3.3.2	Scenario 2 . . . . .	53
2.4	Local/Maneuver Combined Planning Approach . . . . .	61
2.5	Conclusion . . . . .	62
<b>3</b>	<b>Vehicle Modeling using Robotics Formalism</b>	<b>63</b>
3.1	Introduction . . . . .	63
3.2	State of the Art on Existing Vehicle Modeling Techniques . . . . .	64
3.2.1	Closed-form Models . . . . .	64
3.2.1.1	Vehicle Planar dynamics . . . . .	64
3.2.1.1.1	Kinematic Bicycle Model . . . . .	64
3.2.1.1.2	Dynamic Bicycle Model . . . . .	65
3.2.1.1.3	Four wheels Model . . . . .	66
3.2.1.2	Vehicle Vertical Dynamics . . . . .	68
3.2.1.2.1	Automotive suspensions . . . . .	68
3.2.1.2.2	Vertical loads transfer . . . . .	70
3.2.1.3	Tires dynamics . . . . .	70
3.2.1.3.1	Linear model . . . . .	71
3.2.1.3.2	Dugoff's model . . . . .	72
3.2.1.3.3	Burckhardt/Kiencke's model . . . . .	72
3.2.1.3.4	Pacejka's model . . . . .	73
3.2.2	Multi-body Models . . . . .	75
3.3	Robotics Formalism for dynamic modeling . . . . .	78
3.3.1	Geometric description . . . . .	78
3.3.2	Dynamic model development . . . . .	81
3.3.2.1	Modeling the vehicle base . . . . .	81
3.3.2.2	Euler-Lagrange Dynamic model . . . . .	82
3.3.2.3	Vertical Kinematic Constraints . . . . .	88
3.4	Application to a Four Wheeled Vehicle Model . . . . .	90
3.5	Validation of the developed model . . . . .	94
3.5.1	Scaner-Studio Environment . . . . .	95
3.5.2	Model Validation Results . . . . .	96
3.5.2.1	First Scenario . . . . .	96
3.5.2.2	Second Scenario . . . . .	98
3.5.2.3	Third scenario . . . . .	99
3.6	Conclusion . . . . .	100
<b>4</b>	<b>Vehicle Coupled Control</b>	<b>102</b>
4.1	Introduction . . . . .	102
4.2	State of the Art on the Autonomous Vehicles Control . . . . .	103
4.2.1	Lateral Control . . . . .	103
4.2.2	Longitudinal Control . . . . .	106
4.2.3	Coupled Control . . . . .	108
4.3	Developed Coupled Controllers . . . . .	109
4.3.1	Simplified Vehicle Model . . . . .	109
4.3.2	Coupled Controller based on Lyapunov Control Techniques . . . . .	112
4.3.3	Coupled Controller based on an Immersion and Invariance Approach, Combined with Sliding Mode Control . . . . .	114

<b>4.4</b>	<b>Controllers Validation: Simulation Results . . . . .</b>	<b>118</b>
<b>4.4.1</b>	<b>Normal Driving Conditions . . . . .</b>	<b>120</b>
<b>4.4.1.1</b>	<b>Scenario 1 . . . . .</b>	<b>120</b>
<b>4.4.1.2</b>	<b>Scenario 2 . . . . .</b>	<b>123</b>
<b>4.4.2</b>	<b>Controller Robustness . . . . .</b>	<b>125</b>
<b>4.4.2.1</b>	<b>Scenario 3: Strongly Nonlinear Maneuvers . . . . .</b>	<b>126</b>
<b>4.4.2.2</b>	<b>Scenario 4: Parameters uncertainties . . . . .</b>	<b>129</b>
<b>4.5</b>	<b>Controllers validation: Experimental Results . . . . .</b>	<b>131</b>
<b>4.5.1</b>	<b>Presentation of the Experimental Environment . . . . .</b>	<b>131</b>
<b>4.5.1.1</b>	<b>Automated vehicle description . . . . .</b>	<b>131</b>
<b>4.5.1.2</b>	<b>Vehicle parameters . . . . .</b>	<b>132</b>
<b>4.5.1.3</b>	<b>Sending Commands to the ZOE . . . . .</b>	<b>132</b>
<b>4.5.1.4</b>	<b>Dynamic variables of the controllers . . . . .</b>	<b>133</b>
<b>4.5.1.4.1</b>	<b>Lyapunov Based Controller . . . . .</b>	<b>133</b>
<b>4.5.1.4.2</b>	<b>Immersion and Invariance Based Controller . . . . .</b>	<b>141</b>
<b>4.5.2</b>	<b>Results of Validation of the Lyapunov based controller . . . . .</b>	<b>141</b>
<b>4.5.2.1</b>	<b>Results on the Track Seville . . . . .</b>	<b>141</b>
<b>4.5.2.1.1</b>	<b>Presentation of the Track Seville . . . . .</b>	<b>141</b>
<b>4.5.2.1.2</b>	<b>Results of Validation on Seville . . . . .</b>	<b>143</b>
<b>4.5.2.2</b>	<b>Results on the Track Technology Park . . . . .</b>	<b>149</b>
<b>4.5.2.2.1</b>	<b>Presentation of the Track Technology Park . . . . .</b>	<b>149</b>
<b>4.5.2.2.2</b>	<b>Results of Validation on the Technology Park . . . . .</b>	<b>150</b>
<b>4.5.3</b>	<b>Results of validation of the Immersion and Invariance based controller . . . . .</b>	<b>153</b>
<b>4.5.3.1</b>	<b>Test 1: Navigating in Seville with <math>10km/h</math> . . . . .</b>	<b>154</b>
<b>4.5.3.2</b>	<b>Test 2: Navigating in Seville with <math>15km/h</math> . . . . .</b>	<b>157</b>
<b>4.5.4</b>	<b>Some comparison results: Lyapunov vs I &amp; I vs classical PD/P controller . . . . .</b>	<b>159</b>
<b>4.5.4.1</b>	<b>Test 1: Navigating on Seville with <math>10km/h</math> . . . . .</b>	<b>160</b>
<b>4.5.4.2</b>	<b>Test 2: Navigating in Seville with <math>15km/h</math> . . . . .</b>	<b>164</b>
<b>4.5.4.3</b>	<b>Test 3: Navigating in Seville with <math>15km/h</math> with different control parameters . . . . .</b>	<b>167</b>
<b>4.6</b>	<b>Conclusion . . . . .</b>	<b>171</b>
<b>5</b>	<b>Validation of the Navigation Strategy</b>	<b>173</b>
<b>5.1</b>	<b>Combined Navigation Strategy . . . . .</b>	<b>173</b>
<b>5.2</b>	<b>Validation of the Navigation Strategy without the maneuver planner level . . . . .</b>	<b>174</b>
<b>5.3</b>	<b>Validation of the Combined Navigation Strategy . . . . .</b>	<b>177</b>
<b>5.4</b>	<b>Conclusion . . . . .</b>	<b>182</b>
<b>6</b>	<b>Conclusion and Perspectives</b>	<b>183</b>
<b>Abbreviations and Notations</b>		<b>187</b>
<b>Bibliography</b>		<b>190</b>

# List of Figures

1.1	Autonomous navigation key steps . . . . .	3
2.1	Potential Fields Principle [Goo02]: (a)The potential field generated when there is a goal and an obstacle, (b) The selected trajectory. . . . .	9
2.2	Dynamic window approach: search space [FBT97]. In the figure, $V_s$ is the search space of the possible velocities, $V_a$ corresponds to the admissible velocities and $V_r$ is defined as the intersection of the restricted areas ( $V_r = V_s \cap V_d \cap V_a$ ). . . . .	10
2.3	Model Predictive Control for local planning. . . . .	11
2.4	Roadmap methods. . . . .	12
2.5	Partial motion planning concept [BPFP06]. In the figure, $\pi$ means the local planned trajectory . . . . .	12
2.6	Inevitable collision states (ICS) [BPFP06]. . . . .	13
2.7	Lattice planner for on-road driving [MNK <sup>+</sup> 13a]. . . . .	13
2.8	Polynomial trajectories generated in [DFM09]. . . . .	14
2.9	Bezier curve generated in [MYZ12] and shown in dashed line. . . . .	15
2.10	Spline curves used in [WGR11] for trajectory planning. . . . .	15
2.11	Tentacles method with circular arcs form developed in [HHH <sup>+</sup> 08b]. . . . .	16
2.12	Path planning in a 2D search space [TMD <sup>+</sup> 06]: Paths that change lateral offsets with (a) the minimum and (b) the maximum possible lateral acceleration. . . . .	16
2.13	Evaluation of vehicle trajectories: green, yellow, and red curves represent evaluated trajectories; the blue trajectory represents the best one. In the potential map dark areas represent points at low cost, while the light areas are high cost points generated by obstacles. . . . .	17
2.14	Tentacles method strategy [HHH <sup>+</sup> 08b]. . . . .	18
2.15	The LIDAR mounted on the experimental vehicle CARMEN in Heudiasyc laboratory. . . . .	19
2.16	Different clothoids at different speeds and different initial steering angles. . . . .	22
2.17	Classification zone [HHH <sup>+</sup> 08b]. . . . .	23
2.18	Tentacles classification: The red tentacles are the occupied ones while the blue tentacles are navigable. . . . .	23
2.19	$V_{trajectory}$ criterion calculation [HHH <sup>+</sup> 08b]. . . . .	24
2.20	Global map. . . . .	25
2.21	Obstacle avoidance scenario tested with clothoid tentacles. . . . .	26
2.22	Obstacle avoidance scenario tested with circular and clothoid tentacles. . . . .	27
2.23	Moving obstacle overtaking tested with circular and clothoid tentacles. . . . .	28
2.24	Steering wheel angle when using circular tentacles vs clothoid tentacles. . . . .	28
2.25	Steering wheel speed when using circular tentacles vs clothoid tentacles. . . . .	29
2.26	Experimental vehicle CARMEN . . . . .	30
2.27	Occupancy grid examples [Mor13] . . . . .	31

2.28	The road where the experimental test with CARMEN vehicle is performed. . . . .	32
2.29	Occupancy grid with the support area of the chosen tentacle . . . . .	32
2.30	Steering wheel angle: real data vs clothoid tentacles output. . . . .	33
2.31	An overtaking maneuver with its three phases . . . . .	34
2.32	Lane change maneuver regions proposed in [NBCF15]. . . . .	35
2.33	Maneuver planner architecture. . . . .	37
2.34	Phase 1: Lane changing maneuver, from right to left lane. . . . .	38
2.35	Table of variation of the longitudinal acceleration of the vehicle $\ddot{x}(t)$ . . . . .	39
2.36	Table of variation of the lateral acceleration of the vehicle $\ddot{y}(t)$ . . . . .	40
2.37	Phase 2: Navigating on the left lane. . . . .	42
2.38	Phase 3: Returning to the right lane. . . . .	44
2.39	Scenario 1: Vehicle A and B speeds during the ACC phase. . . . .	47
2.40	Scenario 1: Inter-vehicles distance between A and B during the ACC phase. . .	48
2.41	Scenario 1: ACC phase and Phase 1 of the overtaking maneuver (Changing lane from right to left). . . . .	49
2.42	Scenario 1: Speed and acceleration profiles of vehicle A during the phase 1 of the overtaking maneuver . . . . .	50
2.43	Scenario 1: ACC phase and the first two phases of the overtaking maneuver. . .	51
2.44	Scenario 1: ACC phase and the three phases of the overtaking maneuver . . . .	52
2.45	Scenario 1: Speed and acceleration profiles of vehicle A during the phase 3 of the overtaking maneuver . . . . .	53
2.46	Scenario 2: Vehicle A and B speeds during the ACC phase. . . . .	54
2.47	Scenario 2: Inter-vehicles distance between A and B during the ACC phase. . .	55
2.48	Scenario 2: ACC phase and Phase 1 of the overtaking maneuver (Changing lane from right to left). . . . .	56
2.49	Scenario 2: Speed and acceleration profiles of vehicle A during the phase 1 of the overtaking maneuver . . . . .	57
2.50	Scenario 2: ACC phase and the first two phases of the overtaking maneuver. . .	58
2.51	Scenario 2: ACC phase and the three phases of the overtaking maneuver . . . .	59
2.52	Scenario 2: Speed and acceleration profiles of vehicle A during the phase 1 of the overtaking maneuver . . . . .	60
2.53	Navigation strategy . . . . .	62
3.1	Yaw, roll and pitch motions of the vehicle chassis. . . . .	65
3.2	Bicycle Models: (a) Kinematic bicycle Model, (b) Dynamic Bicycle Model . . . .	66
3.3	Four wheels Vehicle Model . . . . .	67
3.4	Quarter car automotive suspension model . . . . .	69
3.5	Half car automotive suspension model . . . . .	69
3.6	Full car automotive suspension model . . . . .	70
3.7	Forces and moments in the contact area Tire/Ground [Jaz13]. . . . .	71
3.8	Parameters of the Pacejka's tire model [Men10]. . . . .	74
3.9	Lateral and longitudinal efforts with respect to different tire models [Baf07]. . .	75
3.10	Diagrammatic motorcycle model developed by [Sha71a] . . . . .	76
3.11	Eleven degrees of freedom motorcycle model developed by [CL02] . . . . .	76
3.12	Fourteen degrees of freedom vehicle model developed by [San16]. . . . .	77
3.13	Representation of a link $i$ with more than one successor [KK86]. . . . .	79
3.14	DHM notation for a tree-structured robot [KK86]. . . . .	80

3.15	Spatial model of the robot mobile base [Maa11]	82
3.16	Euler model of the robot mobile base [Maa11]	82
3.17	Vehicle and inertial frames $R_b$ and $R_f$	84
3.18	Representation of $R_b$ in $R_f$ : Roll ( $\theta$ ), pitch ( $\phi$ ) and yaw ( $\psi$ ) angles	85
3.19	The balance of forces acting on the body $C_j$ .	87
3.20	Direction of null vertical speeds at the four points of contact with the ground.	88
3.21	Model topology with 21 bodies.	90
3.22	Poly-articulated system with 21 bodies and 7 degrees of freedom.	92
3.23	Simulation Model in Matlab/Simulink.	95
3.24	Simulation Mode in Scaner-Studio.	96
3.25	First scenario inputs: Steering angle and wheels torques.	97
3.26	First scenario outputs: Speeds, accelerations, yaw rate and sideslip angle.	97
3.27	Second scenario inputs: Steering angle and wheels torques.	98
3.28	Second scenario outputs: Speeds, accelerations, yaw rate and sideslip angle.	99
3.29	Third scenario inputs: Steering angle and wheels torques.	99
3.30	Third scenario outputs: Speeds, accelerations, yaw rate and sideslip angle.	100
4.1	Coupled Controller layout.	112
4.2	Lateral displacement error computed at a distance $L_s$ in front of the vehicle	114
4.3	Principle of the Immersion and Invariance control [AKO07].	115
4.4	Sliding mode principle.	116
4.5	Experimental vehicle DYNA	119
4.6	Track CERAM in Mortefontaine, France	119
4.7	Scenario 1: Reference and vehicle trajectory	121
4.8	Scenario 1: Desired speed and road curvature.	121
4.9	Scenario 1: Longitudinal speed and lateral error.	122
4.10	Scenario 1: Control inputs.	122
4.11	Scenario 1: Lateral variables: $a_y$ and $\dot{\psi}$ .	123
4.12	Scenario 2: Reference and vehicle trajectory	123
4.13	Scenario 2: Desired speed and road curvature.	124
4.14	Scenario 2: Longitudinal speed and lateral error.	124
4.15	Scenario 2: Control laws.	125
4.16	Scenario 2: Lateral variables: $a_y$ and $\dot{\psi}$ .	125
4.17	Scenario 3: Reference and vehicle trajectories	127
4.18	Scenario 3: Desired speed and road curvature.	127
4.19	Scenario 3: Longitudinal speed and lateral error.	128
4.20	Scenario 3: Control laws.	128
4.21	Scenario 3: Lateral variables: $a_y$ and $\dot{\psi}$ .	129
4.22	Controllers robustness against uncertainties on the vehicle mass	130
4.23	Controllers robustness against uncertainties on the cornering stiffness	130
4.24	Experimental vehicle: ZOE.	132
4.25	Term in $\ddot{x}$	135
4.26	Term in $\ddot{\psi}$	135
4.27	Experimental test: Tracking desired speed of $10km/h$ where the control input $\tau_w$ contains the term in $\delta$	137
4.28	Experimental test: Tracking desired speed of $10km/h$ where the control input $\tau_w$ doesn't contain the term in $\delta$	137

4.29 Experimental test: Tracking desired speed of $25km/h$ where the control input $\tau_w$ contains the term in $\delta$ . . . . .	138
4.30 Simulation test: Tracking desired speed of $10km/h$ with and without considering the term in $\delta$ in the computation of $\tau_w$ . . . . .	140
4.31 Simulation test: Tracking desired speed of $15km/h$ with and without considering the term in $\delta$ in the computation of $\tau_w$ . . . . .	140
4.32 Computing the curvature of an arc using three points from the map. . . . .	142
4.33 Experimental test track: Seville. . . . .	142
4.34 Seville curvature. . . . .	143
4.35 Test 1 on Seville using Lyapunov controller: Desired longitudinal speed tracking. .	144
4.36 Test 1 on Seville using Lyapunov controller: Front wheels torque. . . . .	144
4.37 Test 1 on Seville using Lyapunov controller: Reference trajectory tracking. . . .	145
4.38 Test 1 on Seville using Lyapunov controller: Lateral displacement error at the COG of the vehicle. . . . .	145
4.39 Test 1 on Seville using Lyapunov controller: Steering wheel angle. . . . .	146
4.40 Test 2 on Seville using Lyapunov controller: Desired longitudinal speed tracking. .	146
4.41 Test 2 on Seville using Lyapunov controller: Front wheels torque. . . . .	147
4.42 Test 2 on Seville using Lyapunov controller: Reference trajectory tracking. . . .	148
4.43 Test 2 on Seville using Lyapunov controller: Lateral displacement error. . . . .	148
4.44 Test 2 on Seville using Lyapunov controller: Steering wheel angle. . . . .	149
4.45 Experimental test track: Technology Park in Compiègne. . . . .	150
4.46 Computed curvature of the test track Technology Park. . . . .	150
4.47 Test on Technology Park using Lyapunov based controller: Reference trajectory tracking. . . . .	151
4.48 Test on Technology Park using Lyapunov based controller: Lateral displacement error at the vehicle's COG. . . . .	152
4.49 Test on Technology Park using Lyapunov based controller: Steering wheel angle. .	152
4.50 Test on Technology Park using Lyapunov based controller: Desired longitudinal speed tracking. . . . .	153
4.51 Test on Technology Park using Lyapunov based controller: Front wheels torque. .	153
4.52 Test 1 on Seville using I & I based controller: Desired longitudinal speed tracking. .	154
4.53 Test 1 on Seville using I & I based controller: Front wheels torque. . . . .	155
4.54 Test 1 on Seville using I & I based controller: Reference trajectory tracking. . .	156
4.55 Test 1 on Seville using I & I based controller: Steering wheel angle. . . . .	156
4.56 Test 1 on Seville using I & I based controller: Lateral displacement error. . . . .	157
4.57 Test 2 on Seville using I & I based controller: Desired longitudinal speed tracking. .	157
4.58 Test 2 on Seville using I & I based controller: Front wheels torque. . . . .	158
4.59 Test 2 on Seville using I & I based controller: Reference trajectory tracking. . .	158
4.60 Test 2 on Seville using I & I based controller: Lateral displacement error. . . . .	159
4.61 Test 2 on Seville using I & I based controller: Steering wheel angle. . . . .	159
4.62 Test 1 on Seville, controllers comparison: Desired longitudinal speed tracking. .	161
4.63 Test 1 on Seville, controllers comparison: Front wheels torque. . . . .	162
4.64 Test 1 on Seville, controllers comparison: Reference trajectory tracking. . . . .	163
4.65 Test 1 on Seville, controllers comparison: Steering wheel angle. . . . .	163
4.66 Test 1 on Seville, controllers comparison: Lateral displacement error. . . . .	164
4.67 Test 2 on Seville, controllers comparison: Desired longitudinal speed tracking. .	165
4.68 Test 2 on Seville, controllers comparison: Front wheels torque. . . . .	165

4.69	Test 2 on Seville, controllers comparison: Reference trajectory tracking. . . . .	166
4.70	Test 2 on Seville, controllers comparison: Lateral displacement error. . . . .	167
4.71	Test 2 on Seville, controllers comparison: Steering wheel angle. . . . .	167
4.72	Test 3 on Seville, controllers comparison: Desired longitudinal speed tracking at $V_x = 15km/h$ and $L_s = 4m$ . . . . .	168
4.73	Test 3 on Seville, controllers comparison: Front wheels torque. . . . .	169
4.74	Test 3 on Seville, controllers comparison: Reference trajectory tracking. . . . .	170
4.75	Test 3 on Seville, controllers comparison: Lateral displacement error. . . . .	170
4.76	Test 3 on Seville, controllers comparison: Steering wheel angle. . . . .	171
5.1	Combined navigation strategy . . . . .	173
5.2	Navigation strategy with only the local planner. . . . .	174
5.3	Dynamic obstacle overtaking with clothoid tentacles. . . . .	175
5.4	Longitudinal speed tracking and lateral displacement error with respect to the chosen tentacle in the dynamic obstacle avoidance scenario. . . . .	176
5.5	Control laws computed by the coupled controller in the dynamic obstacle avoid- ance scenario. . . . .	176
5.6	Combined navigation: Vehicle A and B speeds during the ACC phase. . . . .	177
5.7	Combined navigation: Inter-vehicles distance between A and B during the ACC phase. . . . .	178
5.8	Combined navigation: ACC phase and Phase 1 of the overtaking maneuver until $t = t_0 = 12s$ . . . . .	179
5.9	Combined navigation: Speed and acceleration profiles of vehicle A during the phase 1 of the overtaking maneuver . . . . .	180
5.10	Combined navigation: Phase 3 of the overtaking maneuver . . . . .	181
5.11	Combined navigation: Speed and accelerations profiles to execute the phase 3 of the overtaking maneuver . . . . .	181
5.12	Combined navigation: Speed profile tracking and desired reference tracking with the coupled Lyapunov controller . . . . .	182

# List of Tables

3.1 Geometric Description . . . . .	92
-------------------------------------	----

# Chapter 1

## Introduction

### Summary

---

1.1	Context and Motivations . . . . .	1
1.2	Problem formulation . . . . .	3
1.3	Contributions . . . . .	3
1.4	Thesis Outline . . . . .	6

---

### 1.1 Context and Motivations

In today's world, cars are considered as one of the best machines created by mankind. They have proved to be an effective way of transportation and they are prevalent in our society. As a result, ensuring the safety of the car's users is of primary importance. Unfortunately, vehicle accidents continue to be a leading cause of death for a human being. Some statistics show impressive numbers of killed and injured persons due to road accidents. According to the Association for Safe International Road Travel (ASIRT) statistics, road traffic crashes rank as the 9th leading cause of death and account for 2.2 % of all deaths globally. Nearly 1.3 million people die in road crashes each year, on average 3,287 deaths a day. An additional 20-50 million are injured or disabled. Data also indicate that over 90 % of the accidents are caused by human errors [APM<sup>+</sup>05]. For example, when the driver is distracted, or drunk or he exceeds the speed limits, he ends up by losing the control of the vehicle dynamics.

Consequently, over the past few decades, many research groups and industries started searching for solutions to reduce the number of road fatalities and injuries. Passive and active control systems were introduced to enhance the vehicle security.

The passive systems include devices whose role is to minimize the effects of the crash without acting directly on the vehicle. These devices, such as the seat belts and the airbags, are nowadays considered as standard automobile features.

On the other hand, active systems have been used in order to warn the driver and/or to induce some actions directly on the vehicle actuators. The vehicles equipped with such systems are called "Intelligent Vehicles". Among these systems, the ABS (Anti-lock Brake System) and the ESC (Electronic Stability Control) are the most commercial systems. The ABS helps the car to stop on a shorter distance in case of emergency braking. It automatically modulates the brake pressure when the driver makes an emergency stop [Bos00, KN00]. ESC evolved from ABS, but incorporated important additional capabilities [Zan02]. ESC is designed to improve a vehicle's lateral stability by electronically detecting and automatically assisting drivers in

dangerous situations (under-steering, over-steering or even spinning) and under unfavorable conditions (e.g., rain, snow, sleet, ice).

Afterwards, with the progress of intelligent tools in the vehicle, six levels of driving automation were defined, from 'no automation' to 'full automation'. More recently, researches have moved towards fully autonomous driving. This refers to a fully-autonomous system where the vehicle replaces the human driver, in every driving scenario including extreme environments. In that way, the vehicle will be able to securely navigate without any human intervention. In fact, autonomous vehicles are of high interest nowadays, since they have many applications in the human being's life. Besides the potential reduction in traffic collisions, generally caused by human errors, autonomous vehicles could provide enhanced mobility for the young, the elderly and the disabled people. Furthermore, if a human driver isn't required, automated vehicles could release the travelers from driving and navigation tasks, thereby replacing driving hours with more time for leisure, work or even activities such as reading or texting...Additional advantages could include increasing roadway capacity and thus minimizing traffic congestion. There would also be an improved ability to manage traffic flow, since automated vehicles could receive the necessary information by communications. Reduced traffic congestion and the improvements in traffic flow due to the use of autonomous cars will also translate into better fuel efficiency.

Motivated by all these advantages, several laboratories and industries have shown high interest in the development of autonomous vehicles [WSK<sup>+</sup>13].

Moreover, several competitions have been created in order to stimulate the research for the design of autonomous vehicles. Many competitions were funded by the US Defense Advanced Research Projects Agency (DARPA): The first DARPA Grand Challenge was held in 2004 with the aim to spur the development of technologies needed to create the first fully autonomous ground vehicles capable of completing a substantial off-road course within a limited time. The second driverless car competition of the DARPA Grand Challenge, which was held in 2005, was a 212 km off-road course while the third event, the DARPA Urban Challenge, that took place in 2007, extended the initial Challenge to autonomous operations in a mock urban environment. We can also cite the VisLab Intercontinental Autonomous Challenge (VIAC), conceived by VisLab as an extreme test of autonomous vehicles. It ran in 2010, involving four driverless vehicles driving with virtually no human intervention on an almost 16,000 kilometers (9,900 mi) trip. Another competition was also organized in 2010: the Autonomous Vehicle Competition (AVC) organized by the Hyundai-Kia Automotive Group in Korea. The race is driven on a 3.4 km-long course with mixed paved and unpaved roads. The autonomous cars had nine missions to accomplish, such as recognizing crosswalk traffic lights, parking, avoiding on-road obstacles, and passing slow driving cars. Recently, the Grand Cooperative Driving Challenge (GCDC) took place in the Netherlands, as one of the highlights of the i-GAME project, a European research project supported by the European Commission. The competition consists of three trials, all about testing the ability of the self-driving cars in executing a successful cooperative navigation.

Although vehicles that were developed for these challenges exhibit great autonomous driving performance, significant challenges in terms of technology, safety and price still remain for the commercialization of autonomous vehicles.

## 1.2 Problem formulation

One of the major challenges today, in the automobile domain, is to ensure a secure fully autonomous driving even in critical driving scenarios. Indeed, the vehicle autonomy can be accomplished by three main steps (see Fig. 1.1): The perception and localization, the trajectory planning and the vehicle control.

The first key step is the perception of the environment surrounding the vehicle using exteroceptive sensors such as cameras, lidar, radars, velodyne, etc. In this step, the lane boundaries, the lane markings, the pedestrians and eventually the road traffic participants and all the possible obstacles are detected. In most of the cases, the sensors data are used to generate local map grids representing the environment around the vehicle in order to facilitate the trajectory planning tasks. At this level, the vehicle is localized in a global coordinate system, which would allow to define the possible routes to reach the target position. The vehicle localization is accomplished using proprioceptive sensors, such as IMU's (Inertial measurement unit) and GPS (Global Positioning System).

The second essential step is the trajectory planning. In this level, we make use of the perception data to plan a secure and smooth trajectory for the vehicle. The trajectory planning objective is to provide the vehicle with a secure trajectory constrained by the vehicle dynamics limits, the navigation comfort and safety, and the traffic rules.

Once the desired trajectory is generated, the next step is to control the vehicle in order to track this trajectory with the desired speed profile also defined by the planning module. The vehicle control is indeed the control of the vehicle actuators, such as the steering wheel, the accelerator and the braking force, in order to manage the vehicle motions.

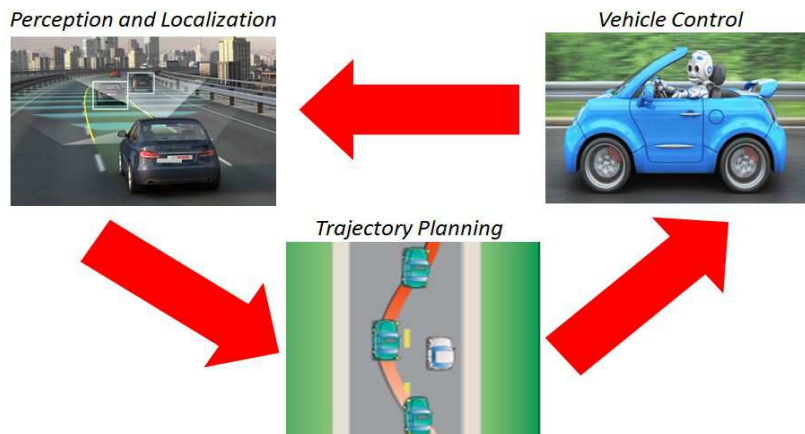


Fig. 1.1: Autonomous navigation key steps

## 1.3 Contributions

This thesis treats the second and the third essential parts of an autonomous navigation: The trajectory planning and the vehicle control.

Concerning the trajectory planning, a state-of-the-art study on the existing methods for trajectory planning, leads us to choose the reactive approach based on tentacles method. This method consists in generating virtual antennas called tentacles in the vehicle frame in order

to detect and avoid possible obstacles in an unknown environment. It was initially proposed by Hundelshausen, [HHH<sup>+</sup>08a], where the generated tentacles are of circular form. Some years after, they proposed to use the tentacles having the clothoids form in [HLH<sup>+</sup>11]. In this work, we make use of this method. In fact, a clothoid is a curve that changes its curvature linearly with respect to the curvilinear abscissa. Using this definition, we generate, at each time step, the trajectory candidates as clothoid tentacles that starts with a curvature representing the actual steering angle of the vehicle. In that way, the vehicle trajectories over time will be continuous and the changing from one local trajectory another, every time step, will be smooth and comfortable. The clothoid form is also a representative form of the road shape, and this fact will allow our vehicle to pass even the narrow driving corridors. In addition, the tentacles width is reduced when using the clothoids, whereas this width was set to almost twice the vehicle width in [HHH<sup>+</sup>08a]. Using the clothoid tentacles, we have reduced this width to nearly the vehicle width plus a safety distance, increasing thereby the navigable space. The tentacles method is a simple, very efficient, and fast-to-implement reactive local motion planning method. It allows an autonomous vehicle to safely navigate in previously unknown static terrain. However, this method does not really suit on-road driving scenarios, since its behavior is not really predictable. This fact motivated us to study the maneuver planning level in order to facilitate the clothoid tentacles task when overtaking a moving vehicle while respecting the road rules of safety.

From here, we have conducted a literature study to check out the existing approaches that deal with the overtaking maneuver planning. After this study, we decided to proceed with a simple method, often used in the literature by including some improvements. The developed strategy consists of generating a polynomial trajectory that will serve to change the lane while respecting the vehicle dynamics, the road rules and the security measurements, e.g. the vehicles inter-distance. The different methods existing in the literature proceed with several steps to generate a safe lane changing trajectory that does not violate the vehicle dynamics constraints. The contribution in this strategy is the consideration of the vehicle stability and safety constraints, to generate the lane changing trajectory, in a single and a simple step.

The overtaking maneuver planner is then combined with the local planner in order to provide a better navigation strategy. The maneuver planner decides when the overtaking will take place and plans the trajectories to be executed by the vehicle during the overtaking maneuver. The planned trajectories are then considered as reference trajectory for the local planner. This latter plans the local trajectories, each time step, that permits to track the reference trajectories, planned by the overtaking planner module, while avoiding possible obstacles. The local and the maneuver planner were validated under Matlab/Simulink and promising results were found.

The desired trajectory tracking problem is also addressed in this thesis. In fact, the vehicle control topic is a very active research topic in the automobile domain. Several control techniques can be found in the literature but most of these techniques address the lateral and the longitudinal vehicle dynamics control separately. Actually, the vehicle dynamics are strongly coupled, and in order to control the vehicle and handle its safety and stability, these dynamics coupling should be taken into account when designing the vehicle controller. Recently, some research groups have been addressing the problem of controlling the lateral and the longitudinal vehicle dynamics in a coupled way. Flatness based solution, sliding mode solution and some other techniques were used. In this thesis, this problem is also addressed and two new solutions are proposed.

The first coupled controller is developed based on Lyapunov control techniques. This solution allows the design in one step of a multivariable nonlinear controller dealing with both the longitudinal and the lateral dynamics of the vehicle. The developed controller can be considered as a generalization of the control law proposed in [APM<sup>+</sup>05], where a Lyapunov function is used to control the longitudinal dynamics of the vehicle. Here, a Lyapunov function with two terms was used to deal with both the longitudinal and lateral vehicle dynamics control.

The second coupled controller is based on the Immersion and Invariance control technique. Indeed, the immersion and invariance (I & I) theory consists in defining a target dynamics (manifold) and to design a control law that makes the target dynamics attractive and invariant. Using the fact that the lateral dynamics converge faster than the longitudinal dynamics of the vehicle, we define the manifold such that when it is reached, the lateral dynamics will be equal to the desired dynamics. Then, in order to reach this target, a sliding mode control (SMC) approach is used to define a suitable steering wheel angle that can guide the vehicle towards the defined manifold. Once the manifold is reached, the stabilisation of the longitudinal dynamics is considered. At this level, the convergence of the longitudinal dynamics is assured by the use of a Lyapunov function where the lateral variables are substituted by their equilibrium values.

The controllers design is based on a four wheeled vehicle model that is developed using robotics formalism. This latter assimilates the vehicle to a robot with multiple bodies related by joints and interacting between them. This modeling technique leads to a more accurate and complete model than the classical modeling tools and that's why it was chosen in this work. Indeed, we have chosen to proceed with the recursive formulation developed in [Maa11] and based on the method of Luh, Walker and Paul [LWP80] where Euler-Lagrange dynamics are used to derive the dynamic model of the vehicle. This formulation was adopted since it allows to automatically calculate the symbolic expressions of the dynamic model with a minimum number of numerical steps. Moreover, the algorithm complexity does not increase with the system's complexity (large number of variables) and the modification of the systems assumptions can be taken into account in a simple way (For example, the consideration or not of some components of the system).

A four wheeled planar vehicle model is then established using this formalism. The model has seven degrees of freedom (the vehicle longitudinal and lateral positions, the yaw angle and the angular positions of the four wheels). The developed model is then validated using Scaner-Studio simulator developed by Oktal and the validation results show that the developed model is close enough from the Scaner-Studio reference model and thus it can be used to develop lateral and longitudinal controllers for the vehicle (the developed vehicle model is planar).

The proposed controllers are validated by simulation under Matlab/Simulink using experimental data that was collected on an intelligent electric vehicle in the Heudiasyc laboratory. Furthermore, an experimental validation was conducted on a robotized vehicle Renault-ZOE to test the proposed solutions in many driving scenarios. The controllers are compared between them and with a classical PID based controller in order to highlight the developed coupled controllers contributions.

Finally, the combined local/maneuver planning strategy is validated under Matlab/simulink where the vehicle dynamics are represented using the developed model based on the robotics formalism and the vehicle dynamics are controlled using the Lyapunov based controller developed in this work. This validation was limited for low vehicle speeds and we aim to extend this validation even for mean and high speeds.

## 1.4 Thesis Outline

This report consists of three main chapters plus an introduction and a conclusion.

The first chapter consists of the introduction where the context, the motivations, the problem formulation, the contributions as well as the report outline are presented. The second chapter deals with the vehicle modeling. After the introduction, several modeling techniques are presented in the second section. Some are based only on the fundamental physics laws while others represent the vehicle as a multi-body system consisting of many subsystems interacting with each other. In the third section, we present the robotics formalism developed in [KK87] and adopted in our work regarding its simplicity and accuracy. In the fourth section, we present the four wheeled planar model developed using the robotics formalism. The model validation is presented in the fifth section while the final section concludes this chapter.

In the third chapter, we address the vehicle control topic. After an introduction, a state of the art on the existing control techniques is presented in the second section. While most of the presented techniques address the lateral and the longitudinal vehicle dynamics control separately, some approaches started recently focusing on the coupled control of the vehicle dynamics. The coupled control consists our domain of interest as well, since many critical driving situations involving the safe handling of vehicles require coupled control. Two developed coupled controllers are presented afterward in the third section. The fourth section presents the controller's validation results by simulation and the fifth section presents the experimental results. We finish this chapter with some conclusions in the sixth section.

The fourth chapter deals with the trajectory planning topic. After an introduction, the local trajectory planning problem is treated in the second section. In this section, we present a state of the art on the local trajectory planning methods. Then we develop the tentacles method adopted in this work and we present some validation results of the chosen method. The third section deals with the maneuver planning issue, especially the overtaking maneuver. After presenting the existing approaches, we present the developed approach and the validation results of this approach. In the fourth section, the maneuver module is combined with the local one in order to improve the planning strategy. The planning module is then validated using the vehicle model and the Lyapunov based coupled controllers that were developed in this work and presented in the previous chapters. This chapter ends with some conclusions and remarks. Finally, we conclude this report and present some interesting future works in the last chapter.

# Chapter 2

## Trajectory Planning

### Summary

---

<b>2.1</b>	<b>Introduction</b>	<b>7</b>
<b>2.2</b>	<b>Local Planning with Clothoid Tentacles Method</b>	<b>8</b>
2.2.1	Existing Local Planning Techniques	8
2.2.2	Tentacles Method with Clothoid Form	17
2.2.3	Tentacles Method Validation	25
<b>2.3</b>	<b>Maneuver Planning: Overtaking Maneuver</b>	<b>34</b>
2.3.1	Existing Approaches for the Overtaking Maneuver Planning	34
2.3.2	Developed Overtaking Maneuver	36
2.3.3	Validation of the maneuver planning algorithm	45
<b>2.4</b>	<b>Local/Maneuver Combined Planning Approach</b>	<b>61</b>
<b>2.5</b>	<b>Conclusion</b>	<b>62</b>

---

### 2.1 Introduction

The planning module in an autonomous navigation can be considered as the system's brain where the vehicle trajectory for the next seconds is planned. In general, planning for autonomous driving is divided into three hierarchical classes: route planning, maneuver choice and trajectory planning.

Route planning is concerned with finding the best global route from a given position to a destination, supplemented occasionally with real-time traffic information. This planning level is not discussed within the scope of this chapter and readers are referred to [BIS09] for more details on a route planner.

The maneuver planning is a high-level description of the vehicle motion, regarding the vehicle position and speed on the road. Maneuver planning addresses the problem of taking the best high-level decision for the vehicle (for example: going straight, turning left or right, overtaking ...), while taking into account the path specified by the path planning level.

The lower planning level is the trajectory planning concerned with the real-time planning of the actual vehicle transition from one feasible state to the next, constrained by the vehicle dynamics limits, the navigation comfort, the traffic rules and the possible obstacles including other road users as well as lane boundaries. As a result, the trajectory is represented as a sequence of

states visited by the vehicle, parameterized by time and, possibly, velocity. Trajectory planning (usually referred to as motion planning) is scheduled at regular intervals of time, the length of which largely depends on the frequency of receiving new sensor data.

This chapter treats the trajectory planning module in the second section and the maneuver planning module, especially the overtaking maneuver in the third one. A combined navigation strategy including the local and the maneuver planner is then proposed.

## 2.2 Local Planning with Clothoid Tentacles Method

Once the best path and the best maneuver are selected, the problem is reduced to finding the best trajectory that satisfies the motion model and the state constraints while guaranteeing the comfort of the passengers and the smoothness of the trip. The approaches caring about trajectory planning are local, they do not seek to model the environment as a whole but rather they use sensor measurements to deduce secure orders [TMD<sup>+</sup>06]. In this section, some local planning methods developed in the literature with their respective strengths and limitations are exposed. We present then the developed tentacles approach with some validation results.

### 2.2.1 Existing Local Planning Techniques

In the following, we present the commonly used local planning techniques that were developed in the literature:

#### 2.2.1.1 Potential fields Method

This method defines an objective function that affects large potential to obstacles and low potential to the objective points of the trajectory [Kha86]. Thus, the problem is reduced to an optimization problem that aims to find the commands causing the robot to a global minimum of the potential function. Fig. 2.1 represents the potential field approach. This method is robust for on-line collision avoidance with proximity sensors since it doesn't require an accurate knowledge of the obstacles shapes. Nevertheless, its implementation requires a lot of calculation which may be constraining in real-time navigation applications. In addition, the function may converge to a local minimum instead of the global one. There are many extensions to this method such as the virtual force fields [BK89], the field vector histograms [BK91],  $VFH^+$  extensions [UB98], and,  $VFH^*$  [UB00].

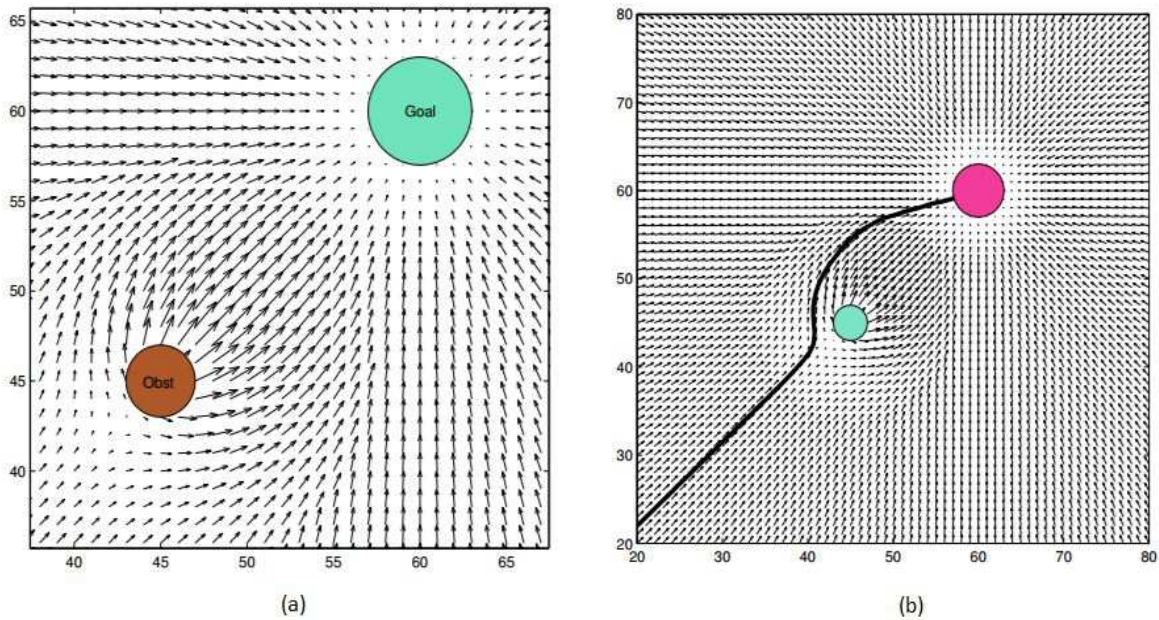


Fig. 2.1: Potential Fields Principle [Goo02]: (a)The potential field generated when there is a goal and an obstacle, (b) The selected trajectory.

### 2.2.1.2 Dynamic Window

The dynamic window approach is derived directly from the dynamics of the robot, and is especially designed to deal with the dynamic constraints imposed by the limited velocities and accelerations of the robot. The search space is also reduced by eliminating the commands that lead to a collision with an obstacle (see Fig. 2.2). Once the navigable space is defined, the control inputs that optimize the objective function are derived [FBT97]. Although this approach yields very good results for obstacle avoidance at high velocities, the problem of local minima persists [BK99].

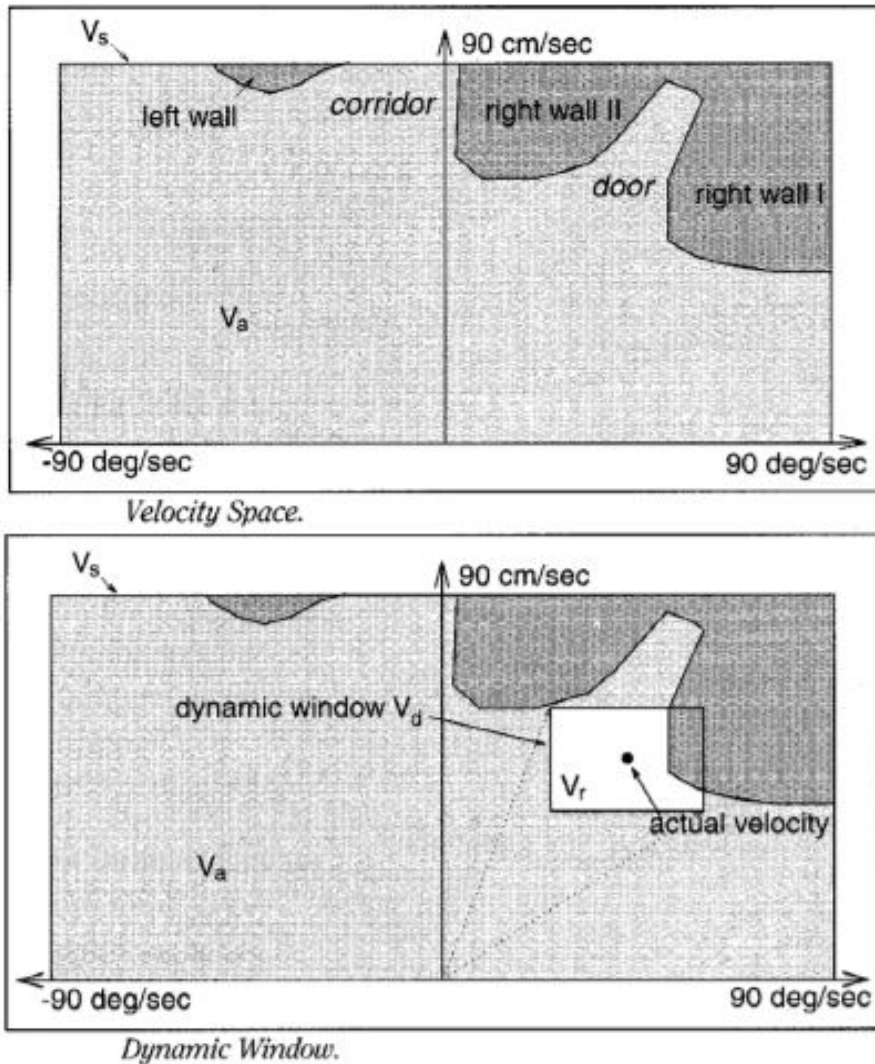


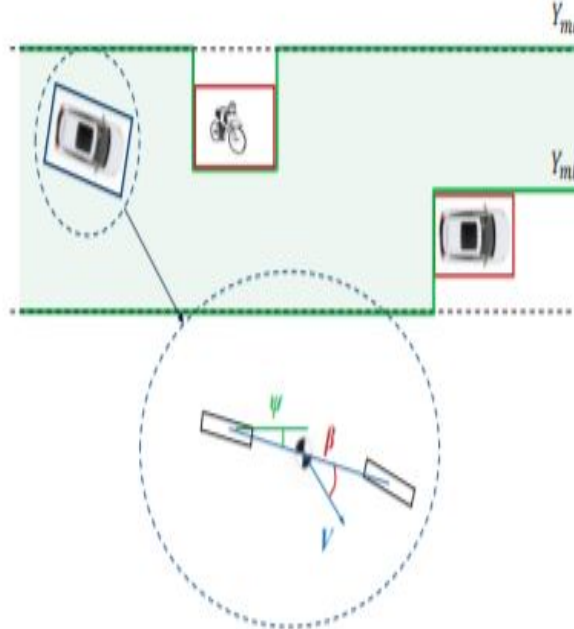
Fig. 2.2: Dynamic window approach: search space [FBT97]. In the figure,  $V_s$  is the search space of the possible velocities,  $V_a$  corresponds to the admissible velocities and  $V_r$  is defined as the intersection of the restricted areas ( $V_r = V_s \cap V_d \cap V_a$ ).

### 2.2.1.3 Model Predictive Control

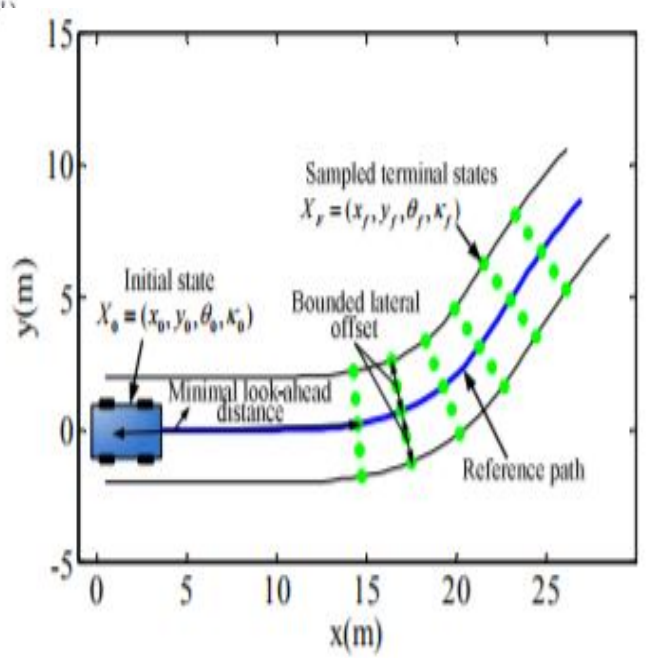
This approach combines aspects of control engineering within the planning module. A dynamic model for the vehicle is used and, through it, inputs from the controller are sampled about the future evolution of the vehicle's motion. From the dynamic model and the control inputs, the optimization problem of finding the best trajectory for the vehicle is solved. In [MNK<sup>+</sup>13b], this method was performed inside the driving corridor (see Fig. 2.3a), which renders it more appropriate for structured domains (e.g. highways). Its performance is not dependent on the increase or decrease of the number of obstacles, but the more variables used to model the vehicle, the harder it gets to optimize its trajectories.

In [LSZL14], a Model Predictive Trajectory Generation planner was employed to generate the paths, which connect the vehicle current state with the sampled terminal states of the reference path (see Fig. 2.3). After that, the best path is selected from the collision-free paths based on an evaluation cost function, which considers : smoothness, obstacle proximity and deviation

from the reference path. The developed planner is very sensitive to the considered variables. Besides, it was tested only for static obstacle avoidance, it requires an important number of on-line calculations.



(a) MPC associated to the driving corridor [MNK<sup>+</sup>13b].



(b) MPC: Terminal states sampling [LSZL14].

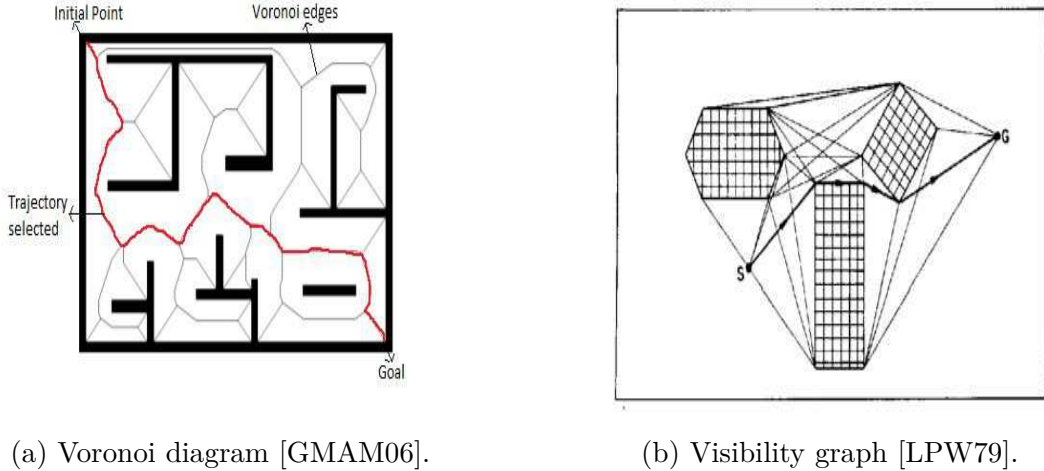
Fig. 2.3: Model Predictive Control for local planning.

#### 2.2.1.4 Roadmap Methods

Roadmap methods are based on the connectivity of the navigable space, where a sequence of curves between the initial point and the end point is selected. Voronoi Diagram [DTMD10] is an example of the application of the roadmap methods. It is based on partitioning the space into regions, in such a way that each present obstacle will be in a separate region. Therefore, the vehicle navigates along Voronoi edges, with a maximum distance from the obstacles. Fig. 2.4a shows an example of Voronoi diagram with the chosen safe path that connects the initial point to the objective point.

The visibility graph [LPW79] is another application of the roadmap methods. It consists of connecting a set of point locations while omitting the edges crossed by an obstacle. Fig. 2.4b shows a visibility graph where: The checked areas represent obstacles. The solid lines are the edges of the graph and connect the vertices of the obstacles, while the line in bold black is the chosen path.

The roadmap methods are guaranteed to be complete, meaning that if a free path exists, it will find it; however, the trade-off for the accuracy is a difficult mathematical process.



(a) Voronoi diagram [GMAM06].

(b) Visibility graph [LPW79].

Fig. 2.4: Roadmap methods.

### 2.2.1.5 Partial Motion Planning approach (PMP)

The Partial Motion Planning approach [BPFP06] uses a short time horizon combined with the Rapidly-exploring Random Trees (RRTs) approach [LaV98] and the concept of Inevitable Collision States (ICS) for a safety check. As can be seen in Fig. 2.5, if an ICS is found, an alternative path is searched and at each time step, the nodes are expanded in an RRT fashion. Even though, the Inevitable Collision States definition guarantee that a collision will not happen (see Fig. 2.6), it requires a full knowledge of the surroundings of the vehicle [AWB11].

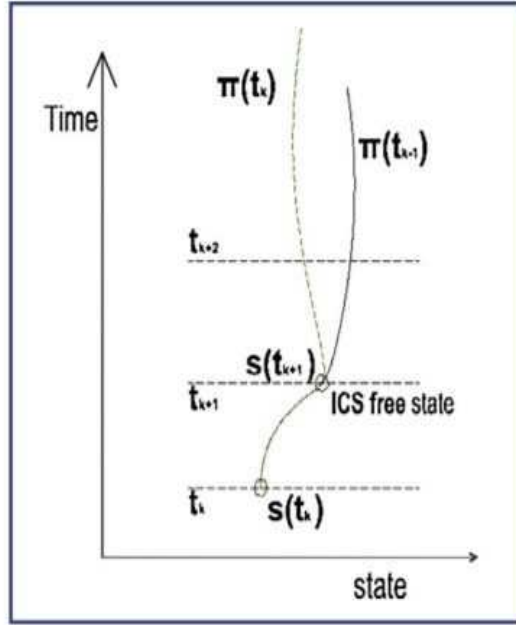


Fig. 2.5: Partial motion planning concept [BPFP06]. In the figure,  $\pi$  means the local planned trajectory

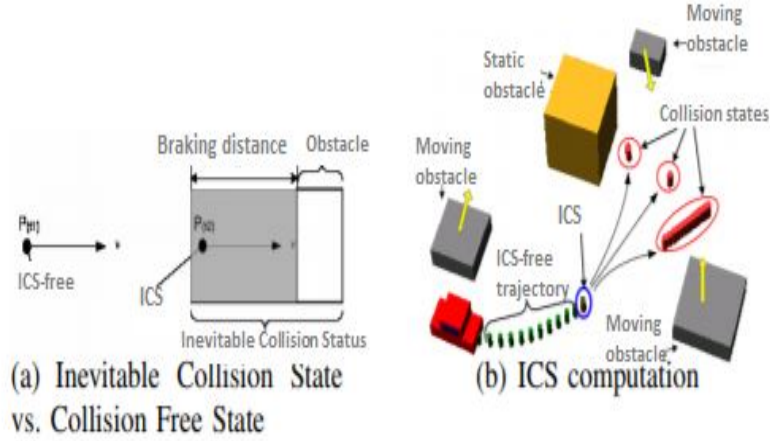


Fig. 2.6: Inevitable collision states (ICS) [BPFP06].

### 2.2.1.6 State Lattices Planners

The lattice grid is constructed by repeating primitive paths connecting possible states of the vehicle (see Fig. 2.7), thus reducing the planning problem to a boundary problem of connecting the original state with the required final state [MUDL11]. Since the pre-computation of edges is possible, a low computational power is needed. Besides, the smoothness and the optimality of the path are guaranteed within the given lattice. This approach is a resolution complete method and is generally appropriate for highly constrained environments. However, it may present some difficulties in dealing with evasive maneuvers and it may lead to oscillations in the vehicle yaw angle. Some extensions of the method have been presented, such as the spatiotemporal state lattices introduced to deal with the environment dynamicity [ZS09], and the multi-resolution state lattice introduced in [LF09] to overcome the exhaustive sampling that may lead to unnecessary computational complexity.

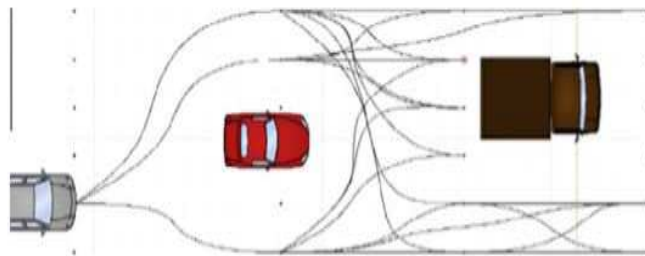


Fig. 2.7: Lattice planner for on-road driving [MNK<sup>+</sup>13a].

### 2.2.1.7 Geometric Curves

Possibly the most popular technique used for on-road autonomous driving in the local search level is the one in which a search space contains a certain geometric curve and several lateral shifts of this curve. Each candidate path is then evaluated through a cost function with several considerations, such as distance and time costs, acceleration and collision checking. The

geometric representations of the trajectories include polynomials, Bezier curves, spline curves, arcs and clothoids:

- In [DFM09], the authors proposed a trajectory generation algorithm which optimizes a set of trajectory candidates illustrated by second order polynomials trajectories, according to the error between the final states and the objective final state. The vehicle velocity and acceleration profiles are computed for each point. Nevertheless, no obstacles are taken into account and the computational complexity increases when the required convergence points are far from the initial state or are unreachable because of the vehicle dynamics constraints (see Fig. 2.8).

In [CSC<sup>+</sup>10], fourth order polynomials are used to generate the vehicle trajectory candidates. A dynamic bicycle model with the flatness property is used to describe the motion of the vehicle. The approach considers overtaking and car-following scenarios at different cost functions for each case, based on a safe distance constraint. In the simulation tests, it is assumed that the vehicles employ a constant velocity; something which may not be applicable to real-world conditions.

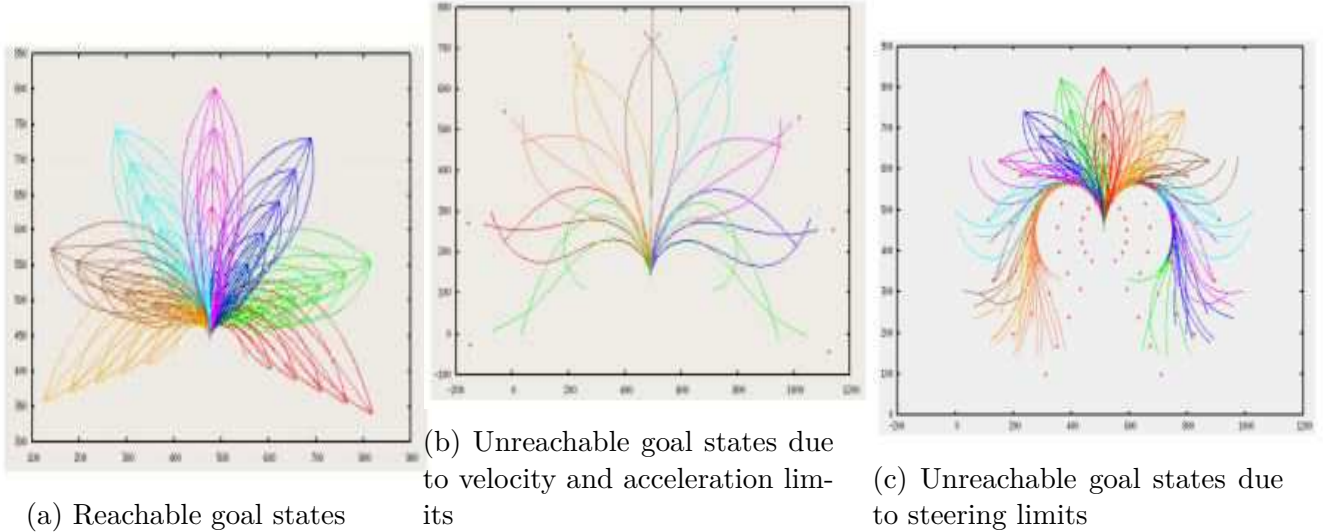


Fig. 2.8: Polynomial trajectories generated in [DFM09].

- Cubic Bezier curves are used in [MYZ12] to generate the vehicle trajectory (see Fig. 2.9). The cost function used includes weights for the length of the trajectory, its smoothness and the offset from the central line of the lane used as a reference path. The obstacles are considered as circles and the collision checking is performed via colliding trajectories which can lead to over-computations.

Cubic Bezier curves are also used in [PGVO13] to generate trajectories in roundabout scenarios; however, collision checking, lateral accelerations and curvature constraints are omitted. In [GPL<sup>+</sup>14], fourth degree Bezier curves are used for better results. Although the road constraints and the velocity and acceleration constraints are considered, the authors assume low speeds and consider only static obstacles.

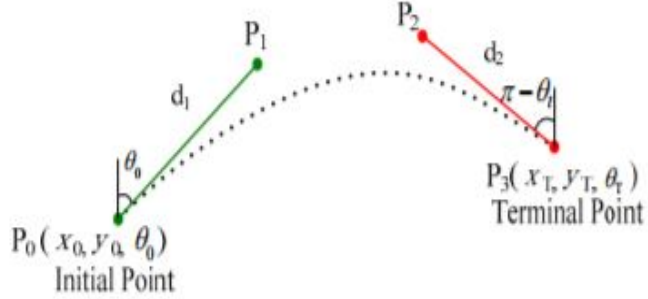


Fig. 2.9: Bezier curve generated in [MYZ12] and shown in dashed line.

- The spline curves were used in [WGR11], where Akima splines interpolation is used to generate the trajectories which comply with checkpoints given by the path planning module and taking into account the road signs (see Fig. 2.10). The trajectories are evaluated by their distance and time to get to the next checkpoint as well as collisions with obstacles. Demonstrations are presented in a simulated environment, as well as a real-world vehicle, and were claimed to be sufficient for the real world autonomous driving, although extensive results are not provided.

In [GD14], a learning method is proposed to imitate human driver's behavior. The trajectories generated to interpolate between the way points given from higher planning modules take the form of splines and are constrained to curvature, speed and acceleration. However, the environment is supposed to be traffic-free, which is not representative for on-road driving. Besides, a substantial quantity of naturalistic driving data must be used for learning human driving patterns.

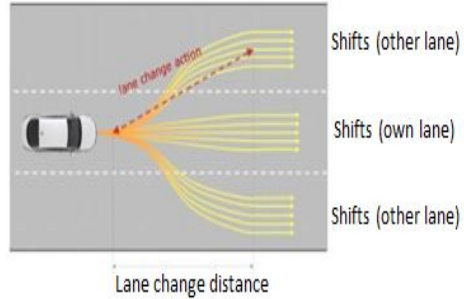


Fig. 2.10: Spline curves used in [WGR11] for trajectory planning.

- The circular form was also used in the literature. In [SDZ<sup>+</sup>14], an optimal trajectory for the lane changing maneuver is chosen through a tradeoff between efficiency and comfort. The trajectory is generated as the combination of two circular arcs. The overall collision probability of the candidate trajectories is assessed with certain confidence level, by predicting the possible future trajectories of the obstacles.

In [HHH<sup>+</sup>08b], an egocentric occupancy grid is used to represent the environment and consequently to decide about the trajectory candidates navigability (see Fig. 2.11). The generated

trajectory candidates are called 'Tentacles' since the method is inspired by the behavior of an insect that uses its antennae to detect and avoid obstacles. The tentacles method will be explained in detail in the next section, since it is used in this work. The weakness of the arcs-of-circle shape appears in considering all the tentacles generated for a certain speed as trajectory candidates even if their curvature is not well-suited to the current vehicle steering angle. Moreover, the width of each tentacle, introduced to take into account the transient phase needed to converge to the trajectory, is much larger than necessary (almost twice the width of the vehicle).

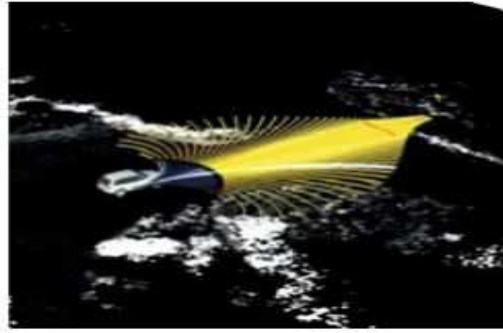


Fig. 2.11: Tentacles method with circular arcs form developed in [HHH<sup>+</sup>08b].

- In [TMD<sup>06</sup>, CLS12], the trajectory candidates are generated in a way to allow the vehicle to go to the left or the right side with different offset shifts, while remaining substantially parallel to the base path (see Fig. 2.12). This form of trajectories is well suited for high speed but its major drawback is its dependence on the reference path.

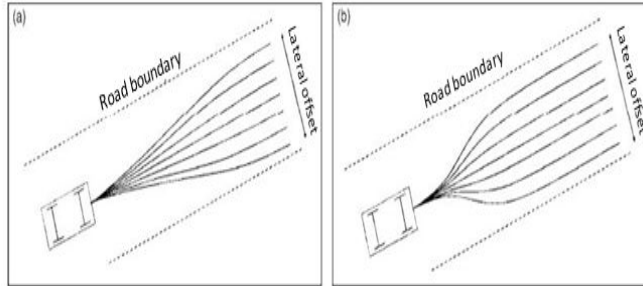


Fig. 2.12: Path planning in a 2D search space [TMD<sup>06</sup>]: Paths that change lateral offsets with (a) the minimum and (b) the maximum possible lateral acceleration.

- In [BMZ<sup>12</sup>], different inputs such as the results of obstacle detection, ditch localization, lane detection, and global path planning information are merged together using potential fields to build a representation of the environment in real time. Kinematically feasible trajectories, based on vehicle dynamics and having the shape of clothoids, are generated on a cost map (see Fig. 2.13). The approach was demonstrated experimentally in very different environments including extreme road conditions.

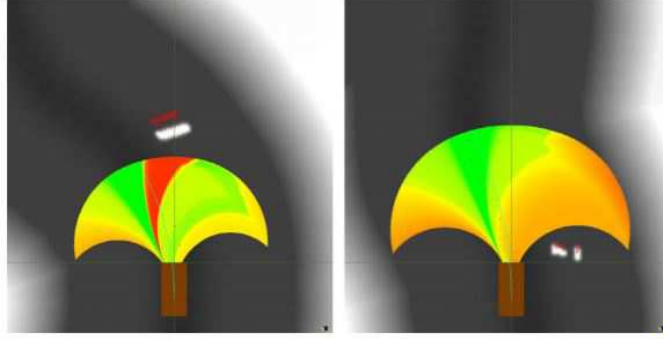


Fig. 2.13: Evaluation of vehicle trajectories: green, yellow, and red curves represent evaluated trajectories; the blue trajectory represents the best one. In the potential map dark areas represent points at low cost, while the light areas are high cost points generated by obstacles.

In the present work, the geometric curves method, assumed to be the simplest method to be implemented, is adopted for on-road trajectory planning for autonomous vehicles. Namely, the tentacles method with clothoids form is used. This approach is a fast-reactive method that considers the current steering angle of the vehicle, resulting in smooth and continuous curvature variations. We also claim that the clothoid shape is the most representative of the road shape. In the next section, the clothoid tentacles method is presented. Some simulations and preliminary experimental results are then exposed.

### 2.2.2 Tentacles Method with Clothoid Form

The developed local planning algorithm aims to guide the vehicle to navigate on a given reference trajectory while avoiding every possible collision. We present in Fig. 2.14 the navigation strategy based on the tentacles method. The first step is the clothoids tentacles generation depending on the vehicle state (speed, steering angle...). Then, to guarantee a secure navigation, we generate around each tentacle a classification zone defined later in this section. In parallel, using sensors data, we construct an occupancy grid that represents the environment state around the vehicle. The superposition of the classification areas with the occupancy grid allows us to determine which tentacle can be classified as navigable. If we find several navigable tentacles, we have to choose the best one using certain criteria defined afterward. The best tentacle is then considered as a local trajectory to execute. If we can't find any navigable tentacle, we search the tentacle having the greatest distance to the first obstacle and we proceed to brake the vehicle with a constant deceleration along this tentacle.

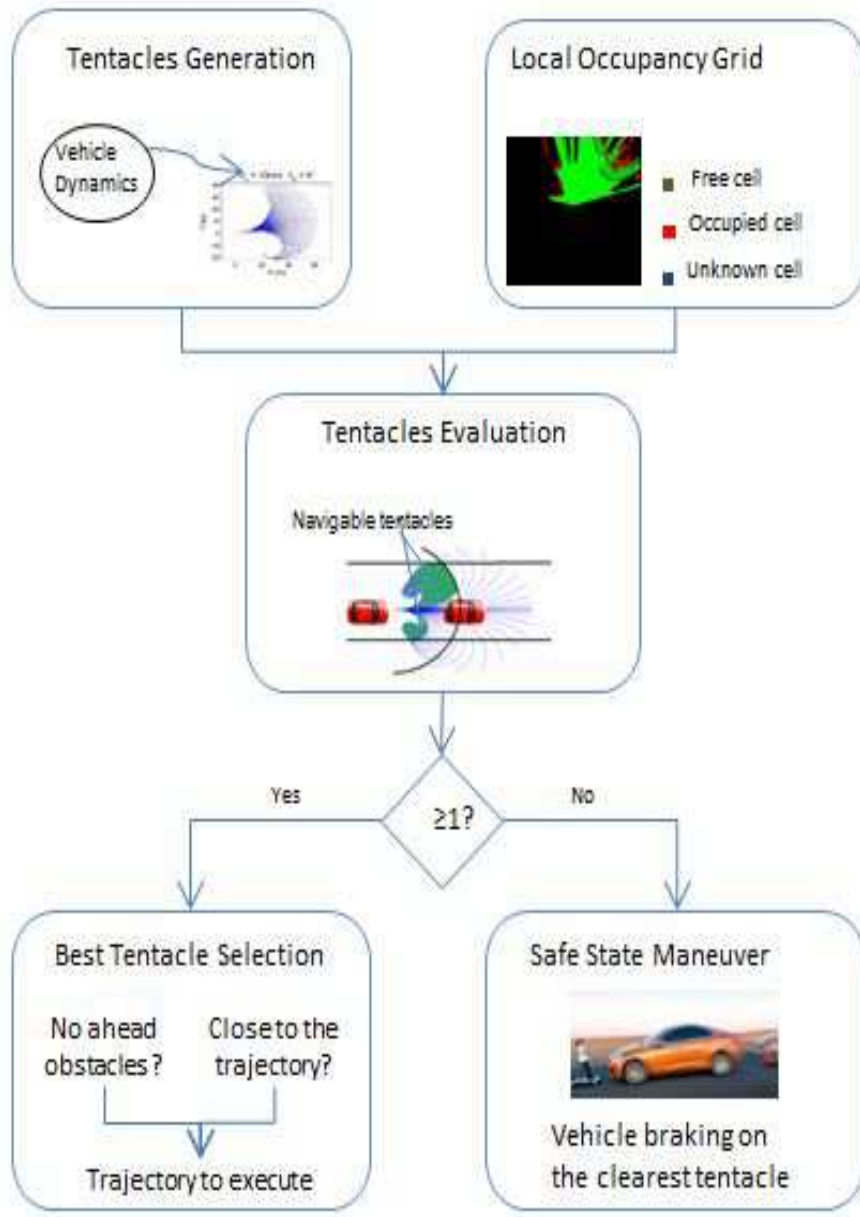


Fig. 2.14: Tentacles method strategy [HHH<sup>+</sup>08b].

### 2.2.2.1 Occupancy Grid

The perception of the environment surrounding the vehicle is the first key step in an autonomous navigation. Numerous works on the localization, the perception and the generation of occupancy grids were developed within the ASER team at Heudiasyc laboratory. In this work, we make use of the occupancy grids generated in [Mor13] for an experimental evaluation of the tentacles method. However, for a simulation validation, the occupancy grids are generated under Matlab/Simulink using the Scaner-Studio simulator data. The use and the generation of the occupancy grids are detailed in the Section 2.2.3. Indeed, the occupancy grid is a metric and discrete representation of the environment, used in robotics. It represents the environment around the vehicle by a set of square cells where each cell could correspond to a free or occu-

pied space. To construct it, the vehicle must be equipped with a set of sensors (camera, lidar, radar...). In [Mor13], a lidar installed in the front axis of the vehicle is used (see Fig. 2.15). The lidar uses laser beams to detect the presence of obstacles and determine their positions. It provides a measurement every 100ms.



Fig. 2.15: The LIDAR mounted on the experimental vehicle CARMEN in Heudiasyc laboratory.

At every sampling time, the sensor provides a new measure. The instant occupancy grid, considered to be ego-centered around the vehicle, is built. We do not accumulate data as the frequency used for grid generation seems sufficient to ensure safe navigation.

### 2.2.2.2 Tentacles Generation

A set of 41 tentacles is generated at each computation step, namely, every 100 ms. The tentacles are generated in the vehicle frame. They start from the vehicle center of gravity and take the form of clothoids.

Indeed, a clothoid has a linearly variable curvature with respect to the curvilinear abscissa. Its expression is given by

$$\rho = As,$$

where  $\rho$  is the clothoid curvature,  $s$  is the curvilinear abscissa and  $A$  is a constant representing the clothoid parameter. For ease of computation, we usually set  $A = \frac{2}{k^2}$ , where  $k$  is also a constant.

To draw a clothoid, we make use of a function, as in [BF13], that takes as inputs:

- The clothoid curvature at initial point:  $\rho_0$
- The curvature variation with respect to the curvilinear abscissa:  $\frac{\Delta\rho}{\Delta s}$
- The length of the clothoid curve from an initial to a final point:  $L_{tentacle}$
- The number of points along the clothoid:  $n$
- The orientation with respect to the x axis at the initial point of the clothoid:  $\phi_0$
- The coordinates of the initial point:  $(x_0 \ y_0)$ .

The clothoid is sampled into  $n$  points and for each point  $i$ ,  $i = 1 \dots n$ , we compute the Cartesian coordinates as follows:

Let  $s_i$  be the curvilinear abscissa of the point  $i$ :

$$s_i = \frac{L_{tentacle}}{n - 1}(i - 1) \quad (2.1)$$

The curvature at the point  $i$  is then computed by:

$$\rho(s_i) = \frac{\Delta\rho}{\Delta s} s_i + \rho_0. \quad (2.2)$$

Let  $x(s_i), y(s_i), \phi(s_i)$  be the Cartesian coordinates of the point  $i$  as well as the orientation of the curve at this point. We can write:

$$\begin{aligned} \frac{dx}{ds}(s_i) &= \cos(\phi(s_i)) \\ \frac{dy}{ds}(s_i) &= \sin(\phi(s_i)) \\ \frac{d\phi}{ds}(s_i) &= \rho(s_i). \end{aligned} \quad (2.3)$$

The Cartesian coordinates and the orientation angle at the point  $i$  are given by:

$$\begin{aligned} x(s_i) &= x_0 + \int_0^{s_i} \frac{dx}{ds}(s) ds \\ &= x_0 + \int_0^{s_i} \cos(\phi(s)) ds \\ y(s_i) &= y_0 + \int_0^{s_i} \frac{dy}{ds}(s) ds \\ &= y_0 + \int_0^{s_i} \sin(\phi(s)) ds \\ \phi(s_i) &= \phi_0 + \int_0^{s_i} \frac{d\phi}{ds}(s) ds \\ &= \phi_0 + \int_0^{s_i} \rho(s) ds. \end{aligned} \quad (2.4)$$

Using (2.2), we can derive  $\phi(s)$  as follows:

$$\begin{aligned} \phi(s_i) &= \phi_0 + \int_0^{s_i} \left( \frac{\Delta\rho}{\Delta s} s + \rho_0 \right) ds \\ &= \phi_0 + \frac{\Delta\rho s_i^2}{\Delta s} + \rho_0 s_i. \end{aligned} \quad (2.5)$$

Finally, integrating (2.5) in (2.4), yields the computation of the Cartesian coordinates of the point  $i$  as follows:

$$\begin{aligned} x(s_i) &= x_0 + \int_0^{s_i} \cos\left(\phi_0 + \frac{\Delta\rho s^2}{\Delta s} + \rho_0 s\right) ds \\ y(s_i) &= y_0 + \int_0^{s_i} \sin\left(\phi_0 + \frac{\Delta\rho s^2}{\Delta s} + \rho_0 s\right) ds. \end{aligned} \quad (2.6)$$

Consequently, we can draw the clothoid specifying just the initial curvature  $\rho_0$ , the curvature variation with respect to the clothoid's arclength variation ( $\frac{\Delta\rho}{\Delta s}$ ), and the clothoid length  $L_{tentacle}$  ( $x_0$ ,  $y_0$  and  $\phi_0$  are set to zero since the clothoids are generated in the vehicle frame).

We assume that all the tentacles have the same length  $L_{tentacle}$  at a given vehicle speed  $V_x$ . This length is set using an empirical equation as:

$$L_{tentacle}(m) = \begin{cases} t_0 V_x - L_0 & V_x > 1(m/s) \\ 2 (m) & V_x \leq 1(m/s) \end{cases} \quad (2.7)$$

where  $t_0 = 7s$  and  $L_0 = 5m$  are chosen empirically so that the clothoid length is larger than the distance required to stop the vehicle in emergency cases.

The initial curvature of the tentacles is computed using a kinematic equation relating the current vehicle steering wheel angle  $\delta_0$ , the vehicle wheelbase  $L$  and the executed curvature  $\rho_0$  [Raj11], namely,

$$\rho_0 = \frac{\tan \delta_0}{L} \quad (2.8)$$

We define the maximum curvature  $\rho_{max}$  as the maximum trajectory curvature that a vehicle can execute at a given vehicle speed  $V_x$  without loosing lateral stability.  $\rho_{max}$  is then given by [Raj11]:

$$\rho_{max} = \frac{a_{y_{max}}}{V_x^2} \quad (2.9)$$

where  $a_{y_{max}}$  is the maximum lateral acceleration that guarantees the stability of the vehicle.

In order to generate the set of tentacles, we proceed as following:

- For the first tentacle (tentacle 1): we consider that a curvature of  $-\rho_{max}$  is reached at a length  $L_s$  of the tentacle, where  $L_s$  is the distance of collision defined later in this section. Therefore, the curvature variation with respect to the clothoid arclength variation of this tentacle,  $(\frac{\Delta\rho}{\Delta l})_1$ , is computed as:

$$(\frac{\Delta\rho}{\Delta l})_1 = \frac{-\rho_{max} - \rho_0}{L_s}.$$

- For the last tentacle (tentacle 41): we consider that a curvature of  $+\rho_{max}$  is reached at the length  $L_s$  of the tentacle. The curvature variation with respect to the clothoid arclength variation of this tentacle,  $(\frac{\Delta\rho}{\Delta l})_{41}$ , is computed as:

$$(\frac{\Delta\rho}{\Delta l})_{41} = \frac{\rho_{max} - \rho_0}{L_s}.$$

- For the other tentacles (tentacle  $i = 2\dots40$ ), the curvature variation is obtained by sampling the vector  $[(\frac{\Delta\rho}{\Delta l})_1 : (\frac{\Delta\rho}{\Delta l})_{41}]$  into 41 samples. The curvature variation with respect to the clothoid arclength variation for the tentacle  $i$ ,  $(\frac{\Delta\rho}{\Delta l})_i$ , is then computed as follows:

$$(\frac{\Delta\rho}{\Delta l})_i = (\frac{\Delta\rho}{\Delta l})_1 + \frac{(\frac{\Delta\rho}{\Delta l})_{41} - (\frac{\Delta\rho}{\Delta l})_1}{41 - 1}(i - 1). \quad (2.10)$$

Fig. 2.16 shows the clothoids computed for different speeds and different initial steering angles.

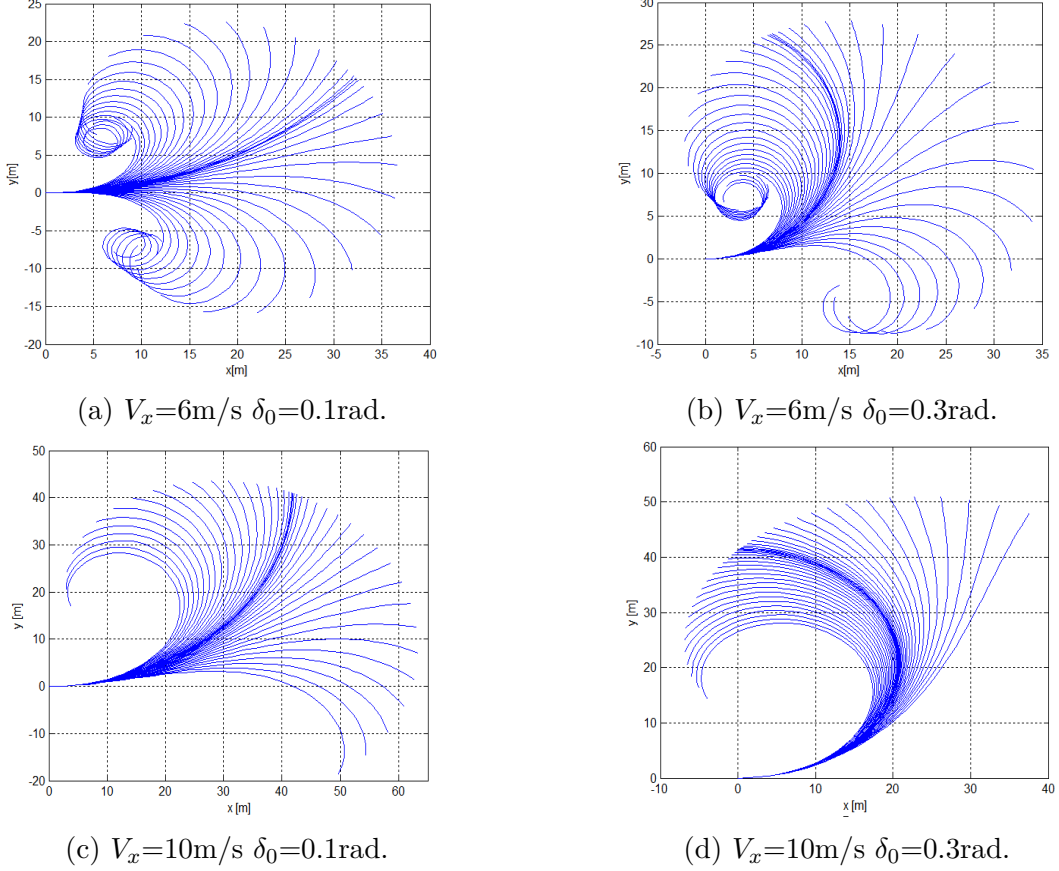


Fig. 2.16: Different clothoids at different speeds and different initial steering angles.

### 2.2.2.3 Navigable Tentacles Selection

The superposition of the generated tentacles with the occupancy grid allows the classification of the tentacles between navigable and non-navigable tentacles. In a first step, since the vehicle cannot precisely follow the tentacle shape, and to take into account the vehicle width, a classification zone is generated around the tentacle in order to guarantee a secure navigation. Using the clothoids form, the width of the classification zone ( $2d_c$  as can be seen in 2.17), is taken slightly greater than the vehicle width, unlike the case of circular arcs where the classification zone width is taken almost two times greater than the vehicle width. In our work, the value of  $d_c$  is empirically specified depending on the vehicle speed  $V_x$ :

$$d_c = \begin{cases} 1.4 + 0.2 \frac{V_x}{3} [m] & V_x < 3\text{m/s} \\ 1.6 + 0.6 \frac{V_x - 3}{15} [m] & 3\text{m/s} < V_x < 15\text{m/s} \end{cases}$$

The geometrical description of the classification area is shown in Fig. 2.17.

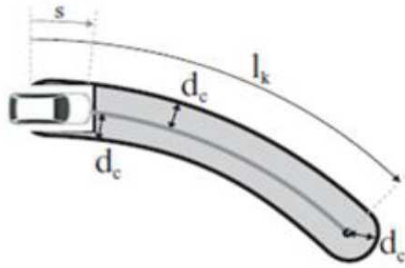


Fig. 2.17: Classification zone [HHH<sup>+</sup>08b].

In the second step we define the collision distance  $L_s$  as the distance required to stop the vehicle traveling at a speed  $V_x$  with the maximum longitudinal deceleration  $a_{x_{max}}$ :

$$L_s = \frac{V_x^2}{a_{x_{max}}} \quad (2.11)$$

To maintain the passenger's comfort,  $a_{x_{max}}$  is set to  $1.5 \text{ m/s}^2$ .

Therefore, the tentacle is classified as non-navigable if an obstacle is detected within a distance less than the collision distance  $L_s$ . If the obstacle is beyond  $L_s$ , the tentacle is classified as navigable. Fig. 2.18 shows an example of classification of the tentacles in the presence of an obstacle.

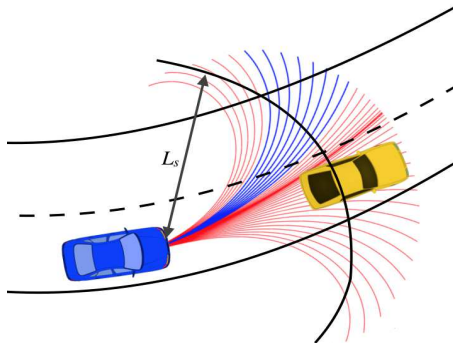


Fig. 2.18: Tentacles classification: The red tentacles are the occupied ones while the blue tentacles are navigable.

#### 2.2.2.4 Best Tentacle Choice

Only one tentacle among the navigable tentacles is chosen as the best tentacle using two criteria  $V_{clearance}$  and  $V_{trajectory}$ . The criteria are calculated for each navigable tentacle, normalized to the interval  $[0, 1]$  and then linearly combined into a single function  $V_{combined}$  defined by:

$$V_{combined} = a_0 V_{clearance} + a_1 V_{trajectory}$$

where  $a_0$  and  $a_1$  are the weighting parameters that can be used to change the planning purposes. This amounts to prefer a criteria more than another.

The clearance and the trajectory criteria are defined as follows:

- Clearance Criterion: This criterion expresses the distance that the vehicle can drive along a tentacle before hitting an obstacle. Its value is directly related to the distance between the vehicle and the first obstacle found on the tentacle,  $L_0$ , as [HHH<sup>+</sup>08b]:

$$V_{\text{clearance}}(L_0) = \begin{cases} 0 & \text{free tentacle} \\ 2 - \frac{2}{1+e^{-c*L_0}} & \text{otherwise} \end{cases} \quad (2.12)$$

where  $c$  is a constant calculated to obtain  $V_{\text{clearance}}(L_{0.5}) = 0.5$  where  $L_{0.5} = 20m$ . The value of  $c$  is then given by:

$$c = \frac{\ln(1/3)}{-L_{0.5}}.$$

- Trajectory Criterion: This criterion aims to guide the vehicle in order to follow a global reference trajectory, defined for example by GPS waypoints and a global map [HHH<sup>+</sup>08b]. The simplest method to estimate  $V_{\text{trajectory}}$  is to consider a single point on the tentacle taken at the collision distance  $L_s$  and its corresponding point on the trajectory as shown in Fig. 2.19. For each tentacle, a measurement  $V_{\text{dist}}$  is computed by taking both the distance between the point on the tentacle and its corresponding point on the trajectory,  $b$ , as well as its relative tangent orientations,  $\alpha$ :

$$V_{\text{dist}} = b + c_a \alpha, \quad (2.13)$$

where  $c_a$  represents a scale between the linear distance and the tangent orientations, set to  $0.3 \text{ m/rad}$ .

$V_{\text{trajectory}}$  is then the normalized value of  $V_{\text{dist}}$ , computed by:

$$V_{\text{trajectory}} = \frac{V_{\text{dist}} - V_{\text{dist}_{\min}}}{V_{\text{dist}_{\max}} - V_{\text{dist}_{\min}}} \quad (2.14)$$

where  $V_{\text{dist}_{\max}}$  and  $V_{\text{dist}_{\min}}$  are the maximum and the minimum values of  $V_{\text{dist}}$  calculated for all the tentacles.

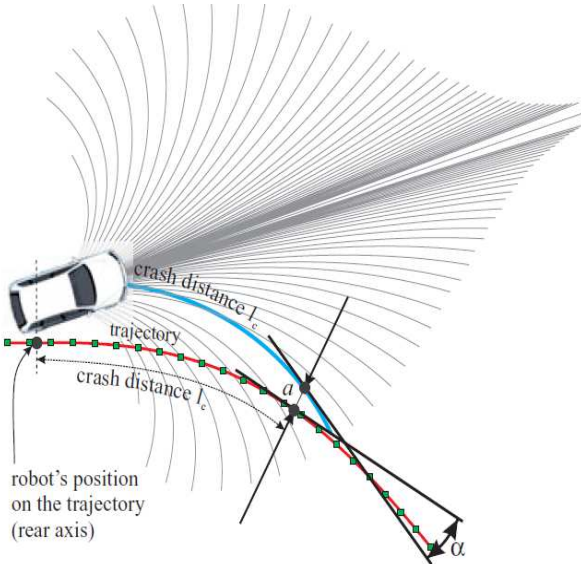


Fig. 2.19:  $V_{\text{trajectory}}$  criterion calculation [HHH<sup>+</sup>08b].

## 2.2.3 Tentacles Method Validation

### 2.2.3.1 Simulation Results

To validate the algorithm, it was applied to a scenario taken from the Scaner-Studio simulator. The data taken from Scaner-Studio was processed and simulated in Matlab. Using this data, we generate a global map showing the reference trajectory with its right and left borders. The global map taken from the Scaner-studio is shown in Fig. 2.20a. This trajectory is then used to generate the global map shown in Fig.2.20b. In this global map, the navigable space of the road is illustrated by black cells (having the value 0) while the non-navigable space is illustrated by white cells (having the value 1).

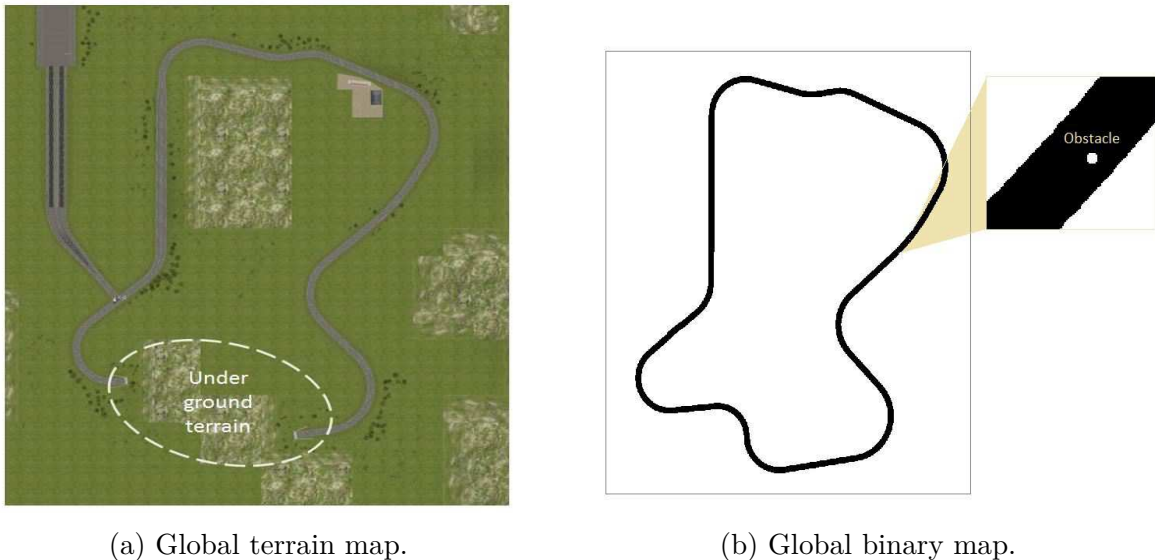


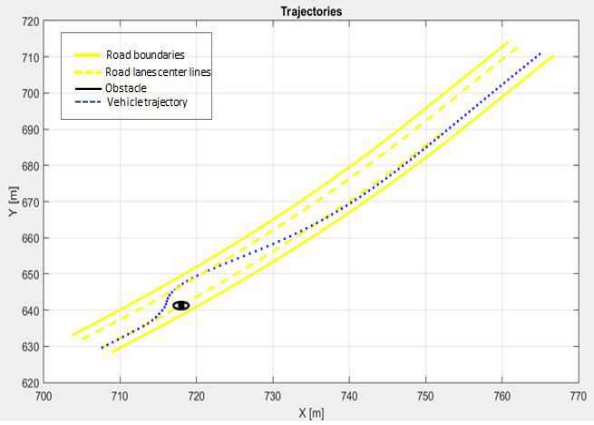
Fig. 2.20: Global map.

As a first step, the vehicle is positioned in the global map, under Matlab.

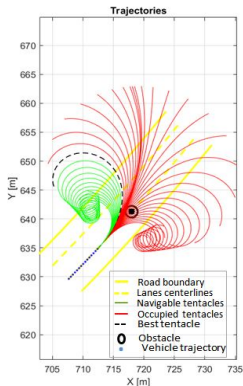
The egocentric local occupancy grid is then generated as a binary grid of 800\*800 cells where each cell is of  $25*25\text{ cm}^2$ . The cells having the value of 1 indicate an occupied space while the cells with a value of 0 represent a navigable space. Then, we apply our algorithm to choose the best tentacle at each sampling step set to  $0.1\text{s}$ . The parameters  $a_0$  and  $a_1$  are set to 0.1 and 0.5 respectively.

For a first validation, the tentacles method is tested to overtake a static obstacle on the road, illustrated by a circle of radius 1m. In this validation test, the vehicle motions are estimated using a kinematic bicycle model and the vehicle speed is set to  $5\text{ m/s}$ .

In Fig. 2.21b, we can see in the left panel the reference trajectory presenting an obstacle on the right lane with the generated tentacles. The occupied and the navigable tentacles as well as the selected tentacle are shown. In the right panel of this figure, the resulting occupancy grid is shown.



(a) The ego vehicle overtaking a static obstacle.



(b) Generated tentacles and local map.

Fig. 2.21: Obstacle avoidance scenario tested with clothoid tentacles.

The algorithm is validated upon the whole scenario shown in Fig. 2.20, yet we just show in Fig. 2.21a an obstacle avoidance scenario. Using the tentacles method in the form of clothoids, the vehicle succeeds to track a given reference trajectory while avoiding a static obstacle.

A second validation of the clothoid tentacles method is presented in Chapter 5. In this validation, a moving obstacle is added, the vehicle dynamics are considered and a coupled controller is used to control the vehicle.

### 2.2.3.2 Comparison with the circular tentacles method

To highlight the contribution of the clothoid tentacles method, a comparison was made with the circular tentacles method developed in [HHH<sup>+</sup>08b], since we have inspired our planning algorithm from it. In this comparison, the vehicle motions are modeled using a kinematic bicycle model and the desired trajectory is supposed to be perfectly tracked (no controllers are applied).

Firstly, we executed the same scenario shown in Fig. 2.21 using the circular tentacles method of [HHH<sup>+</sup>08b]. Fig. 2.22 shows the same overtaking scenario of a static obstacle executed using the clothoid tentacles method and the circular tentacles method with a vehicle speed of 5m/s. We observe that the vehicle succeeds in avoiding the obstacle and returning back to the reference trajectory when using the clothoid tentacles as well as the circular ones. However, the vehicle takes a larger lateral security distance with the circular tentacles when driving around the obstacle, especially when trying to avoid the obstacle (The tentacle width is taken almost two times the vehicle width using the circular tentacles method while it is slightly larger than the vehicle width in the clothoids tentacle method). Moreover, the circular tentacles method does not take into account the actual steering angle of the vehicle, thus the convergence of the vehicle steering angle toward the new steering angle of the selected tentacle requires another study to guarantee the vehicle stability and the continuity of the vehicle trajectory. This problem is not faced when using the clothoid tentacles since all the candidates start from the actual steering angle of the vehicle. Plus, using circular tentacles method, the vehicle would declare a narrow gate as impassable at high speeds while still being able to drive having other tentacles shapes. The clothoid tentacles method solves this ambiguity since the clothoid form matches better the form of the real roads.

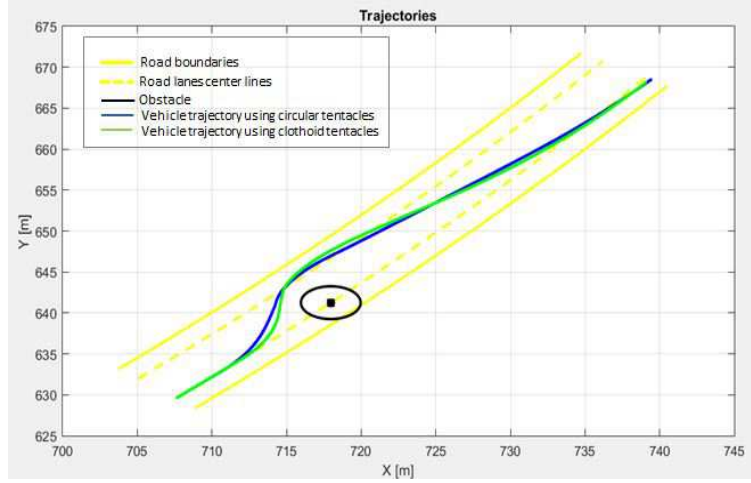


Fig. 2.22: Obstacle avoidance scenario tested with circular and clothoid tentacles.

A moving obstacle scenario is also tested to compare the clothoids with the circular tentacles method. The ego vehicle navigates at  $10m/s$  and the moving obstacle navigates at  $5m/s$ . This scenario differs from the previous scenario executed with a moving obstacle to validate the clothoids tentacles by two parameters:

- the vehicle speed during this scenario is  $10m/s$  while in the previous scenario, it was increasing from  $8.5$  to  $10m/s$ .
- the initial distance between the ego vehicle and the obstacle is in this scenario of  $15m$  while it was set to  $20m$  in the previous scenario.

Fig. 2.23 shows the trajectory executed by the vehicle to overtake the moving obstacle when using the clothoid tentacles method and when using the circular tentacles method. We can remark that, with the circular tentacles method, the vehicle changes its lane roughly and rapidly while, when using the clothoid tentacles, the lane change is executed with a largest time margin and in a smooth way. This is a result of considering the vehicle actual dynamic state in the generation of the trajectory candidates when using the clothoids method. Fig. 2.24 is an obvious proof that the steering angles executed by the vehicle are smoother with the clothoids method. As well, the steering angle speed, reflecting the steering angle variation between two computation time steps, is smaller and smoother when using the clothoids method which consequently guarantees the vehicle stability and the passenger comfort (see Fig. 2.25).

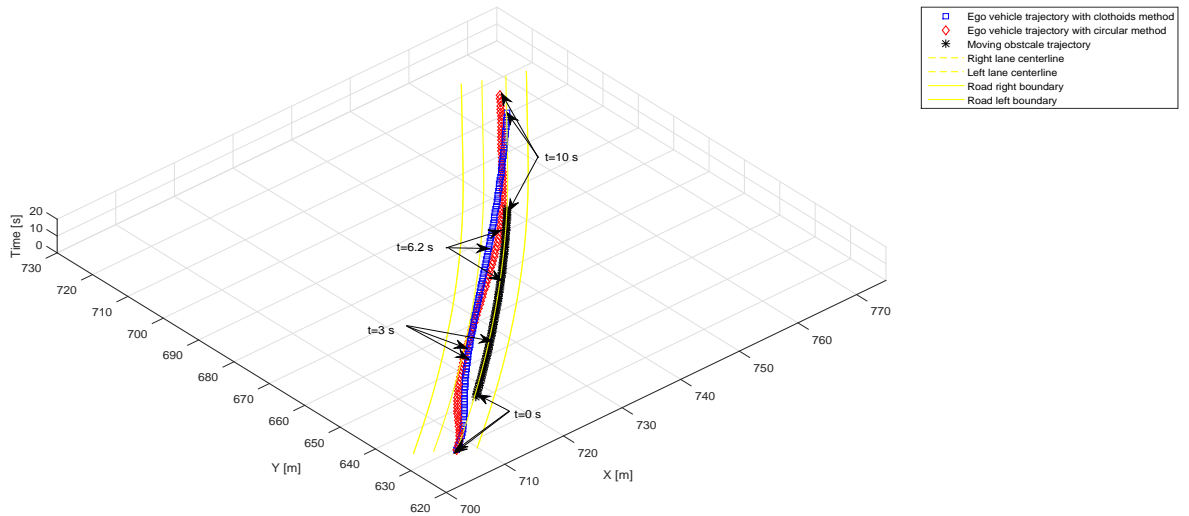


Fig. 2.23: Moving obstacle overtaking tested with circular and clothoid tentacles.

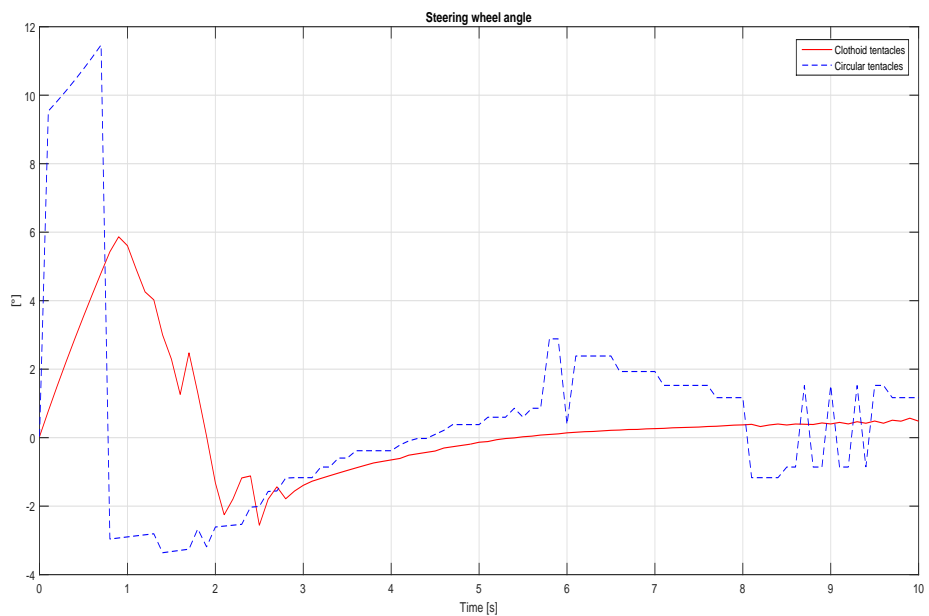


Fig. 2.24: Steering wheel angle when using circular tentacles vs clothoid tentacles.

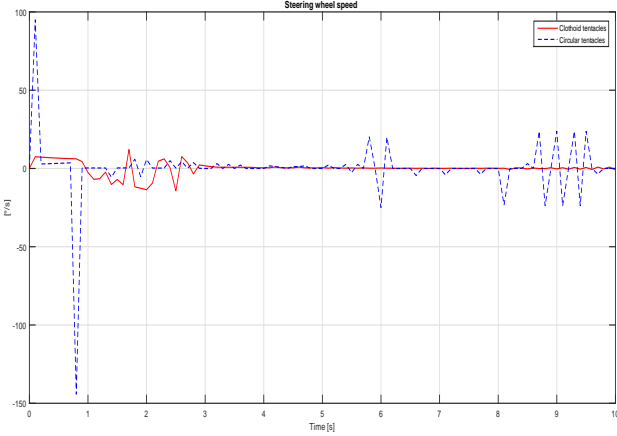


Fig. 2.25: Steering wheel speed when using circular tentacles vs clothoid tentacles.

As a result, we can claim that the clothoid tentacles method is more performant than the circular tentacles method presented in [HHH<sup>+</sup>08b] since it provides the vehicle with a smoother trajectory that guarantees the vehicle stability and the passengers comfort. Besides, the clothoid form matches better the road forms increasing thereafter the navigable space.

Note that, the tentacles method, regardless the tentacles shape, guarantees the vehicle security but doesn't necessarily fit the road rules. In fact, the safety distances satisfied by the vehicle when using the tentacles method are only observable and cannot be controllable or predicted. This restriction is the motivation to develop a maneuver planner module that overpasses this limitation. This module is presented afterwards in this chapter.

### 2.2.3.3 Preliminary Experimental Results

#### 2.2.3.3.1 Experimental tools and Evaluation method

To evaluate the developed algorithm, an experimental test executed using a Citroën vehicle dedicated to the applications of the environment perception (see Fig. 2.26), in the laboratory Heudiasyc, is used. The vehicle is equipped with many sensors:

- Alaska lidar developed by IBEO for embedded automotive applications.
- Differential GPS to measure the coordinates of the vehicle's trajectory with centimeter accuracy.
- Camera to record the scenario executed by the vehicle.
- Mobileye system to provide a list of detected obstacles (pedestrians, vehicles...) and their positions.
- Velodyne for a perception to 360° around the vehicle.
- Inertial unit to measure accelerations.

There are other data available on the CAN bus, such as the angular velocity of the wheels, the lateral acceleration and the steering wheel angle. All these sensors are connected and configured using a software platform PACPUS developed by the laboratory.



Fig. 2.26: Experimental vehicle CARMEN

The dynamic local map, produced by Julien Moras [Mor13], is generated using the Alaska lidar sensor, installed on the front bumper of the vehicle (Fig. 2.26). This sensor has four layers separated by an angle of  $0.8^\circ$ . The sensor measures distances from 0.3 to 200m with precision in the distance of the order of 10cm (resolution in distance of 4cm). It has a rotating mirror which rotates at an adjustable speed between 8Hz and 40Hz. The laser beams of the sensor covers an angle of  $160^\circ$ .

The instantaneous perception grid is constructed at each acquisition of the sensor lidar. A local map is thus constructed at the frequency of 10Hz. We are using a 2D occupation grid, of  $400 \times 400$  cells where each cell is of  $25\text{cm} \times 25\text{cm}$ . Each cell in the generated dynamic map can be a free cell, or an occupied cell or a cell with uncertain state.

We present in Fig. 2.27 some examples of the generated occupancy grids. The green color indicates that the cells are free while the red color indicates that the cells are occupied. The blue color represents an uncertain state; either because of a change of the cell state, or because of the noises. The black color represents the cells which are not in the field of view of the lidar sensor. In our work, the uncertain state is considered as occupied and then the occupancy grids presenting only two states (free and occupied) are transformed into binary grids.

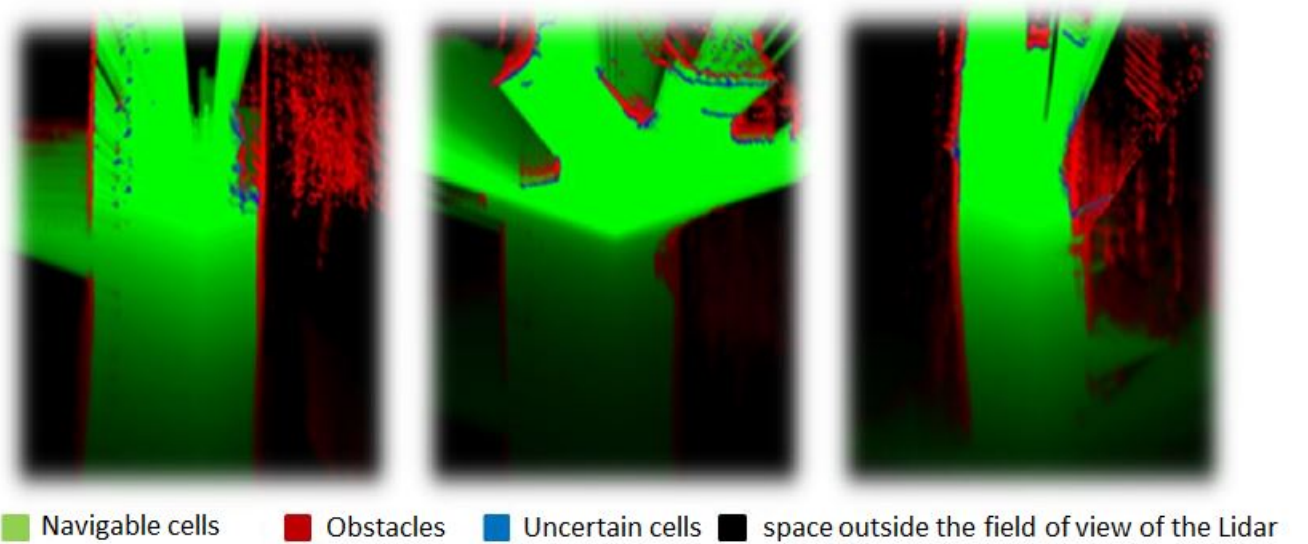


Fig. 2.27: Occupancy grid examples [Mor13]

The off-line evaluation of the tentacles method takes place in two steps: data acquisition and off-line evaluation of the algorithm. To acquire the actual data, the test was carried out in the vicinity of the Research Center of the University of Technology of Compiègne. Fig. 2.28 presents the road where the data acquisition is made. The starting point is indicated by the red vehicle and the red trajectory corresponds to the trajectory executed by the vehicle. During this data acquisition phase, the vehicle is driven by a human driver with a mean speed of 22 *km/h*. The vehicle trajectory is recorded in order to be used as the reference trajectory for the tentacles algorithm. The vehicle speed and the steering wheel angle are also recorded.

The acquired data is then used under Matlab/Simulink in order to evaluate the tentacles method in open loop. Indeed, at each step of calculation, we use the perceptual data and the dynamic data acquired on the vehicle to find the "best tentacle" that avoids obstacles and follows the reference trajectory. We can then evaluate the chosen tentacle by superposing it to the local dynamic map. If the chosen tentacle corresponds to a feasible and safe trajectory, the tentacles algorithm could be considered performant.

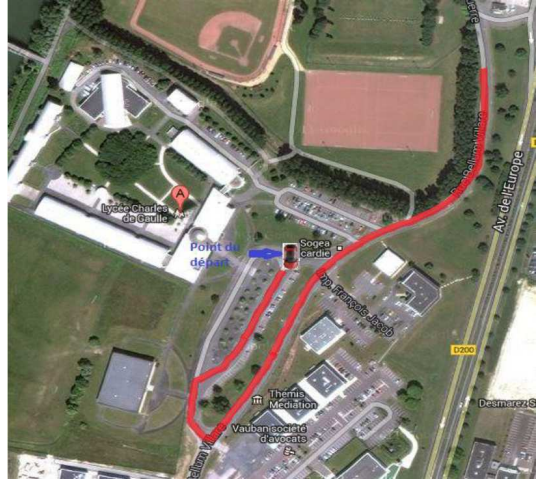
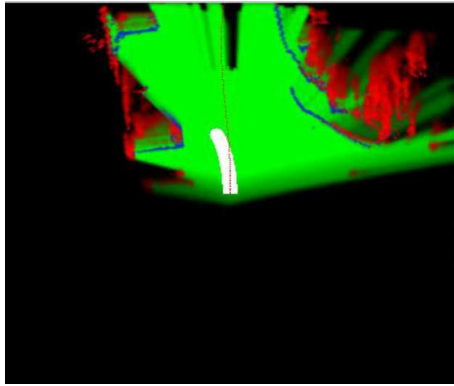


Fig. 2.28: The road where the experimental test with CARMEN vehicle is performed.

#### 2.2.3.3.2 Evaluation Results

In Fig. 2.29, we can see the real image of the road and its corresponding occupancy grid. The white area included in the occupancy grid corresponds to the classification area around the tentacle chosen by our algorithm while the dotted red curve represents the reference trajectory. The latter curve can present some errors because of the GPS measures uncertainties. The algorithm was evaluated along the whole trajectory presented in Fig. 2.28 and Fig. 2.29 only shows the obtained result at a given time. In fact, every 100ms, a new clothoid tentacle is calculated by our algorithm, in the local occupancy grid, based on the acquired real data. The proposed tentacle is compared to the real trajectory of the vehicle which represents the reference trajectory.



(a) Occupancy grid.



(b) Real road image.

Fig. 2.29: Occupancy grid with the support area of the chosen tentacle

Fig. 2.30 presents a comparison between the steering wheel angle executed by the driver in the experimental test and the steering wheel angle proposed by the clothoid tentacles algorithm. Actually, the clothoid tentacles method output is a desired curvature to be executed. The steering wheel angle presented in Fig. 2.30 is computed as a function of the desired curvature given by the algorithm.

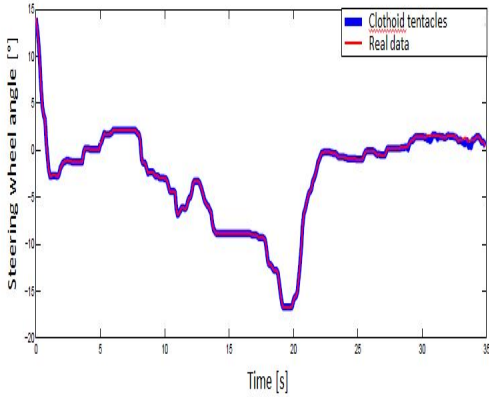


Fig. 2.30: Steering wheel angle: real data vs clothoid tentacles output.

The behavior of our algorithm seems coherent with respect to the desired objective. To proceed to more valid experimental validation, the algorithm will be implemented in the near future on a robotized vehicle in the laboratory Heudiasyc, in closed-loop with one of the developed controllers.

In conclusion, the simulation results show that the clothoid tentacles method is well-suited to the expected objectives. In fact, the method is fast and reactive. Data storage or data fusion techniques are not needed. Besides, the use of clothoids shape makes the method more realistic with respect to the vehicle dynamics constraints and the real roads structure.

On the other hand, the tentacles method, applied alone, is not really appropriate for on-road driving since the tentacles reaction with respect to an obstacle cannot be properly predicted. When an obstacle is detected, the algorithm choose to overtake it if possible. The start time of the lane change and the instant at which the vehicle will turn back to the reference trajectory cannot be directly controlled. Besides, we cannot predict the lateral displacement that will be executed by the vehicle to overpass the obstacle. Note also, that we cannot guarantee a non-evasive navigation with the tentacles method unless imposing some constraints. This is because the algorithm can choose a tentacle guiding the vehicle to the left or the right of the obstacle.

In order to overpass these limitations and adapt our navigation algorithm to on-road driving, a higher level of planning is added. At this level, the overtaking maneuver is planned respecting the road rules, the vehicle dynamics and the safety measurements for on-road driving. Then, the overtaking trajectory is generated and is now considered as the new reference trajectory for the tentacles. In the next section, the overtaking maneuver planner is presented. The combination of the maneuver planner with the local planner based on the tentacles method is then discussed.

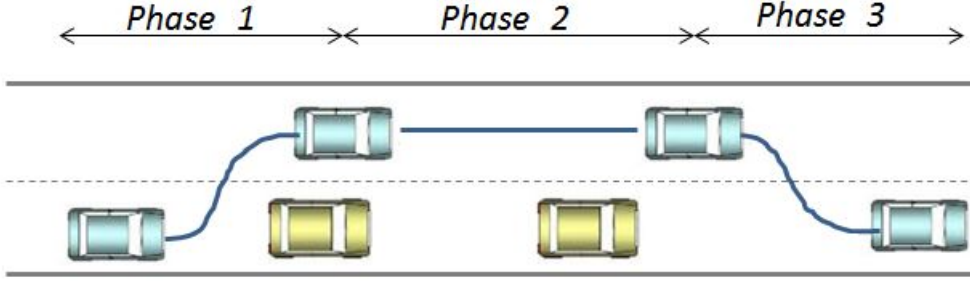


Fig. 2.31: An overtaking maneuver with its three phases

## 2.3 Maneuver Planning: Overtaking Maneuver

The maneuver planner acts as the vehicle brain and aims to reduce the gap between the vehicle behavior and the human driving manner. The interaction with other traffic participants is interpreted at this level, and then, the best maneuver to be executed is chosen regarding the situation. In this work, planning a secure overtaking maneuver is our domain of interest. Indeed, an overtaking maneuver is composed of three phases (see Fig. 2.31):

- Phase 1: Changing lane from the right to the left lane
- Phase 2: Navigating on the left lane
- Phase 3: Returning to the right lane

In the next section, we will present different strategies that were developed in the literature to deal with the planning of a secure overtaking maneuver. Thereafter, we will present our proposed solution in detail provided with some results that validate the proposed approach.

### 2.3.1 Existing Approaches for the Overtaking Maneuver Planning

Several strategies were developed to seek for a safe overtaking maneuver. We present below some of these approaches:

- A general fifth-degree polynomial is used in [Sha04]. The authors suppose that the vehicle leaves the right lane with a given speed and reaches the left lane with this same speed while the vehicle initial and final accelerations are null. This type of equations is well known and is often used to model biological motion, in that context it is called a 'minimal jerk' trajectory. The objective function to be minimized is the total kinetic energy constrained by two conditions, the vehicle speed positivity and the vehicle acceleration limitation. By using this approach, an autonomous vehicle can estimate the best time and place to begin and end the overtaking maneuver and its total time and distance regarding the vehicle actual speed. This may help to make a decision whether to overtake or not. The total time of the maneuver is proven to be bounded from above and below, regardless of the velocity, by using a relatively simple mathematical model. However, for the sake of simplicity and generality, the model does not explicitly take into account the dynamics of the vehicle or the vehicle model. All the forces acting upon the vehicle are embedded into one parameter that is the maximal acceleration during the maneuver.

In [LJC14], an  $H_\infty$  optimal controller is used to track the trajectory generated as in [Sha04]. In [SS98] and [CT95], results are obtained for the distance to begin the diversion, and, the total time the lane-change maneuver takes, considering the vehicle dynamics. The trajectories they generate are not necessarily smooth and they do not obtain closed-form formulas. Furthermore, they only consider lane-change maneuvers and not overtaking a moving vehicle.

- In [NBCF15], the proposed algorithm determines whether there exists a longitudinal trajectory which allows the ego vehicle to safely position itself in a gap between the surrounding vehicles in the target lane. If such a longitudinal trajectory exists, the algorithm plans the corresponding lateral trajectory.

Indeed, a longitudinal corridor is constructed so as the ego vehicle guarantees a safety distance with all the vehicles in its lane, in each step of the lane changing maneuver (see Fig. 2.32). Two parameters are defined: The "time instance" which is the time when the ego vehicle leaves the Pre-region and enters the Peri-region and the "traffic gap" which represents the possible positions of the vehicle when it reaches the Post-Region. A cost function is then minimized for a set of possible "time instance" and "traffic gap" under the dynamic and the corridor constraints to derive the longitudinal trajectory. The lateral trajectory is determined in a similar manner. In [NBCF16], a first step is added to the mentioned algorithm, in order to specify the time instance and the traffic gap a priori to reduce the time-computation and complexity. Although this algorithm is promising, the computational time remains important restricting real time applications.

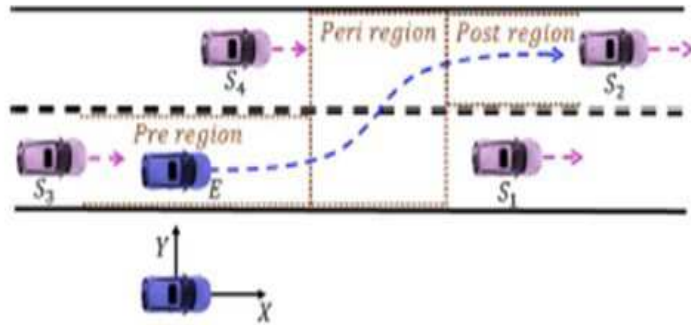


Fig. 2.32: Lane change maneuver regions proposed in [NBCF15].

- In [PT03], a fifth order polynomial trajectory is used to execute the lane changing maneuver. To take into account the vehicle dynamics and the obstacles avoidance, they proceed by adding a sixth degree with a sixth coefficient to the longitudinal equation of motion. Having only five boundary constraints, this added degree is set in order to avoid obstacles represented by s-topes forms and to guarantee the dynamic constraints. In their work, the authors assume that the ego-vehicle and the preceding vehicle will not change their speeds during the overall overtaking maneuver. This method requires a pre-processing step to set the sixth degree before starting the lane change maneuver which may constraint the real time application.
- [GVM<sup>+</sup>10] present a trajectory planner, that firstly defines the feasible maneuvers with respect to the environment, aiming at minimizing the risk of a collision. Then, a more

detailed evaluation of several possible trajectories within the chosen maneuver is executed. The trajectories are optimized according to additional performance indicators such as travel time, traffic rules, consumption, and comfort. For the lane change maneuver, a fourth-order and a fifth-order polynomial time description for longitudinal and lateral positions respectively is used to generate the trajectory candidates. The feasibility of these trajectories in terms of curvature and longitudinal acceleration is then checked using a simple vehicle model. If the trajectory is not feasible, it is discarded from the solution space.

- Support vector machine [DBS<sup>+</sup>15], Bayesian Network [SSW10], Fuzzy Logics [NGGP08] are also used to treat the overtaking maneuvers issue. These types of approach require a very large training phase in order to deal with all possible situations.

In our work, the overtaking maneuver is executed by generating a polynomial trajectory taking into account the vehicle dynamics constraints as well as the traffic road rules related to speed and safety constraints. We chose to proceed with the polynomial trajectories since it is a simple and effective approach. The contribution in this work is that the algorithm permits to generate the trajectory in a single step with a simple method adapted to a real time application. In the following, the proposed solution will be presented together with some simulations that validate the approach. Thereafter, the combined planner including the overtaking maneuver planner and the local planner is presented with the validation results.

### 2.3.2 Developed Overtaking Maneuver

The navigation strategy, where the overtaking decision is made and planned, is presented in this section. Then, in order to execute the overtaking maneuver, a trajectory that takes into account the vehicle dynamics limitations, the road rules and the safety constraints is generated. The approach of the trajectory generation is also presented in this section.

Some assumptions are made in order to simplify the task: The overtaken vehicle is supposed to maintain its speed during the whole overtaking maneuver. Moreover, the left lane is supposed to be free, so that the ego vehicle can overtake without taking into account additional obstacles. In the following, we will refer to the ego-vehicle as vehicle A, and to the preceding obstacle vehicle as vehicle B.

#### 2.3.2.1 Maneuver planning approach

The maneuver planning strategy is shown in Fig. 2.33. While navigating on the right lane, with a certain desired speed  $V_{A_{des}}$ , the vehicle A detects a vehicle in front (vehicle B). Adaptive cruise control [Raj11] is then executed to the vehicle A: the ego vehicle adapts its speed in order to maintain a security inter-vehicle distance corresponding to two seconds of reaction at its speed as defined by the road rules.

The ego vehicle can overtake the preceding vehicle if and only if its desired speed  $V_{A_{des}}$  is greater than the preceding vehicle speed by more than 20 km/h, and if the left lane is not occupied.

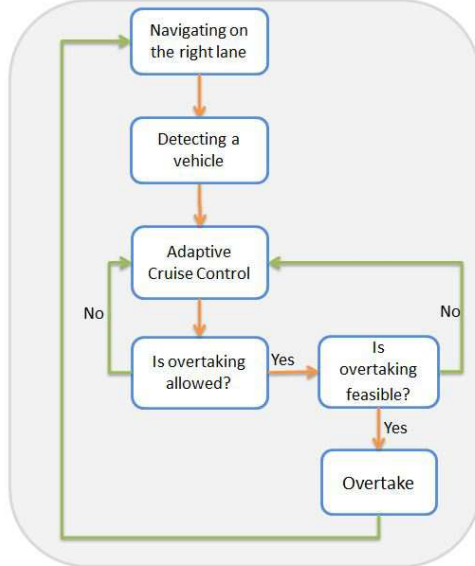


Fig. 2.33: Maneuver planner architecture.

As mentioned above, we consider for the moment that the left lane is free. Once the vehicle decides to overtake, the next step is to check if there is any feasible trajectory that enables the lane changing without violating the dynamic constraints neither the security and the road rules. This study is detailed in the next section. If a suitable trajectory is found, the ego vehicle begins the lane changing phase and end up by reaching the left lane. The ego vehicle navigates on the left lane until a safe returning back to the right lane is possible.

### 2.3.2.2 Overtaking Trajectory Generation

The overtaking maneuver is executed in three phases: a lane changing maneuver from the right to the left lane, a lane keeping maneuver once on the left lane, and a lane changing maneuver to return from the left to the right lane.

**2.3.2.2.1 Phase 1: Lane Changing Maneuver** The first phase of the overtaking maneuver is the phase where the ego-vehicle leaves the right lane and navigates toward the left lane. This navigation is executed using a polynomial trajectory. In order to fix the polynomials degree in the longitudinal and the lateral directions, we define the boundary constraints as follows: The initial values of position, speed, and acceleration and two target values (at a certain time  $T_1$ ) of speed and acceleration are set in the longitudinal direction, while the initial and target values of position, speed, and acceleration are specified in the lateral direction. This defines a fourth- and a fifth-order polynomial time description for the longitudinal and the lateral positions, respectively. The origin of the coordinate frame ( $R$ ) is fixed in the initial position of the vehicle on the right lane,  $x$  being the longitudinal axis in the driving direction of the vehicle, and  $y$  being the right-hand side perpendicular to  $x$  (see Fig. 2.34). We write the equations for the longitudinal and lateral positions with respect to the time  $t$  as follows:

$$x(t) = a_0 + a_1 t + a_2 t^2 + a_3 t^3 + a_4 t^4 \quad (2.15)$$

$$y(t) = b_0 + b_1 t + b_2 t^2 + b_3 t^3 + b_4 t^4 + b_5 t^5 \quad (2.16)$$

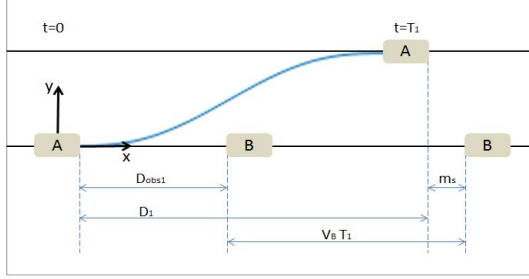


Fig. 2.34: Phase 1: Lane changing maneuver, from right to left lane.

The boundary conditions for the longitudinal motion are given by :

$$\begin{aligned} x(0) &= 0, \dot{x}(0) = V_{A_i}, \ddot{x}(0) = 0 \\ \dot{x}(T_1) &= V_{A_f}, \ddot{x}(T_1) = 0 \end{aligned} \quad (2.17)$$

where  $T_1$  indicates the duration of the phase 1, that is the lane change duration.  $V_{A_i}$  and  $V_{A_f}$  are the initial and the target speed of the vehicle during this phase.

From (2.15) and (2.17), we develop the coefficients  $a_i$  as a function of the constraints, i.e.,

$$\begin{aligned} a_0 &= 0, a_1 = V_{A_i}, a_2 = 0 \\ a_3 &= \frac{V_{A_f} - V_{A_i}}{T_1^2}, a_4 = \frac{V_{A_i} - V_{A_f}}{2T_1^3} \end{aligned} \quad (2.18)$$

In the lateral direction, the fifth-order polynomial is expressed relatively to the frame (R). The boundary conditions for the lateral motion are then set as:

$$\begin{aligned} y(0) &= 0, \dot{y}(0) = 0, \ddot{y}(0) = 0 \\ y(T_1) &= w, \dot{y}(T_1) = 0, \ddot{y}(T_1) = 0 \end{aligned} \quad (2.19)$$

where  $w$  represents the lane width (see Fig. 2.34).

From (2.16) and (2.19), one can find the coefficients  $b_j$  as a function of the constraints, i.e.,

$$\begin{aligned} b_0 &= 0, b_1 = 0, b_2 = 0 \\ b_3 &= \frac{10w}{T_1^3}, b_4 = \frac{-15w}{T_1^4}, b_5 = \frac{6w}{T_1^5} \end{aligned} \quad (2.20)$$

In order to take into account the vehicle dynamic constraints, the road rules dealing with the overtaking maneuver and the safety constraints, we proceed by properly setting the parameters  $T_1$ ,  $V_{A_i}$  and  $V_{A_f}$ .

### Respecting the vehicle dynamic constraints:

The vehicle dynamic constraints are satisfied by limiting the longitudinal and the lateral accelerations of the vehicle. Let  $a_{x_{min}}$  and  $a_{x_{max}}$  be the boundary limits of the admissible longitudinal acceleration of the vehicle.

The vehicle longitudinal acceleration and jerk ( $\ddot{x}$  and  $\frac{d(\ddot{x})}{dt}$ ) are computed using (2.15) by:

$$\ddot{x}(t) = 2a_2 + 6a_3t + 12a_4t^2. \quad (2.21)$$

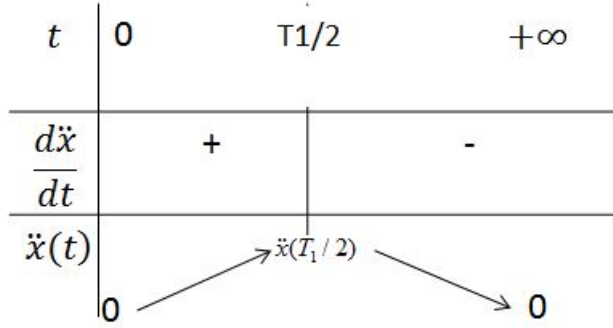


Fig. 2.35: Table of variation of the longitudinal acceleration of the vehicle  $\ddot{x}(t)$

$$\frac{d(\ddot{x})}{dt} = 6a_3 + 24a_4t. \quad (2.22)$$

Noticing that  $a_3 = -2a_4T_1$  (see (2.18)), the vehicle jerk can be rewritten as:

$$\begin{aligned} \frac{d(\ddot{x})}{dt} &= -12a_4T_1 + 24a_4t \\ &= a_4(-12T_1 + 24t). \end{aligned} \quad (2.23)$$

Obviously, the vehicle jerk sign depends on the sign of the coefficient  $a_4$ . We assume that on real roads, when overtaking a vehicle, the driver will probably accelerate and not decelerate. In that concept, we assume that  $a_4$  is negative (since  $a_4 = (V_{A_i} - V_{A_f})/(2T_1^3)$ ). Then, the vehicle jerk is canceled when  $t = T_1/2$ , negative when  $t > T_1/2$ , and positive when  $t < T_1/2$  (see Fig. 2.35). As a result, the vehicle acceleration reaches a maximum value at  $t = T_1/2$ .

This yields the following constraint:

$$\max(\ddot{x}(t)) = \ddot{x}(t = T_1/2) < a_{x_{max}}. \quad (2.24)$$

Replacing  $\ddot{x}(t = T_1/2)$  by its value using (2.21), we obtain the first constraint conditioning the time duration of the lane changing maneuver:

$$T_1 > \frac{V_{A_f} - V_{A_i}}{2/3a_{x_{max}}}. \quad (2.25)$$

In a similar way, the lateral acceleration of the vehicle should be bounded in order to guarantee the vehicle stability and the trajectory feasibility. Let  $a_{y_{min}}$  and  $a_{y_{max}}$  be the boundary limits of the lateral acceleration. The lateral acceleration and jerk of the vehicle are written as:

$$\ddot{y}(t) = 2b_2 + 6b_3t + 12b_4t^2 + 20b_5t^3 \quad (2.26)$$

$$\frac{d(\ddot{y})}{dt} = 6b_3 + 24b_4t + 60b_5t^2 \quad (2.27)$$

The study of the lateral acceleration variation yields that the lateral acceleration starts with zero, increases to reach a maximum at  $t = t_1 = T_1/2 - 0.29T_1$ , decreases to reach a minimum at  $t = t_2 = T_1/2 + 0.29T_1$  and finally increases to reach zero again (see Fig. 2.36). As a result, the constraints on the lateral acceleration are given by:

$$\max(\ddot{y}(t)) = \ddot{y}(t_1) < a_{y_{max}} \quad (2.28)$$

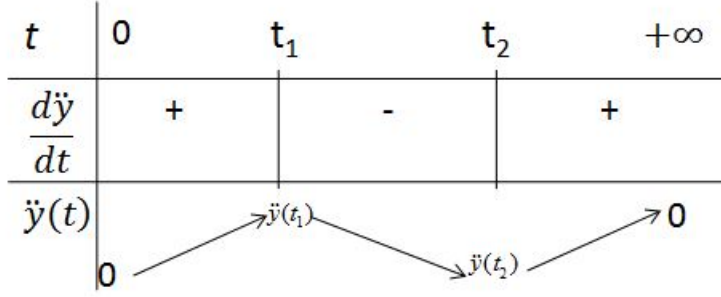


Fig. 2.36: Table of variation of the lateral acceleration of the vehicle  $\ddot{y}(t)$

$$\min(\ddot{y}(t)) = \ddot{y}(t_2) > a_{y_{min}} \quad (2.29)$$

Using (2.26) with (2.28) and (2.29), another constraint on the time duration of the lane changing maneuver is obtained:

$$T_1 > \max \left( \sqrt{\frac{5.77w}{a_{y_{max}}}}, \sqrt{\frac{-5.77w}{a_{y_{min}}}} \right). \quad (2.30)$$

### Respecting the road rules:

In order to respect the road rules [Bau05], the target speed  $V_{A_f}$  should be greater than the overtaken vehicle speed by at least  $20km/h$ , while respecting the maximum speed allowed on the left lane, which yields:

$$V_{A_f} = \min(V_B + 20km/h, V_{x_{max}}^{Lane2}), \quad (2.31)$$

where  $V_B$  is the overtaken vehicle speed and  $V_{x_{max}}^{Lane2}$  is the maximum speed allowed on the left lane.

Notice that, the vehicle A can not overtake the vehicle B unless its speed is greater than or equal to the overtaken vehicle speed. If the speed of the vehicle A exceeds that of the vehicle B by more than  $20km/h$ , the vehicle A executes the lane changing maneuver at a constant speed, since we assume that the ego vehicle will not decelerate during this phase. This yields:

$$V_{A_f} = \max \left( \min(V_B + 20km/h, V_{x_{max}}^{Lane2}), V_{A_i} \right). \quad (2.32)$$

### Respecting safety requirements:

For safety reasons, we assume that the ego-vehicle will reach the left lane slightly behind the position of the overtaken vehicle on the right lane (see Fig. 2.34).

We define  $D_1$  as the distance traveled by the ego-vehicle during the lane changing maneuver,  $D_{obs1}$  as the distance between the ego vehicle and the overtaken vehicle at  $t = 0$  (at the beginning of the lane changing maneuver), and  $m_s$  as a safety distance between the projection of the vehicle A on the right lane and the position of the vehicle B on that lane, when A reaches the left lane.

Since we assume that the vehicle B conserves its speed during the phase 1, then, during the lane changing maneuver, the vehicle B will travel a distance  $V_B T_1$  while the vehicle A will travel a distance  $D_1$ . To guarantee the safety distance  $m_s$ , we have to guarantee that :

$$D_1 \leq D_{obs1} + V_B T_1 - m_s, \quad (2.33)$$

In fact,  $D_1$  is only  $x(t = T_1)$ . From (2.15), we have:

$$\begin{aligned} D_1 &= x(t = T_1) \\ &= (V_{A_f} + V_{A_i})T_1/2. \end{aligned} \quad (2.34)$$

Using (2.34) and (2.33), we obtain:

$$(\frac{V_{A_f} + V_{A_i}}{2} - V_B)T_1 \leq D_{obs1} - m_s, \quad (2.35)$$

Note that  $(V_{A_f} + V_{A_i}) > 2V_B$ , since the ego-vehicle should satisfy  $V_{A_i} \geq V_B$  to have the right to overtake and since  $V_{A_f} \geq V_{A_i}$  as the ego-vehicle accelerates during the lane changing maneuver. Then, (2.35) can be rewritten as:

$$T_1 \leq \frac{2(D_{obs1} - m_s)}{V_{A_f} + V_{A_i} - 2V_B}. \quad (2.36)$$

### Satisfying all the constraints:

Consequently, having the ego vehicle speed and the overtaken vehicle speed, we define the ego vehicle final speed  $V_{A_f}$  using (2.32). Then, we have to find the maneuver duration  $T_1$  that satisfies (2.25), (2.30) and (2.36). These three conditions can be resumed in a single condition, i.e.,

$$\max(T_{min1}, T_{min2}) \leq T_1 \leq T_{max}. \quad (2.37)$$

with:

$$\begin{aligned} T_{min1} &= \max\left(\sqrt{\frac{5.77w}{a_{y_{max}}}}, \sqrt{\frac{-5.77w}{a_{y_{min}}}}\right) \\ T_{min2} &= \frac{V_{A_f} - V_{A_i}}{2/3a_{x_{max}}}, \\ T_{max} &= \frac{2(D_{obs1} - m_s)}{V_{A_f} + V_{A_i} - 2V_B}. \end{aligned} \quad (2.38)$$

In order to satisfy (2.37), the target and the initial vehicle speeds should guarantee that:

$$\max(T_{min1}, T_{min2}) < T_{max} \quad (2.39)$$

If so, we set  $T = T_{max}$  with the aim of satisfying (2.37) and to guaranteeing the equality of the constraint (2.36) so as the vehicle position respects the safety constraint. If the target and the initial vehicle speeds yield that (2.39) is incorrect, which means that (2.37) can not be satisfied, we decide not to overtake since the lane changing maneuver can not be safely executed without violating the dynamic constraints of the vehicle.

**2.3.2.2.2 Phase 2: Navigating on the left lane** Once the vehicle A reaches the left lane, a lane keeping maneuver is executed. For simplicity, we assume that both the vehicle A and the vehicle B maintain their velocities  $V_{A_f}$  and  $V_B$  during this phase. Assuming that the vehicle A will begin the returning phase when it passes the vehicle B by a certain safety margin  $m_{s2}$ , then the distance that the vehicle A will travel on the left lane ( $D_2$ ) can be computed as follows (see Fig. 2.37):

$$\begin{aligned} D_2 &= m_s + m_{s2} + L_A + L_B + V_B T_2 \\ &= V_{A_f} T_2 \end{aligned} \quad (2.40)$$

where  $L_A$  and  $L_B$  are the length of the vehicles A and B respectively, and  $T_2$  is the time duration of the phase 2.

The traveling time on the left lane is then given by:

$$T_2 = \frac{m_{s2} + m_s + L_A + L_B}{V_{A_f} - V_B}, \quad (2.41)$$

Notice that, by taking  $T_1 = T_{max}$  in the phase 1, we suppose that the distance between the vehicle A once on the left lane and the vehicle B is equal to  $m_s$ .

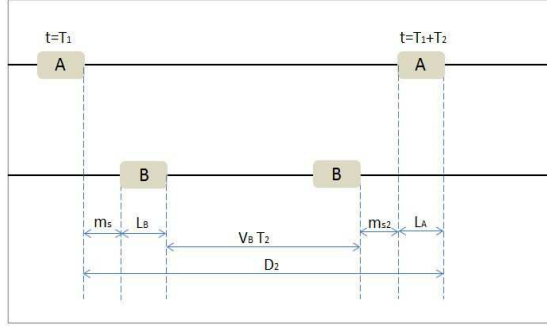


Fig. 2.37: Phase 2: Navigating on the left lane.

**2.3.2.2.3 Phase 3: Returning to the right lane** After navigating for a time  $T_2$  on the left lane, the vehicle A must turn back to the right lane while respecting the vehicle dynamic constraints, the road rules and the safety requirements. In this phase, the trajectory used by the vehicle A to turn back is the symmetrical of the polynomials used in phase 1. The trajectory is generated in the frame having its origin at the final position of the vehicle A on the left lane. The longitudinal axis is always taken in the direction of navigation of the vehicle. Using this configuration, the longitudinal equation of motion remains the same as (2.15), (2.17) and (2.18). Concerning the lateral equation of motion, the only difference in the boundary constraints appears in the final lateral position:  $y(T_3) = -w$ , where  $T_3$  is the time duration of the phase 3. For ease of representation, we present below the longitudinal and the lateral equations of motion with their associated boundary conditions and their coefficients  $a_i$  and  $b_j$ :

$$x(t) = a_0 + a_1 t + a_2 t^2 + a_3 t^3 + a_4 t^4 \quad (2.42)$$

The boundary conditions for the longitudinal motion are given by :

$$\begin{aligned} x(0) &= 0, \quad \dot{x}(0) = V_{A_{i2}}, \quad \ddot{x}(0) = 0 \\ \dot{x}(T_3) &= V_{A_{f2}}, \quad \ddot{x}(T_3) = 0 \end{aligned} \quad (2.43)$$

where  $V_{A_{i2}}$  and  $V_{A_{f2}}$  are the initial and the target speed of the vehicle during the phase 3. Note that  $V_{A_{i2}} = V_{A_f}$ .

The coefficients  $a_i$  are given by:

$$\begin{aligned} a_0 &= 0, \quad a_1 = V_{A_{i2}}, \quad a_2 = 0 \\ a_3 &= \frac{V_{A_{f2}} - V_{A_{i2}}}{T_3^2}, \quad a_4 = \frac{V_{A_{i2}} - V_{A_{f2}}}{2T_3^3} \end{aligned} \quad (2.44)$$

The lateral equation of motion is:

$$y(t) = b_0 + b_1 t + b_2 t^2 + b_3 t^3 + b_4 t^4 + b_5 t^5 \quad (2.45)$$

with the following boundary conditions:

$$\begin{aligned} y(0) &= 0, \quad \dot{y}(0) = 0, \quad \ddot{y}(0) = 0 \\ y(T_3) &= -w, \quad \dot{y}(T_3) = 0, \quad \ddot{y}(T_3) = 0 \end{aligned} \quad (2.46)$$

where  $\omega$  represents the lane width (see Fig. 2.38).

The coefficients  $b_j$  are then given by:

$$\begin{aligned} b_0 &= 0, \quad b_1 = 0, \quad b_2 = 0 \\ b_3 &= \frac{-10w}{T_3^3}, \quad b_4 = \frac{15w}{T_3^4}, \quad b_5 = \frac{-6w}{T_3^5} \end{aligned} \quad (2.47)$$

### Respecting the dynamic constraints:

The dynamic constraints that guarantee the stability of the vehicle are derived as for the phase 1 and are given by:

$$T_3 > \max \left( \sqrt{\frac{5.77w}{a_{y_{max}}}}, \sqrt{\frac{-5.77w}{a_{y_{min}}}} \right). \quad (2.48)$$

$$T_3 > \frac{V_{A_{f2}} - V_{A_{i2}}}{2/3a_{x_{max}}}. \quad (2.49)$$

The equation (2.49) can be rewritten as:

$$V_{A_{f2}} < V_{A_{i2}} + 2/3a_{x_{max}} T_3. \quad (2.50)$$

Besides the ego-vehicle speed must be greater than the obstacle vehicle speed, once the ego-vehicle reaches the right lane. That is:

$$V_{A_{f2}} > V_B. \quad (2.51)$$

### Respecting the road rules:

The only condition to satisfy here is to not overpass the maximum speed allowed on the right lane  $V_{x_{max}}^{Lane1}$ . This condition yields:

$$V_{A_{f2}} \leq V_{x_{max}}^{Lane1} \quad (2.52)$$

### Respecting the safety conditions:

To guarantee the vehicles safety, a third constraint is added claiming that: when the vehicle reaches the right lane, it should guarantee a distance with the vehicle B greater than the security distance (the security distance corresponds to 2 seconds of reaction at its speed, dealing with the road rules [Bau05]). Then, referring to Fig. 2.38, we have to guarantee the following :

$$D_{obs2} = D_3 - V_B T_3 + m_{s2} \geq 2V_B, \quad (2.53)$$

where  $D_{obs2}$  is the distance between the vehicles A and B on the right lane once the returning phase is executed, and  $D_3$  is the longitudinal distance traveled by the vehicle A during this phase.

Replacing  $D_3$  by  $x(t = T_3) = (V_{A_{i2}} + V_{A_{f2}})T_3/2$ , the condition (2.53) can be rewritten as:

$$V_{A_{f2}} \geq \frac{2}{T_3}(V_B T_3 - m_{s2} + 2V_B - \frac{V_{A_{i2}}}{2}T_3) \quad (2.54)$$

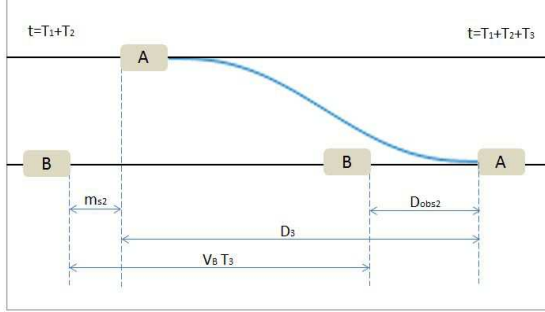


Fig. 2.38: Phase 3: Returning to the right lane.

### Respecting all the constraints:

The overall constraints given in (2.48), (2.50), (2.52) and (2.54) for this phase can be resumed as follows:

$$\begin{aligned} V_{A_{f2}} &\leq \min(V_{A_{i2}} + 2/3a_{x_{max}}T_3, V_{x_{max}}^{Lane1}) \\ V_{A_{f2}} &\geq \max(\frac{2}{T_3}(2V_B - m_{s2} + V_B T_3 - \frac{V_{A_{i2}}}{2}T_3), V_B) \\ T_3 &\geq \max\left(\sqrt{\frac{5.77w}{a_{y_{max}}}}, \sqrt{\frac{-5.77w}{a_{y_{min}}}}\right). \end{aligned} \quad (2.55)$$

In order to find  $T_3$  and  $V_{A_{f2}}$  that satisfy (2.55), we have to guarantee that the solution space for the first two equations is not empty. In other words, we have to guarantee that:

$$\max(V_B, \frac{2}{T_3}(2V_B - m_{s2} + V_B T_3 - V_{A_{i2}} T_3/2)) \leq \min(V_{A_{i2}} + 2/3a_{x_{max}}T_3, V_{x_{max}}^{Lane1}) \quad (2.56)$$

Let's define M and N by:

$$M = \max(V_B, \frac{2}{T_3}(2V_B - m_{s2} + V_B T_3 - V_{A_{i2}} T_3/2))$$

$$N = \min(V_{A_{i2}} + 2/3a_{x_{max}}T_3, V_{x_{max}}^{Lane1})$$

The condition (2.56) can then be written as:

$$M \leq N \quad (2.57)$$

Now, if  $M = V_B$  and  $N = V_{x_{max}}^{Lane1}$ , the condition (2.56) becomes:

$$V_B < V_{x_{max}}^{Lane1} \quad (2.58)$$

This condition ((2.58)) is satisfied since the obstacle vehicle B navigates on the right lane and can not exceeds the maximum speed allowed on that lane ( $V_B < V_{x_{max}}^{Lane1}$ ).

Otherwise, if  $M = V_B$  and  $N = V_{A_{i2}} + 2/3a_{x_{max}}T_3$ , the condition (2.56) becomes:

$$V_B < V_{A_{i2}} + 2/3a_{x_{max}}T_3 \quad (2.59)$$

The condition (2.59) is satisfied since  $V_{A_{i2}} = V_{A_f}$  is the target speed on the left lane at the end of the phase 1 and is greater than  $V_B$ . This yields  $V_B < V_{A_{i2}} < V_{A_{i2}} + 2/3a_{x_{max}}T_3$  which satisfies (2.56).

Now, if  $M = \frac{2}{T_3}(2V_B - m_{s2} + V_B T_3 - V_{A_{i2}} T_3/2)$  and  $N = V_{A_{i2}} + 2/3a_{x_{max}}T_3$ , the condition (2.56) becomes:

$$\frac{2}{T_3}(2V_B - m_{s2} + V_B T_3 - V_{A_{i2}} T_3/2) \leq V_{A_{i2}} + 2/3a_{x_{max}}T_3 \quad (2.60)$$

After some computations, we can find that the equation (2.60) is equivalent to the following condition:

$$T_3 \geq \frac{-V_{A_{i2}} + V_B + \sqrt{(V_{A_{i2}} - V_B)^2 + 8/3V_B a_{x_{max}}}}{2/3a_{x_{max}}} \quad (2.61)$$

Otherwise, if  $M = \frac{2}{T_3}(2V_B - m_{s2} + V_B T_3 - V_{A_{i2}} T_3/2)$  and  $N = V_{x_{max}}^{Lane1}$ , the condition (2.56) becomes:

$$\frac{2}{T_3}(2V_B - m_{s2} + V_B T_3 - V_{A_{i2}} T_3/2) \leq V_{x_{max}}^{Lane1} \quad (2.62)$$

This yields to:

$$T_3 \geq \frac{2(m_{s2} - 2V_B)}{2V_B - V_{A_{i2}} - V_{x_{max}}^{Lane1}} \quad (2.63)$$

As a result, the system of constraints (2.55) is satisfied if and only if the parameter  $T_3$  satisfies (2.63), (2.61) and the last equation of (2.55). Then,  $T_3$  should satisfy:

$$T_3 \geq \max(T_{min1}, T_{min2}, T_{min3}), \quad (2.64)$$

with

$$\begin{aligned} T_{min1} &= \max\left(\sqrt{\frac{5.77w}{a_{y_{max}}}}, \sqrt{\frac{-5.77w}{a_{y_{min}}}}\right) \\ T_{min2} &= \frac{-V_{A_{i2}} + V_B + \sqrt{(V_{A_{i2}} - V_B)^2 + 8/3V_B a_{x_{max}}}}{2/3a_{x_{max}}} \\ T_{min3} &= \frac{2(m_{s2} - 2V_B)}{2V_B - V_{A_{i2}} - V_{x_{max}}^{Lane1}}. \end{aligned} \quad (2.65)$$

Once  $T_3$  is defined by (2.65),  $V_{A_{f2}}$  is set by choosing any value that satisfies the first two conditions of (2.55), i.e.,

$$\max(V_B, 2/T_3(2V_B - m_{s2} + V_B T_3 - V_{A_{i2}} T_3/2)) \leq V_{A_{f2}} \leq \min(V_{A_{i2}} + 2/3a_{x_{max}}T_3, V_{x_{max}}^{Lane1}). \quad (2.66)$$

### 2.3.3 Validation of the maneuver planning algorithm

The maneuver planning approach was validated under Matlab/Simulink for many driving scenarios. In the following, we present the results of the approach for two given scenarios showing the different aspects of the maneuver planner.

### 2.3.3.1 Scenario 1

The vehicle A is initially navigating with a speed of  $20m/s$  while the vehicle B is navigating with a speed of  $10m/s$ . That is:

$$V_{A_i} = 20m/s, V_B = 10m/s. \quad (2.67)$$

The maximum admissible accelerations for the vehicle are set as follows:

$$\begin{aligned} a_{x_{max}} &= 1.5m/s^2, a_{x_{min}} = -2m/s^2 \\ a_{y_{max}} &= 4m/s^2, a_{y_{min}} = -4m/s^2 \end{aligned} \quad (2.68)$$

The maximum speed allowed on the left lane is set to  $28m/s$  while on the right lane the vehicle can only reach  $20m/s$ , that is:

$$V_{x_{max}}^{Lane1} = 20m/s, V_{x_{max}}^{Lane2} = 28m/s. \quad (2.69)$$

The lane width is set to  $3.5m$ , the safety distances  $m_s$  and  $m_{s2}$  are set to  $3m$  while the vehicles length is set to  $4.2m$ .

The vehicle A starts its navigation on the right lane. When it detects the vehicle B, the Adaptive Cruise Control is activated. This means that the vehicle A follows the vehicle B while keeping a minimum inter-vehicle distance of two seconds of reaction.

The speeds of the vehicle A and B during this ACC phase are shown in Fig. 2.39 and the inter-vehicle distance between A and B is shown in Fig. 2.40. The vehicle A starts navigating with  $20m/s$  and the vehicle B starts with  $10m/s$ . The initial distance between A and B is of  $57.5m$ . The Adaptive Cruise Control objective is to keep an inter-vehicle distance between A and B equal or greater than twice the vehicle A speed. Let  $d_{AB}$  be the distance between A and B and  $V_A$  the vehicle A speed, the ACC objective is to satisfy:

$$d_{AB} \geq 2V_A \quad (2.70)$$

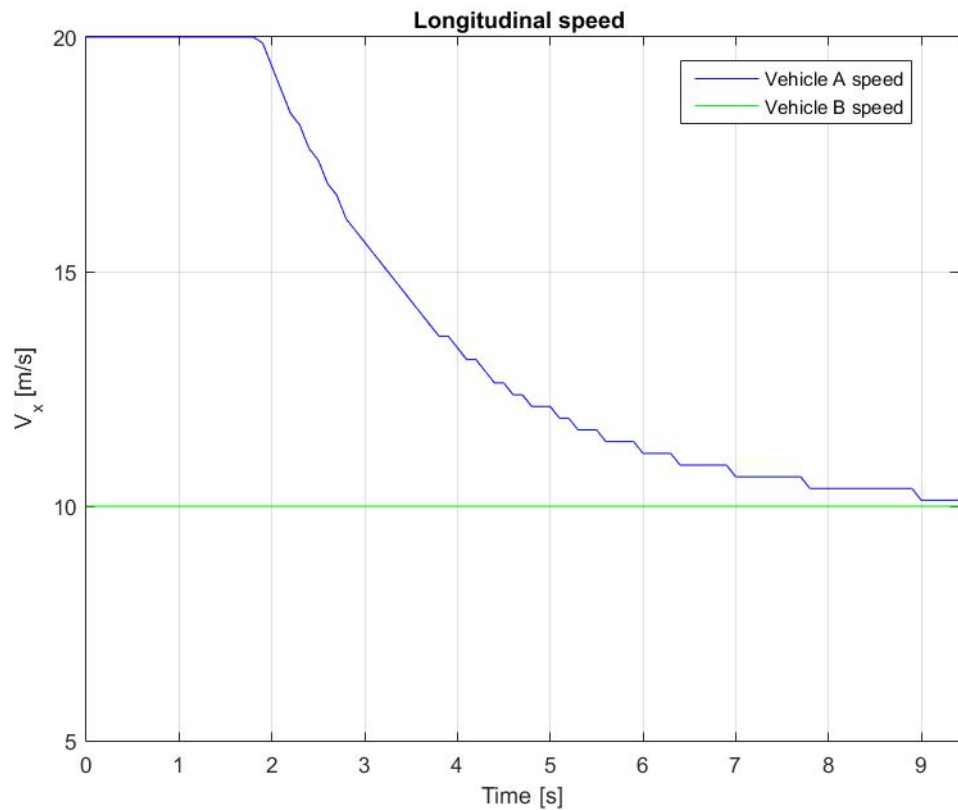


Fig. 2.39: Scenario 1: Vehicle A and B speeds during the ACC phase.

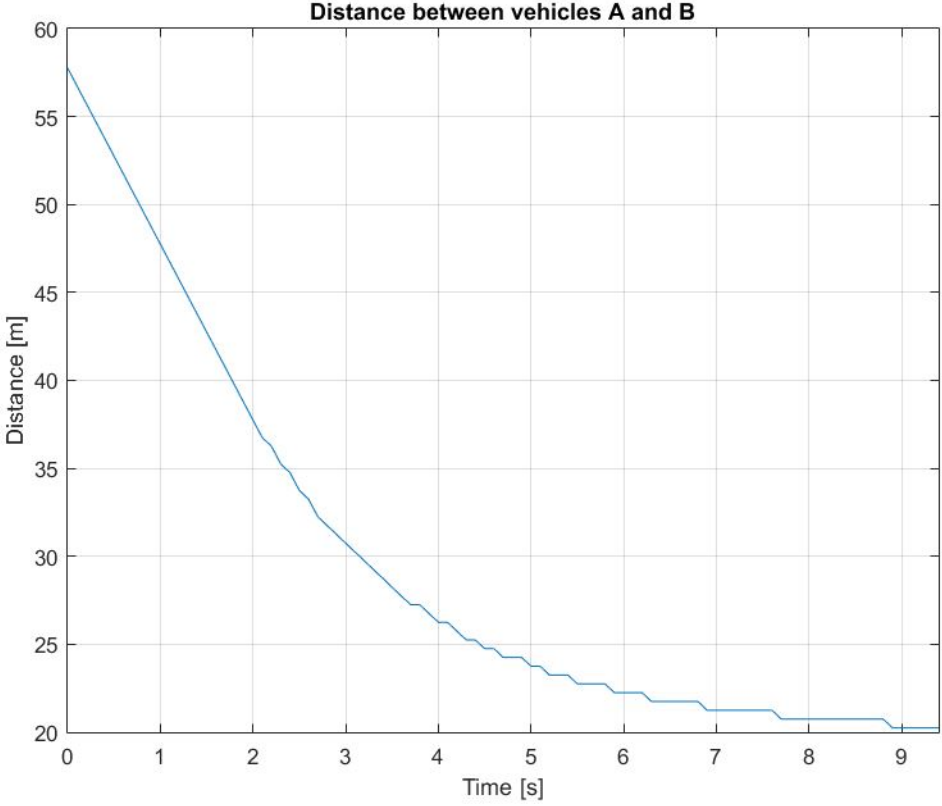


Fig. 2.40: Scenario 1: Inter-vehicles distance between A and B during the ACC phase.

As can be seen in Fig. 2.40 and Fig. 2.39, the vehicle A speed remains  $20m/s$  as long as  $d_{AB}$  is greater than  $40m$  ( $2V_A = 40m$ ). Once  $d_{AB}$  becomes less than  $40m$ , the ACC commands the vehicle A to decelerate in order to increase the distance  $d_{AB}$  so that (2.70) remains satisfied. At  $t = 9s$ , the vehicles A and B navigates with almost the same speed ( $V_A = 10.13m/s$  and  $V_B = 10m/s$ ).

Note that, during the ACC phase, the vehicle A is allowed to overtake B if and only if its desired speed is greater than  $V_B + 20km/h$  and the left lane is free.

The first condition is satisfied here, since the desired speed of the vehicle A is  $20m/s = 72km/h$  and  $V_B = 10m/s = 36km/h$ . We have then  $V_{A_{des}} > V_B + 20km/h$ .

We suppose in this scenario that the left lane is free from  $t = 9.3s$  (we suppose that the left lane was occupied by a vehicle C during the Adaptive Cruise Control phase, and then it becomes free at  $t = 9.3s$ ).

As a result, the vehicle A is allowed to overtake B from  $t = 9.3s$ . Once  $t = 9.3s$ , the maneuver planner starts searching for a suitable lane changing trajectory that satisfies the vehicle dynamic constraints, the vehicle safety constraints and the road rules resumed by (2.32) and (2.37).

Then, in order to find a suitable lane changing trajectory, we specify the target speed of the vehicle A using (2.32), that yields:

$$\begin{aligned} V_{A_f} &= \max(\min(V_B + 20km/h, V_{x_{max}}^{Lane2}), V_{A_i}) \\ &= \max(\min(56km/h, 100.8km/h), 36.46km/h) = 56km/h \simeq 15.55m/s. \end{aligned}$$

Now, the maneuver planner has to check if the condition (2.37) can be satisfied with the current situation (depending on  $V_{A_i}$ ,  $V_{A_f}$ ,  $d_{AB}$  and the other parameters).

In the current situation, at  $t = 9.3s$ , the condition (2.37) is as follows:

$$\begin{aligned} \max(T_{min1}, T_{min2}) &\leq T_1 \leq T_{max} \\ \max(2.27s, 5.42s) &\leq T_1 \leq 6.07s \end{aligned}$$

This means that, by choosing  $T_1$  in  $[5.42s, 6.07s]$ , we can satisfy (2.37) and then we can declare that the overtaking maneuver is feasible.

Therefore, we choose to set  $T_1$  to  $6.07s$  and the lane changing maneuver is safely executed using the generated trajectory. Fig 2.41 shows the ACC phase and the phase 1 of the overtaking maneuver. We note  $t_0$  the time at which the overtaking maneuver starts. In this scenario,  $t_0 = 9.3s$ . The distance between A and B, at  $t = t_0$  is  $D_{obs1} \simeq 20m$ . When the vehicle A reaches the left lane, the vehicle B is slightly positioned in front of it, with a safety distance of  $3m$ .

The longitudinal and the lateral speed and acceleration profiles executed by the vehicle A during the lane changing maneuver are shown in Fig. 2.42. We can observe that the dynamic constraints are respected since the longitudinal acceleration is less than  $a_{x_{max}}$  and the lateral acceleration is also less than its limit  $a_{y_{max}}$ .

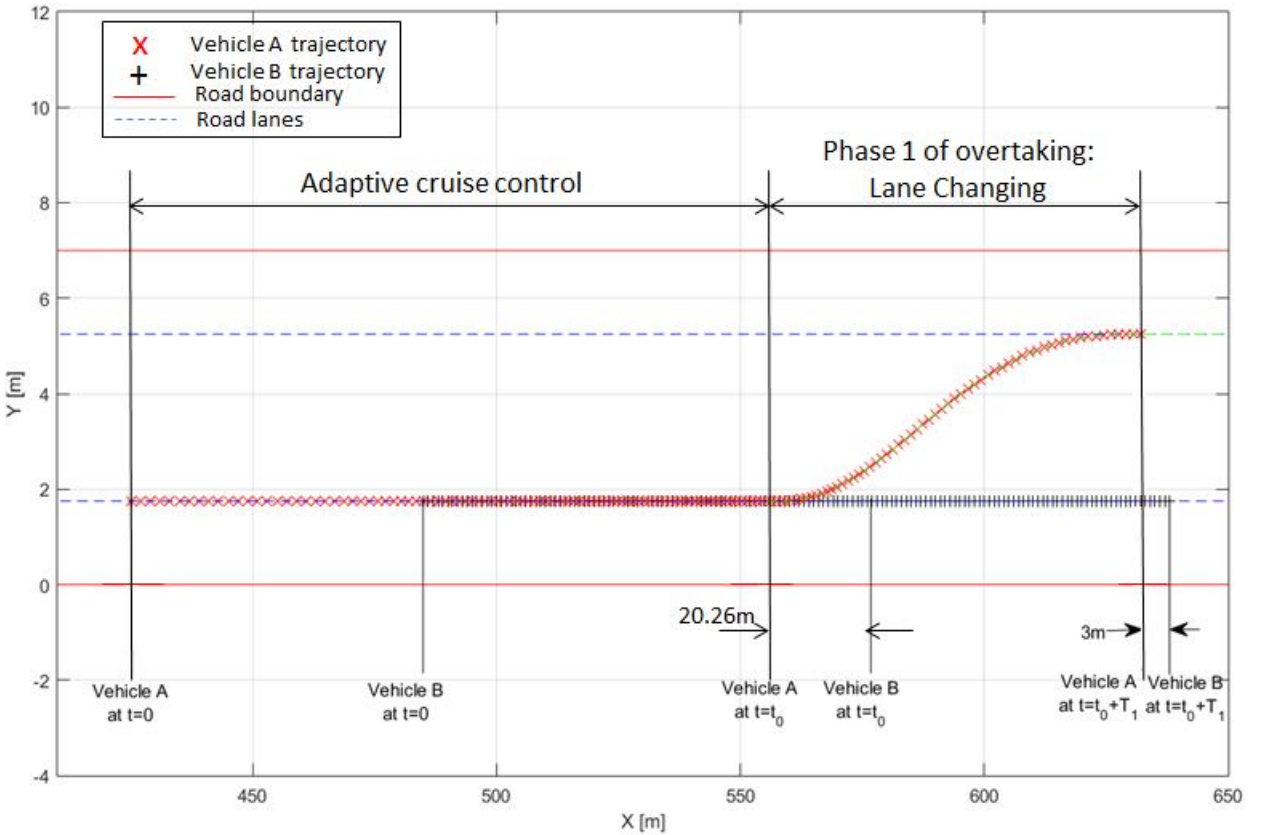


Fig. 2.41: Scenario 1: ACC phase and Phase 1 of the overtaking maneuver (Changing lane from right to left).

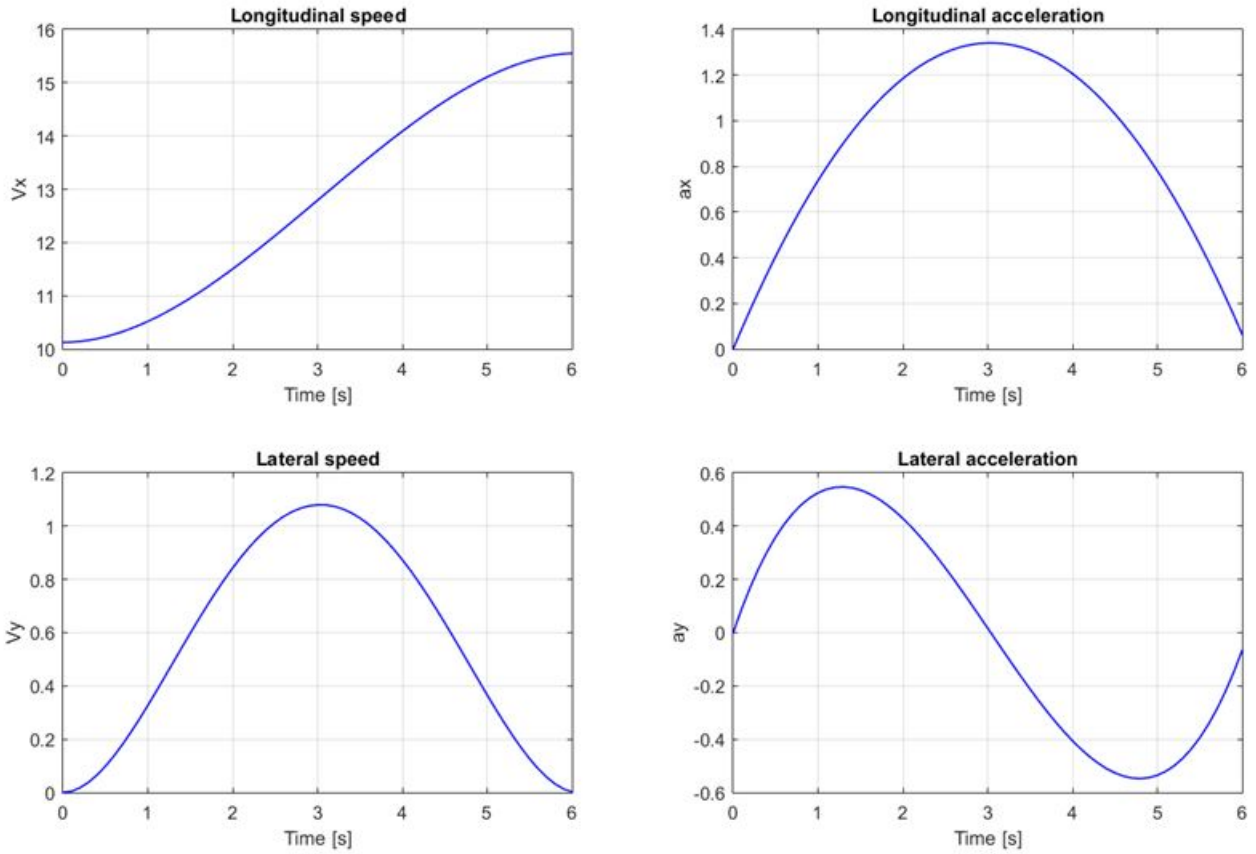


Fig. 2.42: Scenario 1: Speed and acceleration profiles of vehicle A during the phase 1 of the overtaking maneuver

In the second phase, the vehicle A navigates on the left lane at  $15.5m/s$  for a time duration of  $T_2$  derived from (2.41):

$$T_2 = 2.59s.$$

This phase is illustrated in Fig. 2.43. This phase ends when the vehicle A exceeds the vehicle B by  $3m$ . At this instant, phase 3 begins.

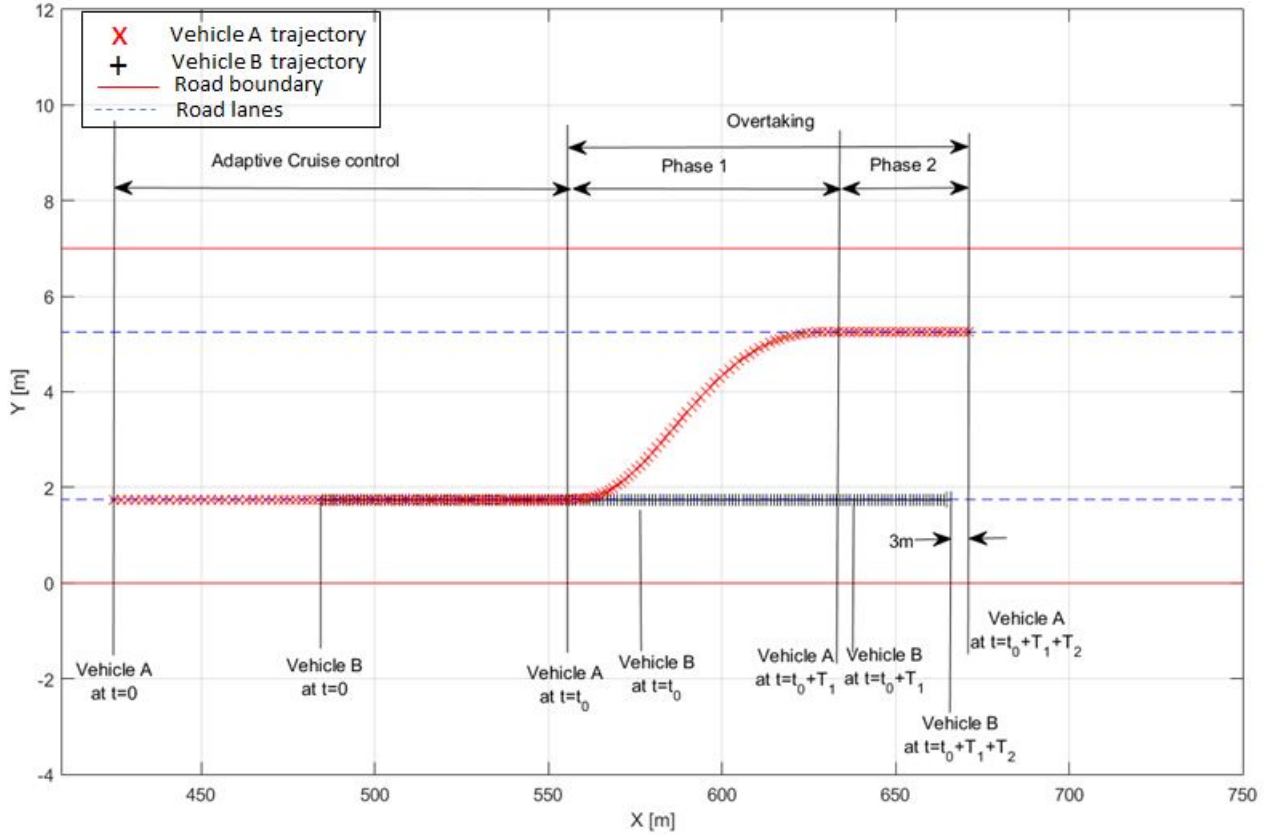


Fig. 2.43: Scenario 1: ACC phase and the first two phases of the overtaking maneuver.

For the third phase, the time duration of the lane changing is specified by (2.64). In this scenario, (2.64) becomes:

$$\begin{aligned}
 T_3 &\geq \max(T_{min1}, T_{min2}, T_{min3}) \\
 T_3 &\geq \max(2.27s, 2.864s, 2.1935s) \\
 T_3 &\geq 2.864s
 \end{aligned} \tag{2.71}$$

In this scenario, we have chosen  $T_3 = 2.864s$ .

The target speed in this phase is then set according to (2.66):

$$\begin{aligned}
 \max(10, 16.37) &\leq V_{A_{f2}} \leq \min(18.41, 20) \\
 16.37m/s &\leq V_{A_{f2}} \leq 18.41m/s
 \end{aligned} \tag{2.72}$$

This means that the vehicle A should accelerate in this phase in order to satisfy all the imposed constraints. However, if we have chosen  $T_3$  greater than its minimum value (2.864s here), the vehicle can execute the third phase without accelerating. Actually, a human driver don't really accelerate when returning to the right lane during an overtaking maneuver. This point is taken into consideration in the next scenario.

We have chosen  $V_{A_{f2}} = 16.37m/s$ . The ego vehicle dynamic profiles for the phase 3 are shown in Fig. 2.45. Note that the choice of  $V_{A_{f2}}$  fulfills the safety condition (2.53), that guarantees a safety distance greater than two seconds of reaction between the vehicles A and B once this third phase is finished, that is at  $t = t_0 + T_1 + T_2 + T_3$ . This distance is of  $D_{obs2} = 20.75m$  as

shown in Fig. 2.44.

In this scenario, a secure overtaking maneuver was planned. In order to show, furthermore, the planner degrees of freedom, a second scenario starting with the same initial speeds of vehicle A and B is shown hereafter.

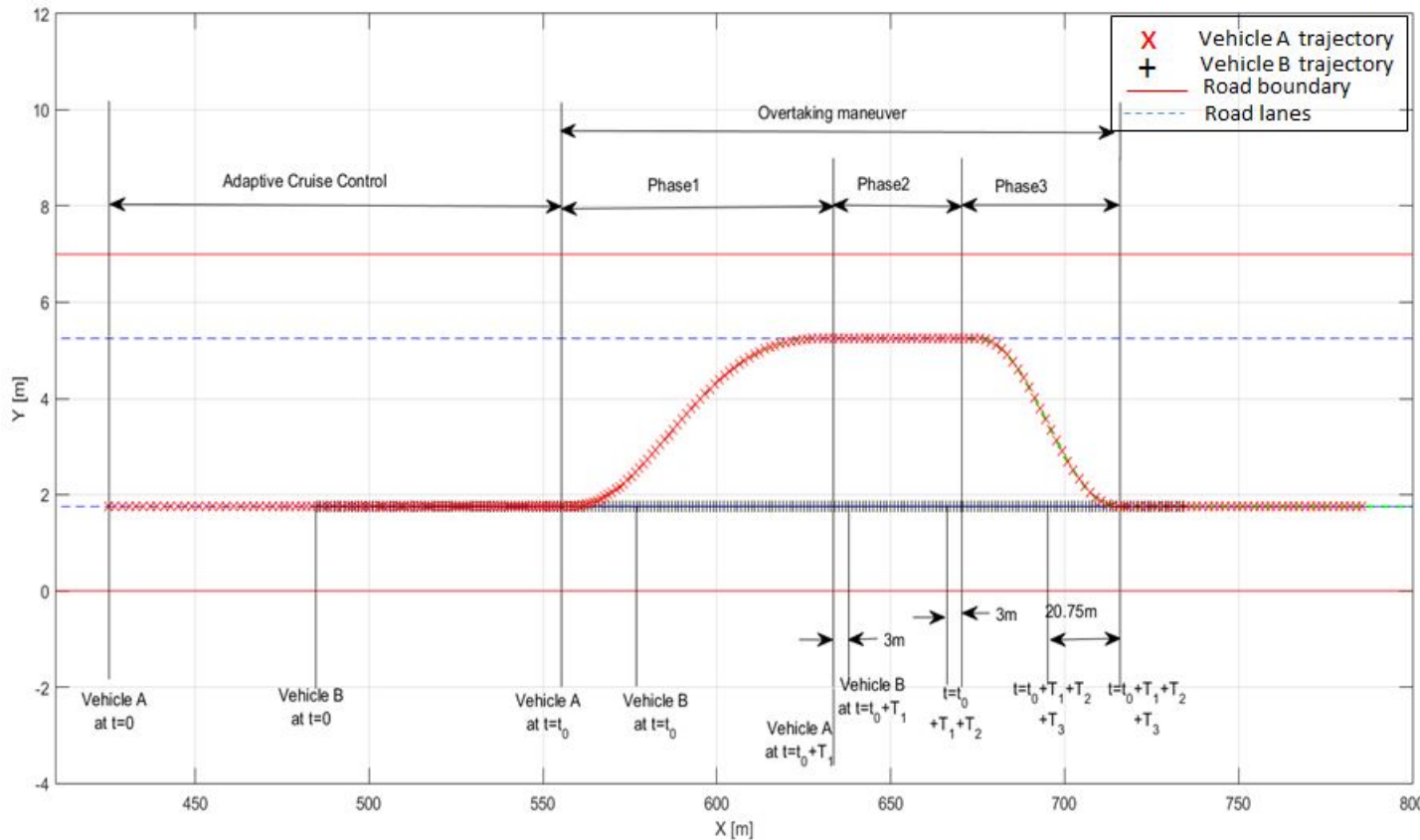


Fig. 2.44: Scenario 1: ACC phase and the three phases of the overtaking maneuver

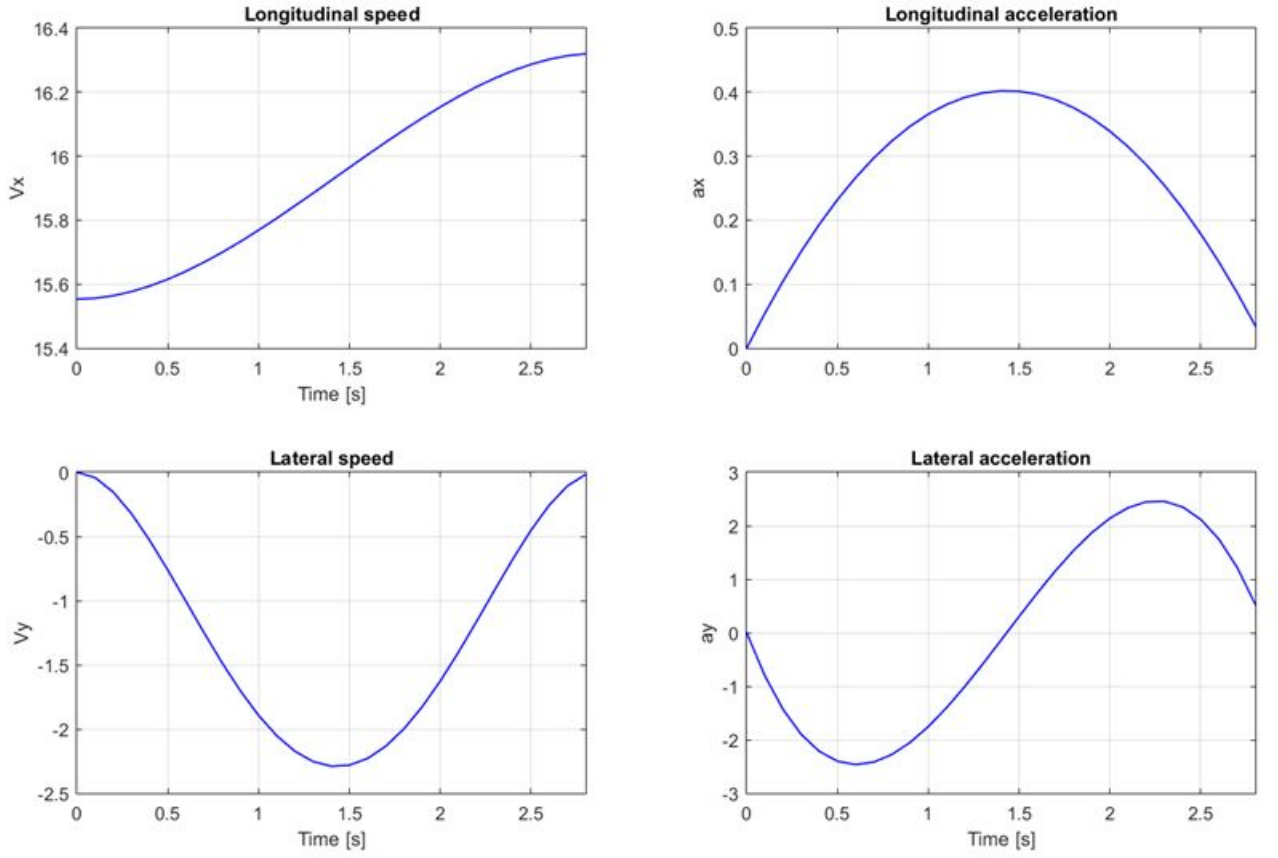


Fig. 2.45: Scenario 1: Speed and acceleration profiles of vehicle A during the phase 3 of the overtaking maneuver

### 2.3.3.2 Scenario 2

This scenario is presented here, in order to highlight the different degrees of freedom of the maneuver planning algorithm such as the time at which the overtaking maneuver begins ( $t_0$ ), the time duration of the first phase ( $T_1$ ) and the time duration of the third phase ( $T_3$ ).

In order to analyze the impact of each of these parameters variations, we set the initial speeds of the vehicles A and B identically to scenario 1:

$$V_{A_i} = 20 \text{m/s}, V_B = 10 \text{m/s}. \quad (2.73)$$

The maximum admissible accelerations and the maximum speeds allowed on the right and the left lane are set identically to scenario 1. The lane width, the safety distances  $m_s$  and  $m_{s2}$ , and the vehicles length are also set identically to scenario 1.

Then, identically to scenario 1, the vehicle A starts its navigation on the right lane. When it detects the vehicle B, the Adaptive Cruise Control is activated.

The speeds of the vehicle A and B during this ACC phase are shown in Fig. 2.46 and the inter-vehicle distance between A and B is shown in Fig. 2.47. The initial distance between A

and B is of  $57.5\text{m}$  and the vehicle A starts the navigation with  $20\text{m/s}$  and the vehicle B starts with  $10\text{m/s}$ .

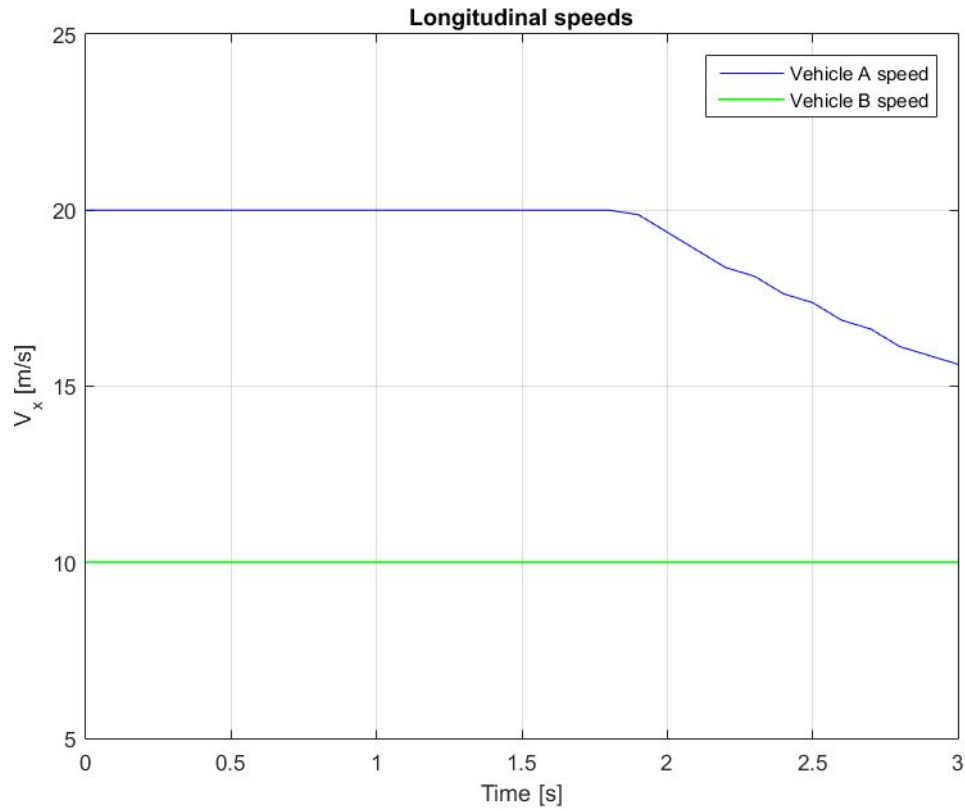


Fig. 2.46: Scenario 2: Vehicle A and B speeds during the ACC phase.

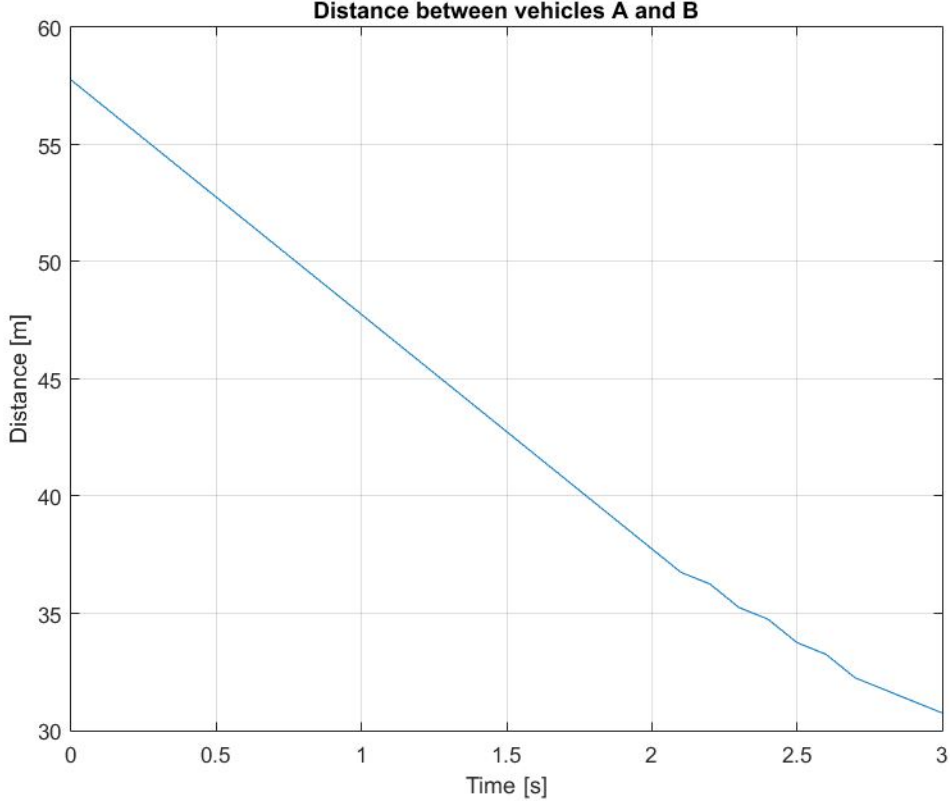


Fig. 2.47: Scenario 2: Inter-vehicles distance between A and B during the ACC phase.

As can be seen in Fig. 2.47 and Fig. 2.46, the vehicle A speed remains  $20m/s$  as long as  $d_{AB}$  is greater than  $40m$  ( $2V_A = 40m$ ). Once  $d_{AB}$  becomes less than  $40m$ , the ACC controls the vehicle A to decelerate in order to increase the distance  $d_{AB}$  so that (2.70) remains satisfied. Again, during the ACC phase, the vehicle A is allowed to overtake B if and only if its desired speed is greater than  $V_B + 20km/h$  and the left lane is free.

The first condition is satisfied here, since the desired speed of the vehicle A is  $20m/s = 72km/h$  and  $V_B = 10m/s = 36km/h$ . We have then  $V_{A_{des}} > V_B + 20km/h$ .

The difference here is that we suppose in this scenario that the left lane is free from  $t = 3s$  (we suppose that the left lane was occupied by a vehicle C during the Adaptive Cruise Control phase, and then it becomes free at  $t = 3s$ ).

As a result, the vehicle A is allowed to overtake B from  $t = t_0 = 3s$ . Once  $t = 3s$ , the maneuver planner starts searching for a suitable lane changing trajectory that satisfies the vehicle dynamic constraints, the vehicle safety constraints and the road rules resumed by (2.32) and (2.37).

The overtaking maneuver then starts when  $t = t_0 = 3s$ ,  $d_{AB} = 31.25m$  and  $V_{A_i} = 15.62m/s$ . The target speed of the vehicle A at the end of the lane changing maneuver is then found using (2.32), that yields:

$$\begin{aligned} V_{A_f} &= \max(\min(V_B + 20km/h, V_{x_{max}}^{Lane2}), V_{A_i}) \\ &= \max(\min(56km/h, 100.8km/h), 56.32km/h) = 56.32km/h \simeq 15.62m/s. \end{aligned}$$

Now, the maneuver planner has to check if the condition (2.37) can be satisfied with the current situation (depending on  $V_{A_i}$ ,  $V_{A_f}$ ,  $d_{AB}$  and the other parameters).

In the current situation, the condition (2.37) is as follows:

$$\max(T_{min1}, T_{min2}) \leq T_1 \leq T_{max}$$

$$\max(2.27s, 0s) \leq T_1 \leq 5.022s$$

This means that, by choosing  $T_1$  in  $[2.27s, 5.022s]$ , we can satisfy (2.37) and then we can declare that the overtaking maneuver is feasible.

Therefore, we choose to set  $T_1$  to  $4.46s$  and the lane changing maneuver is safely executed using the generated trajectory. Fig 2.48 shows the ACC phase and the phase 1 of the overtaking. The longitudinal and the lateral speed and acceleration profiles executed by the vehicle A during the lane changing maneuver are shown in Fig. 2.49. We can observe that the dynamic constraints are respected since the longitudinal acceleration is less than  $a_{x_{max}}$  and the lateral acceleration is also less than its limit  $a_{y_{max}}$ .

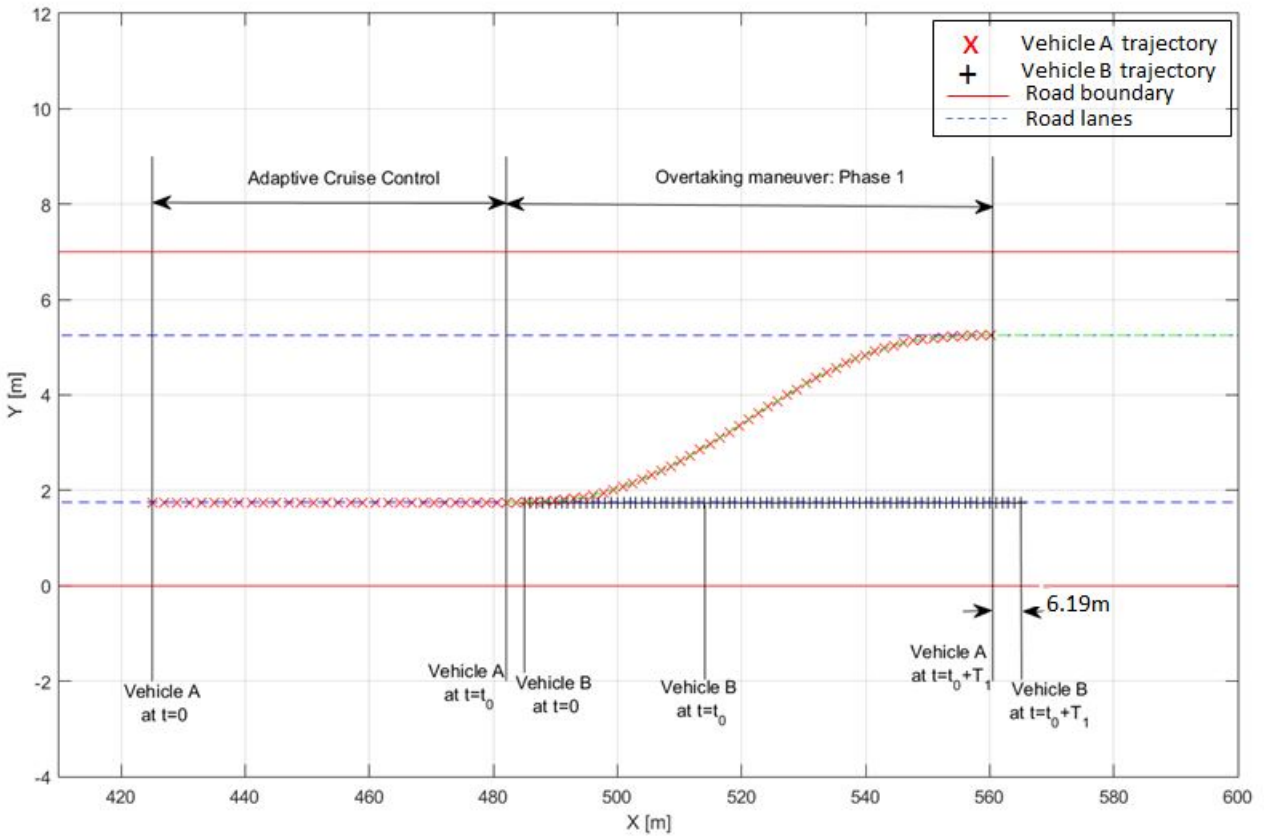


Fig. 2.48: Scenario 2: ACC phase and Phase 1 of the overtaking maneuver (Changing lane from right to left).

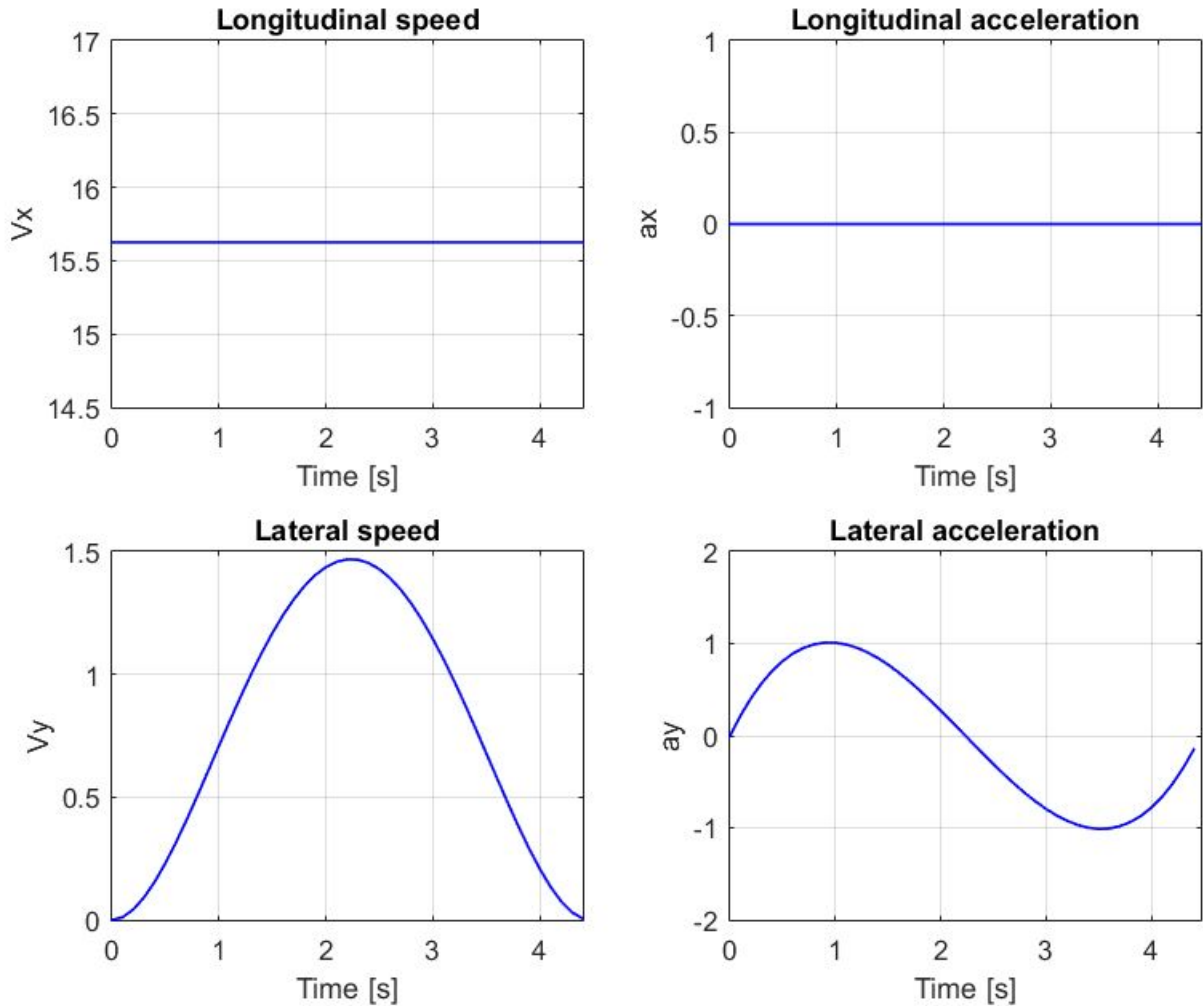


Fig. 2.49: Scenario 2: Speed and acceleration profiles of vehicle A during the phase 1 of the overtaking maneuver

In the second phase of the scenario 2, the vehicle A navigates on the left lane at  $15.62m/s$  for a time duration of  $T_2$  derived from (2.41):

$$T_2 = 2.56s.$$

This phase is illustrated in Fig. 2.50. This phase ends when the vehicle A exceeds the vehicle B by  $3m$ . At this instant, phase 3 begins.

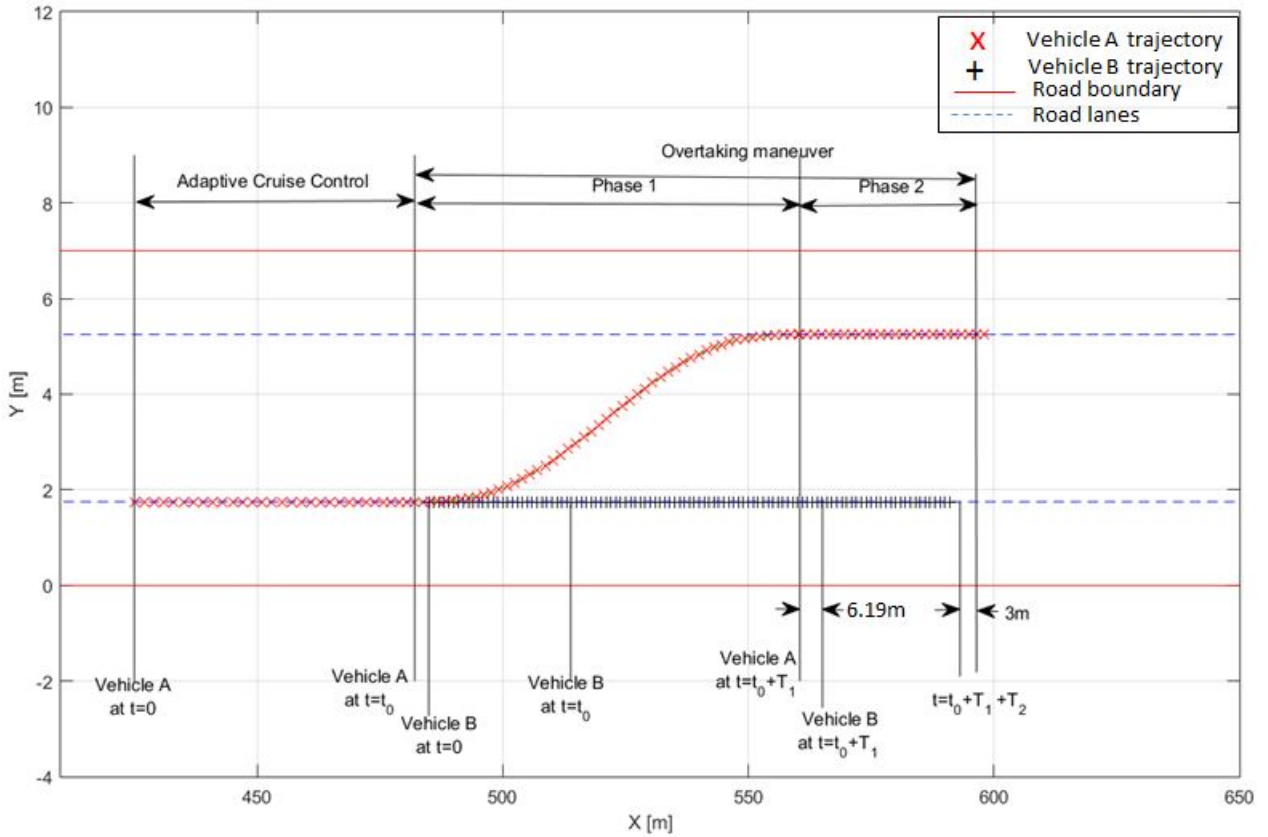


Fig. 2.50: Scenario 2: ACC phase and the first two phases of the overtaking maneuver.

For the third phase, the time duration of the lane changing is specified by (2.64). In this scenario, (2.64) becomes:

$$\begin{aligned} T_3 &\geq \max(T_{min1}, T_{min2}, T_{min3}) \\ T_3 &\geq \max(2.27s, 2.84s, 2.17s) \\ T_3 &\geq 2.84s \end{aligned} \quad (2.74)$$

In this scenario, we have chosen  $T_3 = 4.84s$ .

The target speed in this phase is then set according to (2.66):

$$\begin{aligned} \max(10, 11.40) &\leq V_{A_{f2}} \leq \min(20.46, 20) \\ 11.40m/s &\leq V_{A_{f2}} \leq 20m/s \end{aligned} \quad (2.75)$$

This means that the vehicle A can either accelerate, or decelerate or stay with the same speed, in this phase in order to satisfy all the imposed constraints. We have chosen  $V_{A_{f2}} = V_{A_{i2}} = 15.62m/s$ . The ego vehicle dynamic profiles for the phase 3 are shown in Fig. 2.52. Note that the choice of  $V_{A_{f2}}$  fulfills the safety condition (2.53), that guarantees a safety distance greater than two seconds of reaction between the vehicles A and B once this third phase is finished, that is at  $t = t_0 + T_1 + T_2 + T_3$ . This distance is of  $D_{obs2} = 28.8m$  as shown in Fig. 2.51.

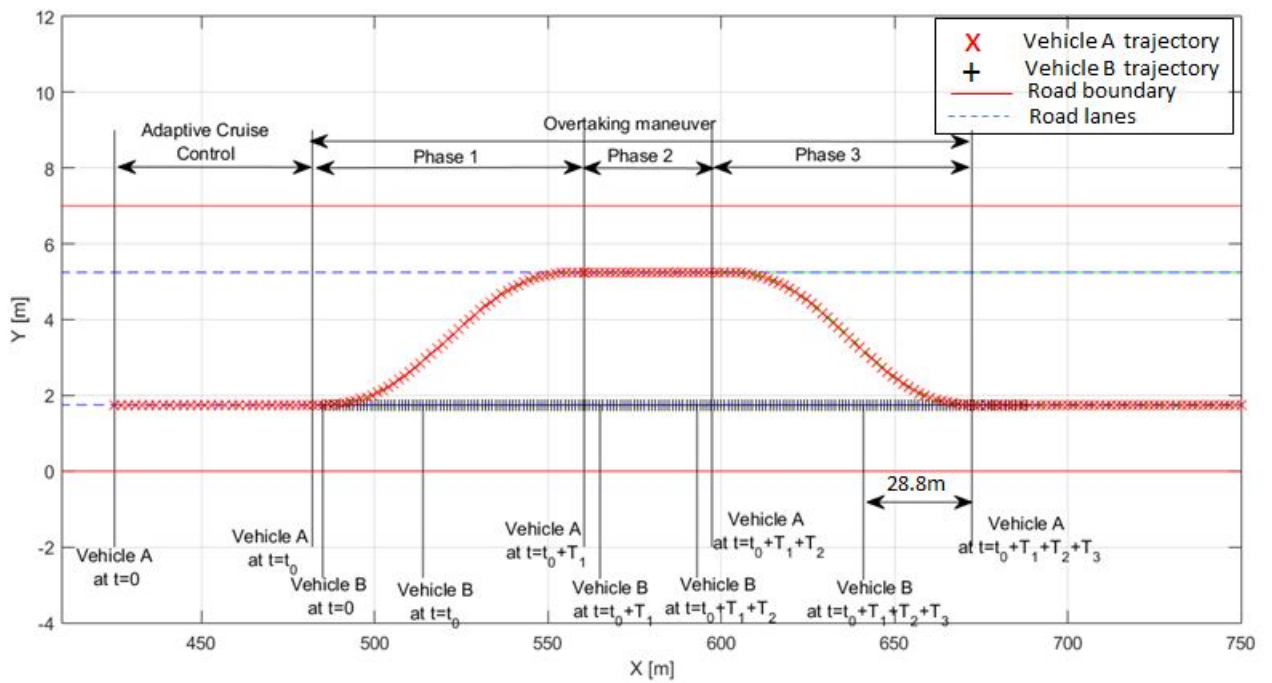


Fig. 2.51: Scenario 2: ACC phase and the three phases of the overtaking maneuver

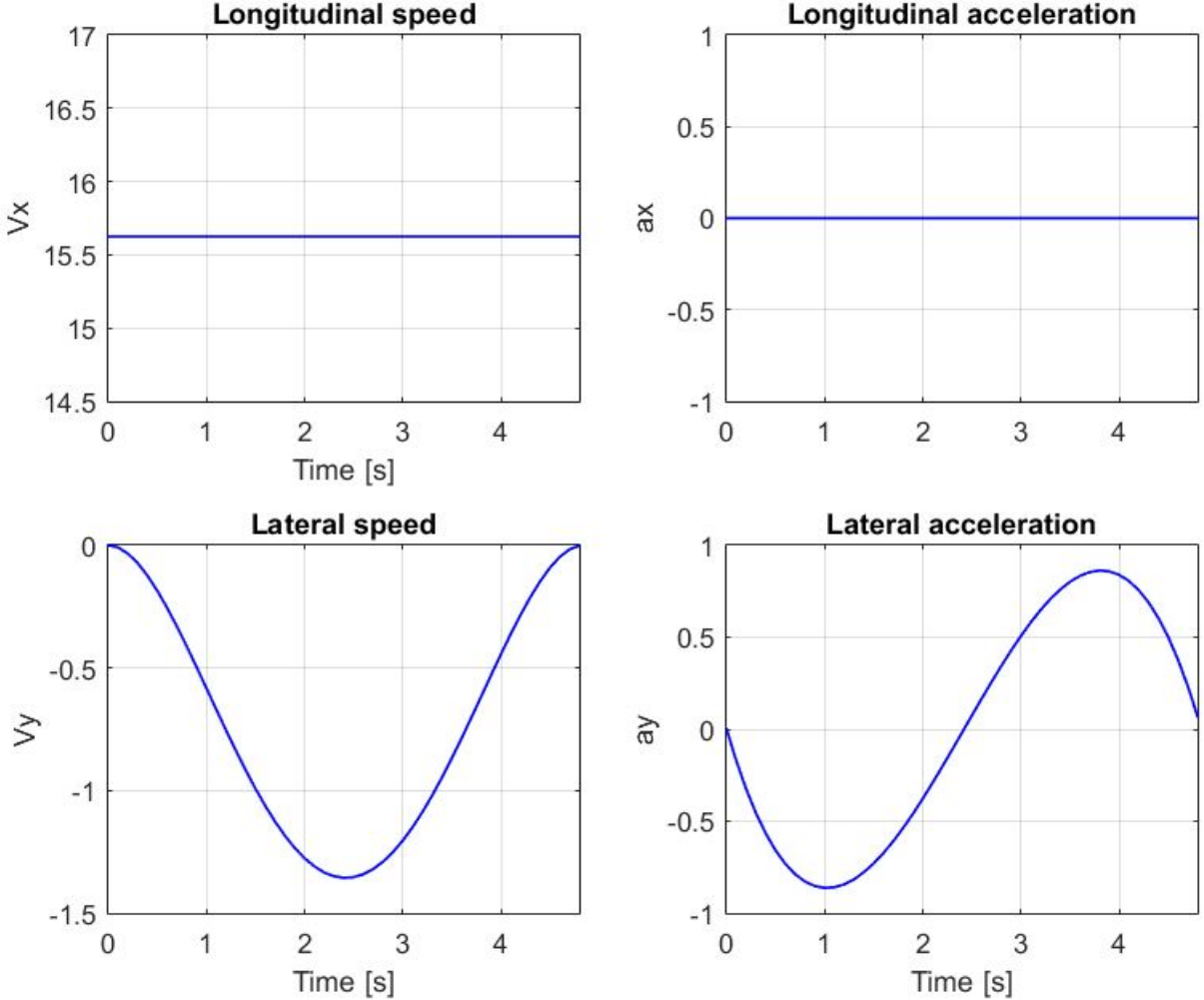


Fig. 2.52: Scenario 2: Speed and acceleration profiles of vehicle A during the phase 1 of the overtaking maneuver

*Parameters  $t_0$ ,  $T_1$  and  $T_3$  variations effects:* In the first scenario,  $t_0$  was set to 9.3s while in scenario 2,  $t_0$  is set to 3s. When the parameter  $t_0$  decreases, the distance between the vehicle A and B ( $d_{AB}$ ) at  $t = t_0$  increases. This means that the time duration of the first phase  $T_1$  will increase if the vehicle A starts from the same speed  $V_{A_i}$ . Here, in the presence of the ACC, the vehicle speed at  $t = t_0$  also changes when  $t_0$  changes. In the scenario 1,  $V_{A_i}$  was of 10.13m/s at  $t = t_0 = 9.3$ s while in the scenario 2,  $V_{A_i}$  is of 15.62m/s at  $t = t_0$ . And this yields to choose  $V_{A_f} = 15.55$ m/s in the scenario 1 and 15.62m/s in the scenario 2. In other words, the planner choose to accelerate in the scenario 1 from 10.13 to 15.55m/s and imposes  $T_1$  to be chosen between 5.42s and 6.07s. While in scenario 2, the planner choose to stay on the same speed of 15.62m/s and imposes  $T_1$  to be chosen between 2.27s and 5.022s which corresponds to a time duration  $T_1$  less than that of the scenario 1. This result validates the maneuver planning algorithm for different values of  $t_0$  and  $V_{A_i}$ . The choice of the parameter  $t_0$  gives the vehicle more flexibility in choosing when to start the overtaking maneuver depending for example on the occupation state of the left lane.

Now, in the first scenario, we have chosen  $T_1$  as the maximum value allowed by the constraints,  $T_1 = T_{max} = 6.07$ s. This yields that the condition (2.36) is satisfied with equality and the

longitudinal distance between the vehicles A and B when A reaches the left lane will be exactly equal to the safety distance  $m_s = 3m$  (see Fig. 2.41). However, in the second scenario, we have chosen  $T_1 < T_{max}$  which yields that the longitudinal distance between the vehicles A and B when A reaches the left lane will be greater than the safety distance  $m_s = 3m$  (see Fig. 2.48). This means that the choice of the parameter  $T_1$  could be tuned with respect to the situation in order to choose the vehicle A position on the left lane once the lane changing maneuver is over.

Finally, the choice of the parameter  $T_3$  could constraint the possible longitudinal maneuvers in the third phase of the overtaking maneuver. For example, in the scenario 1, as  $T_3$  was chosen as  $T_3 = \max(T_{min1}, T_{min2}, T_{min3})$ , the vehicle A was obliged to accelerate in order to reach the right lane with a safe inter-vehicle distance with respect to vehicle B. This behavior is not very similar to a human driver behavior. However, in scenario 2, the vehicle A had the choice either to accelerate, decelerate or keep the same speed while maintaining the same safe distance to the vehicle B as in scenario 1. The same result could be obtained by increasing  $m_{s2}$ . When  $m_{s2}$  is chosen high enough, the vehicle A could return to the right lane, while maintaining a safe inter-vehicle distance with vehicle B, without need to mandatory accelerate.

To conclude, the developed algorithm is a very promising planning approach with many degrees of freedom that can be very useful to deal with the actual situation around the vehicle. We look forward to ameliorate the approach by taking into account more complex scenarios with for example the presence of other obstacles on the left or the right lane. Taking into account varying curvatures road is also an important perspective of this work.

## 2.4 Local/Maneuver Combined Planning Approach

In this part, we present the combined navigation strategy that includes the maneuver planning level and the local planning level.

Fig. 5.1 shows the developed navigation strategy. In the maneuver planning level, the surrounding situation is interpreted and a decision about the best maneuver to execute is made. By default, the desired maneuver is to keep the right lane with a given speed profile. Once the ego vehicle detects a vehicle in front, an adaptive cruise control maneuver is executed in order to maintain a safety distance between the considered vehicles. If an overtaking maneuver is possible, which means the vehicle can overtake while respecting the dynamic constraints and the road safety rules, the maneuver planner calculates an overtaking trajectory.

The maneuver planner decision is transmitted to the local planner based on the tentacles method. The tentacles method role is to track the desired reference trajectory while avoiding the possible obstacles. When the maneuver planner commands to keep the right lane, the tentacles method have to track the right lane as the desired trajectory. If the maneuver planner commands the vehicle to overtake, the trajectory generated to execute the overtaking maneuver as well as the desired speed profile are transmitted to the local planner. The tentacles method objective is then to track the trajectory generated to change lane from the right to the left lane, keep the left lane for a given time and then track the lane changing trajectory generated to return back to the right lane. During the overall journey, it's the tentacles method duty to guarantee the ego-vehicle safety and collision avoidance, by selecting the best tentacle among the navigable ones. At every time step, set to 100ms based on the sensors frequency, the local planner outputs the best navigable tentacle to track with the desired speed provided from the maneuver planner. If the local planner can't find any navigable tentacle, the ego vehicle should

brake on the tentacle presenting the largest distance to the obstacle. As a last step, the local desired trajectory defined by the best tentacle and the desired speed are transmitted to the coupled controller that derives the control laws necessary to track the given trajectory with the desired speed.

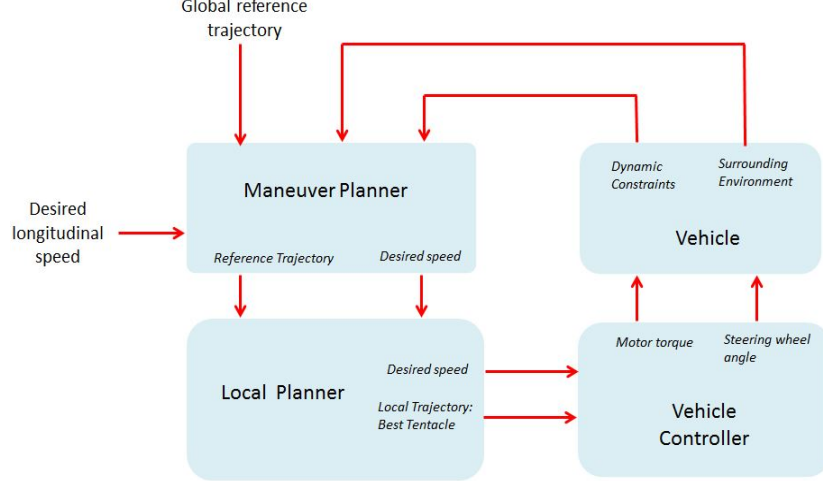


Fig. 2.53: Navigation strategy

## 2.5 Conclusion

A local trajectory planner is developed based on the clothoid tentacles method. The clothoid tentacles method objective is to guarantee a secure navigation on a given reference trajectory while avoiding the present obstacles. This method is tested with a static obstacle and then with a moving one and proves to be performant. In order to complete the tentacles method and to adapt the navigation to an on-road navigation, a maneuver level is added. This level treats essentially the overtaking maneuver and provides the local planner with the desired trajectory to change lane and then to return back to the initial lane. The overtaking maneuver planner has to guarantee a secure overtaking maneuver that respects the vehicle dynamic constraints and the road rules.

Further, the combined planner is evaluated while considering dynamic obstacles in Chapter 5. In this evaluation, the developed vehicle model and the developed Lyapunov based controller presented in the next chapters are used to estimate the vehicle motions and to control its dynamics.

# Chapter 3

## Vehicle Modeling using Robotics Formalism

### Summary

---

<b>3.1</b>	<b>Introduction</b>	<b>63</b>
<b>3.2</b>	<b>State of the Art on Existing Vehicle Modeling Techniques</b>	<b>64</b>
3.2.1	Closed-form Models	64
3.2.2	Multi-body Models	75
<b>3.3</b>	<b>Robotics Formalism for dynamic modeling</b>	<b>78</b>
3.3.1	Geometric description	78
3.3.2	Dynamic model development	81
<b>3.4</b>	<b>Application to a Four Wheeled Vehicle Model</b>	<b>90</b>
<b>3.5</b>	<b>Validation of the developed model</b>	<b>94</b>
3.5.1	Scaner-Studio Environment	95
3.5.2	Model Validation Results	96
<b>3.6</b>	<b>Conclusion</b>	<b>100</b>

---

### 3.1 Introduction

Modeling and simulating vehicle dynamics are fundamental tools for intelligent vehicles development. They allow understanding the dynamics of the vehicle and improving its design in order to ensure the major challenge of having safe and comfortable intelligent vehicles. Hence, the vehicle modeling goal is to build a mathematical model that illustrates significant aspects of the physical dynamics and then facilitates the performance analysis and the development of new controlling tools.

Several methods were proposed in the literature to model the vehicle kinematics and dynamics [Sha71b]. The well-known models, that are usually used, are the closed-form models developed using the fundamental principles of physics such as Newton-laws. Most of these models are built on simplifying kinematic constraints or neglecting some dynamic aspects. Lately, some advanced models have been developed using multi-body systems to model a complex system. The main advantage of this strategy is the accuracy of the multi-body models with respect to

the simplified closed-form models. Moreover, multi-body models usually provide more information (as it will be illustrated in the next sections), which are usually neglected when using a closed-form model. Diverse approaches are used to develop a multi-body system, such as Newton-Euler, Lagrange, Appell's method and many others.

In this work, a multi-body vehicle modeling technique is used, where the vehicle is considered as a multi-articulated system consisting of  $n$  bodies wherein the chassis is the movable base and the wheels are the terminals. We proceed in a systematic geometrical description, based on the modified Denavit Hartenberg parameterization [KK86]. The modeling is then conducted by applying recursive methods used in robotics, more precisely, recursive Newton-Euler based Algorithm [KK87]. This description allows the direct computation of the symbolic expression of the geometric, kinematic and dynamic models of the vehicle with a minimum number of numerical steps.

In this chapter, we will present a summary of well-known closed-form models and existing multi-body methodologies in Section 3.2. We conclude this section with our motivation to use the robotics formalism to develop the multi-body vehicle model. In Section 3.3, the robotics formalism is presented in detail. Then, the developed model is presented in Section 3.4. Finally, Section 3.5 shows the model validation results.

## 3.2 State of the Art on Existing Vehicle Modeling Techniques

In this section, a review of existing vehicle models is presented. The closed-form models as well as the multi-body modeling techniques are exposed. We conclude this section justifying the choice of the selected modeling approach.

### 3.2.1 Closed-form Models

The closed form models are generally derived using the fundamental physics laws, especially Newton's laws. The vehicle dynamic behavior is usually analyzed by modeling the chassis planar dynamics (in the lateral and the longitudinal directions), the vertical dynamics and the tire/road friction dynamics that will be detailed in the following.

#### 3.2.1.1 Vehicle Planar dynamics

Three main models can be found in the literature to represent the vehicle dynamics in the lateral and the longitudinal directions: the kinematic bicycle model, the dynamic bicycle model and the dynamic four-wheel vehicle model.

##### 3.2.1.1.1 Kinematic Bicycle Model

This model is derived in a geometric way, where the sideslip angle and the dynamic aspects are neglected (Fig. 3.2(a)). Note that the sideslip angle is the angle between the wheel's speed direction and the direction of the wheel itself (angles  $\alpha_f$  and  $\alpha_r$  in Fig. 3.2(b)). Regarding its simplicity, this model is used for control objectives, especially for low-speed maneuvers [Raj11, TMD<sup>+</sup>06]. Notice that this model is suitable for high-steering angle maneuvers (roads with high curvature, parking maneuvers, etc.).

Its equations are given by [Raj11]:

$$\dot{\psi} = \frac{V_x}{L} \tan(\delta) \quad (3.1)$$

$$\dot{X} = V_x \cos(\psi) \quad (3.2)$$

$$\dot{Y} = V_x \sin(\psi) \quad (3.3)$$

where (X,Y) represents the position of the vehicle center of gravity in the inertial frame and  $\psi$  represents the vehicle yaw angle.  $V_x$  is the vehicle longitudinal speed computed in the vehicle frame,  $\delta$  the steering wheel angle and  $L$  the vehicle wheelbase.

### 3.2.1.1.2 Dynamic Bicycle Model

This model takes into account the longitudinal and the lateral dynamics of the vehicle [AGS<sup>+</sup>95a]. However, the roll and the pitch motions (shown in Fig. 3.1) are neglected and the assumption of small angles is usually made (Fig. 3.2(b)). Moreover, the vehicle is assumed to be symmetric, for example, the sideslip angles of the left and the right wheels on the same axle are supposed to be equal.

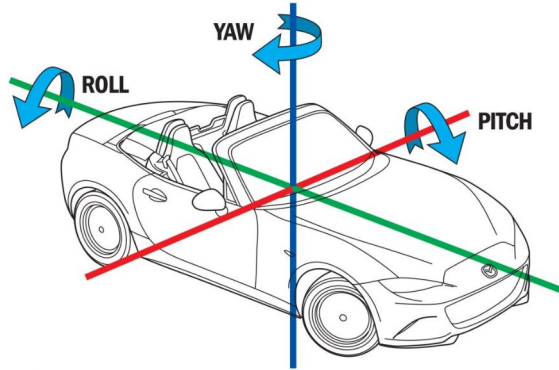


Fig. 3.1: Yaw, roll and pitch motions of the vehicle chassis.

The dynamic equations given by this model are as follows[Baf07]:

$$\dot{\beta} = \frac{1}{mV_g} [F_{x_f} \sin(\delta - \beta) + F_{y_f} \cos(\delta - \beta) - F_{x_r} \sin(\beta) + F_{y_r} \cos(\beta)] - \dot{\psi} \quad (3.4)$$

$$\dot{V}_g = \frac{1}{m} [F_{x_f} \cos(\delta - \beta) + F_{y_f} \sin(\beta - \delta) + F_{x_r} \cos(\beta) + F_{y_r} \sin(\beta)] \quad (3.5)$$

$$\ddot{\psi} = \frac{1}{I_z} [L_f(F_{y_f} \cos(\delta) + F_{x_f} \sin(\delta)) - L_r F_{y_r}], \quad (3.6)$$

where  $\beta$  and  $V_g$  refer respectively to the slip angle and the speed at the vehicle's center of gravity.  $m$  and  $I_z$  represent the vehicle mass and the moment of inertia around the z axis while  $L_f$  and  $L_r$  are the distances between the center of gravity and the front and the rear axles respectively.  $F_{x_i}$  and  $F_{y_i}$ , where the index  $i$  corresponds to  $r$  when considering the rear wheel and to  $f$  when considering the front wheel, are the forces generated in the contact surface between the wheels and the ground.

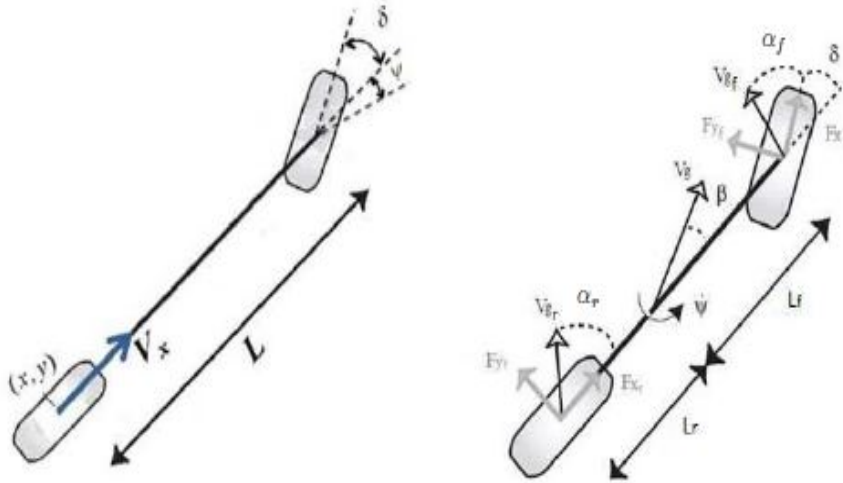


Fig. 3.2: Bicycle Models: (a) Kinematic bicycle Model, (b) Dynamic Bicycle Model

The linear velocities of the front and the rear wheels are given as follows:

$$\begin{aligned} V_{wx_f} &= \dot{x} \cos(\delta) + (\dot{y} + \dot{\psi} L_f) \sin(\delta) \\ V_{wx_r} &= \dot{x} \end{aligned} \quad (3.7)$$

where  $\dot{x}$  and  $\dot{y}$  are the longitudinal and the lateral speeds represented in the vehicle frame. The expressions for the sideslip angles  $\alpha_f$  and  $\alpha_r$  for the front and the rear wheels are given by ([Raj11]) :

$$\begin{aligned} \alpha_f &= \delta - \beta - \frac{L_f \dot{\psi}}{V_g} \\ \alpha_r &= -\beta + \frac{L_r \dot{\psi}}{V_g}. \end{aligned} \quad (3.8)$$

### 3.2.1.1.3 Four wheels Model

In nonlinear driving zones, the bicycle models with all their simplifying assumptions lose some of their representativity. The four wheels model (Fig. 3.3) is claimed to represent the vehicle dynamics in a better way [KN05]. Contrariwise, this model results in complex equations, limiting its application to the validation of embedded developed algorithms.

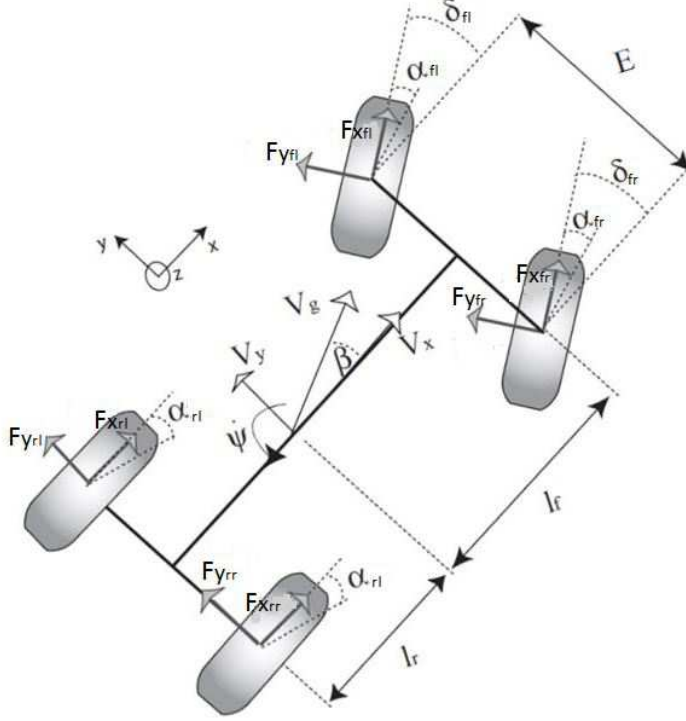


Fig. 3.3: Four wheels Vehicle Model

The dynamic equations taking into account the roll motion are given by:

$$a_x = \ddot{x} - \dot{\psi}\dot{y} = \frac{1}{m} [F_{xy_1} - F_{aero} + m_s h \dot{\psi} \phi_v] \quad (3.9)$$

$$a_y = \ddot{y} + \dot{\psi}\dot{x} = \frac{1}{m} [F_{xy_2} - m_s h \ddot{\phi}_v \psi] \quad (3.10)$$

$$\ddot{\psi} = \frac{1}{I_z} [F_{xy_3} + E/2F_{xy_4} + I_{xz} \ddot{\phi}_v] \quad (3.11)$$

$$\ddot{\phi}_v = \frac{1}{I_{xx}} [(m_s g h - (K_{\phi_f} + K_{\phi_r})) \phi_v - (C_{\phi_f} + C_{\phi_r}) \dot{\phi}_v - m_s h (\ddot{y} + \dot{\psi} \dot{x}) + I_{xz} \ddot{\psi}] \quad (3.12)$$

with:

$$\begin{aligned} F_{xy_1} &= -(F_{y_{fl}} + F_{y_{fr}}) \sin(\delta) + (F_{x_{fl}} + F_{x_{fr}}) \cos(\delta) + F_{x_{rl}} + F_{x_{rr}} \\ F_{xy_2} &= (F_{y_{fl}} + F_{y_{fr}}) \cos(\delta) + (F_{x_{fl}} + F_{x_{fr}}) \sin(\delta) + F_{y_{rl}} + F_{y_{rr}} \\ F_{xy_3} &= L_f ((F_{y_{fl}} + F_{y_{fr}}) \cos(\delta) + (F_{x_{fl}} + F_{x_{fr}}) \sin(\delta)) - L_r (F_{y_{rl}} + F_{y_{rr}}) \\ F_{xy_4} &= ((F_{y_{fl}} - F_{y_{fr}}) \sin(\delta) + (-F_{x_{fl}} + F_{x_{fr}}) \cos(\delta) + F_{x_{rr}} - F_{x_{rl}}) \end{aligned} \quad (3.13)$$

$\dot{x}$  and  $\dot{y}$  are the longitudinal and the lateral speeds represented in the vehicle frame while  $a_x$  and  $a_y$  are the longitudinal and the lateral accelerations of the vehicle with respect to the inertial reference frame.  $\phi_v$  is the roll angle,  $K_{\phi_f}$ ,  $K_{\phi_r}$  and  $C_{\phi_f}$ ,  $C_{\phi_r}$  are respectively the friction coefficients and the roll stiffness of the front and the rear wheels.  $m_s$ ,  $h$ ,  $E$  and  $g$  are respectively the suspended mass, the center of gravity height, the vehicle track and the gravity constant.  $I_{xz}$ ,  $I_z$ ,  $I_{xx}$  are the moments of inertia with respect to the roll and the yaw motions, the yaw

motion and the roll motion respectively. The indexes *fl*, *fr*, *rl* and *rr* refer to the front left, front right, rear left and rear right wheel respectively.

$F_{aero}$  represents the aerodynamic force in the direction of navigation and is given by:

$$F_{aero} = 1/2\rho_a s c_d \dot{x}^2, \quad (3.14)$$

where  $\rho_a$ ,  $s$  and  $c_d$  are the air density, the vehicle frontal surface and the aerodynamic constant.

Using the vehicle longitudinal, lateral, and yaw speeds, the linear velocity of each wheel can be derived [OS06]:

$$\begin{aligned} V_{wxfl} &= (\dot{x} - \frac{E\dot{\psi}}{2}) \cos(\delta) + (\dot{y} + \dot{\psi}L_f) \sin(\delta) \\ V_{wxfr} &= (\dot{x} + \frac{E\dot{\psi}}{2}) \cos(\delta) + (\dot{y} + \dot{\psi}L_f) \sin(\delta) \\ V_{wxrl} &= (\dot{x} - \frac{E\dot{\psi}}{2}) \\ V_{wxrr} &= (\dot{x} + \frac{E\dot{\psi}}{2}) \end{aligned} \quad (3.15)$$

The longitudinal and the lateral velocities, the steering angle and the yaw rate are then used to compute the tires slip angles  $\alpha_{ij}$  as well as the slip angle at the vehicle's center of gravity  $\beta$ :

$$\begin{aligned} \alpha_{fl} &= \delta - \arctan \frac{\dot{y} + L_f \dot{\psi}}{\dot{x} - E/2\dot{\psi}} \\ \alpha_{fr} &= \delta - \arctan \frac{\dot{y} + L_f \dot{\psi}}{\dot{x} + E/2\dot{\psi}} \\ \alpha_{rl} &= - \arctan \frac{\dot{y} - L_r \dot{\psi}}{\dot{x} - E/2\dot{\psi}} \\ \alpha_{rr} &= - \arctan \frac{\dot{y} - L_r \dot{\psi}}{\dot{x} + E/2\dot{\psi}} \\ \beta &= \arctan \frac{\dot{y}}{\dot{x}} \end{aligned} \quad (3.16)$$

### 3.2.1.2 Vehicle Vertical Dynamics

The vehicle planar dynamics are strongly coupled to the vertical dynamics. Therefore, to better analyze the vehicle behavior, the modeling and the interpretation of the vertical dynamics are a must. In the following, the automotive suspension models and the vertical load transfer are addressed.

#### 3.2.1.2.1 Automotive suspensions

The automotive suspensions aim to isolate a car body from road disturbances in order to provide good ride quality. Several models dealing with the automotive suspensions can be found in the literature [Raj11]: The 'quarter car', the 'half car' and the 'full car' models.

##### a) The 'quarter car' model

It represents the automotive system at each wheel, namely, the motion of the axle and of the vehicle body at any one of the four wheels of the vehicle. The suspension itself is shown to

consist of a spring  $K_s$ , a damper  $b_s$  and an active force actuator  $F_a$ . The sprung mass  $m_s$  is the quarter car equivalent of the vehicle body mass and the unsprung mass  $m_u$  represents the equivalent mass due to the axle and tire.  $K_t$  represents the vertical stiffness of the spring representing the tire, while the variables  $z_s$ ,  $z_u$  and  $z_r$  represent the vertical displacements from static equilibrium of the sprung mass, the unsprung mass and the road respectively. Note that, the active force can be set to zero in a passive suspension.

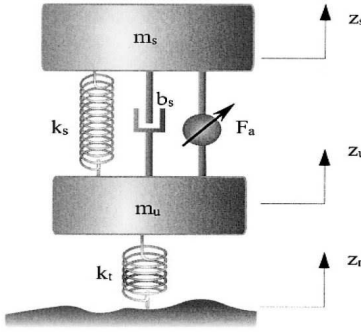


Fig. 3.4: Quarter car automotive suspension model

### b) The 'half car' model

In this model, the pitch and heave motions of the vehicle body ( $\theta$  and  $z$ ) and the vertical translation of the front and rear axles ( $z_1$  and  $z_2$ ) are represented.

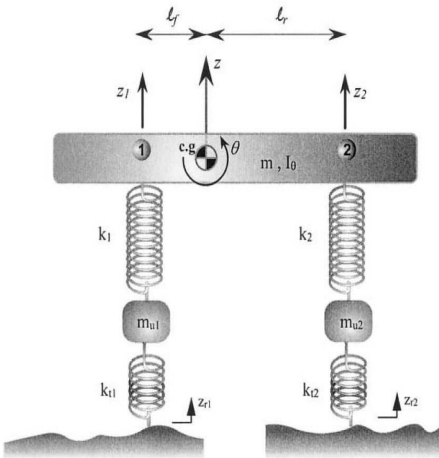


Fig. 3.5: Half car automotive suspension model

### c) The 'full car' model

This model represents the vertical dynamics with seven degrees of freedom: the heave  $z$ , the pitch  $\theta$  and the roll  $\phi$  and the vertical motions of each of the four unsprung masses. The variables  $z_{r1}$ ,  $z_{r2}$ ,  $z_{r3}$  and  $z_{r4}$  are the road profile inputs that excite the system.

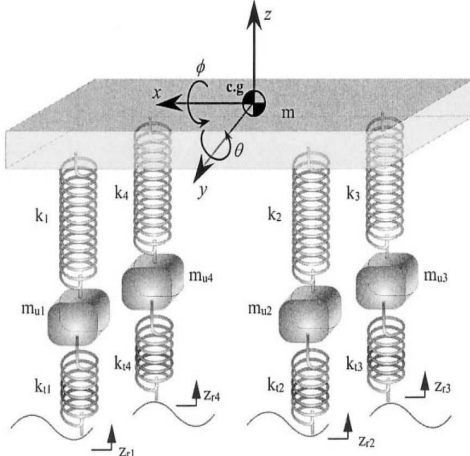


Fig. 3.6: Full car automotive suspension model

### 3.2.1.2.2 Vertical loads transfer

As mentioned above, the longitudinal and the lateral forces generated on each wheel are directly related to the vertical loads applied to this wheel. Moreover, the maximum force in the longitudinal and the lateral directions is determined by the vertical load applied to each tire. Indeed, the vertical loads are the result of the gravitational efforts and the vehicle accelerations. When the vehicle speed is constant, the vertical efforts are distributed on the four wheels, depending on the repartition of the different masses of the vehicle components (for example, the fuel and the passengers masses). However, when the vehicle acceleration is not null, the vertical loads distribution on the four wheels is modified. This phenomenon is called 'Vertical Load Transfer'. For example, when the vehicle speed increases, the vertical loads applied to the front wheels decrease while those applied to the rear wheels increase.

Referring to the work of Kiencke [KN05] and Lechner [Lec02], the vertical loads on the four wheels can be computed as follows:

$$\begin{aligned}
 F_{z_{fl}} &= \frac{1}{2}m\left(\frac{L_r}{L}g - \frac{h}{L}a_x\right) - m\left(\frac{L_r}{L}g - \frac{h}{L}a_x\right)h\frac{a_y}{Eg} \\
 F_{z_{fr}} &= \frac{1}{2}m\left(\frac{L_r}{L}g - \frac{h}{L}a_x\right) + m\left(\frac{L_r}{L}g - \frac{h}{L}a_x\right)h\frac{a_y}{Eg} \\
 F_{z_{rl}} &= \frac{1}{2}m\left(\frac{L_f}{L}g + \frac{h}{L}a_x\right) - m\left(\frac{L_f}{L}g + \frac{h}{L}a_x\right)h\frac{a_y}{Eg} \\
 F_{z_{rr}} &= \frac{1}{2}m\left(\frac{L_f}{L}g + \frac{h}{L}a_x\right) + m\left(\frac{L_f}{L}g + \frac{h}{L}a_x\right)h\frac{a_y}{Eg}
 \end{aligned} \tag{3.17}$$

where  $L$  is the vehicle wheel base corresponding to the distance between the front and the rear axles,  $a_x$  is the vehicle longitudinal acceleration and  $a_y$  is the vehicle lateral acceleration.

### 3.2.1.3 Tires dynamics

From a physical point of view, the movement of the vehicle is a result of the forces applied to this vehicle and the sliding exerted in the contact zone between the tires and the road.

Consequently, the choice of a model that represents the relations between the sliding and the generated forces is an important step to analyze the vehicle dynamic behavior. Fig. 3.7 shows

the forces and the moments generated in the contact zone between the tires and the ground. Several models can be found in the literature [Men10] to estimate these forces. We cite in this paragraph the linear model, Dugoff's model, Burckhardt/Kiencke's model and Pacejka's model.

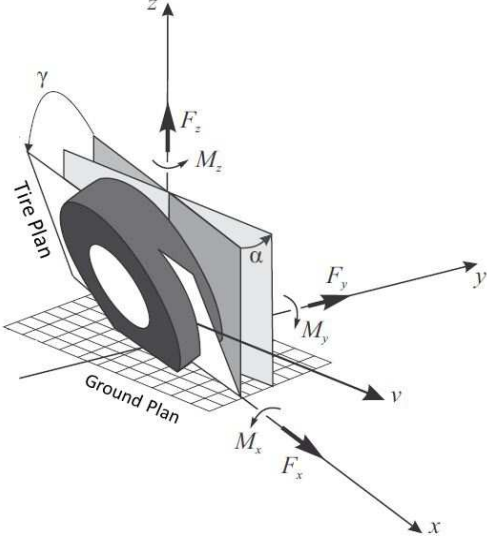


Fig. 3.7: Forces and moments in the contact area Tire/Ground [Jaz13].

### 3.2.1.3.1 Linear model

The linear model is the most used model, regarding its simplicity. It represents the tire forces in the linear zone, where the vehicle is subjected to moderate dynamic loads. According to the work of D. Lechner [Lec02], the linear model remains valid for small lateral drifts and longitudinal slip ratios, which is equivalent to small accelerations ( $\leq 0.4g$ ). Under these conditions, the longitudinal and the lateral forces are approximately linear functions of the slip ratio and the slip angle with a slope equal to the longitudinal and the cornering stiffness respectively. Let  $C_\sigma$  and  $C_\alpha$  be the longitudinal and the lateral (cornering) stiffness of the tire and  $\sigma_x$  and  $\alpha$  be the longitudinal slip ratio and the side slip angle of the tire under consideration (In the following, the index  $ij$  of the wheel is dropped for simplicity). Then, the longitudinal and the lateral tire forces are given by:

$$\begin{aligned} F_x &= C_\sigma \sigma_x \\ F_y &= C_\alpha \alpha \end{aligned} \tag{3.18}$$

The longitudinal slip ratio of the tire under consideration  $\sigma_x$  is given by:

$$\sigma_x = \begin{cases} \frac{R_{eff}\omega - V_{wx}}{R_{eff}\omega} & \text{during the acceleration} \\ \frac{R_{eff}\omega - V_{wx}}{V_{wx}} & \text{during braking} \end{cases}$$

where  $R_{eff}$ ,  $\omega$  and  $V_{wx}$  are the effective radius of the wheel, its angular velocity and its linear velocity respectively.

The sideslip angle  $\alpha_{ij}$  and the linear velocity  $V_{wxij}$  of the wheel  $ij$  are given by the equations 3.15 and 3.16 if the vehicle is modeled by a four wheeled model and by the equations 3.7 and 3.8 when a bicycle model is used.

Note that, for an acceleration beyond  $0.4g$ , the vehicle tires are strongly nonlinear and they eventually saturate with a subsequent degradation in force capability. Due to the negligence of

the efforts saturation, the tire forces tend to be over estimated by the linear model, especially when the tire slip is important.

### 3.2.1.3.2 Dugoff's model

This model is an alternative to the analytical tire model developed by Fiala (1954) [Fia54] to generate lateral forces as well as the model developed by Pacejka and Sharp (1991) [PS91] to generate combined lateral and longitudinal forces [DFS69, DFS70]. It can be considered as a good compromise in terms of simplicity and representativity (see [Baf07] for a comparison between different Tire/Ground models in terms of simplicity and representativity). Dugoff's model takes into account the coupling between the lateral and the longitudinal forces, the friction coefficient, the wheels adhesion and stiffness, the slip ratio and the vertical forces. Moreover, this model assumes a uniform distribution of the vertical load on the tire contact area.

Let  $\mu$  be the friction coefficient and  $F_z$  the vertical load applied to the wheel. Then, the longitudinal and the lateral forces on each wheel are given by:

$$\begin{aligned} F_x &= C_\sigma \frac{\sigma_x}{1 + \sigma_x} f(\lambda), \\ F_y &= C_\alpha \frac{\tan(\alpha)}{1 + \sigma_x} f(\lambda), \end{aligned} \quad (3.19)$$

where  $\lambda$  is computed as:

$$\lambda = \frac{\mu F_z (1 + \sigma_x)}{2 \sqrt{(C_\sigma \sigma_x)^2 + (C_\alpha \tan(\alpha))^2}}, \quad (3.20)$$

and  $f(\lambda)$  is computed according to  $\lambda$  as:

$$f(\lambda) = \begin{cases} (2 - \lambda)\lambda & \text{if } \lambda < 1 \\ 1 & \text{if } \lambda \geq 1 \end{cases} \quad (3.21)$$

### 3.2.1.3.3 Burckhardt/Kiencke's model

This model is an exponential type model based on the friction computation. It characterizes the friction between the tires and the ground as a function of the slip ratio ( $\sigma$ ) and three parameters specific to the ground surface ( $c_1$ ,  $c_2$  and  $c_3$ ). Burckhardt/Kiencke's model extends by adding a pair of parameters ( $c_4$  and  $c_5$ ) to describe the influences of the speed and the vertical loads on the lateral and the longitudinal forces generated in the contact area between the tire and the ground [KN05].

The friction coefficient is then computed as:

$$\mu(g) = [c_1(1 - e^{-c_2\sigma}) - c_3\sigma] e^{(-c_4\sigma V_g)(1 - c_5 F_z^2)} \quad (3.22)$$

This coefficient is then used to compute the longitudinal and the lateral tire forces as:

$$\begin{aligned} F_x(\sigma, \sigma_x) &= \frac{\sigma_x}{\sigma} \mu(\sigma) F_z \\ F_y(\sigma, \alpha) &= \frac{\alpha}{\sigma} \mu(\sigma) F_z \end{aligned} \quad (3.23)$$

where  $\sigma = \sqrt{\sigma_x^2 + \sigma_y^2}$  is the geometric sum of the longitudinal and the lateral slip ratios of the wheel. Note that  $c_4$  and  $c_5$  are positive parameters, which means that the friction coefficient decreases when the vehicle speed or the vertical load  $F_z$  increases.  $c_1$ ,  $c_2$  and  $c_3$  are defined

according to the ground type. For example, for a dry concrete surface,  $c_1 = 1.197$ ,  $c_2 = 25.17$  and  $c_3 = 0.54$  [Baf07].

### 3.2.1.3.4 Pacejka's model

The best known tires model used in the modeling of the tires/ground contact is the one developed by Pacejka [PB97]. This model is commonly referred to as the "Magic formula". It uses an empirical reasoning based on the identification of parameters from experimental tests. This model offers one of the best performances since it represents the real behavior of the tire in particular when the coupling between the longitudinal and the lateral forces and the loads transfer are considered. On the other hand, the model's parameters identification and the computational power needed to implement this model remain an essential challenge.

The basic formula for this model is:

$$y = D \sin[C \arctan(Bx) - E(Bx - \arctan(Bx))] \quad (3.24)$$

with

$$Y(x) = y(x) + S_v x = X + S_h \quad (3.25)$$

In these formulas, Y is the output variable that stands for the longitudinal force  $F_x$  or the lateral force  $F_y$ . X is the input variable, it stands for the longitudinal slip ratio  $\sigma_x$  or the lateral slip angle  $\alpha$ . Therefore, the following equations are deduced:

$$\begin{aligned} F_x(\sigma_x + S_{hx}) &= D_x \sin[C_x \arctan(B_x \sigma_x - E_x(B_x \sigma_x - \arctan(B_x \sigma_x)))] + S_{vx}, \\ F_y(\alpha + S_{hy}) &= D_y \sin[C_y \arctan(B_y \alpha - E_y(B_y \alpha - \arctan(B_y \alpha)))] + S_{vy}, \end{aligned} \quad (3.26)$$

The parameters B,C,D,E,  $S_v$  and  $S_h$  of this formula are defined as follows (see Fig. 3.8):

- D : the peak value.
- C : the shape factor that controls the range limits of the sine function appearing in the formula (3.24) and thereby determines the shape of the resulting curve.
- B : the stiffness factor. This factor determines the slope at the origin and is also called the stiffness factor.
- E : the curvature factor, it controls the value of the slip at which the peak of the curve occurs.
- BCD : this product corresponds to the slope at the origin ( $x = y = 0$ ). For lateral force, this factor corresponds to the cornering stiffness.

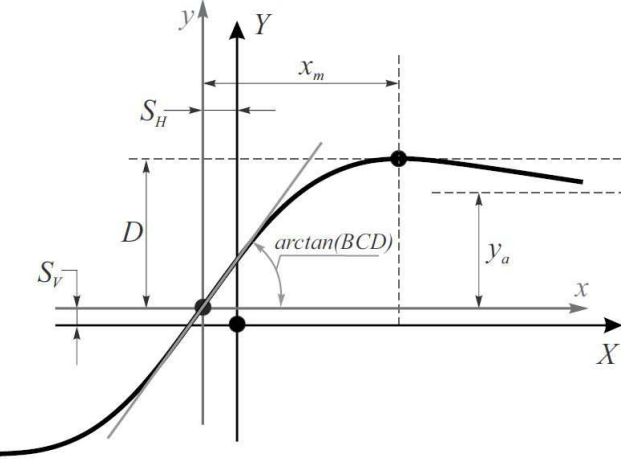


Fig. 3.8: Parameters of the Pacejka's tire model [Men10].

In 1991, Pacejka proposed a model that takes into account the camber angle, the cornering stiffness and the load variations. The longitudinal force parameters are then given by:

$$\begin{aligned}
 D_x &= F_z(b_1 F_z + b_2) \\
 B_x &= \frac{1}{C_x D_x} (b_3 F_z + b_4) F_z e^{(-b_5 F_z)} \\
 C_x &= b_0 \\
 E_x &= (b_6 F_z^2 + b_7 F_z + b_8)(1 - b_9 \text{sign}(\sigma_x + S_{hx})) \\
 S_{hx} &= b_{10} F_z + b_{11} \\
 S_{vx} &= b_{12} F_z + b_{13}
 \end{aligned} \tag{3.27}$$

The lateral force parameters are given by:

$$\begin{aligned}
 D_y &= F_z(a_1 F_z + a_2)(1 - a_3 c) \\
 B_y &= \frac{1}{C_y D_y} a_4 \sin(2 \arctan(F_z a_5)(1 - a_6 ||c||)) \\
 C_y &= a_0 \\
 E_y &= (a_7 F_z + a_8)(1 - (a_9 c + a_{10} \text{sign}(\alpha + S_{hy}))) \\
 S_{hy} &= a_{11} F_z + a_{12} + a_{13} c \\
 S_{vy} &= a_{14} F_z + a_{15} + c(a_{16} F_z^2 + a_{17} F_z)
 \end{aligned} \tag{3.28}$$

The variable  $c$  represents the camber angle. The parameters  $a_i$ ,  $b_j$  and  $c_k$  are empirically identified. They depend on the road structures and conditions and the tire state (road friction, structure, pressing, etc. ).

Fig. 3.9 presents the output of three models (Linear, Buckhardt and Pacejka) for the same ground surface and the same vertical loads. We can distinguish three active zones: Linear, transitory and saturation zones. In the first zone, the efforts are considered approximately linear with respect to the side slip angle and the slip ratio respectively. In the second zone, the forces reach the maximum adherence while in the third zone a phase of saturation is observed. This observation verifies the suitability of the linear model only in the linear zone. Moreover, we can observe a clear offset between Pacejka's model output and Kiencke's model output.

This offset highlights the representativity of Pacejka's model which is considered a benchmark model.

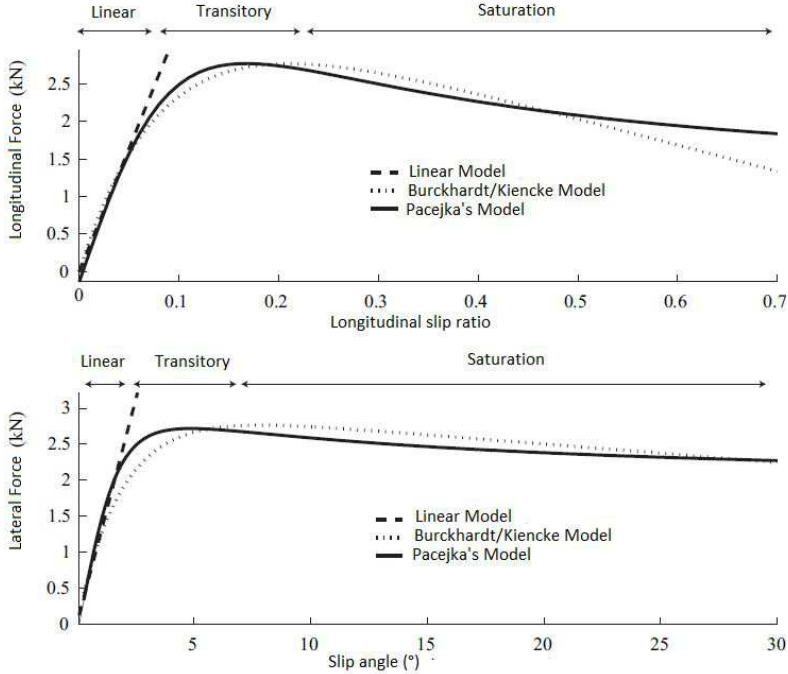


Fig. 3.9: Lateral and longitudinal efforts with respect to different tire models [Baf07].

### 3.2.2 Multi-body Models

During the last decade, some research groups started to employ multi-body tools to model the vehicle, as reviewed in the following:

- R.S. Sharp provided a model [Sha71a] for a two wheeled vehicle (motorcycles) with the aim of developing new control tools to improve the motorcycles stability. The equations of motion are derived from the application of Lagrange's equation:

$$\frac{d}{dt} \left( \frac{\partial L(q, \dot{q})}{\partial \dot{q}} \right) - \frac{\partial L(q, \dot{q})}{\partial q} = Q_q, \quad (3.29)$$

$$L(q, \dot{q}) = T(\dot{q}) - V(q), \quad q \in \mathbf{R}^n \quad (3.30)$$

where,  $T$  and  $V$  are the kinetic and the potential energies of the system respectively,  $Q_q$  are the generalized forces applied to the system and  $q$  is the vector of the system's degrees of freedom. The yaw angle, the roll angle, the steer angle and the angles which define the rotational positions of the road wheels are the seven degrees of freedom used to compute the kinetic and the potential energy expressions (Fig. 3.10). The equations describing the longitudinal motion of the motorcycle, and those describing the rotations of the wheels, are not given since a constant forward speed is considered and the assumption of a null longitudinal tire slip ratio is made. The generalized forces are derived in terms of the tire forces which are obtained in terms of the vehicle motion parameters, the tire side slip and the camber angles. The consideration of small perturbations allows the elimination of all second and higher order terms; resulting in

linear equations of motion. In 2001, R.S. Sharp used the *Autosim* software to develop the two wheeled vehicle model [Sha01].

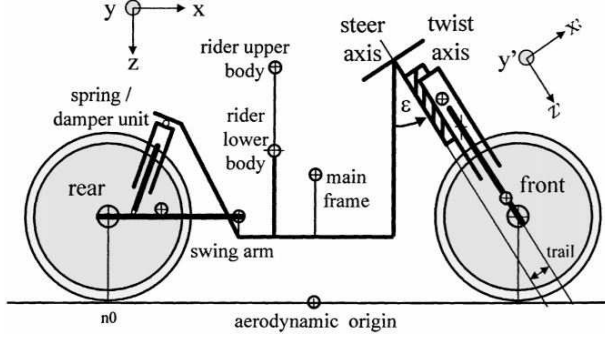


Fig. 3.10: Diagrammatic motorcycle model developed by [Sha71a]

- Cossalter et al developed a model based on the Lagrange Formalism that consists of interconnected rigid bodies together with suspensions and sophisticated tire and engine models [CL02]. An eleven degrees of freedom, nonlinear, multi-body dynamics model of a motorcycle is developed (Fig. 3.11). Front and rear chassis, steering system, suspensions and tires are the main features of the model. An original tire model was developed, which takes into account the geometric shape of tires and the elastic deformation of tire carcass. Equations of motion stem from the natural coordinates approach. First, each rigid body is described with a set of fully cartesian coordinates. Then, the links between the bodies are obtained by means of algebraic equations. This makes it possible to obtain simple equations of motion, even though the coordinates are redundant. However, this technique leads to a complicated model with the case of the motorcycle, hard to implement.

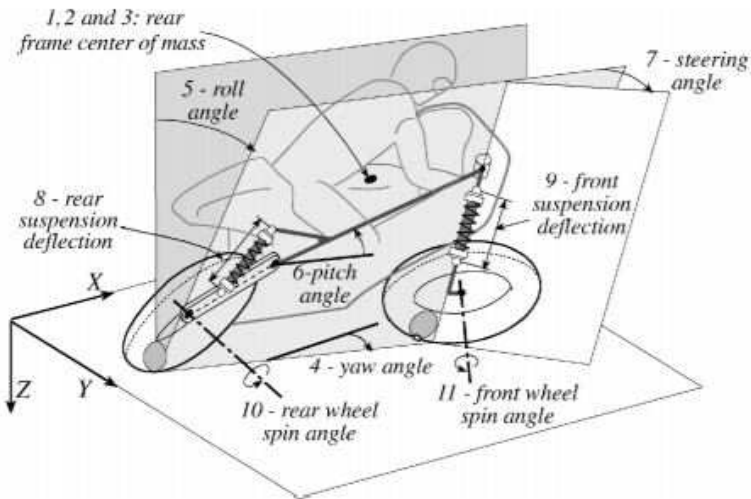


Fig. 3.11: Eleven degrees of freedom motorcycle model developed by [CL02]

- In [CDBD09, PRCT13], multibody dynamics techniques are employed to design state observers. In [San16], E. Sanjurjo uses an index-3 augmented Lagrangian formulation with mass-orthogonal projections [CDNG04, DGCK14] to model the vehicle (Fig. 3.12). The developed

model is then combined with a state observer, namely, the Kalman filter observer. The equations of motion have the following form:

$$M\ddot{q} + \phi_q^T \alpha \phi + \phi_q^T \lambda^* = Q \quad (3.31)$$

where  $M$  is the mass matrix,  $\ddot{q}$  is the vector of dependent accelerations,  $\phi_q$  the Jacobian matrix of the constraint equations,  $\alpha$  the penalty factor,  $\phi$  the constraints vector,  $\lambda^*$  the Lagrange multipliers and  $Q$  the vector of applied forces. The Lagrange multipliers are obtained from the following iterative process:

$$\lambda_{i+1}^* = \lambda_i^* + \alpha \phi_{i+1} \quad i = 0, 1, 2, \dots \quad (3.32)$$

The integration scheme employed is the trapezoidal rule. The corresponding dynamics equations of velocities and accelerations are given by:

$$\dot{q}_{k+1} = \frac{2}{\Delta t} q_{k+1} + \hat{\dot{q}}_k \quad \text{with} \quad \hat{\dot{q}}_k = -\left(\frac{2}{\Delta t} q_k + \dot{q}_k\right); \quad (3.33)$$

$$\ddot{q}_{k+1} = \frac{4}{\Delta t^2} q_{k+1} + \hat{\ddot{q}}_k \quad \text{with} \quad \hat{\ddot{q}}_k = -\left(\frac{4}{\Delta t^2} q_k + \frac{4}{\Delta t} \dot{q}_k + \ddot{q}_k\right); \quad (3.34)$$

where  $q$  and  $\dot{q}$  are the vectors of dependent coordinates and velocities, respectively, and  $\Delta t$  is the integration time step. The subindex  $k$  stands for the time step, while the subindex  $i$  refers to the iteration step within a time step. Then, the equations of motion are discretized by introducing the equations (3.33) and (3.34) into (3.31). The solution of this nonlinear discrete system is obtained using an iterative Newton-Raphson method.

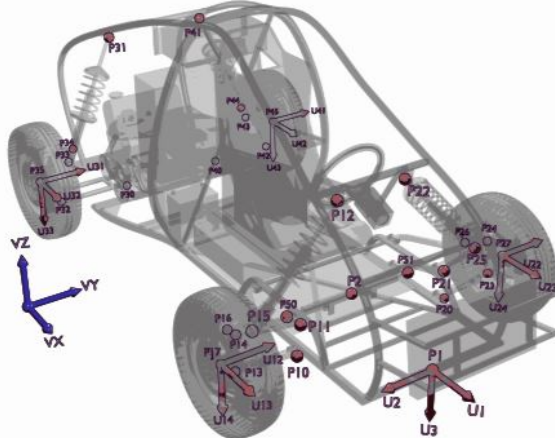


Fig. 3.12: Fourteen degrees of freedom vehicle model developed by [San16].

- In [Maa11], S. Maakaroun used a recursive formulation, namely the Newton-Euler method, to model the vehicle. They proceed in a systematic geometrical description in order to obtain the vehicle model directly with a minimum number of numerical steps. This recursive method was used to develop a two-wheeled and a four-wheeled vehicle models in [MCGK11], and then a narrow tilted vehicle model in [MCGK11]. In [Ven03], this same formalism was used to identify the vehicle parameters.

G. Max [ML15] also used a recursive formulation to model the vehicle, namely the Appell's method based on the Gibbs function (acceleration energy). This kind of methods can be extended for use of any treelike robotic system by modifying the external force/torque and the

constraint equations.

- In [CCB97], Cuadrado et al. compared four methods that are used to simulate multi-body dynamics with constraints: the augmented Lagrange formulation index-1 and index-3 with projections [BL96], a modified state-space formulation (equations of motion in independent coordinates) [Jer12] and a fully recursive formulation [OW82]. A number of rigid multibody problems were solved with all four methods to compare their performance. The index-3 formulation with projections failed to converge when using small time step sizes ( $< 10^{-5}$  sec), while the index-1 formulation failed to converge when using time step sizes larger than  $10^{-2}$  seconds. The space state and the recursive formulations behaved poorly in the presence of stiff systems. Nevertheless, for non-stiff problems of large size (such as a vehicle system), the fully recursive method became competitive. Therefore, it may be seen that with the fully recursive formulation, there is no need of solving a system of equations. This fact suggests a good speed competitiveness of this method as the size of the problem increases. In those cases, non-recursive formulations are forced to cope with large sets of equations.

To conclude this section, we have chosen to proceed with the recursive formulation developed in [Maa11], since it allows to automatically calculate the symbolic expressions of the geometric, kinematic and dynamic models with a minimum number of numerical steps. The approach elaborates systematically the symbolic equations of motion and facilitates the implementation of the dynamic model. Moreover, the algorithm complexity does not increase with the system's complexity (large number of variables) and the modification of the systems assumptions can be taken into account in a simple way (For example, the consideration or not of some components of the system). A four wheeled vehicle model with 7 degrees of freedom is developed in this thesis. The 7 degrees of freedom include: The chassis variables of motion (Longitudinal and lateral positions and the yaw angle) and the four angles representing the positions of the four wheels while rotating around their axes. The algorithm is developed under Matlab/Simulink, then the provided four wheels-vehicle model is validated using Scaner-Studio simulator data. In the next sections, the robotics formalism is presented in detail, then the developed vehicle model is presented and validated.

### 3.3 Robotics Formalism for dynamic modeling

#### 3.3.1 Geometric description

The robotics formalism considers that the vehicle is a multi-articulated system consisting of  $n$  bodies wherein the base is the mobile chassis and the wheels are the end effectors [Maa11]. Each body is connected to its antecedent by a joint which represents a translational or a rotational degree of freedom. Notice that a body can be virtual or real, the virtual bodies (with zero mass) are introduced to describe joints with multiple degrees of freedom or to define intermediate fixed frames.

The geometrical description of the vehicle is based on the modified Denavit-Hartenberg (DHM) description [KK87] of a tree-structured robot (Fig. 3.14). The system is composed of  $n + 1$  links,  $n$  joints and  $m$  end effectors. The link 0 is the fixed base of the robot and the numbers of links and joints are increasing at each branch when traversing from the base to an end effector. The link  $i$  is articulated on joint  $i$  and connects the link  $a_i$  and the link  $s_i$ , where  $a_i$  and  $s_i$  are the indices of the antecedent and successor links of the link  $i$  starting from the base frame. Each

joint  $i$  is associated with a joint variable  $q_i$  describing its rotational or translational motion. The frame  $R_i : (O_i, X_i, Y_i, Z_i)$  is fixed to the link  $i$  where  $Z_i$  is the axis of motion of the joint  $i$ . The different frames are defined as follows:

- As a first step, we find the common perpendiculars to  $Z_i$  and  $Z_j$ , where  $j = s_i = (k, l, m\dots)$  represent the indexes of bodies that succeed the body  $i$  (see Fig. 3.13).
- Then, let one of these common perpendiculars be  $X_i$ . It is preferable to take  $X_i$  on the joint articulated on the longest branch.
- The other perpendiculars will be denoted as  $X'_i, X''_i\dots$  Thus many frames  $(R_i, R'_i \dots)$  will be defined with respect to the link  $i$ .
- Finally, the axis  $Y_i$  for each frame  $R_i$  is defined so as  $R_i : (O_i, X_i, Y_i, Z_i)$  corresponds to a direct orthonormal frame.

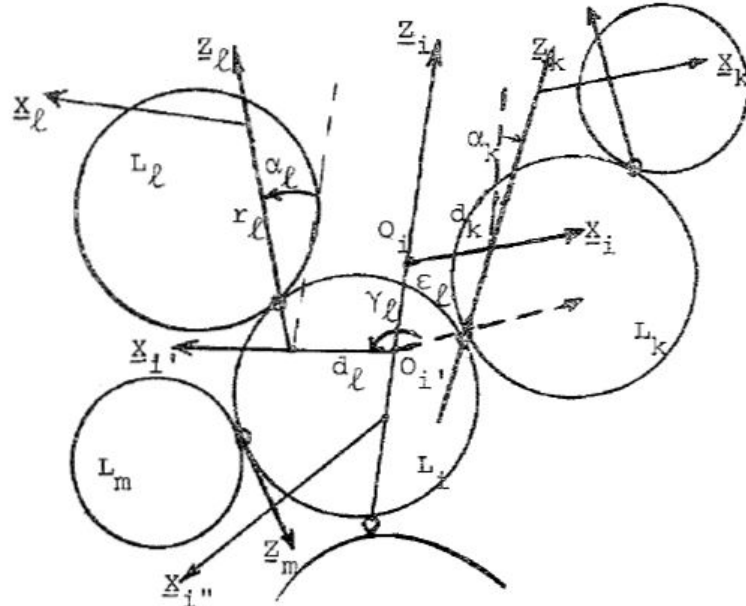


Fig. 3.13: Representation of a link  $i$  with more than one successor [KK86].

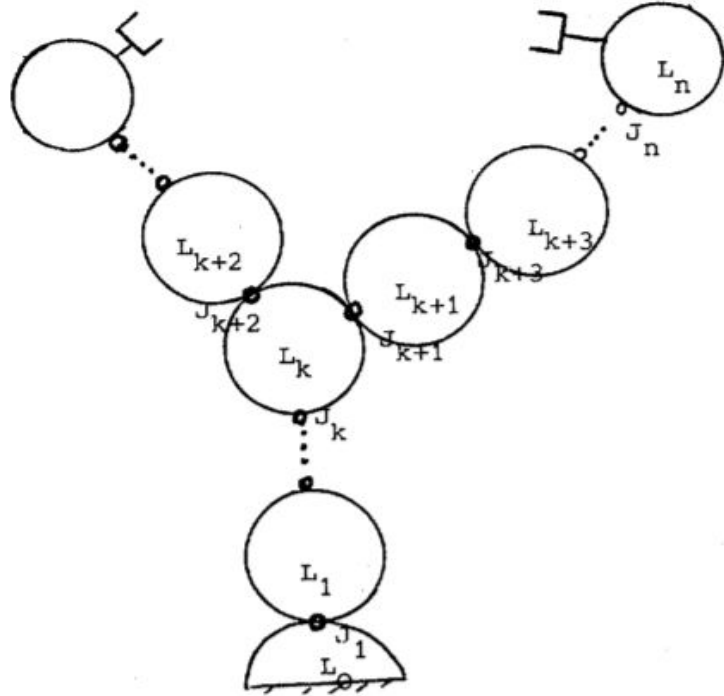


Fig. 3.14: DHM notation for a tree-structured robot [KK86].

The computation of the geometric, Kinematic and dynamic model of a robot makes use of the transformation matrices between the succeeding frames. We define the transformation matrices between the frames  $R_i$  and  $R_j$ , where  $j$  represents the successors of the body  $C_i$  noted as  $j = s_i = (k, l, m, \dots)$ , using six parameters defined as follows:

- $\gamma_j$ : The angle between  $X_i$  and  $X'_i$  about  $Z_i$
- $\epsilon_j$ : The distance between  $X_i$  and  $X'_i$  about  $Z_i$  (or the distance between  $O_i$  and  $O'_i$ )
- $\alpha_j$ : The angle between  $Z_i$  and  $Z_j$  about  $X'_i$
- $d_j$ : The distance between  $Z_i$  and  $Z_j$  about  $X'_i$  (or the distance between  $O'_i$  and  $Z_j$ )
- $\beta_j$ : The angle between  $X'_i$  and  $X_j$  about  $Z_j$
- $r_j$ : The distance between  $X'_i$  and  $X_j$  about  $Z_j$  (or the distance between  $O_j$  and  $X'_i$ )

Notice that if the joint  $i$  has only one successor  $j$ , then the parameters  $\gamma_j$  and  $\epsilon_j$  are set to zero. So, if each joint in the tree structure has only one successor, then the parameters  $\gamma$  and  $\epsilon$  of all the joints are set to zero.

The joint variable  $q_i$  associated to the joint  $i$  is then defined as:

$$\begin{aligned} q_i &= \bar{\sigma}_i \beta_i + \sigma_i r_i \\ \bar{\sigma}_i &= 1 - \sigma_i \end{aligned} \tag{3.35}$$

where:

$\sigma_i = 0$  for a rotoid articulation,

$\sigma_i = 1$  for a prismatic articulation,

$\sigma_i = 2$  for a blocked articulation that describes a virtual body. (In this case, the virtual body doesn't have a joint variable ( $q_i = 0$ )).

The matrix of transformation between the frames  $R_i$  and  $R_j$ ,  ${}^i T_j$ , is then given by

$${}^i T_j = \begin{bmatrix} C\gamma_j C\beta_j - S\gamma_j C\alpha_j S\beta_j & -C\gamma_j S\beta_j - S\gamma_j C\alpha_j C\beta_j & S\gamma_j S\alpha_j & d_j C\gamma_j + r_j S\gamma_j S\alpha_j \\ S\gamma_j C\beta_j + C\gamma_j C\alpha_j S\beta_j & -S\gamma_j S\beta_j + C\gamma_j C\alpha_j C\beta_j & -C\gamma_j S\alpha_j & d_j S\gamma_j - r_j C\gamma_j S\alpha_j \\ S\alpha_j S\beta_j & S\alpha_j C\beta_j & C\alpha_j & r_j C\alpha_j + \epsilon_j \\ 0 & 0 & 0 & 1 \end{bmatrix} \quad (3.36)$$

Reversely, the matrix of transformation between the frames  $R_j$  and  $R_i$ ,  ${}^j T_i$  is obtained by a simple inversion of the matrix  ${}^i T_j$ :

$${}^i T_j {}^j T_i = I_4, \quad (3.37)$$

where  $I_4$  is the identity matrix of dimension 4.

The geometric description of an end effector in the base frame can thus be obtained by the successive multiplications of the transformation matrices going from the base to this end effector:

$${}^m T_0 = {}^m T_{a_m} \dots {}^{s_0} T_0 \quad (3.38)$$

where  $m$  is the index of the end effector,  $a_m$  is the index of the antecedent of the body  $m$  and  $s_0$  is the successor of the base (body of the index 0).

### 3.3.2 Dynamic model development

Once the geometric description of the vehicle is established, we proceed to develop the dynamic model. In fact, the dynamic model represents the relation between the torque and/or the forces applied to the actuators and the articular positions, speeds and accelerations. It is given by:

$$\tau = f(q, \dot{q}, \ddot{q}, f_e) \quad (3.39)$$

where  $\tau$  is the vector of the actuators torque,  $q$ ,  $\dot{q}$  and  $\ddot{q}$  represent the articular positions, speed and acceleration vectors respectively and  $f_e$  is the vector of external forces applied by the environment on the robot.

The direct dynamic model is derived from the equation (3.39) by:

$$\ddot{q} = g(q, \dot{q}, \tau, f_e). \quad (3.40)$$

where  $f$  and  $g$  represent two functions in  $\mathbf{R}$ .

#### 3.3.2.1 Modeling the vehicle base

At a first step, since the base of our robot is moving, we have to choose how to represent its movement. The vehicle chassis is characterized by six degrees of freedom with respect to a fixed frame  $R_f$ : Three translations (longitudinal, lateral and vertical) and three rotations (roll, pitch, yaw). Two methods exist in the robotics formalism to represent the base motion: Spatial model and Euler Model.

The Spatial model represents the robot base by a simple chain of six virtual bodies, linking the reference body ( $C_0$ ) to the chassis body ( $C_b$ ). Each body represents a degree of freedom of the vehicle chassis (see Fig. 3.15). This method was used by [Gui00, Ven03, NMN10].

The Euler model (see Fig. 3.17) uses only one virtual body to represent the base related to

the ground ( $C_0$ ) and another one to represent the chassis ( $C_b$ ). In this model, the degrees of freedom of the chassis are represented using Euler variables  ${}^bV_b$  and  ${}^b\omega_b$  that corresponds to the chassis linear and angular speeds represented in the chassis frame  $R_b$ .

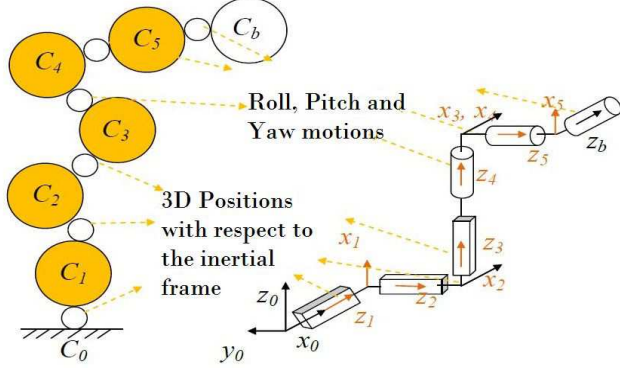


Fig. 3.15: Spatial model of the robot mobile base [Maa11]

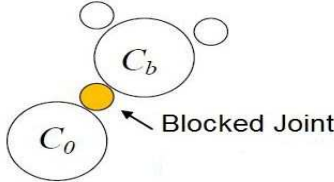


Fig. 3.16: Euler model of the robot mobile base [Maa11]

The Euler model is preferred in our modeling regarding many reasons:

- Adding six virtual bodies as in the Spatial model increases the computation time
- The frames used in Euler model are co-linear to the frames usually used in the automotive domain
- Usually, we use an inertial central unit to measure the chassis speeds in a frame related to the chassis  $R_c$ . So, using the Euler model, we can set  $R_c = R_0 = R_b$  and then we can compute the Euler variables by using the inertial central data directly. In contrast, the Spatial model represents the relative rotations of each body with respect to its antecedent, so we have to project these variables in the fixed frame to compute the chassis speeds absolute values.

In our work, we choose to use a mixed Euler-Lagrange method to model the vehicle. The chassis is then represented using Euler variables ( ${}^bV_b$  and  ${}^b\omega_b$ ) while the other bodies are represented using Lagrange variables ( $\dot{q}_i$ ).

### 3.3.2.2 Euler-Lagrange Dynamic model

The computation of the dynamic model of the vehicle is based on the method of Luh, Walker and Paul [LWP80] where two recurrences are used. The forward recursive equations (from

the mobile base to the effectors) compute successively the velocities and accelerations of each body and their dynamic torsor. The backward recurrence (from the effectors to the mobile base) computes the forces and the moments exerted on each body by its antecedent taking into account the external forces applied to the robot.

- **Forward Recurrence:**

In this first recurrence, we compute the dynamic torsor of each joint using these equations:

For  $j = 1 \dots n$  :

$${}^j\omega_j = {}^j\omega_i + \bar{\sigma}_j \dot{q}_j {}^j a_j, \quad {}^j\omega_i = {}^j T_i^i \omega_i \quad (3.41)$$

$${}^j\dot{\omega}_j = {}^j T_i^i \dot{\omega}_i + \bar{\sigma}_j [\ddot{q}_j {}^j a_j + {}^j\omega_i \times \dot{q}_j {}^j a_j] \quad (3.42)$$

$${}^j\dot{V}_j = {}^j T_i^i ({}^i\dot{V}_i + {}^i Y_i^i P_j) + \sigma_j [\ddot{q}_j {}^j a_j + 2{}^j\omega_i \times \dot{q}_j {}^j a_j] \quad (3.43)$$

$${}^j F_j = M_j {}^j \dot{V}_j + {}^j Y_j {}^j M S_j \quad (3.44)$$

$${}^j M o_j = {}^j I_j {}^j \dot{\omega}_j + {}^j\omega_j \times {}^j I_j {}^j \omega_j + {}^j M S_j \times {}^j \dot{V}_j \quad (3.45)$$

$${}^j a_j = [0 \ 0 \ 1]^t, \quad {}^j M S_j = M_j S_j, \quad {}^j Y_j = {}^j \hat{\omega}_j + {}^j \hat{\omega}_j {}^j \hat{\omega}_j \quad \text{and} \quad {}^j \hat{\omega}_j = \begin{bmatrix} 0 & -\omega_z & \omega_y \\ \omega_z & 0 & -\omega_x \\ -\omega_y & \omega_x & 0 \end{bmatrix} \quad (3.46)$$

where  ${}^i P_j$  is the vector representing the coordinates of  $O_j$  in the frame  $R_i$ .  $M_j$ ,  ${}^j\omega_j$  and  ${}^j V_j$  are the mass, the angular and the linear velocities of the body  $C_j$ .  ${}^j I_j$  is the inertia matrix,  $S_j$  is the vector of coordinates of the center of gravity of the body  $C_j$  in the frame  $R_j$ ,  ${}^j M o_j$  is the moment of external efforts applied on the body  $C_j$  at the point  $O_j$  and  ${}^j F_j$  is the resulting force of the external forces applied to the body  $C_j$ .

Note that the operation  $\times$  means the vector product here.

This recurrence is initialized by  ${}^b\omega_b = [{}^b\omega_{bx} {}^b\omega_{by} {}^b\omega_{bz}]$ ,  ${}^b\dot{\omega}_b = [{}^b\dot{\omega}_{bx} {}^b\dot{\omega}_{by} {}^b\dot{\omega}_{bz}]$ ,  ${}^b V_b = [{}^b V_{bx} {}^b V_{by} {}^b V_{bz}]$  and  ${}^b a_b = [{}^b a_{bx} {}^b a_{by} {}^b a_{bz}]$  that represent the angular and the linear velocities and accelerations of the vehicle with respect to the frame  $R_f$ , computed in the frame  $R_b$ .  $R_f$  and  $R_b$  refer to the inertial frame and the base frame of the robot which is the frame related to the vehicle chassis.

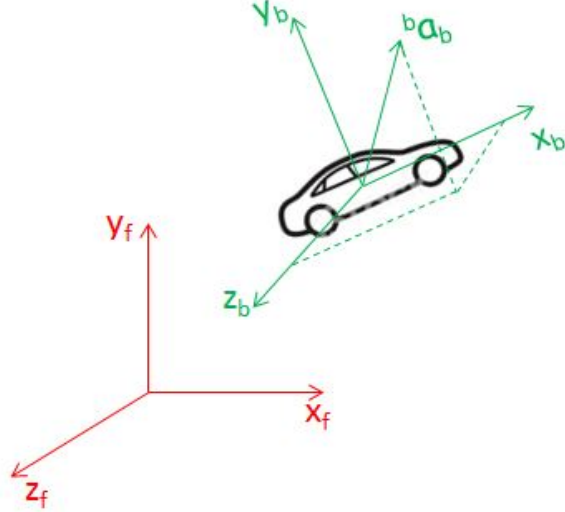


Fig. 3.17: Vehicle and inertial frames  $R_b$  and  $R_f$

${}^bV_b$  and  ${}^b\omega_b$  are defined as follows:

$$\begin{aligned} {}^bV_b &= {}^bR_f {}^fV_b \\ {}^b\omega_b &= {}^bR_f {}^f\omega_b \end{aligned} \quad (3.47)$$

where  ${}^bR_f$  is the rotation matrix that represents the vehicle frame  $R_b$  in the inertial frame  $R_f$ .  ${}^fV_b$  and  ${}^f\omega_b$  are the linear and the angular speeds of the vehicle base expressed in the frame  $R_f$ .

In the same way, the accelerations  ${}^b a_b$  and  ${}^b \dot{\omega}_b$  are given by:

$$\begin{aligned} {}^b a_b &= {}^bR_f {}^f a_b \\ {}^b \dot{\omega}_b &= {}^bR_f {}^f \dot{\omega}_b \end{aligned} \quad (3.48)$$

where  ${}^f a_b$  and  ${}^f \dot{\omega}_b$  are the linear and the angular accelerations of the vehicle base expressed in the frame  $R_f$ .

Using Eq. (3.47) and (3.48), one can find that the acceleration  ${}^b a_b$  is not the derivative of  ${}^b V_b$ !! Contrariwise,  ${}^b a_b = \frac{d({}^b V_b)}{dt} + {}^b \omega_b \times {}^b V_b$  since we have:

$$\begin{aligned} {}^b \dot{V}_b &= {}^bR_f {}^f \dot{V}_b + {}^b \dot{R}_f {}^f V_b \\ &= {}^bR_f {}^f a_b + {}^b \dot{R}_f {}^f V_b \\ &= {}^b a_b + {}^b \dot{R}_f {}^f V_b \end{aligned} \quad (3.49)$$

However, the angular acceleration  ${}^b \dot{\omega}_b$  is the time derivative of the angular speed of the vehicle chassis  ${}^b \omega_b$ :

$$\begin{aligned} {}^b \dot{\omega}_b &= {}^bR_f {}^f \dot{\omega}_b + {}^b \dot{R}_f {}^f \omega_b \\ &= {}^b \dot{\omega}_b + {}^b \dot{R}_f {}^f \omega_b \end{aligned} \quad (3.50)$$

After some computations, one can prove that  ${}^b \dot{R}_f x = {}^b R_f ({}^f \omega_b \times x)$ , with  $x$  a three dimensionnel vector. As a result, Eq. (3.49) and (3.50) become:

$$\begin{aligned}
{}^b\dot{V}_b &= {}^b\dot{a}_b - {}^bR_f({}^f\omega_b \times {}^fV_b) \\
&= {}^b\dot{a}_b - ({}^bR_f {}^f\omega_b \times {}^bR_f {}^fV_b) \\
&= {}^b\dot{a}_b - {}^b\omega_b \times {}^bV_b
\end{aligned} \tag{3.51}$$

and

$$\begin{aligned}
{}^b\dot{\omega}_b &= {}^b\dot{\omega}_b - {}^bR_f({}^f\omega_b \times {}^f\omega_b) \\
&= {}^b\dot{\omega}_b
\end{aligned} \tag{3.52}$$

To compute  ${}^b\omega_b$ , we note that the frame  $R_b$  is the result of three rotations of the frame  $R_f$  (see Fig. 3.18). A first rotation of angle  $\psi$  around the  $z_f$  axis (frame  $R_{1f}$ ), a second rotation of angle  $\phi$  around the axis  $y_{1f}$  (frame  $R_{2f}$ ) and a third rotation of angle  $\theta$  around the axis  $x_{2f}$ . The angles  $\theta$ ,  $\phi$  and  $\psi$  correspond to the roll, pitch and yaw angles. The angular velocity of the frame  $R_b$  with respect to  $R_f$ ,  ${}^f\omega_b$ , is then computed as:

$$\begin{aligned}
{}^f\omega_b &= \dot{\psi} {}^f\vec{z}_f + \dot{\phi} {}^f\vec{y}_{1f} + \dot{\theta} {}^f\vec{x}_{2f} \\
&= \begin{bmatrix} 0 \\ 0 \\ 1 \end{bmatrix} \dot{\psi} + \begin{bmatrix} -\sin \psi \\ \cos \psi \\ 0 \end{bmatrix} \dot{\phi} + \begin{bmatrix} \cos \phi \cos \psi \\ \cos \phi \sin \psi \\ -\sin \phi \end{bmatrix} \dot{\theta} \\
&= \begin{bmatrix} 0 & -\sin \psi & \cos \phi \cos \psi \\ 0 & \cos \psi & \cos \phi \sin \psi \\ 1 & 0 & -\sin \phi \end{bmatrix} \begin{bmatrix} \dot{\psi} \\ \dot{\phi} \\ \dot{\theta} \end{bmatrix}
\end{aligned}$$

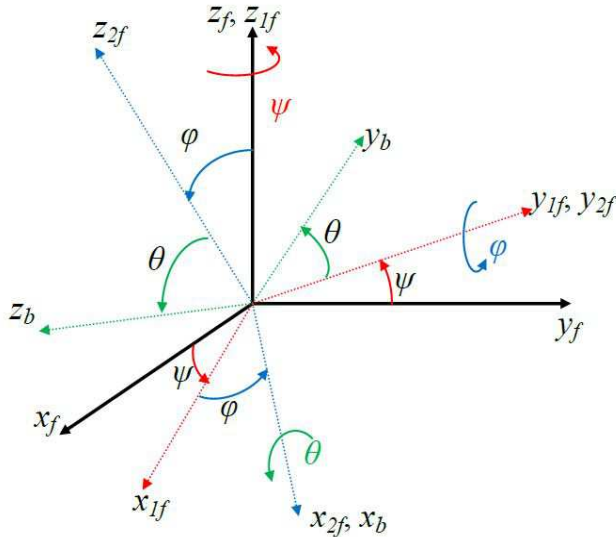


Fig. 3.18: Representation of  $R_b$  in  $R_f$ : Roll ( $\theta$ ), pitch ( $\phi$ ) and yaw ( $\psi$ ) angles

The angular velocity of the chassis computed in the frame  $R_b$ ,  ${}^b\omega_b$ , is then given by :

$${}^b\omega_b = {}^bR_f {}^f\omega_b,$$

where  ${}^bR_f$ , the matrix of transformation (rotation) between the frames  $R_b$  and  $R_f$ , is computed as the product of three consecutive rotations matrices and given by:

$${}^bR_f = \begin{bmatrix} \cos(\phi) \cos(\psi) & \cos(\phi) \sin(\psi) & -\sin(\phi) \\ \cos(\psi) \sin(\phi) \sin(\theta) - \cos(\theta) \sin(\psi) & \cos(\psi) \cos(\theta) + \sin(\phi) \sin(\psi) \sin(\theta) & \cos(\phi) \sin(\theta) \\ \sin(\psi) \sin(\theta) + \cos(\psi) \cos(\theta) \sin(\phi) & \cos(\theta) \sin(\phi) \sin(\psi) - \cos(\psi) \sin(\theta) & \cos(\phi) \cos(\theta) \end{bmatrix} \quad (3.53)$$

After some calculations, one can find:

$${}^b\omega_b = \begin{bmatrix} \dot{\theta} - \dot{\psi} \sin \phi \\ \dot{\phi} \cos \theta + \dot{\psi} \sin \theta \cos \phi \\ \dot{\psi} \cos \theta \cos \phi - \dot{\phi} \sin \theta \end{bmatrix}. \quad (3.54)$$

Concerning  ${}^bV_b$ , it is computed using (3.47), as:

$$\begin{aligned} {}^bV_b &= {}^bR_f {}^fV_b \\ &= {}^bR_f \begin{bmatrix} \dot{X} \\ \dot{Y} \\ \dot{Z} \end{bmatrix} \end{aligned} \quad (3.55)$$

where  $X$ ,  $Y$  and  $Z$  are the vehicle center of gravity position in the inertial frame. For ease of presentation, we note  $\dot{x} = {}^bV_b(1)$ ,  $\dot{y} = {}^bV_b(2)$  and  $\dot{z} = {}^bV_b(3)$  to refer to the vehicle speeds in the longitudinal, the lateral and the vertical directions computed in the vehicle frame  $R_b$ . Using (3.55), we have:

$$\begin{aligned} {}^bV_b &= \begin{bmatrix} \dot{x} \\ \dot{y} \\ \dot{z} \end{bmatrix} \\ &= \begin{bmatrix} \cos(\phi) \cos(\psi) \dot{X} + \cos(\phi) \sin(\psi) \dot{Y} - \sin(\phi) \dot{Z} \\ (\cos(\psi) \sin(\phi) \sin(\theta) - \cos(\theta) \sin(\psi)) \dot{X} + (\cos(\psi) \cos(\theta) + \sin(\phi) \sin(\psi) \sin(\theta)) \dot{Y} + \cos(\phi) \sin(\theta) \dot{Z} \\ (\sin(\psi) \sin(\theta) + \cos(\psi) \cos(\theta) \sin(\phi)) \dot{X} + (\cos(\theta) \sin(\phi) \sin(\psi) - \cos(\psi) \sin(\theta)) \dot{Y} + \cos(\phi) \cos(\theta) \dot{Z} \end{bmatrix} \end{aligned} \quad (3.56)$$

The gravity efforts can be taken into account by substituting  ${}^b g$  from the acceleration of the chassis  ${}^b a_b$ , where  ${}^b g$  represents the gravity acceleration expressed in the frame  $R_b$  and computed as:

$${}^b g = {}^b R_f {}^f g, \quad (3.57)$$

Knowing that,  ${}^f g$  is the gravity acceleration in the frame  $R_f$  ( ${}^f g = [0 \ 0 \ g]^t$ ),  ${}^b g$  is given by:

$${}^b g = [-\sin(\phi)g \ \cos(\phi)\sin(\theta)g \ \cos(\phi)\cos(\theta)g]^t. \quad (3.58)$$

### • Backward Recurrence:

The backward recurrence equations allow the computation of the forces and the moments exerted on each body  $C_j$  by its antecedent  $C_{a_j}$ :

For  $j = n \dots 1$ :

$${}^j f_j = {}^j F_j + {}^j f e_j + \underbrace{\sum_{s(j)} {}^j f_{s(j)}}_{} \quad (3.59)$$

$${}^j mo_j = {}^j Mo_j + {}^j me_j + \underbrace{\sum_{s(j)} {}^j T_{s(j)} {}^{s(j)} mo_{s(j)}}_{{}^j f_s} + {}^j P_{s(j)} \times {}^j f_{s(j)} \quad (3.60)$$

where  ${}^j Mo_j$  is the moment of external efforts applied on the body  $C_j$  at the point  $O_j$  and  ${}^j F_j$  is the resulting force of the external forces applied to the body  $C_j$  ( ${}^j Mo_j$  and  ${}^j F_j$  are computed in the forward recurrence).  ${}^j f_j$  and  ${}^j mo_j$  are the resulting forces and torques applied by the body  $C_{aj}$  on the body  $C_j$ ,  ${}^j f_{s(j)}$  and  ${}^j mo_{s(j)}$  are the resulting forces and torques applied by the body  $C_j$  on its successors, and  ${}^j fe_j$  and  ${}^j me_j$  are the external forces and torques applied to  $C_j$ . The balance of forces acting on the body  $C_j$  is represented in Fig. 3.19: In this figure,  $L_k$  and  $L_{j+1}$  are the distances between the origin of the frame  $R_j$  and the frames  $R_k$  and  $R_{j+1}$  respectively.

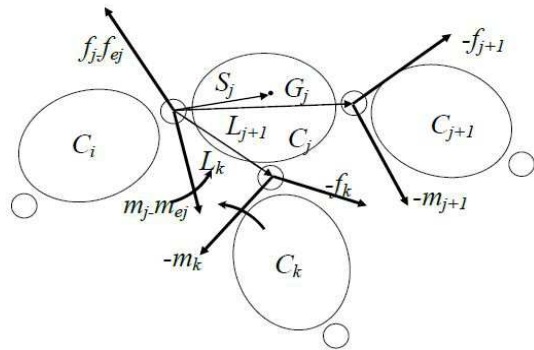


Fig. 3.19: The balance of forces acting on the body  $C_j$ .

The backward recurrence is initialized by  ${}^k f_{s(k)} = [0 \ 0 \ 0]$  et  ${}^k mo_{s(k)} = [0 \ 0 \ 0]$ , where  $C_k$  is an end effector.

The inverse dynamic model gives the joint torques as a function of the joint coordinates, speeds and accelerations. The joint forces or torques of the body  $C_j$  are obtained by projecting  ${}^j f_j$  or  ${}^j mo_j$  on the joint axis  $Z_j$  as follows:

$$\tau_j = (\sigma_j {}^j f_j + \bar{\sigma}_j {}^j mo_j)^{tj} a_j \quad (3.61)$$

And by taking into account the effects of actuators inertia, friction and elasticity it follows:

$$\tau_j = (\sigma_j {}^j f_j + \bar{\sigma}_j {}^j mo_j)^{tj} a_j + {}^j F_s sgn(\dot{q}_j) + {}^j F_v \dot{q}_j + I_{aj} \ddot{q}_j + {}^j K(q_j - q_{j0}) \quad (3.62)$$

where  ${}^j F_s$  and  ${}^j F_v$  are the dry and viscous friction vectors,  $I_{aj}$  is the actuator inertia and  ${}^j K$  and  $q_{j0}$  the stiffness and the initial position of the articulation  $j$ . ( ${}^j K$  and  $q_{j0}$  are null if the articulation is not elastic).

For the body  $C_1$ , there is no projection on the joint axis, so the equations of the chassis will be represented by the total forces  $f_1$  and moments  $mo_1$  exerted by link 0 on link 1. Thus the Newton-Euler equations of the chassis are derived as follows:

$$\begin{bmatrix} 0_{6*1} \\ 1 f_1 \\ 1 mo_1 \end{bmatrix}$$

$f_1$  and  $mo_1$  are equal to zero since the chassis is not motorized.

Once the expression of  $\tau$  is established function of  $q$ ,  $\dot{q}$  and  $\ddot{q}$ , the inverse dynamic model can be written as

$$\tau = A(q)\ddot{q} + H(q, \dot{q}) + J(q)f_e \quad (3.63)$$

where  $H$  is the vector of centrifugal, Coriolis and gravity forces,  $A$  is the inertial matrix of the system,  $f_e$  is the vector of external forces,  $J$  is the Jacobian matrix and  $q$ ,  $\dot{q}$  and  $\ddot{q}$  are positions, velocities and accelerations of all the joints.

The external efforts applied by the vehicle to the environment are the contact efforts between the wheels and the ground. These forces are taken into account by the end effectors bodies(wheels). The aerodynamic force is also an important external effort especially with high speeds, its effect is considered on the vehicle, especially in the longitudinal direction.

The computation of the matrices  $A$ ,  $H$  and  $J$  is done by comparing (3.63) and (3.39):

$$\begin{aligned} \tau &= f(q, \dot{q}, \ddot{q}, f_e) \\ &= A(q)\ddot{q} + H(q, \dot{q}) + J(q)f_e \end{aligned} \quad (3.64)$$

Therefore, the column  $ca$  of the matrix  $A$  is given by

$$A(:, ca) = \frac{\partial f}{\partial \ddot{q}(ca)}, \quad ca \in [1, l], \quad (3.65)$$

where  $l$  is the number of degrees of freedom of the system (the dimension of the vector  $q$ ).

The column  $cj$  of the matrix  $J$  is computed identically to  $A$  by

$$J(:, cj) = \frac{\partial f}{\partial f_{qe}(cj)}, \quad cj \in [1, r_f], \quad (3.66)$$

where  $r_f$  represents the dimension of the vector  $f_e$ .

Finally, the matrix  $H$  is obtained from  $H(q, \dot{q}) = \tau$  when  $\ddot{q} = f_e = 0$ . Then,

$$H = f(q, \dot{q}, 0, 0, g, F_v, F_s, K) \quad (3.67)$$

The direct dynamical model is then given by

$$\ddot{q} = [A(q)]^{-1}(\tau - H(q, \dot{q}) - J(q)f_e). \quad (3.68)$$

### 3.3.2.3 Vertical Kinematic Constraints

The four vertical speeds at the contact between the four tires and the ground must be null in order to cancel the vertical displacement of the vehicle (see Fig. 3.20).

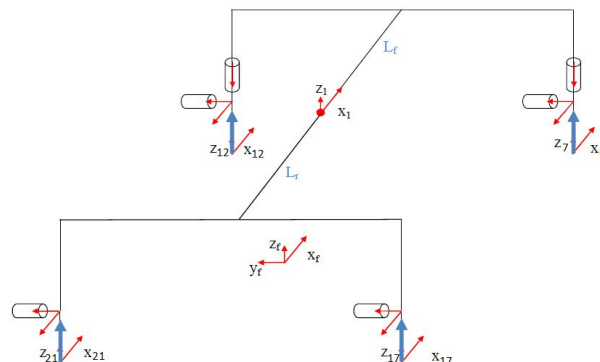


Fig. 3.20: Direction of null vertical speeds at the four points of contact with the ground.

The equations representing these constraints are:

$$\begin{aligned} {}^fV_{7z} &= {}^fR_1(3,:){}^1V_7 = 0 \\ {}^fV_{12z} &= {}^fR_1(3,:){}^1V_{12} = 0 \\ {}^fV_{17z} &= {}^fR_1(3,:){}^1V_{17} = 0 \\ {}^fV_{21z} &= {}^fR_1(3,:){}^1V_{21} = 0 \end{aligned} \quad (3.69)$$

where  ${}^fR_1$  is the inverse matrix of  ${}^bR_f$  given in (3.53).  ${}^fV_{7z}$ ,  ${}^fV_{12z}$ ,  ${}^fV_{17z}$  and  ${}^fV_{21z}$  are the vertical components with respect to the z axis of the velocities  ${}^fV_7$ ,  ${}^fV_{12}$ ,  ${}^fV_{17}$  and  ${}^fV_{21}$  respectively.

The derivatives of these equations are given by :

$$\begin{aligned} \frac{d}{dt}({}^fV_{7z}) &= \frac{d}{dt}({}^fR_1(3,:){}^1V_7) = \frac{d}{dt}({}^fR_1(3,:)){}^1V_7 + {}^fR_1(3,:) \frac{d}{dt}({}^1V_7) = 0 \\ \frac{d}{dt}({}^fV_{12z}) &= \frac{d}{dt}({}^fR_1(3,:){}^1V_{12}) = \frac{d}{dt}({}^fR_1(3,:)){}^1V_{12} + {}^fR_1(3,:) \frac{d}{dt}({}^1V_{12}) = 0 \\ \frac{d}{dt}({}^fV_{17z}) &= \frac{d}{dt}({}^fR_1(3,:){}^1V_{17}) = \frac{d}{dt}({}^fR_1(3,:)){}^1V_{17} + {}^fR_1(3,:) \frac{d}{dt}({}^1V_{17}) = 0 \\ \frac{d}{dt}({}^fV_{21z}) &= \frac{d}{dt}({}^fR_1(3,:){}^1V_{21}) = \frac{d}{dt}({}^fR_1(3,:)){}^1V_{21} + {}^fR_1(3,:) \frac{d}{dt}({}^1V_{21}) = 0 \end{aligned} \quad (3.70)$$

Since the speeds  ${}^1V_7$ ,  ${}^1V_{12}$ ,  ${}^1V_{17}$  and  ${}^1V_{21}$  can be written as function of the articulations speeds  $\dot{q}$ , the equation (3.69) can be written as a product of a matrix  $J_4$  and the speed vector  $\dot{q}$ :

$$\begin{bmatrix} {}^fV_{7z} \\ {}^fV_{12z} \\ {}^fV_{17z} \\ {}^fV_{21z} \end{bmatrix} = J_4 \dot{q} = 0. \quad (3.71)$$

As a result, the equation (3.70) can be written as :

$$\frac{d}{dt} \begin{bmatrix} {}^fV_{7z} \\ {}^fV_{12z} \\ {}^fV_{17z} \\ {}^fV_{21z} \end{bmatrix} = \dot{J}_4 \dot{q} + J_4 \ddot{q} = 0. \quad (3.72)$$

The dynamic model taking into account the vertical constraints becomes :

$$\begin{aligned} \tau &= A(q)\ddot{q} + H(q, \dot{q}) + J_4^T \lambda_v \\ 0 &= J_4 \ddot{q} + \dot{J}_4 \dot{q} \end{aligned} \quad (3.73)$$

where  $\lambda_v$  is the vector of the Lagrange multipliers which represent the vertical forces at the contact points of the wheels with the ground.

Eq. (3.73) forms a system of the form :

$$\begin{bmatrix} \tau \\ 0 \end{bmatrix} = \begin{bmatrix} A(q) & J_4^T \\ J_4 & 0 \end{bmatrix} \begin{bmatrix} \ddot{q} \\ \lambda_v \end{bmatrix} + \begin{bmatrix} H(q, \dot{q}) \\ \dot{J}_4 \dot{q} \end{bmatrix} \quad (3.74)$$

Finally, the direct dynamic model is given by :

$$\begin{bmatrix} \ddot{q} \\ \lambda_v \end{bmatrix} = \begin{bmatrix} A(q) & J_4^T \\ J_4 & 0 \end{bmatrix}^{-1} \left( \begin{bmatrix} \tau \\ 0 \end{bmatrix} - \begin{bmatrix} H(q, \dot{q}) \\ \dot{J}_4 \dot{q} \end{bmatrix} \right). \quad (3.75)$$

Notice that :

- The forces exerted on the chassis are null,
- The system (3.75) permits the computation of the accelerations  $\ddot{q}$  as well as the lagrange multipliers  $\lambda_v$  which represent the vertical loads on the four wheels respectively.

## 3.4 Application to a Four Wheeled Vehicle Model

A four wheeled vehicle model is developed using the robotics formalism. The developed model is composed of 21 bodies (Fig. 3.21) defined as follows:

- $C_1$  represents the chassis
- $C_2, C_3, C_8, C_{13}, C_{14}$  and  $C_{18}$  are virtual bodies introduced as intermediate fixed frames
- $C_4$  and  $C_9$  are the front right and front left steering columns respectively
- $C_5, C_{10}, C_{15}, C_{19}$  are virtual bodies fixed to the four wheels by blocked joints
- $C_6, C_{11}, C_{16}$  and  $C_{20}$  are the front right, front left, rear right and rear left wheels respectively
- $C_7, C_{12}, C_{17}$  and  $C_{21}$  are virtual bodies fixed to the four wheels.

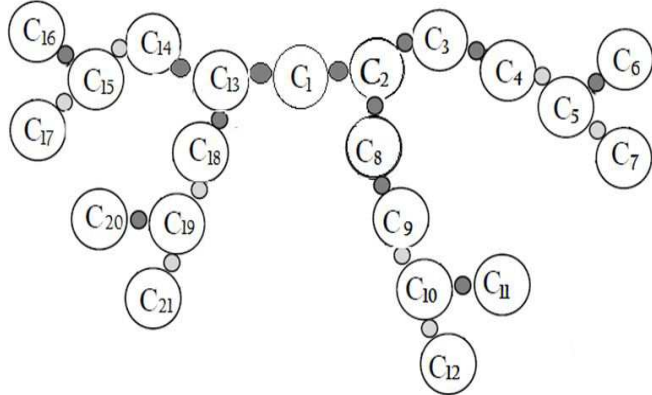


Fig. 3.21: Model topology with 21 bodies.

The eight virtual bodies fixed to the four wheels are introduced to indicate that the wheels are in rotation around their axes while maintaining their contact with the ground. The contact forces between the four wheels and the ground are computed in the frames of the virtual bodies  $C_7, C_{12}, C_{17}$  and  $C_{21}$ , which are linked to the fixed virtual bodies  $C_5, C_{10}, C_{15}$  and  $C_{19}$ . That means that the frames representing the contacts Tires/road are not rotating with the wheels. The four bodies  $C_6, C_{11}, C_{16}$  and  $C_{20}$  are related to the four wheels and they represent the wheels rotation in their frames. The wheels equations of motion are then taken on the fixed virtual bodies  $C_5, C_{10}, C_{15}$  and  $C_{19}$  in order to take into account the wheels rotation and the forces generated in the contact zone between the wheels and the ground.

In this model, we are interested in the lateral and the longitudinal dynamics of the vehicle. The roll and the pitch motions are neglected. The suspension dynamics are not modeled too.

We consider 7 degrees of freedom:

$$q = [x \ y \ \psi \ \theta_{fl} \ \theta_{fr} \ \theta_{rl} \ \theta_{rr}]^t, \quad (3.76)$$

where  $x, y$  and  $\psi$  are the longitudinal position, the lateral position and the yaw angle of the vehicle computed in the vehicle frame  $R_b$ .  $\theta_{ij}$  is the angular position of a wheel, where  $ij$  stands for front right (fr), front left (fl), rear right (rr) and rear left (rl) wheels.  $V_x = \dot{x}$  and  $V_y = \dot{y}$  are the longitudinal and the lateral speeds of the vehicle computed in the vehicle frame  $R_b$  and  $w_{ij} = \dot{\theta}_{ij}$  is the angular velocity of the wheel ( $ij$ ).

The geometric representation is given in Fig. 3.22. According to this description, the geometric parameters of the robot are shown in Table 3.1, where  $j$  refers to the body  $j$  in the poly-articulated system,  $i$  stands for the index of the body antecedent to the body  $j$ ,  $\sigma_j$  represents the articulation type as defined in (3.35) and the rest are the parameters of the DHM notation defined in Subsection 3.3.1. These parameters are used to compute the matrices of transformations between the frames according to the Modified Denavit-Hartenberg description. The Euler variables of the chassis, corresponding to the angular and the linear velocities and accelerations of the vehicle with respect to the frame  $R_f$ , computed in the frame  $R_b$  are used to initialize the forward recurrence of the Newton-Euler algorithm.

The linear velocity and acceleration,  ${}^bV_b$  and  ${}^b\dot{a}_b$ , are given by:

$$\begin{aligned} {}^bV_b &= \begin{bmatrix} (\dot{x} \ \dot{y} \ 0) \end{bmatrix} \\ {}^b\dot{a}_b &= \begin{bmatrix} (\ddot{x} - \dot{y}\dot{\psi} \ \ddot{y} + \dot{x}\dot{\psi} \ 0) \end{bmatrix} \end{aligned} \quad (3.77)$$

The angular velocity  ${}^b\omega_b$  is derived from (3.54) where  $\phi$  and  $\theta$  are set to zero. As a result, the angular acceleration  ${}^b\dot{\omega}_b$  is computed as the derivative of  ${}^b\omega_b$ :

$$\begin{aligned} {}^b\omega_b &= \begin{bmatrix} (0 \ 0 \ \dot{\psi}) \end{bmatrix} \\ {}^b\dot{\omega}_b &= \begin{bmatrix} (0 \ 0 \ \ddot{\psi}) \end{bmatrix} \end{aligned} \quad (3.78)$$

Table 3.1: Geometric Description

$j$	$i = a_j$	$\sigma_j$	$\gamma_j$	$\epsilon_j$	$\alpha_j$	$d_j$	$\beta_j$	$r_j$	Description
1	0	2	0	0	0	0	0	0	Chassis
2	1	2	0	0	0	$L_f$	$-\pi/2$	0	Virtual body
3	2	2	0	0	0	$E/2$	$\pi/2$	0	Virtual body
4	3	0	0	0	0	0	$\delta_{fr}$	$-R_{eff}$	Front right steering column
5	4	2	0	0	$-\frac{\pi}{2}$	0	0	0	Virtual body
6	5	0	0	0	0	0	$\theta_{fr}$	0	Front right wheel
7	5	2	0	0	$\pi/2$	0	0	$-R_{eff}$	Virtual body
8	2	2	0	0	0	$-E/2$	$\frac{\pi}{2}$	0	Virtual body
9	8	0	0	0	0	0	$\delta_{fl}$	$-R_{eff}$	Front left steering column
10	9	2	0	0	$-\pi/2$	0	0	0	Virtual body
11	10	0	0	0	0	0	$\theta_{fl}$	0	Front left wheel
12	10	2	0	0	$\pi/2$	0	0	$-R_{eff}$	Virtual body
13	1	2	0	0	0	$-L_r$	$-\pi/2$	0	Virtual body
14	13	2	0	0	0	$t_r$	$\pi/2$	0	Virtual body
15	14	2	0	0	$\pi/2-$	0	0	$-R_{eff}$	Virtual body
16	15	0	0	0	0	0	$\theta_{rr}$	0	Rear right wheel
17	15	2	0	0	$\pi/2$	0	0	$-R_{eff}$	Virtual body
18	13	2	0	0	0	$-t_r$	$\pi/2$	0	Virtual body
19	18	2	0	0	$-\pi/2$	0	0	$-R_{eff}$	Virtual body
20	19	0	0	0	0	0	$\theta_{rl}$	0	Rear left wheel
21	19	2	0	0	$\pi/2$	0	0	$-R_{eff}$	Virtual body

The contact forces between the ground and the tires are modeled using Dugoff's modeling ([DFS69]), presented in Section 4.2. The aerodynamic forces are computed as in (3.14). Concerning the vertical loads, we make use of (3.17) to estimate  $F_z$  on each wheel. This estimation is then used by Dugoff's model to compute  $F_x$  and  $F_y$  on the four wheels.

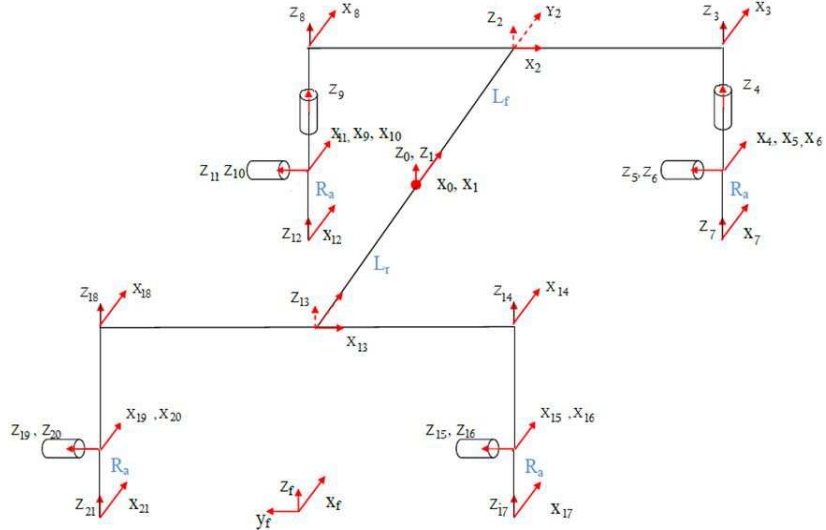


Fig. 3.22: Poly-articulated system with 21 bodies and 7 degrees of freedom.

The developed dynamic model is then given by:

$$\ddot{q} = [A(q)]^{-1}(\tau - H(q, \dot{q}) - J(q)f_e). \quad (3.79)$$

where the matrices A, H and J are as follows:

$$A = \begin{pmatrix} m & 0 & 0 & 0 & 0 & 0 & 0 \\ 0 & m & -L_3 & 0 & 0 & 0 & 0 \\ 0 & -L_3 & I_3 & 0 & 0 & 0 & 0 \\ 0 & 0 & 0 & I_w & 0 & 0 & 0 \\ 0 & 0 & 0 & 0 & I_w & 0 & 0 \\ 0 & 0 & 0 & 0 & 0 & I_w & 0 \\ 0 & 0 & 0 & 0 & 0 & 0 & I_w \end{pmatrix}, \quad (3.80)$$

$$H = \begin{pmatrix} 1/2\rho_a c_d s \dot{x}^2 - m\dot{\psi}\dot{y} + L_3\dot{\psi}^2 \\ m\dot{\psi}\dot{x} \\ -L_3\dot{\psi}\dot{x} \\ 0 \\ 0 \\ 0 \\ 0 \end{pmatrix}, \quad (3.81)$$

and  $J = [J_1 \ J_2]$ , where  $J_1$  and  $J_2$  are given by:

$$J_1 = \begin{pmatrix} -\cos(\delta_{fl}) & -\cos(\delta_{fr}) & -1 & -1 \\ -\sin(\delta_{fl}) & -\sin(\delta_{fr}) & 0 & 0 \\ -L_f \sin(\delta_{fl}) + E/2 \cos(\delta_{fl}) & -L_f \sin(\delta_{fr}) - E/2 \cos(\delta_{fr}) & E/2 & -E/2 \\ R_{eff} & 0 & 0 & 0 \\ 0 & R_{eff} & 0 & 0 \\ 0 & 0 & R_{eff} & 0 \\ 0 & 0 & 0 & R_{eff} \end{pmatrix}, \quad (3.82)$$

$$J_2 = \begin{pmatrix} \sin(\delta_{fl}) & \sin(\delta_{fr}) & 0 & 0 \\ -\cos(\delta_{fl}) & -\cos(\delta_{fr}) & -1 & -1 \\ -L_f \cos(\delta_{fl}) - E/2 \sin(\delta_{fl}) & -L_f \cos(\delta_{fr}) + E/2 \sin(\delta_{fr}) & L_r & L_r \\ 0 & 0 & 0 & 0 \\ 0 & 0 & 0 & 0 \\ 0 & 0 & 0 & 0 \\ 0 & 0 & 0 & 0 \end{pmatrix}. \quad (3.83)$$

The vectors  $\tau$  and  $f_e$  are given by:

$$\tau = (0 \ 0 \ 0 \ \tau_{w_{fl}} \ \tau_{w_{fr}} \ \tau_{w_{rl}} \ \tau_{w_{rr}})^T, \quad (3.84)$$

$$f_e = (F_{x_{fl}} \ F_{x_{fr}} \ F_{x_{rl}} \ F_{x_{rr}} \ F_{y_{fl}} \ F_{y_{fr}} \ F_{y_{rl}} \ F_{y_{rr}})^T. \quad (3.85)$$

Explicitly, the vehicle model is given by:

$$\begin{aligned}
m\ddot{x} - m\dot{\psi}\dot{y} + L_3\dot{\psi}^2 + F_{aero} + F_{a_x} &= 0 \\
m\ddot{y} + m\dot{\psi}\dot{x} - L_3\dot{\psi} + F_{a_y} &= 0 \\
I_3\ddot{\psi} - L_3\ddot{y} - L_3\dot{\psi}\dot{x} + F_{\psi_x} + F_{\psi_y} &= 0 \\
I_w\dot{w}_{fl} + R_{eff}F_{x_{fl}} &= \tau_{w_{fl}} \\
I_w\dot{w}_{fr} + R_{eff}F_{x_{fr}} &= \tau_{w_{fr}} \\
I_w\dot{w}_{rl} + R_{eff}F_{x_{rl}} &= \tau_{w_{rl}} \\
I_w\dot{w}_{rr} + R_{eff}F_{x_{rr}} &= \tau_{w_{rr}}.
\end{aligned} \tag{3.86}$$

with:

$$\begin{aligned}
F_{x_a} &= -\cos(\delta_{fl})F_{x_{fl}} - \cos(\delta_{fr})F_{x_{fr}} - F_{x_{rl}} - F_{x_{rr}} + \sin(\delta_{fl})F_{y_{fl}} + \sin(\delta_{fr})F_{y_{fr}} \\
F_{y_a} &= -\sin(\delta_{fl})F_{x_{fl}} - \sin(\delta_{fr})F_{x_{fr}} - \cos(\delta_{fl})F_{y_{fl}} - \cos(\delta_{fr})F_{y_{fr}} - F_{y_{rl}} - F_{y_{rr}} \\
F_{\psi_x} &= (-L_f \sin(\delta_{fl}) + \frac{E}{2} \cos(\delta_{fl}))F_{x_{fl}} + (-L_f \sin(\delta_{fr}) - \frac{E}{2} \cos(\delta_{fr}))F_{x_{fr}} + \frac{E}{2}F_{x_{rl}} - \frac{E}{2}F_{x_{rr}} \\
F_{\psi_y} &= (-L_f \cos(\delta_{fl}) - \frac{E}{2} \sin(\delta_{fl}))F_{y_{fl}} + (-L_f \cos(\delta_{fr}) + \frac{E}{2} \sin(\delta_{fr}))F_{y_{fr}} + L_r F_{y_{rl}} + L_r F_{y_{rr}}.
\end{aligned} \tag{3.87}$$

where  $I_w$  is the rotational inertia of the wheel,  $F_{x_{ij}}$  and  $F_{y_{ij}}$  represent the longitudinal and the lateral forces developed on the wheel (ij),  $\delta_{fl}$  and  $\delta_{fr}$  are the front left and the front right steering wheel angles and  $\tau_{w_{ij}}$  is the driving/braking torque applied to the wheel (ij).

Note that  $\omega_{ij} = \dot{\theta}_{ij}$  represents the angular speed of the wheel  $ij$ . The terms in  $L_3$  and  $I_3$  in the vehicle model represent the interconnection between the different bodies composing the vehicle. Their presence makes the robotic approach more interesting, since it permits to develop a complete model of the vehicle showing the influence of each body on the other bodies.  $L_3$  and  $I_3$  are defined as

- $L_3 = L_r(m_{rr} + m_{rl}) - L_f(m_{fl} + m_{fr}),$
- $I_3 = I_z + E^2/4(m_{rl} + m_{rr} + m_{fr} + m_{fl}) + L_1^2(m_{fl} + m_{fr}) + L_2^2(m_{rr} + m_{rl})$

where  $I_z$  is the vertical inertia moment and  $m_{ij}$  is the mass of the wheel  $ij$ .

### 3.5 Validation of the developed model

The developed model is implemented under Matlab/Simulink. Fig. 3.23 presents the developed model under Simulink.

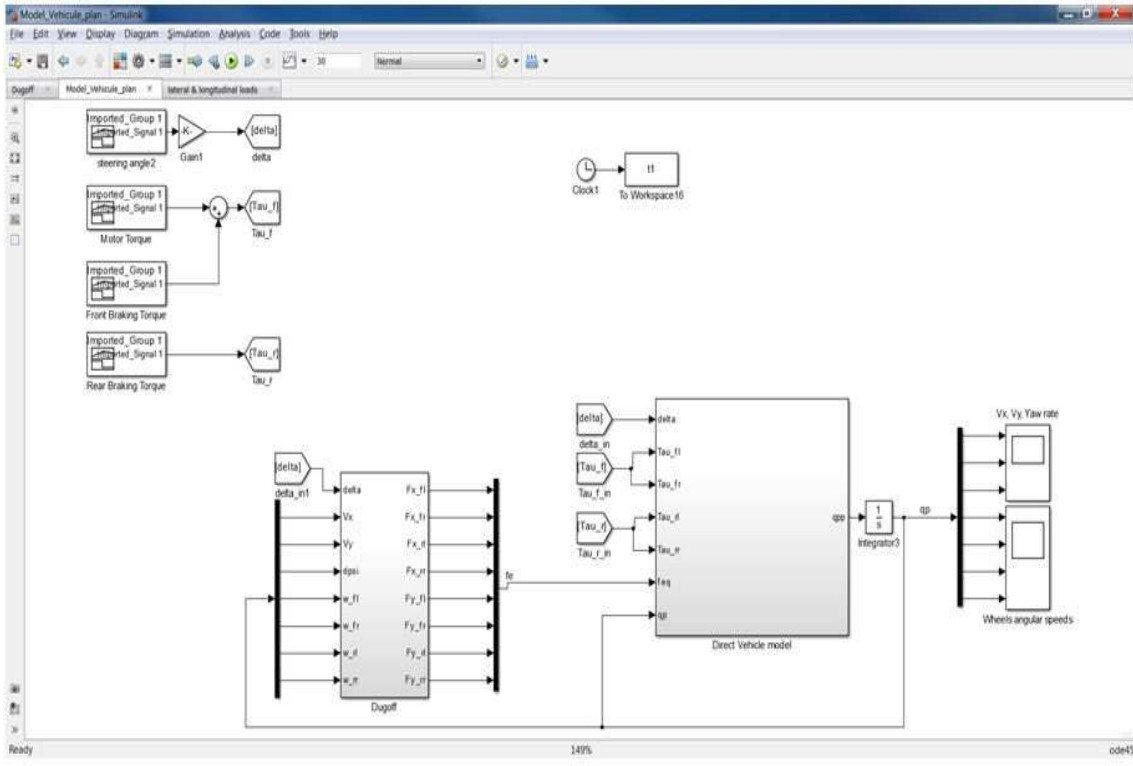


Fig. 3.23: Simulation Model in Matlab/Simulink.

The model inputs are the steering angle  $\delta$  and the wheels Driving/Braking torques, while the model outputs are the vehicle speeds in the longitudinal and the lateral directions, the yaw rate and the wheels angular velocities as well as the derivatives of these variables. To validate the developed model, we make use of a simulation environment developed by OKTAL: Scaner-Studio simulator [Okt16]. We compare then, for a given scenario executed in Scaner-studio, the model outputs to the dynamic variables estimated in the simulator.

### 3.5.1 Scaner-Studio Environment

Scaner-studio is a complete software tool meeting all the challenges of driving simulation. Far from being a 'black box' tool, it is a genuine evolving simulation platform, extendable and open, answering the needs of researchers and engineers. The main modules offered by Scaner-Studio are:

- Models: Dynamic Vehicle, Autonomous Traffic, Pedestrians, Scripting, etc.
- Restitutors: Visual, Sound, Dynamic Platform, etc.
- Acquisitions: Virtual or Real Pilot, tracking systems , physiological data, etc.

The idea of the software is to be used around the operational processes of driving simulators, structured around five dedicated modes of the graphic interface:

- Terrain mode: Road network creator RoadXML allowing the rapid creation of realistic road networks-usable directly in the simulation
- Vehicle mode: Tool for the fine-tuning and study of dynamic models.

- Scenario mode: Driving Simulator scenario editing tools.
- Simulation mode: Simulation supervision tools.
- Analysis mode: Detailed Graphical Analysis tools.

Fig. 3.24 presents a screen capture of the simulation mode in the Scaner-Studio Simulator.

### 3.5.2 Model Validation Results

To validate our model, we have executed many simulations using the Scaner-Studio simulator. The model inputs which are the steering angle and the motor driving/braking torque are taken from the scenarios conducted on Scaner-Studio. The model outputs, which are the vehicle dynamic variables such as the speeds and the accelerations, are compared to the outputs obtained by the simulator. The comparison is done under Matlab/Simulink.

Several scenarios that validate the model were executed. We present in this section four scenarios: The first one validates the longitudinal dynamics of the vehicle, while the other scenarios validate the longitudinal and the lateral coupled vehicle dynamics.



Fig. 3.24: Simulation Mode in Scaner-Studio.

#### 3.5.2.1 First Scenario

For the first scenario, the chosen vehicle parameters ('Segment-B Callas') are as follows:

$$\begin{aligned} m_{ij} &= 23.2 \text{kg}, \quad m = 1500 \text{kg}; \quad g = 9.8 \text{m/s}^2; \quad \rho_a = 1.3 \text{kg/m}^3, \quad s = 2 \text{m}^2, \quad c_d = 0.3, \\ h &= 0.485 \text{m}, \quad I_z = 1652.7 \text{kg.m}^2, \quad L_f = 1.099 \text{m}, \quad L_r = 1.441 \text{m}, \quad \mu = 1, \quad I_w = 2 \text{kg.m}^2, \quad (3.88) \\ C_\sigma &= 67689 \text{N/rad}, \quad C_\alpha = 69253 \text{N/rad}, \quad R_{eff} = 0.28793 \text{m}, \quad E = 1.546 \text{m}. \end{aligned}$$

Fig. 3.25 presents the model inputs for the first scenario. The objective of this scenario is to validate the behavior of the vehicle when navigating in a straight line trajectory. The steering angle is null while the longitudinal acceleration reaches  $2.5 \text{m/s}^2$ . The vehicle speed is increasing continuously and reaches  $111 \text{Km/h}$ .

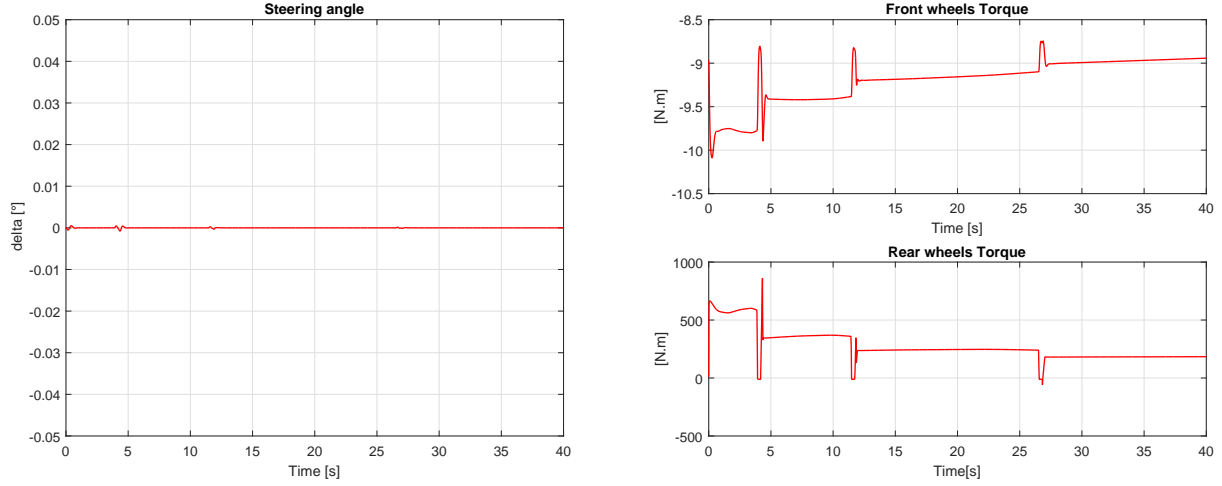


Fig. 3.25: First scenario inputs: Steering angle and wheels torques.

The model outputs presented here are: the longitudinal and the lateral speeds in the vehicle frame, the yaw rate, the longitudinal and the lateral accelerations and the sideslip angle computed at the center of gravity of the vehicle. Fig. 3.26 shows these variables as given by the Scaner-Studio simulator and by the developed model. Obviously, the outputs of both models are very close, which validates the longitudinal dynamics of the model developed using the robotics formalism.

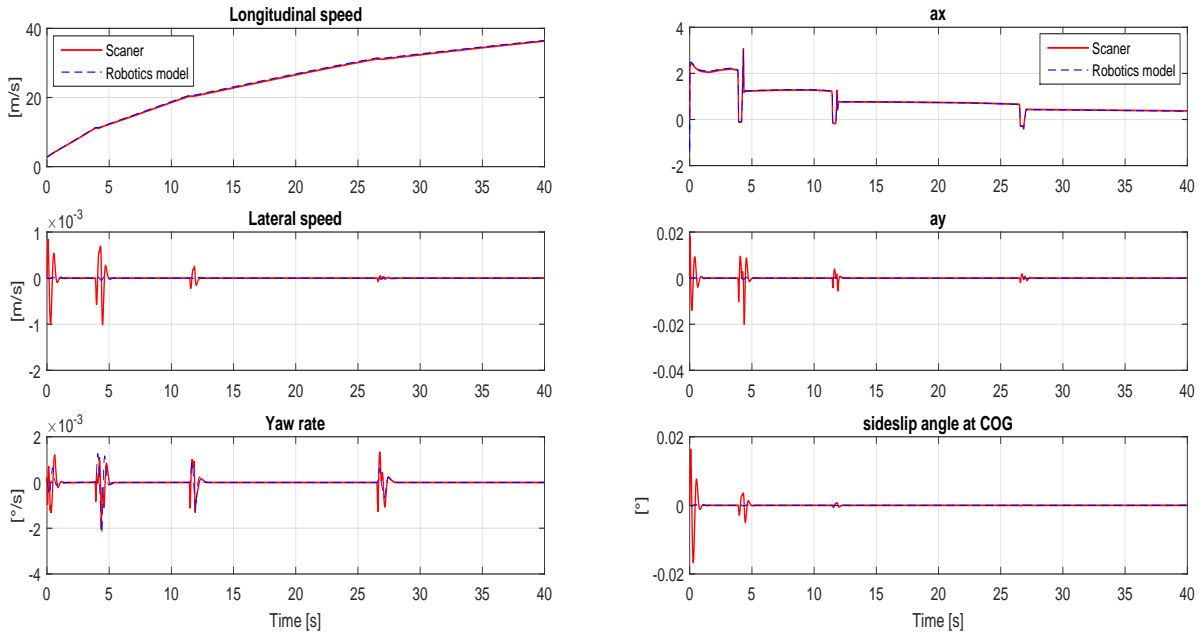


Fig. 3.26: First scenario outputs: Speeds, accelerations, yaw rate and sideslip angle.

### 3.5.2.2 Second Scenario

The second and the third scenarios were executed with another vehicle ('Large Family Car') having the following parameters:

$$m_{ij} = 20kg, \ m = 1744.6kg; \ g = 9.8m/s^2; \ \rho_a = 1.3kg/m^3, \ s = 3m^2, \ c_d = 0.63, \\ h = 0.501m, \ Iz = 3015kg.m^2, \ L_f = 1.207m, \ L_r = 1.543m, \ \mu = 1, \ I_w = 1.062kg.m^2, \ (3.89) \\ C_\sigma = 100000N/rad, \ C_\alpha = 77349N/rad, \ R_{eff} = 0.35m, \ E = 1.492m.$$

The second scenario is executed in order to validate the lateral and the longitudinal coupled dynamics of the developed vehicle model. In this scenario, a sinusoidal steering angle is applied to the vehicle as shown in Fig. 3.27 and the vehicle speed is fixed to almost  $10m/s$ . The Driving/Braking torques applied to the front and the rear wheels are shown in Fig. 3.27.

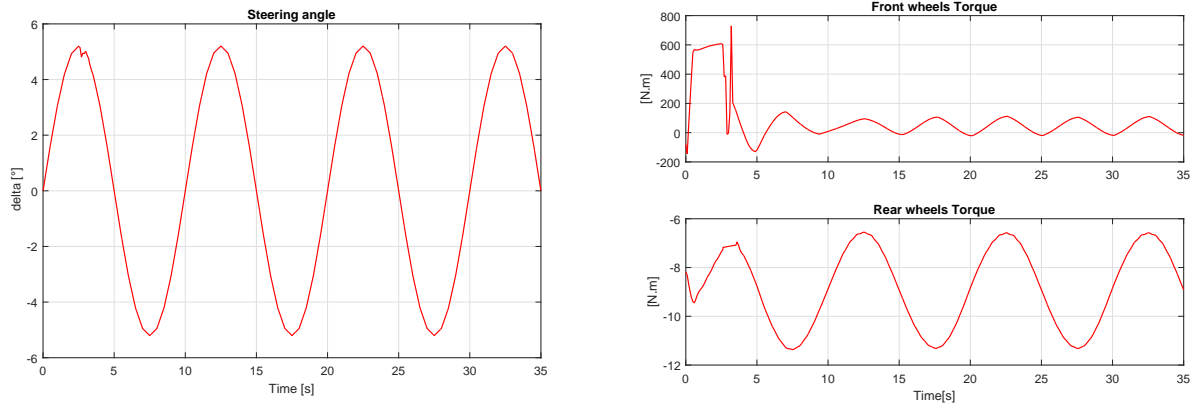


Fig. 3.27: Second scenario inputs: Steering angle and wheels torques.

The vehicle behavior as estimated by the Scaner-Studio simulator and by the developed model is shown in Fig. 3.28. As can be seen, the vehicle longitudinal and lateral speeds and accelerations have almost the same values in both models. The same holds for the yaw rate and the vehicle side-slip angle.

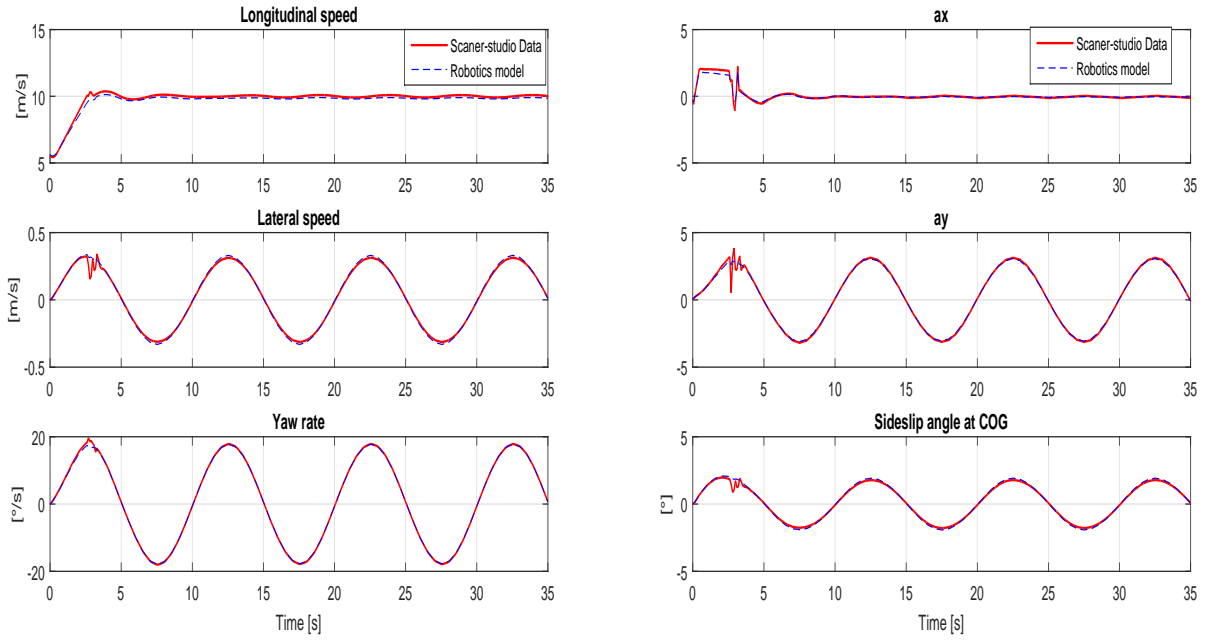


Fig. 3.28: Second scenario outputs: Speeds, accelerations, yaw rate and sideslip angle.

### 3.5.2.3 Third scenario

This scenario aims to validate the coupled lateral and longitudinal dynamics of the developed model at a high speed. The model inputs are shown in Fig. 3.29 while the model outputs are given in Fig. 3.30. The vehicle speed varies between  $15$  and  $25\text{m/s}^2$  and the steering angle goes from  $-8^\circ$  to  $2^\circ$ . Observing Fig. 3.30, we can remark that the model outputs are very close to the outputs given by the Scaner-Studio model and this validates our developed model even when executing roundabouts with a high speed.

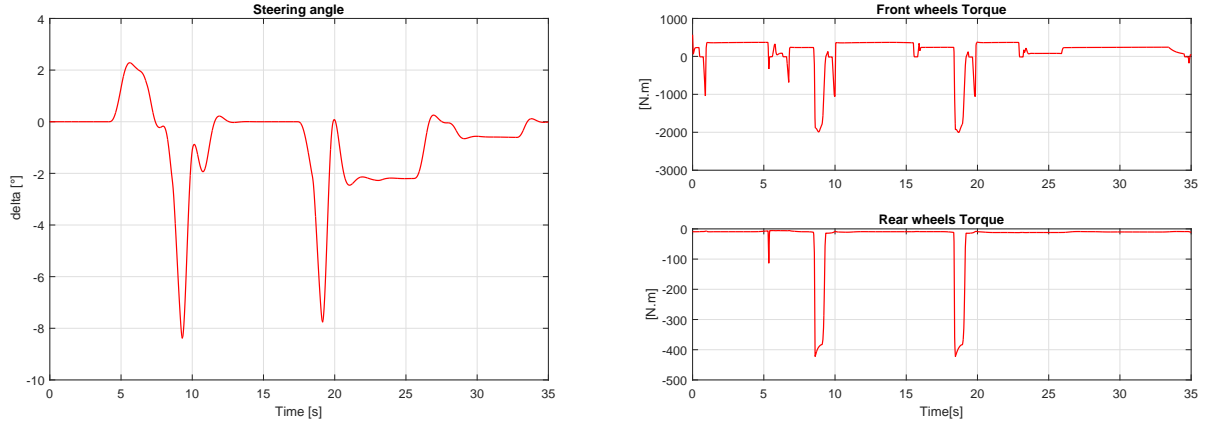


Fig. 3.29: Third scenario inputs: Steering angle and wheels torques.

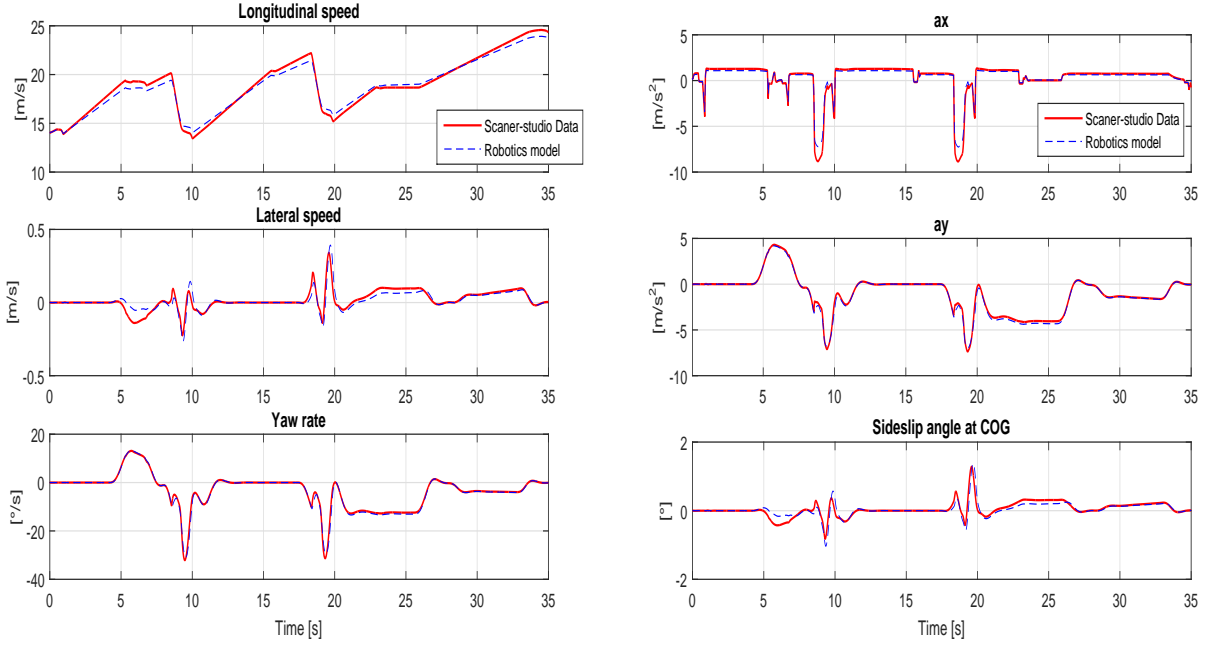


Fig. 3.30: Third scenario outputs: Speeds, accelerations, yaw rate and sideslip angle.

Other tests have been carried out to validate the model in different driving conditions. To conclude this section, we note that the developed model is valid in a large marge of driving conditions and can be used for control objectives.

## 3.6 Conclusion

In this chapter, a state of the art on the existing vehicle modeling tools was presented. Some modeling techniques are based only on the fundamental physics laws while some other modeling techniques make use of multi-body modeling tools. This latter assimilates the vehicle to a robot with multiple bodies related by joints and interacting between them. This modeling technique leads to a more accurate and complete model than the classical modeling tools and that's why it was chosen in this work. Indeed, we have chosen to proceed with the recursive formulation developed in [Maa11] and based on the method of Luh, Walker and Paul [LWP80] where Euler-Lagrange dynamics are used to derive the dynamic model of the vehicle. This formulation was adopted since it allows to automatically calculate the symbolic expressions of the dynamic model with a minimum number of numerical steps. Moreover, the algorithm complexity does not increase with the system's complexity (large number of variables) and the modification of the systems assumptions can be taken into account in a simple way (For example, the consideration or not of some components of the system).

A four wheeled planar vehicle model is then established using this formalism. The model has seven degrees of freedom (the vehicle longitudinal and lateral positions, the yaw angle and the angular positions of the four wheels). The developed model is then validated using Scanner-Studio simulator developed by Oktal and the validation results show that the developed model is close enough from the Scanner-Studio reference model and thus it can be used to develop lateral and longitudinal controllers for the vehicle (the developed vehicle model is planar). The next chapter of this thesis presents two coupled controllers for the lateral and the longitudinal

vehicle dynamics designed based on the developed model. The controllers theory is explained in detail and we present further the controller's validation results.

# Chapter 4

## Vehicle Coupled Control

### Summary

---

<b>4.1</b>	<b>Introduction</b>	<b>102</b>
<b>4.2</b>	<b>State of the Art on the Autonomous Vehicles Control</b>	<b>103</b>
4.2.1	Lateral Control	103
4.2.2	Longitudinal Control	106
4.2.3	Coupled Control	108
<b>4.3</b>	<b>Developed Coupled Controllers</b>	<b>109</b>
4.3.1	Simplified Vehicle Model	109
4.3.2	Coupled Controller based on Lyapunov Control Techniques	112
4.3.3	Coupled Controller based on an Immersion and Invariance Approach, Combined with Sliding Mode Control	114
<b>4.4</b>	<b>Controllers Validation: Simulation Results</b>	<b>118</b>
4.4.1	Normal Driving Conditions	120
4.4.2	Controller Robustness	125
<b>4.5</b>	<b>Controllers validation: Experimental Results</b>	<b>131</b>
4.5.1	Presentation of the Experimental Environment	131
4.5.2	Results of Validation of the Lyapunov based controller	141
4.5.3	Results of validation of the Immersion and Invariance based controller	153
4.5.4	Some comparison results: Lyapunov vs I & I vs classical PD/P controller	159
<b>4.6</b>	<b>Conclusion</b>	<b>171</b>

---

### 4.1 Introduction

Once the environment has been discovered and a secure trajectory has been generated, the vehicle actuators, such as the Driving/Braking torque and the steering angle, have to be controlled in order to guide the vehicle to track the desired trajectory. In fact, the vehicle dynamic control has been widely discussed in the literature and several studies on longitudinal and lateral control have been conducted. However, the longitudinal and the lateral controllers are addressed separately in most of the cases. For lane keeping, lane-change maneuvers, pedestrian and obstacle avoidance, a lateral control is used. While, for adaptive cruise control and

platooning tasks, the longitudinal control is developed. Unfortunately, many critical driving situations involving the safe handling of vehicles require coupled control, and, such a strategy is rarely addressed in the literature. A brief presentation of the techniques dealing with the lateral, the longitudinal and the coupled control is conducted in the first section of this chapter, underlining the major axes of each technique. We present therefore two new controllers dealing with two coupled control algorithms for longitudinal and lateral dynamics of an autonomous vehicle. In the first controller, the control is designed using Lyapunov functions while in the second controller an Immersion and Invariance technique is used. Both of the controllers aim to ensure a robust tracking of the reference trajectory especially in coupled maneuvers such as lane-change maneuvers, obstacle avoidance maneuvers and combined lane-keeping and steering control during critical driving situations.

The proposed controllers are then validated by simulation under Matlab/Simulink. And then, the controllers are validated by experimental tests using a robotized vehicle within the Heudiasyc laboratory. Some comparisons are then conducted and some conclusions are made.

## 4.2 State of the Art on the Autonomous Vehicles Control

Several strategies dealing with the vehicle dynamics control can be found in the literature. In most of the cases, two independent controllers are used to control the longitudinal and the lateral dynamics of the vehicle. The lateral control is used when a lane keeping or a lane change maneuver is needed, while the longitudinal control is often used for cruise control, adaptive cruise control and platooning tasks. Lately, some approaches dealing with coupled control have been proposed. Indeed, the vehicle dynamics in the longitudinal and the lateral directions are strongly coupled. That reflects the necessity to treat the vehicle dynamics in a coupled way in order to guarantee the vehicle safety handling, especially in critical driving situations.

In this section, a state of the art on existing strategies for lateral, longitudinal and coupled vehicle dynamics control is presented. The major methodologies of the used-control laws are identified, which allows us to propose thereafter new controllers.

### 4.2.1 Lateral Control

The lateral control of an autonomous vehicle consists of guiding the vehicle to follow a given reference trajectory by acting on the steering angle or torque. Considering the non-linearity of the system, the parametric uncertainties and the possible perturbations encountered in automotive applications, one of the main challenges today is to design a robust controller capable of accounting for these imperatives. The controller must therefore perform well despite the disturbances, the parametric uncertainties, the effect of wind, the change of road grip, etc.

The development of the control strategies is based on a model representing the vehicle dynamics. The most used model is the dynamic bicycle model [LW07] since it represents the non-linearity of the vehicle system with relatively simple equations. Some approaches proceed by linearizing the vehicle model in order to reduce the time computation and the complexity [BNM11, FV09]. The most used linear models are the Linear Time Invariant (LTI) model, the Linear Time Varying (LTV) model and the Linear Parameter Varying (LPV) model. This latter is shown to be of high interest [PVSD<sup>+</sup>11, Men10], since it allows to synthesize robust

and adaptive controllers using linear tools.

In the following, we will present some of the existing control laws that deal with the control of the lateral dynamics of an autonomous vehicle :

- Proportional (P), Integral (I) and Derivative (D) controllers as well as their combinations (PI, PD, PID) are the feedback controllers commonly used in the control of autonomous systems. Regarding its simplicity, this type of controllers is usually used, especially when the identification of the vehicle physical parameters is not accurate. In [BBF<sup>+</sup>99], a 'Gain Scheduled Proportional Controller' is used. The control input which is the steering angle  $\delta$  is calculated through a variable gain proportional controller, where the gain inversely depends on the vehicle velocity. It has been demonstrated that, as the vehicle speed increases, the damping factor of the closed loop system gets worse and can be improved, under certain limits, by increasing the look-ahead distance at which the lateral error is computed. One example of PID control is given in [MSN11], where a nested PID steering control in vision based autonomous vehicles is designed and experimentally tested to perform path following in the case of roads with an uncertain curvature.
- State feedback controllers are also used to control the lateral dynamics of a vehicle. The main idea of this control technique is the positioning of the closed loop eigenvalues in desired locations [KND85]. In [BNM11], a lane keeping assistance system for passenger vehicles based on a piecewise affine state feedback controller is designed. This control approach is also discussed in [Raj11] and it is shown that the lateral position steady state error can be canceled by an appropriate choice of an added feed-forward input. However, the yaw angle steady state error cannot be canceled.
- In [KKY11], the lateral dynamics of the vehicle are controlled using a linear quadratic regulator (LQR), and a bicycle model is used to obtain the feed-forward and feedback terms of the steering input. This approach was also used in [PT91], where a preview control action based on the Frequency-Shaped Linear Quadratic (FSLQ) control theory is used. The frequency-domain analysis results show that the preview control law improves the low frequency tracking performance. In fact, the goal is to minimize a weighted quadratic cost function that represents the deviations of key measurements from their desired value. However, the difficulties in finding the right weighting factors limit the application of the LQR based controllers.
- The fuzzy control is widely used [NGGP08, PGM<sup>+</sup>12, HB03] in this domain. Indeed, fuzzy logic is a powerful artificial intelligence tool that facilitates the control of complex processes as those that are involved in autonomous vehicle driving. In 1985, Sugeno demonstrated that a scale model car can be controlled by fuzzy logic using only human experience [SN85] as a knowledge base. Nevertheless, this approach makes use of many parameters that should be correctly tuned. Moreover, we may find thousands of different configurations of the same system depending on the conjunction, disjunction, implications and defuzzification choices.
- We can also cite the backstepping approach, where we start by guaranteeing the stability of some internal subsystems and progressively step back out of the system, maintaining stability at each step. The backstepping technique was used in [NN12], where an integrated control method of a light road vehicle driving at low speeds (under 50 km/h) on a known and high secured itinerary is presented.

- In [MDNFM14], a combined longitudinal and lateral vehicle control that employs flatness-based control is presented. This technique is based on controlling the system flat outputs, which can be used to explicitly express all the states and the inputs of the system as a function of the flat outputs and a finite number of their derivatives. Using this property, deriving the inputs that guide the system outputs to track some desired values becomes a simple task.
- The Model Predictive Control (MPC) has been developed to integrate the performance of the optimal control with the robustness of the feedback control [GPM89]. Similar to the optimal control, the Model Predictive Control selects the actions by optimizing a cost function while accounting for the system dynamics and constraints. Linear and nonlinear MPC have been widely used in the autonomous vehicles control [KFB<sup>+</sup>06, FBT<sup>+</sup>08, BM09, ADL<sup>+</sup>12, FTA<sup>+</sup>07]. However, the implementation of this technique requires significant computing infrastructure which might not be available on the commercial vehicles.
- The sliding mode approach (SMC) is a well-known technique used in the lateral control domain. It consists of two steps [Pis00]: The first step is the choice of a manifold in the state space such that, once the state trajectory is constrained on it, the controlled plant exhibits the desired performance. The second step is represented by the design of a discontinuous state-feedback capable of forcing the system state to reach, in a finite time, such a manifold (accordingly called sliding manifold). This approach was used to control autonomous vehicles in order to track a given reference trajectory, as in [AGS<sup>+</sup>95b, HT97]. The sliding mode control is one of the most promising control techniques for trajectory tracking. However, its main drawback is the chattering. Some solutions have been proposed to reduce the chattering problem, such as the use of higher order sliding mode controllers [TTC13].
- $H_\infty$  controllers introduced into control theory in the late 1970s-early 1980s by [Zam81, Tan80] are also used to control the lateral dynamics of the vehicle, in order to achieve stabilization with guaranteed performance. This approach treats the control problem as a mathematical optimization problem and has the advantage over classical control techniques in that it is readily applicable to problems involving multivariate systems. This technique was used in [HLV<sup>+</sup>11, CFJCSH14] where the lateral control of autonomous vehicles is treated.
- Some hybrid controllers were proposed in the litterature: In [MEG<sup>+</sup>10, SSPD12], a hybrid controller combining fuzzy logic with linear quadratic tools is employed and in [NGG<sup>+</sup>05], a fuzzy controller is combined with a PID controller to achieve the vehicle lateral control.

An overview of four controllers is provided in [CNM04]: The first one is the output feedback self-tuning controller proposed in [MT96] and applied in [NCM04] to deal with the lateral control problem. The interest of this solution is that only the lateral displacement at a look ahead distance is used as a measure for the controller. The second one, is an  $H_\infty$  controller based on the loop shape procedure. The third one is a simple proportional controller while the fourth one is a fuzzy controller. A comparison among these four controllers was carried out. Simulations considering curvature, speed, adherence variations and the lateral wind are presented. The authors conclude that the four controllers are robust with respect to the considered situations. Whether the proportional controller presents the largest errors systematically, the self-tuning regulator presents the smallest errors. The  $H_\infty$  and the fuzzy controllers have

equivalent responses, being comparable in many of the tests to the self-tuning regulator. It should be also remarked that, in spite of the well functioning of the fuzzy controller, it is an heuristic controller, where no stability proof is presented, and then it is less reliable. The authors also observe that, as expected, the errors increase as the adherence coefficient decreases and as the speed increases. Globally, the self-tuning regulator shows to be the most performing one, from the simulations study. Further experimental tests could also test it with respect to its complexity.

Lately, some comparisons were presented in [LW07], [HAS13], [MKDN13]. In [HAS13], the comparison of the two inversion-based controllers developed in [Wer10] and [FSR05] is presented. A set of test methodologies considering the most significant deviations in the initial states and the vehicle parameters is used for a thorough evaluation:

- Monte-Carlo simulations for the average control performance,
- Rapidly exploring random trees for the worst-case performance.

The specific comparison of the inversion-based controllers only revealed significant differences with respect to the worst-case deviation, where the control concept proposed in [Wer10] produced better results.

In [MKDN13], two robust steering vehicle control laws based on continuous time and discrete time switching  $H_\infty$  controllers were proposed. Using common Lyapunov function and switched Lyapunov function, sufficient conditions for the existence of two controllers are obtained in terms of linear matrix inequalities (LMIs). The proposed approaches are tested under high lateral acceleration using experimental data. The controllers were validated but the performances were not really compared.

#### 4.2.2 Longitudinal Control

The speed tracking task is a relevant task in fully automated driving. In fact, the longitudinal control aims to track a given speed profile generated by a higher module. Many applications can be found:

- The Cruise Control (CC), which is widely used, aims to ensure the regulation of the vehicle speed.
- The Adaptive Cruise Control (ACC) is an extension of the cruise control which employs external information for regulation of both vehicle speed and inter-vehicular distance. An interesting review of the development of Adaptive Cruise Control systems is presented in [XG10].
- The platooning tasks where several vehicles operate under automatic control as a unit and travel at the same speed with relatively small inter-vehicle spacing. A well-organized platoon control may have advantages in terms of increasing highway capacity and decreasing fuel consumption and emissions.

Indeed, the vehicle longitudinal dynamics are based on the transmission system integrated in the vehicle, e.g. the engine type, the gear box, the braking system, etc. In [SOAL10], the longitudinal dynamics of a vehicle with automatic transmission are modeled. In their work, the dynamics of the power train consisting of the engine, the torque converter, the gear box, the final drive and the wheels are considered. Then, the effects of the external forces including the aerodynamic drag, the gravitational effects, the rolling resistance and the longitudinal tire effects are added. This modeling was intended to be used in the design of an Adaptive Cruise Control system. However, most of the approaches dealing with the longitudinal control don't take into consideration the whole transmission system dynamics, due to its complexity and the

differences it can present from a vehicle to another. Many assumptions are made instead and a kinematic model is often used to represent the longitudinal dynamics of the vehicle [H<sup>+</sup>97]. We present in the following some strategies that have been used in the literature to control the vehicle's longitudinal dynamics:

- PID controllers are widely used for cruise control objectives since they are simple to implement and do not require an accurate identification of the vehicle model. In [KKY11], the longitudinal dynamics of the vehicle are controlled using a PID controller, which is based on the inverse dynamics of the vehicle powertrain model. In [HTMT07], a Proportional Integral controller (PI) is used, and a PID controller is used in [HLV<sup>+</sup>11].
- In [AAAO11], a nonlinear static state feedback control is applied to the vehicle speed. The control is obtained by suitable change of variables and after applying some feedback. In this study, the authors are interested in the stabilization of the vehicle velocities, i.e longitudinal, lateral and yaw rate, using Lyapunov stability theory and LaSalle invariance principle.
- Fuzzy logic is also a common control approach used to control the longitudinal speed of the vehicle. In [NGR<sup>+</sup>03], an adaptive cruise controller based on fuzzy logic is developed and then validated using an automatic driving system instrumented for testing the work of the controller in a real environment. The results obtained in their experiments show a very good performance of the controller, which is adaptable to all the speeds and safe inter-vehicle gap selections. Fuzzy logic was also used in [ZK10], where a coordinated throttle and brake fuzzy controller is designed.
- In [EM11], a machine-learning alternative that estimates stochastic driver models from their behavior traces is proposed. They proposed a Bayesian Autonomous Driver Mixture-of-Behaviors (BAD-MoB) model for the longitudinal control of human drivers in an inner-city traffic scenario. Besides mimicking human driver behavior, they suggest using the model for prototyping intelligent assistance systems with human-like behavior.
- In [N<sup>+</sup>07], a cruise controller design based on a sliding mode technique is proposed and experimentally validated. The controller is implemented for the vehicle longitudinal control at low speed and aims to increase the traffic capacity and improve safety and comfort. In [FV09], a second order sliding mode control of vehicles is used for platooning tasks.
- Linear Quadratic (LQ) control is used in [SOLA11], where the authors present a comparison between the (LQ) controller and a PI controller with adjustable gain. They conclude that both of the controllers are useful and present similar performances in global.
- Some control approaches were developed to overpass the modeling phase, especially when the identification of the system parameters is not intuitive. In [DNBF<sup>+</sup>10], a 'model free' controller is developed. The estimation of the derivative of the vehicle speed is accomplished using algebraic techniques. The proposed controller was validated using an experimental vehicle and has proved good results.
- In [H<sup>+</sup>97], a brake system model and an integrated brake/throttle switching control are developed based on Lyapunov control laws. The model was validated by comparison to an experimental vehicle data, while the control laws were validated only by simulations.

### 4.2.3 Coupled Control

In the above studies, lateral and longitudinal control problems have been investigated in a decoupled way. Besides, numerous studies dealing with the lateral guidance of automotive vehicles consider the vehicle speed as a changing parameter or simply assume a constant speed. On the other hand, those dealing with longitudinal control do not take into account the coupling with the lateral motion. However, there are strong couplings between the two dynamics at several levels: dynamic, kinematic and tire forces. Consequently, the simultaneous inclusion of longitudinal and lateral control designed on a coupled model becomes unavoidable in order to improve performance guidance in a large operating range. Nevertheless, the control design based on a complex mathematical model of the vehicle becomes a difficult task due to these couplings. Therefore, different control approaches have been proposed in the literature to cope with this problem:

- A coupled longitudinal and lateral control based on a sliding mode technique is proposed in [Lim98]. The idea is to calculate the desired tire forces to obtain the steering angle by inverting the tire model. Note that the analytical inversion of the tire model is not possible. This makes the operation somehow complex. Beside this, their solution requires an estimation of the slip ratio and since this estimate is unavailable, only the proposed lateral controller is experimentally tested.
- Recently, a solution based on the flatness control theory has been proposed in [MDNFM14]. New algebraic estimation techniques for noise removal and numerical differentiation are addressed. The proposed controller is validated by simulations using noisy experimental data, which were acquired by a laboratory vehicle with highly dynamic loads and high lateral accelerations.
- Another solution based on a backstepping synthesis is proposed in [NN12]. The two control inputs considered are the traction torque and the steering angle. Both are calculated using a standard backstepping synthesis. The controller validation is conducted by a simulation using data from a real experimentation carried out on the Versailles Satory test track (France).
- In [AOB14], a global guidance strategy is proposed. The lateral guidance is accomplished using a Nonlinear Model Predictive Control strategy. A nonlinear longitudinal control strategy considering power-train dynamics is also proposed to cope with the longitudinal speed tracking problem. Indeed, the speed tracking and the vehicle positioning problems can be decoupled using the proposed controllers. The coupling of the longitudinal and the lateral dynamics is handled by the nonlinear model used to develop the lateral and the longitudinal controllers. An interesting contribution in this work is the use of heterogeneous criteria to update the longitudinal speed reference in order to improve the lateral stability level, thus increasing the autonomous guidance safety. The proposed solution is validated through simulations showing promising results.

In this thesis, two coupled controllers for the lateral and the longitudinal dynamics are developed. The first one is based on Lyapunov control techniques. This solution allows the design in one step of a multivariable nonlinear controller dealing with both the longitudinal and the lateral dynamics of the vehicle. While the control law (based on a given Lyapunov function) proposed in [AOB14] deals only with the longitudinal dynamics, we propose a generalization

(addition of two terms to form the Lyapunov function) to deal with both the longitudinal and lateral dynamics. The developed controller is based on a simple strategy and can be therefore simply implemented. The controller validation is conducted through a simulation under Matlab/Simulink using experimental data collected by performing several tests on the vehicle DYNA present in the Heudiasyc laboratory (Peugeot 308 sw). Then, an experimental validation is conducted using the robotized vehicle 'ZOE' also within the Heudiasyc laboratory. The second proposed controller is based on an immersion and invariance technique. Indeed, the immersion and invariance (I & I) theory consists in defining a target dynamics (manifold) and to design a control law that makes the target dynamic attractive and invariant. Using the fact that the lateral dynamics converge faster than the longitudinal dynamics of the vehicle, we define the manifold as the equilibrium surface of the lateral dynamics. Then, in order to reach this target, a sliding mode control (SMC) approach is used in order to define a suitable steering wheel angle that can guide the vehicle towards the defined manifold. Once the manifold is reached, the stabilisation of the longitudinal dynamics is considered. At this level, the convergence of the longitudinal dynamics is assured by the use of a Lyapunov function where the lateral variables are substituted by their equilibrium values.

This solution was also validated under Matlab/Simulink using the experimental data collected on DYNA. Both of the proposed controllers are based on the vehicle model developed using robotics formalism (**see chapter 3**). The simulations and the experimental results are very promising.

In the following, we present the controllers strategy and the results of their validations under Simulink/Matlab. A comparison between the two controllers and a classical PID controller is conducted. Then, the experimental validation results of both controllers are presented and some comparisons and conclusions are made.

## 4.3 Developed Coupled Controllers

We present in this section, the proposed solutions for the coupled control problem. The controllers strategy and the derivation of the control laws are explained in detail, then the controllers validity is discussed with respect to the simulation and the experimentation results.

Note that, we don't propose any discussion about the management of the maximum admissible speed or other security aspects; since we assume that all those points should be managed in the trajectory generator (upper layer) and the control law duty is to ensure the path following and the speed tracking.

### 4.3.1 Simplified Vehicle Model

The developed model presented in chapter 3 is used here to accomplish the control objectives. For convenience, we recall here the dynamic equations obtained for a four wheeled vehicle:

$$\begin{aligned}
m\ddot{x} - m\dot{\psi}\dot{y} + L_3\dot{\psi}^2 + F_{aero} + F_{a_x} &= 0 \\
m\ddot{y} + m\dot{\psi}\dot{x} - L_3\dot{\psi} + F_{a_y} &= 0 \\
I_3\ddot{\psi} - L_3\ddot{y} - L_3\dot{\psi}\dot{x} + F_{\psi_x} + F_{\psi_y} &= 0 \\
I_w\dot{w}_{fl} + R_{eff}F_{x_{fl}} &= \tau_{w_{fl}} \\
I_w\dot{w}_{fr} + R_{eff}F_{x_{fr}} &= \tau_{w_{fr}} \\
I_w\dot{w}_{rl} + R_{eff}F_{x_{rl}} &= \tau_{w_{rl}} \\
I_w\dot{w}_{rr} + R_{eff}F_{x_{rr}} &= \tau_{w_{rr}}.
\end{aligned} \tag{4.1}$$

with:

$$\begin{aligned}
F_{a_x} &= -\cos(\delta_{fl})F_{x_{fl}} - \cos(\delta_{fr})F_{x_{fr}} - F_{x_{rl}} - F_{x_{rr}} + \sin(\delta_{fl})F_{y_{fl}} + \sin(\delta_{fr})F_{y_{fr}} \\
F_{a_y} &= -\sin(\delta_{fl})F_{x_{fl}} - \sin(\delta_{fr})F_{x_{fr}} - \cos(\delta_{fl})F_{y_{fl}} - \cos(\delta_{fr})F_{y_{fr}} - F_{y_{rl}} - F_{y_{rr}} \\
F_{\psi_x} &= (-L_f \sin(\delta_{fl}) + \frac{E}{2} \cos(\delta_{fl}))F_{x_{fl}} + (-L_f \sin(\delta_{fr}) - \frac{E}{2} \cos(\delta_{fr}))F_{x_{fr}} + \frac{E}{2}F_{x_{rl}} - \frac{E}{2}F_{x_{rr}} \\
F_{\psi_y} &= (-L_f \cos(\delta_{fl}) - \frac{E}{2} \sin(\delta_{fl}))F_{y_{fl}} + (-L_f \cos(\delta_{fr}) + \frac{E}{2} \sin(\delta_{fr}))F_{y_{fr}} + L_r F_{y_{rl}} + L_r F_{y_{rr}}.
\end{aligned} \tag{4.2}$$

However, to simplify the dynamic equations, some usual assumptions are made:

- Only the rear wheels are motorized, so

$$\begin{aligned}
\tau_{w_{fl}} &= 0, \quad \tau_{w_{fr}} = 0 \\
\tau_w &= \tau_{w_{rl}} + \tau_{w_{rr}}
\end{aligned} \tag{4.3}$$

**Remark:** We consider here a rear-wheel-drive vehicle (where the rear wheels are motorized) instead of a front-wheel-drive vehicle (where the front wheels are motorized) in order to simplify the control inputs computation. Subsequently, these control inputs are used to control front-wheel-drive vehicles, such as Peugeot 308 sw and Renault-ZOE. This means that we have neglected the difference between a rear-wheel-drive vehicle and a front-wheel-drive vehicle. The impact of this assumption on the controllers performance may be studied in future works.

- The estimation of the contact forces between the ground and the tires is based on the linear model, namely:

$$\begin{aligned}
F_{x_{ij}} &= C_{\sigma_{ij}} \sigma_{x_{ij}} \\
F_{y_{ij}} &= C_{\alpha_{ij}} \alpha_{ij}
\end{aligned} \tag{4.4}$$

where  $ij$  is the wheel index,  $i$  stands for front or rear and  $j$  stands for left or right.

- The approximation of small angles is made.
- The front left and the front right wheel's steering angles are supposed to be equal ( $\delta_{fl} = \delta_{fr} = \delta$ ).

- The longitudinal slip ratio is considered approximatively null, that renders:

$$R_{eff}w_{ij} = \dot{x}. \quad (4.5)$$

The wheels dynamics equations can be written in the following form:

$$I_w \ddot{w}_{ij} = \tau_{ij} - R_{eff} F_{x_{ij}}. \quad (4.6)$$

where  $ij$  is the wheel index designating any of the four wheels. Using (4.5) and (4.6), we can find:

$$F_{x_{ij}} = \frac{\tau_{w_{ij}}}{R_{eff}} - \frac{I_w \ddot{x}}{R_{eff}^2}. \quad (4.7)$$

Integrating (4.3) and (4.7) in the first equation of (4.1), we obtain:

$$m\ddot{x} - m\dot{y}\dot{\psi} + L_3\dot{\psi}^2 + F_{aero} - \frac{\tau_w}{R_{eff}} + 4\frac{I_w \ddot{x}}{R_{eff}^2} + \delta(F_{y_{fl}} + F_{y_{fr}}) = 0. \quad (4.8)$$

This assumption permits to reduce the wheels dynamic equations by relating directly the longitudinal acceleration to the wheels torque. The vehicle longitudinal dynamics are then represented by a single equation ((4.8)).

In the following, we will note  $C_{\alpha_f}$  and  $C_{\alpha_r}$  the cornering stiffness of the front and the rear wheels, where  $C_{\alpha_f} = C_{\alpha_{fl}} = C_{\alpha_{fr}}$  and  $C_{\alpha_r} = C_{\alpha_{rl}} = C_{\alpha_{rr}}$ .

With all these assumptions, the vehicle model presented in (4.1) can be rewritten as:

$$\begin{aligned} m_e \ddot{x} - m\dot{y}\dot{\psi} + L_3\dot{\psi}^2 + F_{aero} + \delta(2C_{\alpha_f}\delta - 2C_{\alpha_f} \frac{\dot{x}(\dot{y} + L_f\dot{\psi})}{\dot{x}^2 - (\frac{E}{2}\dot{\psi})^2}) &= g_1 \\ m\ddot{y} + m\dot{x}\dot{\psi} - L_3\ddot{\psi} + 2C_{\alpha_f} \frac{\dot{x}(\dot{y} + L_f\dot{\psi})}{\dot{x}^2 - (\frac{E}{2}\dot{\psi})^2} + 2C_{\alpha_r} \frac{\dot{x}(\dot{y} - L_r\dot{\psi})}{\dot{x}^2 - (\frac{E}{2}\dot{\psi})^2} &= g_2 \\ I_3 \ddot{\psi} + 2L_f C_{\alpha_f} \frac{\dot{x}(\dot{y} + L_f\dot{\psi})}{\dot{x}^2 - (\frac{E}{2}\dot{\psi})^2} - 2L_r C_{\alpha_r} \frac{\dot{x}(\dot{y} - L_r\dot{\psi})}{\dot{x}^2 - (\frac{E}{2}\dot{\psi})^2} - L_3(\ddot{y} + \dot{x}\dot{\psi}) &= g_3 \end{aligned} \quad (4.9)$$

where  $m_e, g_1, g_2$  and  $g_3$  are given by:

$$\begin{aligned} m_e &= m + 4\frac{I_w}{R_{eff}^2}, \\ g_1 &= \frac{\tau_w}{R_{eff}}, \\ g_2 &= (2C_{\alpha_f} - 2\frac{I_w}{R_{eff}^2}\ddot{x})\delta, \\ g_3 &= L_f g_2 + (-\frac{E}{2}C_{\alpha_f} \frac{E\dot{\psi}(\dot{y} + L_f\dot{\psi})}{\dot{x}^2 - (\frac{E}{2}\dot{\psi})^2})\delta. \end{aligned}$$

The reduced model (4.9) is then used to establish control laws.

The control objective is to cancel the errors between the dynamic variables and their desired values. In other words, we search to design a control such that the desired dynamics become an equilibrium.

When this is achieved,  $\dot{x}, \dot{y}, \dot{\psi}$  and  $\delta$  are given by (using (4.9) and canceling the accelerations  $\ddot{x}, \ddot{y}$  and  $\ddot{\psi}$ ):

$$\begin{aligned} \dot{x} &\triangleq \dot{x}_{eq} = \dot{x}^* \\ \dot{\psi} &\triangleq \dot{\psi}_{eq} = \rho_{ref}\dot{x} \\ \dot{y} &\triangleq \dot{y}_{eq} = L_r \dot{\psi}_{eq} - \frac{mL_f + L_3}{2(L_f + L_r)C_{\alpha_f}} \dot{\psi}_{eq} \dot{x}^2 \\ \delta &\triangleq \delta_{eq} = \frac{(2L_f C_{\alpha_f} - 2L_r C_{\alpha_r})\dot{y}_{eq} + (2L_f^2 C_{\alpha_f} + 2L_r^2 C_{\alpha_r})\dot{\psi}_{eq} - L_3 \dot{x}^2 \dot{\psi}_{eq}}{2L_f C_{\alpha_f} \dot{x}} \end{aligned} \quad (4.10)$$

### 4.3.2 Coupled Controller based on Lyapunov Control Techniques

The objective of our controller is to ensure a robust tracking of the reference trajectory for any time varying maneuvers. The tracking objective is reached by controlling the longitudinal velocity and the lateral displacement of the vehicle in order to track a desired longitudinal speed while canceling the lateral displacement error with respect to a given reference trajectory. The control inputs are the steering wheel angle,  $\delta$ , and the Driving/Braking wheels torque,  $\tau_w$ . (see Fig. 4.1)

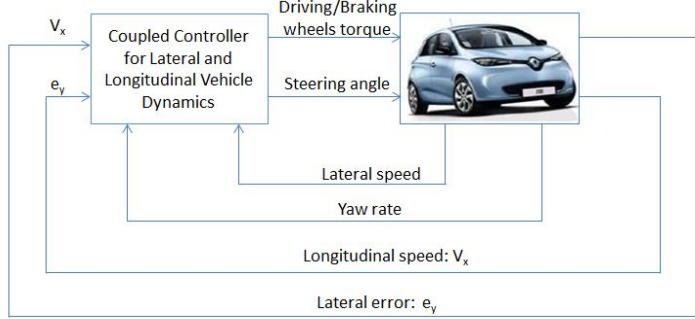


Fig. 4.1: Coupled Controller layout.

To accomplish the control objective, we define two error signals as:

$$s_1 = \dot{e}_y + \lambda_y e_y, \quad \lambda_y > 0 \quad (4.11)$$

$$s_2 = e_{vx} + \lambda_x \int e_{vx}, \quad \lambda_x > 0 \quad (4.12)$$

where  $s_1$  is a function of the lateral displacements error ( $e_y$ ) and its derivative, and  $s_2$  is a function of the vehicle longitudinal speed error  $e_{vx} = \dot{x} - \dot{x}^*$  and its integral.  $\lambda_x$  and  $\lambda_y$  are positive constants. The vectors with superscript (\*) represent desired outputs.

Assuming that the desired lateral acceleration of the vehicle on the reference trajectory can be written as [GTP96]:

$$a_y^* = \dot{x}^2 \rho_{ref}, \quad (4.13)$$

where  $\rho_{ref}$  is the reference trajectory curvature, we have:

$$\ddot{e}_y = a_y - a_y^* = \ddot{y} + \dot{x}\dot{\psi} - \dot{x}^2 \rho_{ref} \quad (4.14)$$

The trajectory tracking is then guaranteed if and only if  $s_1$  and  $s_2$  converge asymptotically to zero. The control objective is then to ensure:

$$\lim_{t \rightarrow +\infty} s_1 = \lim_{t \rightarrow +\infty} \dot{e}_y = \lim_{t \rightarrow +\infty} e_y = 0. \quad \lim_{t \rightarrow +\infty} s_2 = \lim_{t \rightarrow +\infty} e_{vx} = 0, \quad (4.15)$$

We make use of the concept of the control Lyapunov function to deduce the suitable control laws. Indeed, the control strategy proposed in this work provides an algorithm to design in one step a nonlinear controller dealing with both the longitudinal and the lateral dynamics of the vehicle.

We define then a Lyapunov function as:

$$V = \frac{1}{2}s_1^2 + \frac{1}{2}\gamma s_2^2 \quad (4.16)$$

where  $\gamma$  is a positive parameter.

The derivative of this function is given by

$$\dot{V} = s_1\dot{s}_1 + \gamma s_2\dot{s}_2. \quad (4.17)$$

To ensure the convergence of  $s_1$  and  $s_2$ , which guarantees the convergence of  $e_y$ ,  $\dot{e}_y$  and  $e_{vx}$ , we impose a negative variation of  $V$  as:

$$\begin{aligned} \dot{V} &= s_1\dot{s}_1 + \gamma s_2\dot{s}_2 \\ &= -K_{lyy}s_1^2 - \gamma K_{lyx}s_2^2 \end{aligned} \quad (4.18)$$

where  $K_{lyx}$  and  $K_{lyy}$  represent the positive gains of the controller.

The condition (4.18) can be satisfied by taking:

$$s_1\dot{s}_1 = -K_{lyy}s_1^2. \quad (4.19)$$

$$s_2\dot{s}_2 = -K_{lyx}s_2^2. \quad (4.20)$$

which yields:

$$\dot{s}_1 = -K_{lyy}s_1. \quad (4.21)$$

$$\dot{s}_2 = -K_{lyx}s_2. \quad (4.22)$$

Using (4.11) and (4.12), we have:

$$\dot{s}_1 = \ddot{e}_y + \lambda_y\dot{e}_y \quad (4.23)$$

$$\dot{s}_2 = \dot{e}_{vx} + \lambda_x e_{vx} = \ddot{x} - \ddot{x}^* + \lambda_x(\dot{x} - \dot{x}^*) \quad (4.24)$$

Integrating (4.23) and (4.24) into (4.21) and (4.22), we obtain:

$$\ddot{e}_y = -(K_{lyy} + \lambda_y)\dot{e}_y - K_{lyy}\lambda_y e_y. \quad (4.25)$$

$$\ddot{x} = \ddot{x}^* - (K_{lyx} + \lambda_x)e_{vx} - K_{lyx}\lambda_x \int e_{vx}. \quad (4.26)$$

Integrating (4.14) in (4.25) yields:

$$\ddot{y} = \dot{x}^2\rho_{ref} - \dot{x}\dot{\psi} - (K_{lyy} + \lambda_y)\dot{e}_y - K_{lyy}\lambda_y e_y. \quad (4.27)$$

By replacing (4.26) and (4.27) in the reduced system (4.9), we can deduce the longitudinal and the lateral control inputs as follows:

$$\begin{aligned} \tau_w &= R_{eff}[m_e\ddot{x}^* - m_e(K_{lyx} + \lambda_x)e_{vx} - m_eK_{lyx}\lambda_x \int e_{vx} - m\dot{y}\dot{\psi} \\ &\quad + L_3\dot{\psi}^2 + \delta(2C_{\alpha_f}\delta - 2C_{\alpha_f}\frac{\dot{x}(\dot{y} + L_f\dot{\psi})}{\dot{x}^2 - (\frac{E}{2}\dot{\psi})^2}) + F_{aero}] \end{aligned} \quad (4.28)$$

$$\begin{aligned}\delta = & \frac{1}{(2C_{\alpha_f} - 2\frac{I_w}{R_{eff}^2}\ddot{x})} [m\dot{x}^2\rho_{ref} - m(K_{lyy} + \lambda_y)\dot{e}_y - L_3\ddot{\psi} \\ & - mK_{lyy}\lambda_y e_y + 2C_{\alpha_f} \frac{\dot{x}(\dot{y} + L_f\dot{\psi})}{\dot{x}^2 - (\frac{E}{2}\dot{\psi})^2} + 2C_{\alpha_r} \frac{\dot{x}(\dot{y} - L_r\dot{\psi})}{\dot{x}^2 - (\frac{E}{2}\dot{\psi})^2}],\end{aligned}\quad (4.29)$$

**Remark:** In order to improve the controllers robustness with respect to the disturbances and the parameters uncertainties, one can define  $s_1$  as This new control law can be interpreted as a dynamic state feedback plus a PID controller (with adaptive gains depending on the parameters of the system), to ensure the robustness and cancel the effect of uncertainties parametric and disturbances.

To take into account the delay of the actuators, the lateral displacement error is computed at a look-ahead distance  $L_s$  from the center of gravity of the vehicle (see Figure 4.2).  $e_y$  is then replaced by  $e_{y_f}$  in (4.29), where :

$$e_{y_f} = e_y + L_s e_\psi.$$

where  $e_y$  is the lateral displacement error computed at the vehicle's center of gravity and  $e_\psi$  is the yaw angle error with respect to the reference trajectory.

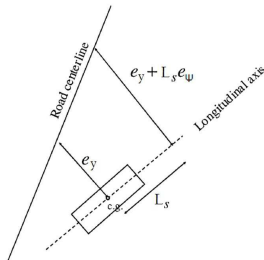


Fig. 4.2: Lateral displacement error computed at a distance  $L_s$  in front of the vehicle

Notice that the computation of the torque takes into consideration the lateral dynamics and the computation of the steering angle includes the longitudinal speed and acceleration values. The lateral and the longitudinal dynamics of the vehicle are controlled simultaneously. In order to validate this controller, we proceed by simulating some real scenarios under Matlab/Simulink and we conduct some robustness tests. Furthermore, experimental tests were accomplished to further validate the developed controller.

#### 4.3.3 Coupled Controller based on an Immersion and Invariance Approach, Combined with Sliding Mode Control

The immersion and invariance approach is a relatively recent method for designing nonlinear and adaptive controllers [AKO07]. This method uses the notions of immersion and invariance to design the controller. Indeed, the idea of this method consists in achieving the control goal by immersing the dynamics of the system in a target dynamic that ensures the desired behavior. This is done by finding a manifold in the state space that can be made invariant and attractive - with an internal dynamics which reflects the dynamics of the closed loop system (see Fig.

4.3). In other words, the Immersion and Invariance (I & I) theory consists of defining a target dynamics and to design a control law that makes the target dynamic attractive and invariant. The advantage of such an approach is to reduce the problem of the controller design into a sub-problem that could be more easily solved.

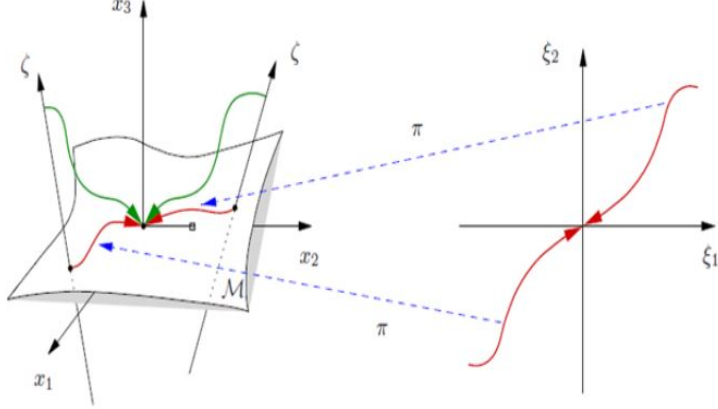


Fig. 4.3: Principle of the Immersion and Invariance control [AKO07].

Using the fact that the lateral dynamics converge faster than the longitudinal dynamics of the vehicle, we define the manifold as the desired dynamics surface of the lateral dynamics, that is  $s_1 = \dot{e}_y + \lambda_y e_y = 0$ .

In order to reach this manifold, the goal is to make converge the "off-the-manifold" variable  $s_1$  to zero. A sliding mode control (SMC) approach is then used to control the "off-the-manifold" variable. The objective is then to define a suitable steering wheel angle that can guide the vehicle to the defined manifold.

The SMC approach has been developed since the 1950s and is recognized as one of the most promising techniques for robust control. The idea is to define a sliding surface that represents the desired dynamic state of the system and then constrain the system in order to reach the sliding surface in a finite time and remain on it (see Fig. 4.4).

The sliding mode control has many advantages:

- Only the measurement of the sliding surface variable in real time is required to design the control law.
- A problem of trajectory tracking for a system of dimension  $n$  is reduced to the stabilization of a first-order system.
- The sliding regime is insensitive to disturbances occurring in the same direction as the control inputs.

However, the discontinuities in the control law can cause a phenomenon of chatter, called, 'chattering'. This is characterized by high frequency oscillations of the trajectories of the system around the sliding surface. This is the main disadvantage of the SMC technique. The chattering can be eliminated by replacing the discontinuous function sign by smooth functions, or by using asymptotically stable observers, or by using higher order sliding mode [BFPU07].

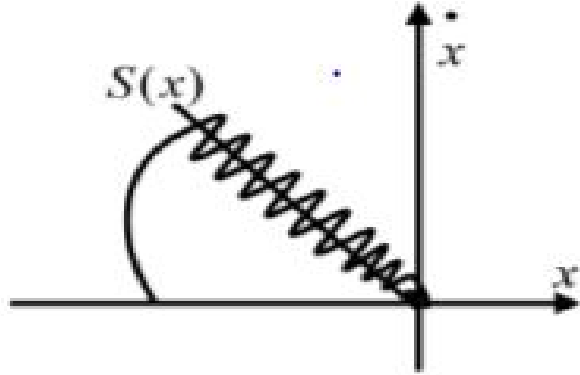


Fig. 4.4: Sliding mode principle.

In this work, we choose to proceed with a higher order sliding mode (second order) based on the super-twisting algorithm. The super-twisting algorithm is developed to control systems with a relative degree 1, and to ensure robust stability while reducing chattering. Consider a system of the form:

$$\dot{x} = f(t, x) + g(t, x)u(t) \quad (4.30)$$

where  $u$  is the control input,  $x \in R^n$  the state vector, and,  $f$  and  $g$  continuous functions. We define a sliding variable  $s$  of relative degree 1, whose derivative can be expressed as follows:

$$\dot{s}(t, s) = \phi(t, s) + \varphi(t, s)u(t) \quad (4.31)$$

The controller aims to ensure the system convergence to the sliding surface defined by  $s = 0$ . It is assumed that there exist positive constants  $s_0$ ,  $b_{min}$ ,  $b_{max}$  and  $C_0$  such that  $\forall x \in R^n$  and  $|s(t, x)| < s_0$ , the system satisfies the following conditions:

$$\begin{cases} |u(t)| \leq U_{max} \\ 0 < b_{min} \leq \varphi(t, s) \leq b_{max} \\ |\phi(t, s)| < C_0 \end{cases} \quad (4.32)$$

The sliding mode control algorithm based on super-twisting is given by:

$$u(t) = u_1 + u_2 \begin{cases} u_1 = -\alpha|s|^{\tau}sign(s), \tau \in ]0, 0.5] \\ \dot{u}_2 = -\beta sign(s) \end{cases} \quad (4.33)$$

with  $\alpha$  and  $\beta$  positive constants. The finite time convergence to the sliding surface is guaranteed by the following conditions[Lev93, Lev98]:

$$\begin{cases} \beta \geq \frac{C_0}{b_{min}} \\ \alpha \geq \sqrt{\frac{4C_0(b_{max}\beta + C_0)}{b_{min}^2(b_{min}\beta - C_0)}} \end{cases} \quad (4.34)$$

To apply this control technique to the vehicle lateral dynamic system, we define the sliding surface by  $s_1$  given by (4.11) as:

$$s_1 = \dot{e}_y + \lambda e_y, \quad \lambda > 0 \quad (4.35)$$

That is:

$$\dot{s}_1 = \ddot{e}_y + \lambda \dot{e}_y \quad (4.36)$$

Using (4.14) and (4.9), we can find:

$$\dot{s}_1 = \frac{1}{m} (L_3 \ddot{\psi} - 2C_{\alpha_f} \frac{\dot{x}(\dot{y} + L_f \dot{\psi})}{\dot{x}^2 - (\frac{E}{2} \dot{\psi})^2} - 2C_{\alpha_r} \frac{\dot{x}(\dot{y} - L_r \dot{\psi})}{\dot{x}^2 - (\frac{E}{2} \dot{\psi})^2} + (2C_{\alpha_f} - 2 \frac{I_w}{R_{eff}^2} \ddot{x}) \delta) - \dot{x}^2 \rho_{ref} + \lambda \dot{e}_y. \quad (4.37)$$

Note that the relative degree ( $\delta \rightarrow s_1$ ) is one. By identification with (4.31), we have:  
 $\dot{s}_1(t, s_1) = \phi(t, s_1) + \varphi(t, s_1) \delta$ , with:

$$\begin{cases} \phi(t, s_1) = \frac{1}{m} (L_3 \ddot{\psi} - 2C_{\alpha_f} \frac{\dot{x}(\dot{y} + L_f \dot{\psi})}{\dot{x}^2 - (\frac{E}{2} \dot{\psi})^2} - 2C_{\alpha_r} \frac{\dot{x}(\dot{y} - L_r \dot{\psi})}{\dot{x}^2 - (\frac{E}{2} \dot{\psi})^2}) - \dot{x}^2 \rho_{ref} + \lambda \dot{e}_y \\ \varphi(t, s_1) = \frac{1}{m} (2C_{\alpha_f} - 2 \frac{I_w}{R_{eff}^2} \ddot{x}) \end{cases} \quad (4.38)$$

Applying the super-twisting theorem, the control input can be defined as follows:

$$u(t) = u_1 + u_2 \begin{cases} u_1 = -\alpha |s_1|^{0.5} sign(s_1) \\ \dot{u}_2 = -\beta sign(s_1) \end{cases} \quad (4.39)$$

Finally, the equivalent control input  $\delta^*$ , corresponding to the steering wheels angle at the equilibrium when  $\dot{s}_1 = 0$ , is added as a feed forward term that approaches the system to the sliding surface [SEFL14]. This term is obtained from (4.37):

$$\delta^* = \frac{1}{m(2C_{\alpha_f} - 2 \frac{I_w}{R_{eff}^2} \ddot{x})} (L_3 \ddot{\psi} - 2C_{\alpha_f} \frac{\dot{x}(\dot{y} + L_f \dot{\psi})}{\dot{x}^2 - (\frac{E}{2} \dot{\psi})^2} - 2C_{\alpha_r} \frac{\dot{x}(\dot{y} - L_r \dot{\psi})}{\dot{x}^2 - (\frac{E}{2} \dot{\psi})^2} - \dot{x}^2 \rho_{ref} + \lambda \dot{e}_y). \quad (4.40)$$

Hence, the steering angle representing the control input of the system is defined as follows:

$$\delta = u_1 + u_2 + \delta^* \quad (4.41)$$

Once the manifold is reached, the stabilisation of the longitudinal dynamics is considered inside the manifold corresponding to  $s_1 = 0$ . This means that, at this level, the lateral dynamic variables have converged to the desired dynamics. In other words,  $\dot{y} = \dot{y}_{eq}$ ,  $\dot{\psi} = \dot{\psi}_{eq}$  and  $\delta = \delta_{eq}$ .

The convergence of the longitudinal dynamics inside the manifold is then assured by the use of a Lyapunov function defined as follows:

$$V = \frac{1}{2} s_2^2. \quad (4.42)$$

The derivative of this function is then:

$$\dot{V} = s_2 \dot{s}_2. \quad (4.43)$$

In order to ensure the convergence of the longitudinal speed, we impose:

$$\begin{aligned} \dot{V} &= s_2 \dot{s}_2 \\ &= -K_{imx} s_2^2 \end{aligned} \quad (4.44)$$

This yields:

$$\begin{aligned}\dot{s}_2 &= -K_{imx}s_2 \\ \dot{e}_{vx} + \lambda_x e_{vx} &= -K_{imx}(e_{vx} + \lambda_x \int e_{vx})\end{aligned}\quad (4.45)$$

Replacing  $e_{vx}$  by  $\dot{x} - \dot{x}^*$ , we obtain:

$$\ddot{x} = \ddot{x}^* - (K_{imx} + \lambda_x)e_{vx} - K_{imx}\lambda_x \int e_{vx} \quad (4.46)$$

Using (4.46) and (4.9) and replacing the lateral variables by their equilibrium states, we deduce the Driving/Braking wheels torque as:

$$\begin{aligned}\tau_w &= R_{eff}[m_e \ddot{x}^* - m_e(K_{imx} + \lambda_x)e_{vx} - m_e K_{imx} \lambda_x \int e_{vx} - m \dot{y}_{eq} \dot{\psi}_{eq} \\ &\quad + L_3 \dot{\psi}_{eq}^2 + \delta_{eq} (2C_{\alpha_f} \delta_{eq} - 2C_{\alpha_f} \frac{\dot{x}(\dot{y}_{eq} + L_f \dot{\psi}_{eq})}{\dot{x}^2 - (\frac{E}{2} \dot{\psi}_{eq})^2}) + F_{aero}]\end{aligned}\quad (4.47)$$

## 4.4 Controllers Validation: Simulation Results

To validate our control laws by simulation, we make use of the real experimental data collected by performing several tests on the vehicle DYNA (Peugeot 308 sw) present in the Heudiasyc laboratory. The tests were conducted on the track CERAM ("Centre d'Essais et de Recherche Automobile de Mortefontaine") shown in Fig. 4.6.

This vehicle is equipped with several sensors (see Fig. 4.5): an Inertial Measurement Unit (IMU) to measure the accelerations ( $x, y, z$ ) and the yaw rate. The CORREVIT for measuring the sideslip angle and longitudinal velocity. Torque hubs for measuring tire-road efforts and vertical loads on each tire. Four laser sensors to measure the height of the chassis. GPS and a CCD camera. Data provided via the CAN bus of the vehicle are also used, as the steering angle, and the rotational speed of the wheels.

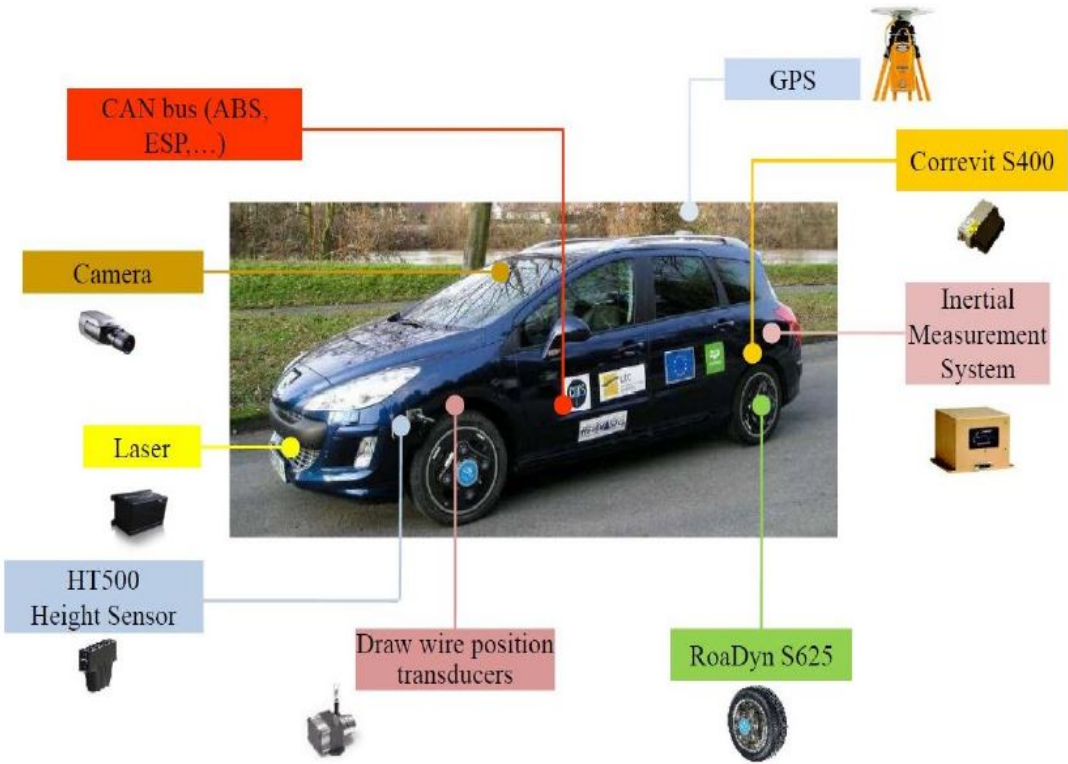


Fig. 4.5: Experimental vehicle DYNA

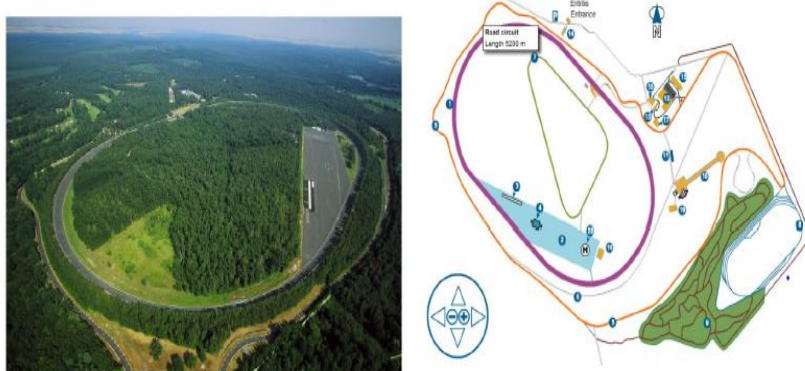


Fig. 4.6: Track CERAM in Mortefontaine, France

The vehicle and the aerodynamic parameters are as follows:

- Chassis parameters:  $m = 1719\text{kg}$ ,  $I_z = 3300\text{kg.m}^2$ .
- Wheel's parameters:  $m_{ij} = 12.2\text{kg}$ ,  $R_{eff} = 0.316\text{m}$ ,  $C_{\sigma_{fl}} = C_{\sigma_{fr}} = 80574\text{N.rad}^{-1}$ ,  $C_{\alpha_f} = 85275\text{N.rad}^{-1}$ ,  $C_{\alpha_r} = 68922\text{N.rad}^{-1}$ ,  $I_w = 1.02\text{kg.m}^2$  (this latter is estimated by assimilating the wheel to a full cylinder with known mass and dimensions)
- Geometric parameters:  $L_f = 1.195\text{m}$ ,  $L_r = 1.513\text{m}$ ,  $E = 1.4\text{m}$
- Aerodynamic parameters:  $s = 2.31\text{m}^2$ ,  $c_d = 0.314$ .

The collected data is considered as reference data that will be compared to those obtained by simulation on Matlab/simulink of the closed-loop system with the developed 4-wheels vehicle model and the developed controllers.

Several tests have been done during normal driving conditions (including the scenarios described below), and showed that the controlled vehicle is able to track the reference profile with small errors. The controllers robustness have been then studied by executing a strongly nonlinear maneuver and by considering the vehicle parameters uncertainties. Both of the controllers show good performances even in critical driving situations.

For a further evaluation of the proposed controllers, a comparison with a PD/PI based controller has been made. The PD/PI based control laws are as follows:

$$\delta = -K_{dy}\dot{e}_y - K_{py}e_y \quad (4.48)$$

$$\tau_w = -K_{px}e_{vx} - K_{ix}\int e_{vx}; \quad (4.49)$$

Note that the PD/PI controller is sometimes referenced by PID in the figures of this section. The validation and the comparison of the controllers are presented thereafter.

For the control laws, we used the gains  $K_{lyx} = 1$ ,  $K_{lyy} = 8$ ,  $K_{imx} = 1$ ,  $\alpha = 0.2$ ,  $\beta = 0.0001$ ,  $\lambda_x = 0.001$ ,  $\lambda_y = 8$ ,  $K_{px} = 436$ ,  $K_{ix} = 0.45$ ,  $K_{dy} = 0.7$ ,  $K_{py} = 1$  and  $L_s$  is fixed to  $3m$ .

**Remark 1:** The choice of the controllers gain is done as follows: The range of the controller gains is set due to the vehicle dynamics analyses. We proceed than to tune this gains by simulation under Matlab/Simulink.

**Remark 2:** The results of the comparison between the coupled controllers and the PD/PI controller depends on the controller gains chosen during the test. This means that all the conclusion made in this thesis about this comparison are preliminary and we look forward to enforce our conclusions in the future works by comparing the controllers performances with different gains.

#### 4.4.1 Normal Driving Conditions

##### 4.4.1.1 Scenario 1

We present in Fig. 4.7 to 4.11, a test that validates our controllers during normal driving at high and varying speed and road curvature. The longitudinal desired speed varies between  $18km/h$  and  $90km/h$ . Note that the maximal lateral acceleration is  $5m/s^2$ . In this scenario, the vehicle executes some maneuvers at low speed with large curvature and some at high speed with very low curvature. In other words, the vehicle navigates within a very narrow turn at low speed then it accelerates to reach a high speed on a low curvature road. The results presented in Fig. 4.9 validate both of the developed controllers and show that, using these control laws, the vehicle is able to navigate with the desired speed while staying on the reference trajectory with a very small lateral displacement error. The PD/PI controller also performs well. However, the lateral and the speed errors produced by this controller are larger than those produced by the developed controllers (see Fig. 4.9). In this test, the assumption of small angles is not respected ( $\delta$  reaches about  $20^\circ$ ), and, despite this, the developed controllers show a good performance during these driving conditions. Moreover, we note that the slip ratio reaches an absolute value of around 0.02.

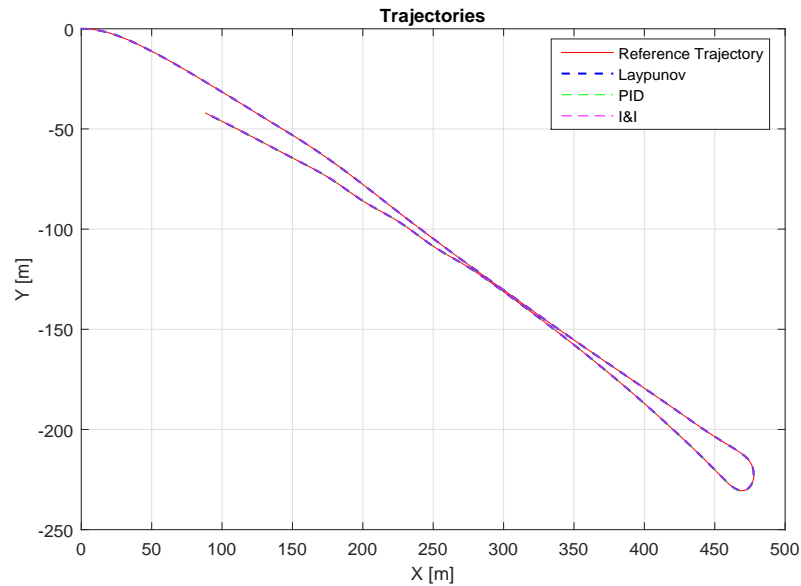


Fig. 4.7: Scenario 1: Reference and vehicle trajectory

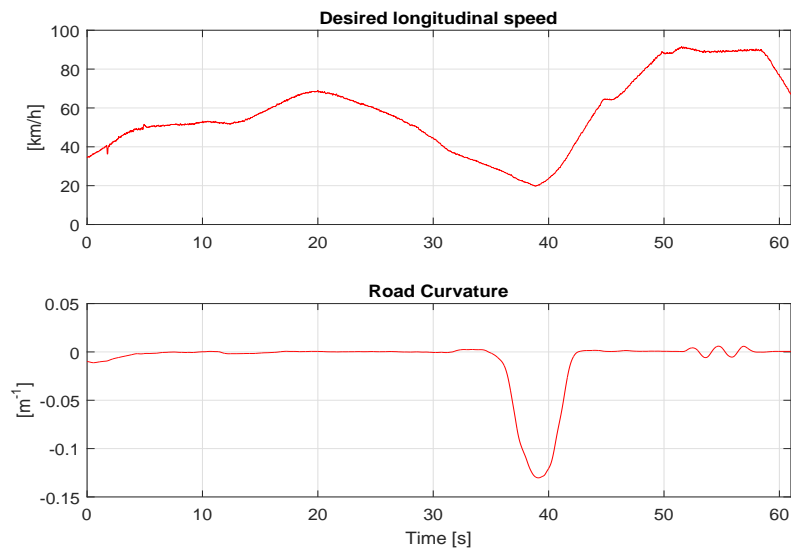


Fig. 4.8: Scenario 1: Desired speed and road curvature.

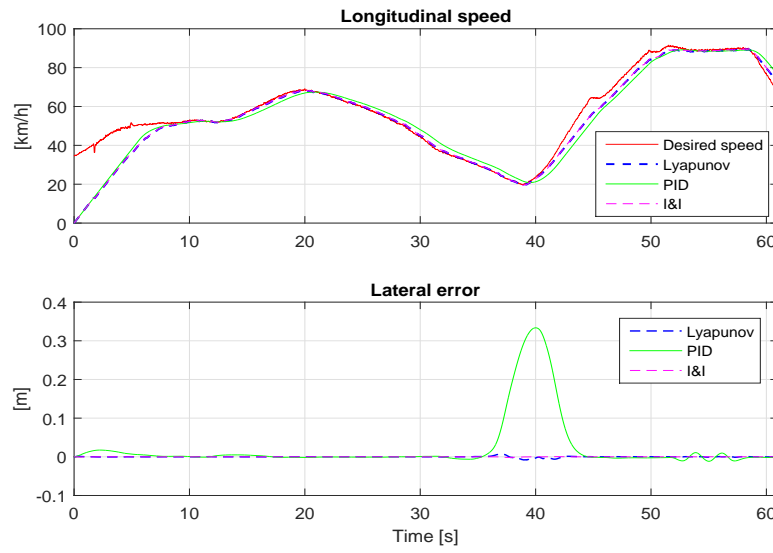


Fig. 4.9: Scenario 1: Longitudinal speed and lateral error.

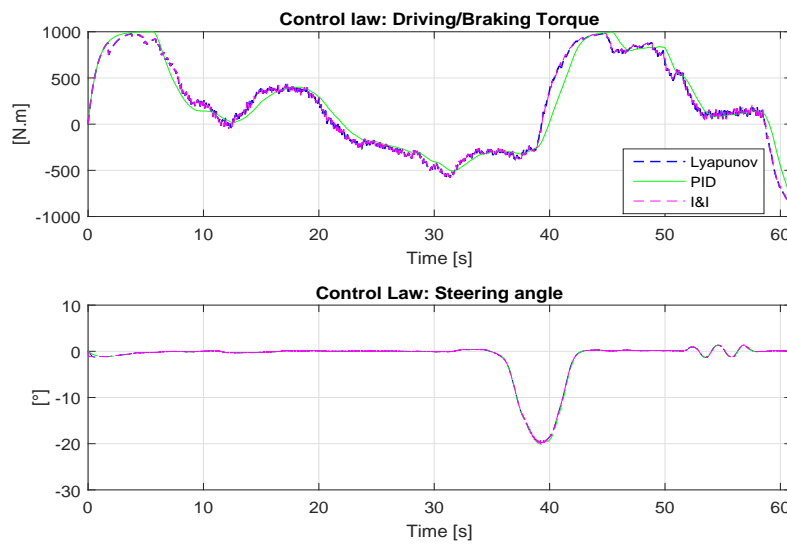


Fig. 4.10: Scenario 1: Control inputs.

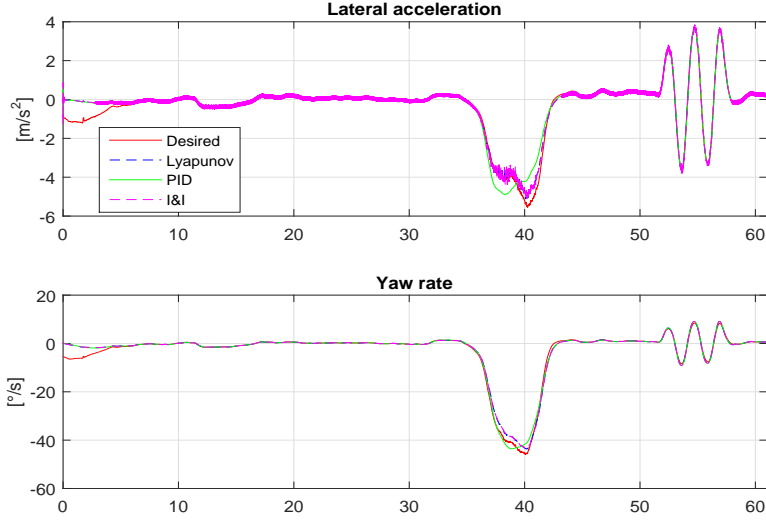


Fig. 4.11: Scenario 1: Lateral variables:  $a_y$  and  $\dot{\psi}$ .

#### 4.4.1.2 Scenario 2

Another scenario used to validate our controllers is presented in Fig. 4.12 to 4.16. In this test, the longitudinal desired speed is almost  $13m/s$  except on the roundabout, where the driver decelerates to reach near  $7m/s$ . The lateral acceleration varies between  $-4m/s^2$  and  $4m/s^2$  almost. Fig. 4.14 shows that the vehicle navigates with the desired speed while tracking the reference trajectory either with the I&I or the Lyapunov or the PD/PI based controllers. The comparison of the lateral acceleration, the yaw rate and the steering angle with the experimental data shows that the controllers execute the desired trajectory profile in a similar way to the vehicle driver. The control laws computed by the controllers are shown in Fig. 4.15. Again, in this normal driving scenario, the Lyapunov and the *I&I* based controls present a lateral and a longitudinal error smaller than that provided by the PD/PI based one.

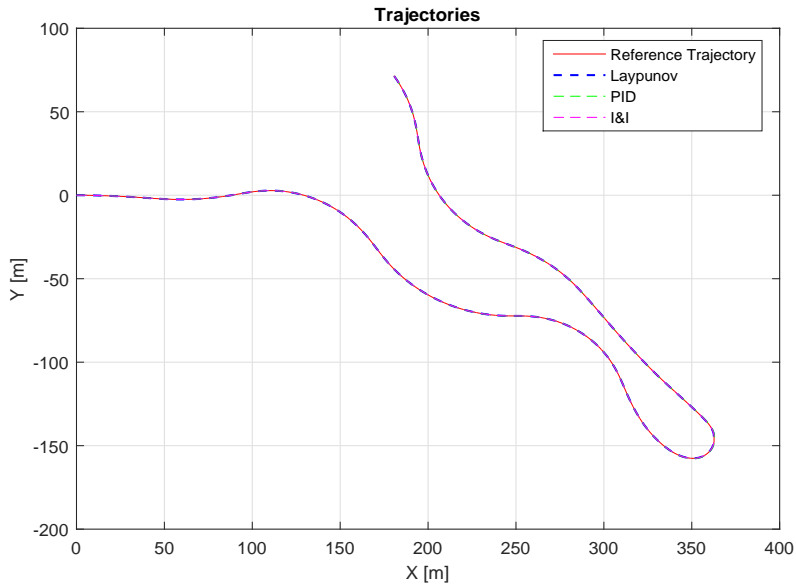


Fig. 4.12: Scenario 2: Reference and vehicle trajectory

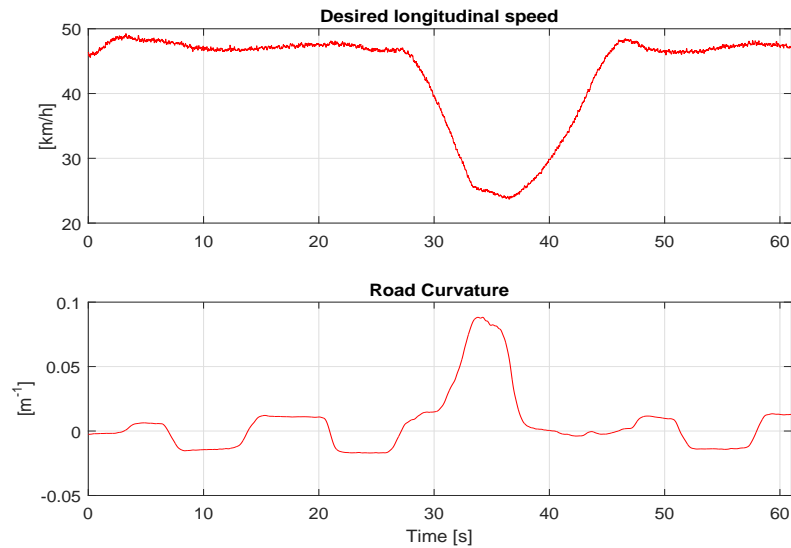


Fig. 4.13: Scenario 2: Desired speed and road curvature.

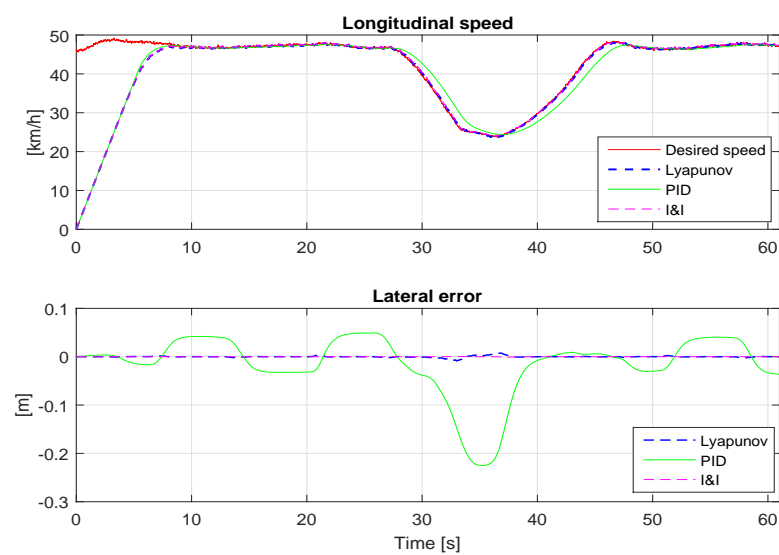


Fig. 4.14: Scenario 2: Longitudinal speed and lateral error.

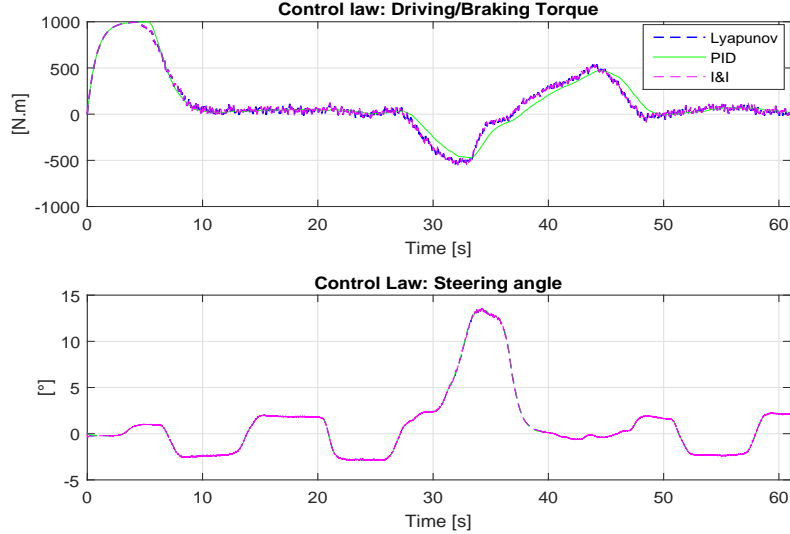


Fig. 4.15: Scenario 2: Control laws.

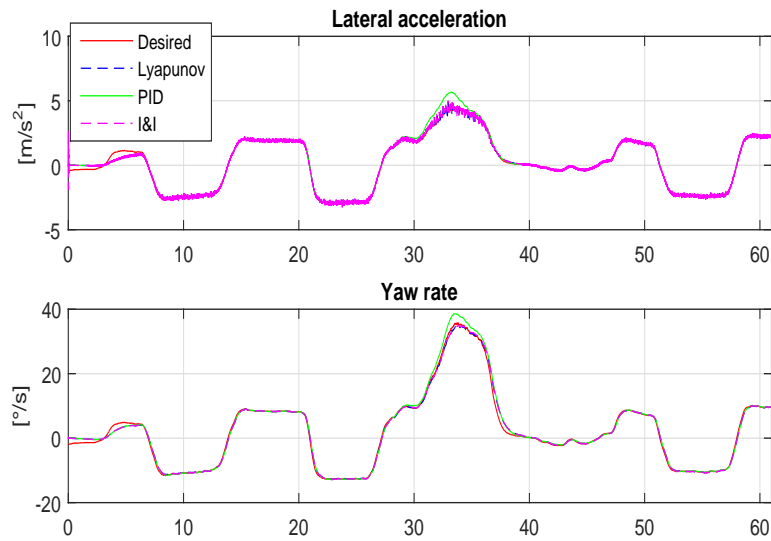


Fig. 4.16: Scenario 2: Lateral variables:  $a_y$  and  $\dot{\psi}$ .

The comparison between the Lyapunov based controller, the Immersion and Invariance controller and the PD/PI controller was done using several scenarios. The performances of these three controllers are similar to what is shown in this section. The results suggest that the proposed coupled controllers (Lyapunov and I & I) are more performant in normal driving conditions than a classical PD/PI controller.

#### 4.4.2 Controller Robustness

The robustness of the controlled system is then tested with respect to strongly nonlinear maneuvers and some uncertainties and disturbances encountered in automotive applications.

#### 4.4.2.1 Scenario 3: Strongly Nonlinear Maneuvers

The test presented in Figures 4.17 to 4.20 shows a highly nonlinear maneuver. It consists of increasing progressively the vehicle speed while executing a J-turn having a radius of about 50m. The reference trajectory is shown in Fig. 4.17 while the desired speed profile and the road curvature are presented in Fig. 4.18. The lateral acceleration and the longitudinal speed are increasing remarkably (the speed is increasing with a rate of  $1m/s^2$  and the lateral acceleration reaches  $7.5m/s^2$ ). This type of test is used to evaluate the stability and the robustness of the controllers against strong nonlinear dynamics. Figure 4.19 shows the speed profile tracking and the lateral error displacement of the three controllers, the Lyapunov based controller, the *I&I* controller and the PD/PI controller. In Figure 4.21, the dynamic variables are compared to those measured in open loop (curves in red). Fig. 4.20 shows the steering wheel angle computed by the controllers with respect to that executed by the driver in open loop, and the Driving/Braking wheels torque.

The PD/PI and the *I&I* controllers present almost the same behavior they have presented in normal driving conditions. The lateral error produced by the *I&I* controller is always very small and smaller than the lateral error produced by the PD/PI controller. However, the Lyapunov based controller performance is decreasing since the lateral error it produced is higher than that produced in normal driving scenarios (it is almost 100 times the lateral error in normal driving scenarios), even if it remains acceptable. By consequence, the *I&I* and the Lyapunov performances are better than that of the PD/PI based controller in critical driving scenarios where the vehicle approaches the limits of stability. However, the Lyapunov based controller performance decreases at the limit of stability. This performance lost can be explained by the simplifications of the vehicle model (see Section 4.3.1). Since the Lyapunov based controller depends on the vehicle model even to regulate the lateral dynamics and the longitudinal dynamics, the vehicle model used to derive its control laws must be very accurate, especially in critical driving situations. However, using a complete vehicle model to derive the control laws of the Lyapunov based controller increases the problem complexity. For example, the assumption of small angles doesn't hold when executing big roundabouts. This assumption violation was tested in scenario 1 but with normal driving conditions. When violating this assumption with high speed, the performance of the controller will be affected. Besides, in order to design our Lyapunov controller, we have modeled the contact forces between the wheels and the ground by a linear model. This model is not valid in critical driving scenarios and should be replaced by a nonlinear model, such as Dugoff's model, piece-wise linear tire model and others. However, the use of a nonlinear tire model renders the derivation of the control laws more complex when using Lyapunov based control.

To conclude, we can claim that the developed controllers have good performances in normal and critical driving situations. In normal driving scenarios as in critical driving scenarios, the coupled controllers, the Lyapunov and the *I&I* based ones, presents better performances than a classical PD/PI controller.

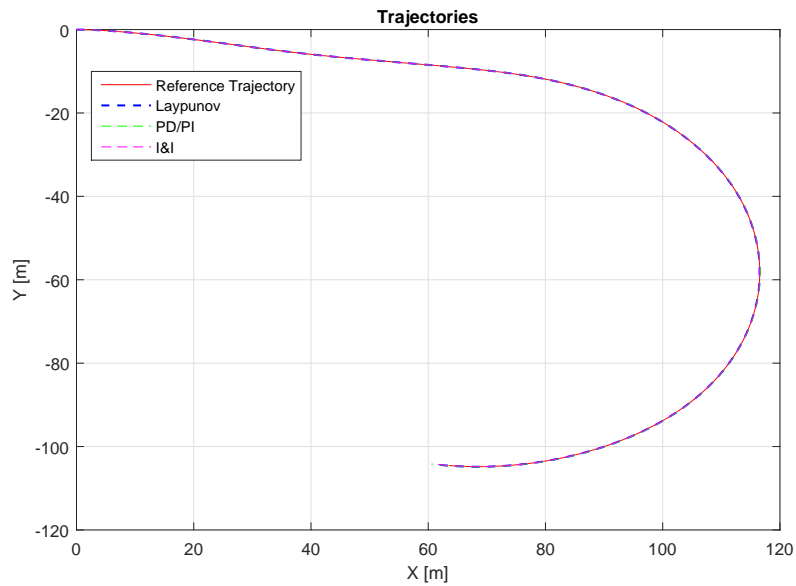


Fig. 4.17: Scenario 3: Reference and vehicle trajectories

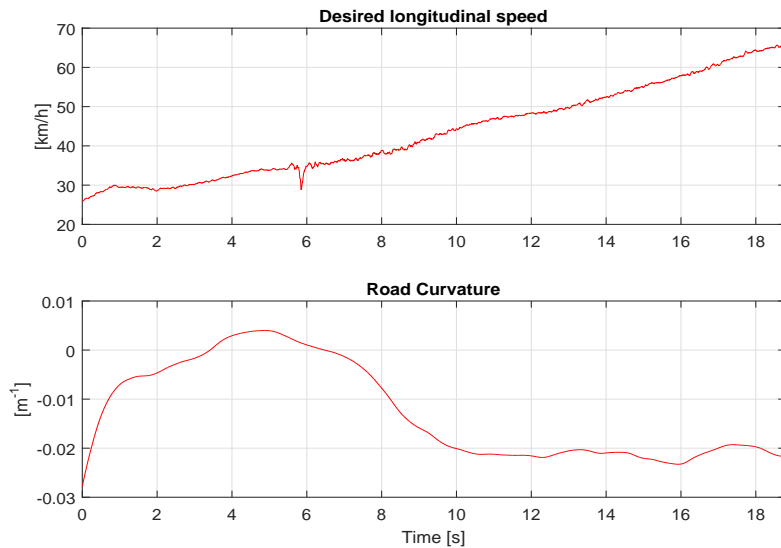


Fig. 4.18: Scenario 3: Desired speed and road curvature.

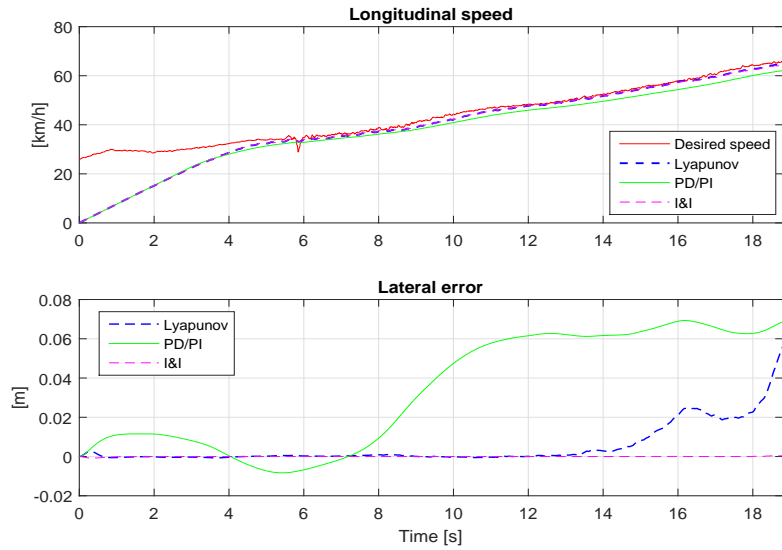


Fig. 4.19: Scenario 3: Longitudinal speed and lateral error.

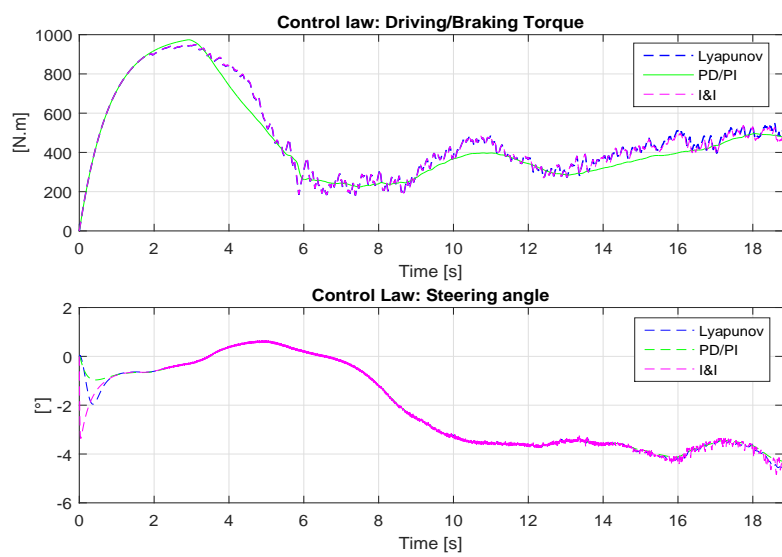


Fig. 4.20: Scenario 3: Control laws.

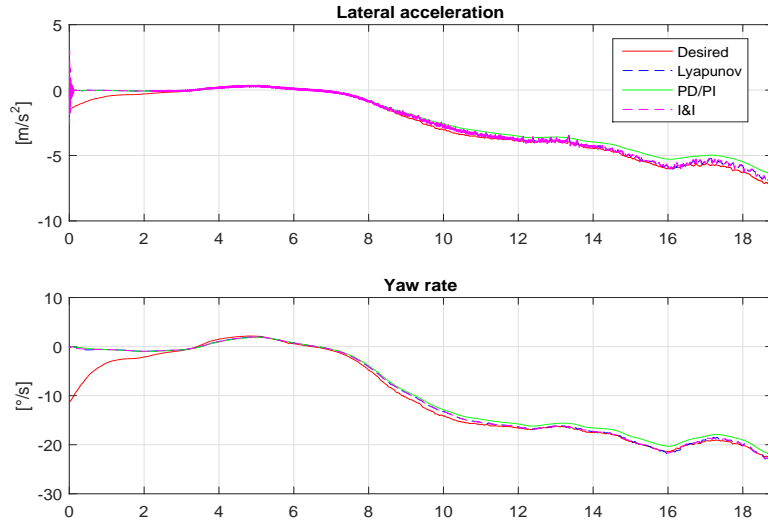


Fig. 4.21: Scenario 3: Lateral variables:  $a_y$  and  $\dot{\psi}$ .

#### 4.4.2.2 Scenario 4: Parameters uncertainties

The robustness of the controllers is evaluated over the vehicle parameters uncertainty, especially the vehicle mass and the cornering stiffness. Indeed, it is difficult to estimate accurately the stiffness of the tire since it is related to the road coefficient of friction, the type of the road, the vertical load, etc. Also, the vehicle mass could be poorly estimated or variable since it is dependent on the passengers and the amount of fuel. The controllers robustness was evaluated for different parameters values. We present in Fig. 4.22, using Scenario 2 (presented in Fig. 4.12), the lateral displacement error and the longitudinal speed regulated by the Lyapunov based controller, the *I&I* based controller and the PD/PI controller for different values of the vehicle mass ( $\pm 30\%$ ).

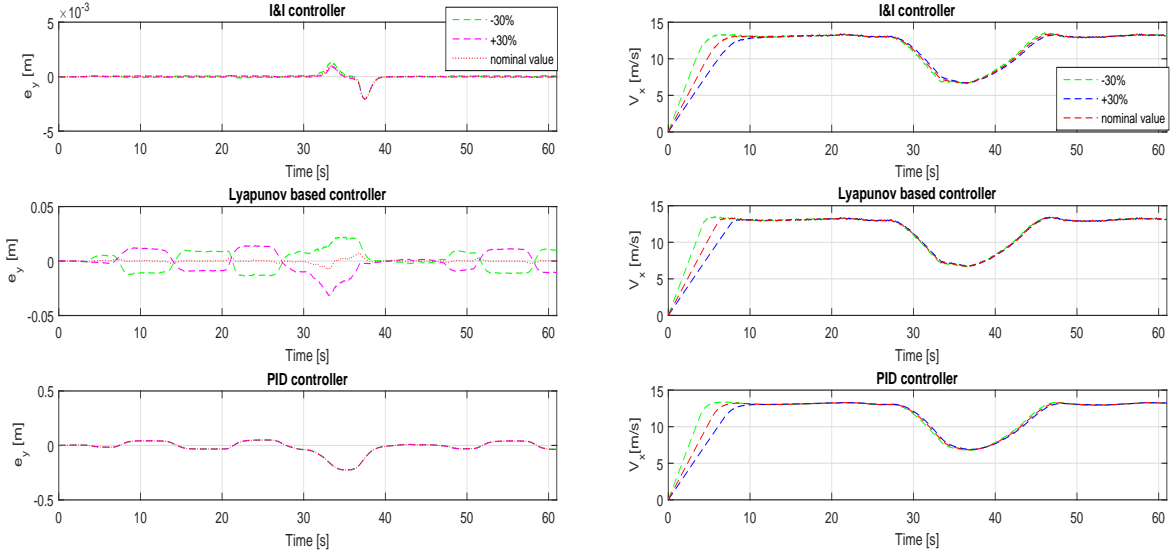


Fig. 4.22: Controllers robustness against uncertainties on the vehicle mass

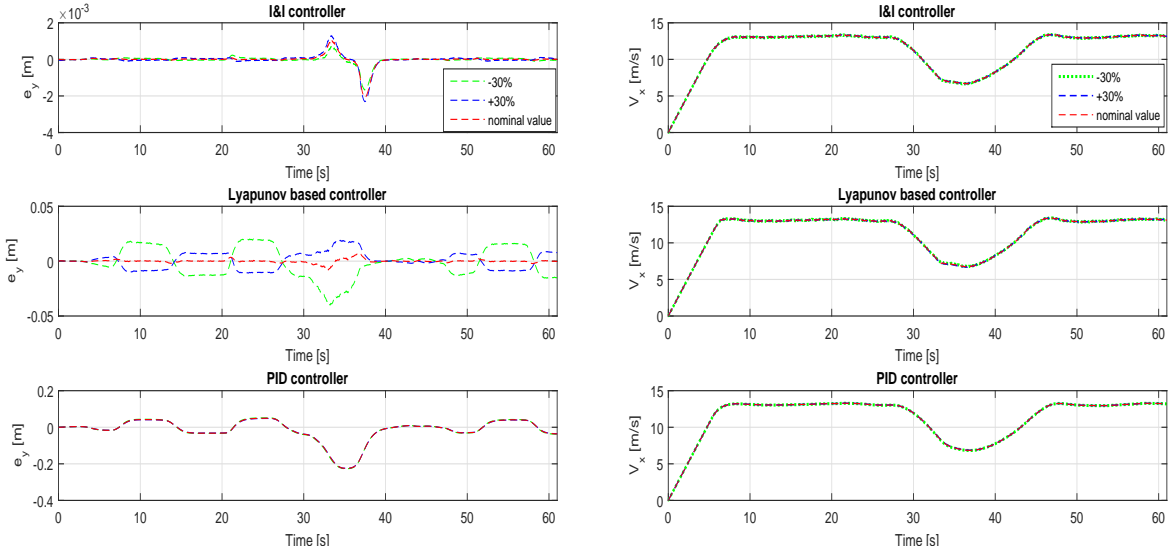


Fig. 4.23: Controllers robustness against uncertainties on the cornering stiffness

Fig. 4.23 shows the variation of the lateral error and the speed in the presence of cornering stiffness uncertainties using the developed controllers and the PD/PI controller.

Regarding the longitudinal speed (Fig. 4.23b) and Fig. 4.22b), we cannot extract important differences in the behavior of the controllers. In fact, only the transitory state of the speed regulation is affected by the mass uncertainties but the three controllers present almost the same behavior. However, the cornering stiffness uncertainties don't really affect the longitudinal speed, regardless of the used controller (the longitudinal speed is almost the same even

with the parameter uncertainties).

Regarding the lateral displacement error in Fig. 4.22a and Fig. 4.23a, some conclusions can be made: The lateral displacement error produced when using the Lyapunov based control increases with a non-null parameters uncertainty but remains acceptable even with a parameter uncertainty of  $\pm 30\%$ . The *I&I* controller is slightly affected by the parameters uncertainties (the maximum lateral error is the most affected value by the parameters variations). And the PD/PI controller is almost not affected by the parameters variations.

In conclusion, both of the developed controllers and the classical PD/PI controller are able to follow the path and the desired speed with acceptable errors despite the parameters variations. However, the Lyapunov based controller is more sensitive to the parameters uncertainties than the *I&I* and the PD/PI controllers.

Note that an analytical study could be conducted to further evaluate the controllers robustness with respect to the parameters uncertainties (We can for example estimate the maximum admissible uncertainties for each controller).

## 4.5 Controllers validation: Experimental Results

### 4.5.1 Presentation of the Experimental Environment

#### 4.5.1.1 Automated vehicle description

The experimental vehicle used to validate the controller is an autonomous vehicle (APACHE) based on ZOE cars from the equipment of the ROBOTEX project (see Fig. 4.24). Indeed, ROBOTEX is a national network of experimental robotic platforms that constitutes "the equipment of excellence" - ( N° ANR-10-EQPX-44-01 ) - funded as a part of future investments.

The APACHE car design presents several navigation modes [XDH<sup>+</sup>17]: manual, cooperative and autonomous. In the manual mode, the driver is in charge of the navigation, no command can be sent to the vehicle. The cooperative mode allows the driver to control at least one subsystem of the vehicle (acceleration, braking or steering) while the rest is done autonomously. The third mode is fully autonomous navigation: the system manages both longitudinal and lateral controls of the vehicle. For safety reasons, any intervention from the driver in the autonomous mode automatically switches the vehicle to the manual mode. Moreover, the vehicle is limited to a maximum speed of 50 km/h while driving autonomously. The automated control of the vehicle is done through a dSpace MicroAutoBox prototyping hardware. It is designed to send commands such as Driving/Braking motor torque and the steering wheel angle through the vehicle CAN bus. The autonomous vehicle is equipped with several sensors, meanwhile, to validate the developed controller, we make use of a Novatel's SPAN-CPT in order to have centimeter accuracy localization data. This system combines a Global Navigation Satellite System (GNSS) and an Inertial Navigation System (INS). In addition to Real Time Kinematic (RTK) corrections, the combined GNSS/INS solution can provide both absolute accuracy and continuity for localization. The SPAN is used with the higher frequency of the Inertial Measurement Unit (IMU), which corresponds to 50 Hz. The system provides information on localization (latitude, longitude, height), velocity (w.r.t. east, north, up directions), acceleration (lateral, longitudinal, vertical), rotation (roll, pitch, azimuth) and rotation rate (roll rate, pitch rate, yaw rates). It also provides the standard deviations of the previously mentioned quantities.

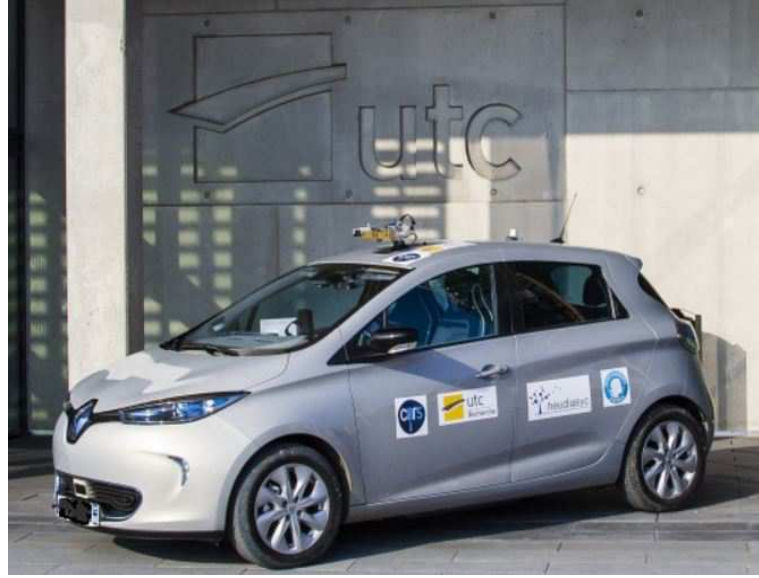


Fig. 4.24: Experimental vehicle: ZOE.

#### 4.5.1.2 Vehicle parameters

To find the parameters of our vehicle ZOE, we have used the Scaner-Studio simulator developed by Oktal. Many vehicles are modeled in this simulator which enables to create different driving scenarios, record necessary data, study the vehicles behavior and many other applications useful for an engineer or a researcher. From the given resources, a vehicle representing the vehicle ZOE is used. The extracted parameters given in the SI units are the following:

- Chassis parameters:  $m = 1456.4\text{kg}$ ,  $I_z = 2400\text{kg.m}^2$ .
- Wheel's parameters:  $m_{ij} = 15\text{kg}$ ,  $R_{eff} = 0.30678\text{m}$ ,  $C_\sigma = 19000\text{N/rad}$ ,  $C_{\alpha_f} = 77349\text{N/rad}$ ,  $C_{\alpha_r} = 77349\text{N/rad}$ ,  $I_w = 1.83\text{kg.m}^2$ .
- Geometric parameters:  $L_f = 1.0847\text{m}$ ,  $L_r = 1.5553\text{m}$ ,  $E = 1.546\text{m}$ .
- Aerodynamic parameters:  $s = 2.22\text{m}^2$ ,  $c_d = 0.333$ .

#### 4.5.1.3 Sending Commands to the ZOE

As mentioned above, the autonomous vehicle ZOE can be controlled via the Driving/Braking motor torque and the steering wheel angle. Contrariwise, our controller sends the Driving/Braking wheels torque and the steering wheel angle that corresponds to the angle between the wheel and the vehicle longitudinal axis.

To do so, we estimated the relation between the motor torque and the torque transmitted to the wheels (front wheels in our case) by measuring these two variables and comparing them. Namely, we had two variables : The torque transmitted to the wheels ( $\tau_w$ ) and the mean effective motor torque ( $\tau_m$ ). The established relation is as follows:

$$\tau_w = 9.3\tau_m - 46.5 \quad (4.50)$$

**Remark 1:** We suppose here that the relation between the motor torque and the wheels torque is linear, while in reality there exists a non linear transmission system between the vehicle engine

and the wheels. A further investigation could be done to study the impact of this assumption on the controllers performance.

**Remark 2:** We can remark that when the vehicle is stopped and the motor torque is null, the wheels torque is negative (-46.5N.m referring to (4.50)). In fact, the wheels torque are also null when the vehicle is stopped since there exists a positive torque of +46.5N.m that compensates the negative one. Indeed, this positive torque is provided by the low level architecture of the vehicle's driveline in order to keep the vehicle driving even with a null motor torque, when the road inclination is not null.

Concerning the relation between the angle of the steering wheel ( $\delta_{sw}$ ) and the real angle of rotation of the wheel with respect to the vehicle direction ( $\delta$ ), we assume that there is a linear relation between these two angles. Referring to the documentation, a ratio of 14.04 exists between these two angles:

$$\delta_{sw} = 14.04 \delta. \quad (4.51)$$

#### 4.5.1.4 Dynamic variables of the controllers

##### 4.5.1.4.1 Lyapunov Based Controller

In this paragraph, we will discuss how the different variables used to compute the control laws of the Lyapunov based controller are measured. For the convenience of the reader, we recall here the control laws:

$$\begin{aligned} \tau_w = R_{eff} [m_e \ddot{x}^* - m_e(K_{lyx} + \lambda_x)e_{vx} - m_e K_{lyx} \lambda_x \int e_{vx} - m \dot{y} \dot{\psi} \\ + L_3 \dot{\psi}^2 + \delta(2C_{\alpha_f} \delta - 2C_{\alpha_f} \frac{\dot{x}(\dot{y} + L_f \dot{\psi})}{\dot{x}^2 - (\frac{E}{2} \dot{\psi})^2}) + F_{aero}] \end{aligned} \quad (4.52)$$

$$\begin{aligned} \delta = \underbrace{\frac{1}{(2C_{\alpha_f} - 2 \frac{I_w}{R_{eff}^2} \ddot{x})}}_N [m \dot{x}^2 \rho_{ref} - m(K_{lyy} + \lambda_y) \dot{e}_y \\ - m K_{lyy} \lambda_y e_y + 2C_{\alpha_f} \frac{\dot{x}(\dot{y} + L_f \dot{\psi})}{\dot{x}^2 - (\frac{E}{2} \dot{\psi})^2} + 2C_{\alpha_r} \frac{\dot{x}(\dot{y} - L_r \dot{\psi})}{\dot{x}^2 - (\frac{E}{2} \dot{\psi})^2}] + \underbrace{\frac{-L_3 \ddot{\psi}}{(2C_{\alpha_f} - 2 \frac{I_w}{R_{eff}^2} \ddot{x})}}_Q, \end{aligned} \quad (4.53)$$

The dynamic variables used to compute the control laws are the following:

- The desired longitudinal acceleration ( $\ddot{x}^*$ ): this variable is computed as the derivative of the desired speed set by the user via the user interface developed in the Pacpus software (Qt creator software).
- The vehicle actual speed ( $\dot{x}$ ): this variable is computed as the mean of the front wheels linear speed that are read by the means of the bus CAN in ZOE.
- The speed error ( $e_{vx}$ ): this is simply the difference between the vehicle actual speed and the required one.

- The steering wheel angle ( $\delta$  at the wheel level): the steering wheel angle ( $\delta_{sw}$ ) is measured by the vehicle sensors. Then, we compute  $\delta$  using (4.51).
- The reference trajectory curvature ( $\rho_{ref}$ ): using the coordinates of the test track provided as the Cartesian coordinates (X, Y) in the local East, North, Up (ENU) frame [TBFIG13], the trajectory curvature is computed offline (the method of evaluation of the curvature is detailed in the next paragraphs). Once online, the localization module returns the vehicle position in the ENU frame and then the curvature of the reference trajectory corresponding to the vehicle position is deduced.
- The lateral error ( $e_y$ ): The lateral error is computed as the minimum distance from the vehicle current position to the reference trajectory. It is computed at a non-null distance in front of the vehicle, computed from the vehicle front axle ( $L_s$ ), which allows us to take into account the lateral actuator delay estimated to 80 ms (The lateral error is negative when the vehicle is on the right side of the trajectory and positive otherwise). Notice that while all the SPAN messages are received with a frequency of 50hz, the bus CAN messages are received either at 50hz or at 100hz. This means that, for the messages received at 100hz one measure over two is used in the computation of the control laws.
- The terms in  $\ddot{x}$  and  $\ddot{\psi}$  were neglected based on the simulations analysis. We present in Fig. 4.25, using the scenario 2 from the normal driving scenarios presented in Section 4.4, the value of the term in  $\ddot{x}$ ,  $N$ , compared to the denominator of (4.53), named  $M$ , where:

$$\begin{aligned} N &= -2 \frac{I_w}{R_{eff}^2} \ddot{x} \\ M &= 2C_{\alpha_f} - 2 \frac{I_w}{R_{eff}^2} \ddot{x} \end{aligned} \quad (4.54)$$

The term  $M$  reaches a value of about  $17.10^4 N$  while the term  $N$  varies between  $-200$  and  $200$  approximately. Obviously, the value of  $N$  is negligible with respect to the value of  $M$ . Fig. 4.26 shows the value of the term in  $\ddot{\psi}$ ,  $Q$ , compared to the value of  $\delta$ , with:

$$Q = \frac{-L_3 \ddot{\psi}}{(2C_{\alpha_f} - 2 \frac{I_w}{R_{eff}^2} \ddot{x})} \quad (4.55)$$

$$R = \delta$$

Meanwhile the term  $R$  reaches a maximum of  $0.25 rad$ , the maximum value of the term  $Q$  is around  $2.10^{-5}$ . Again, we can observe that the value of  $Q$  is negligible with respect to  $R$ .

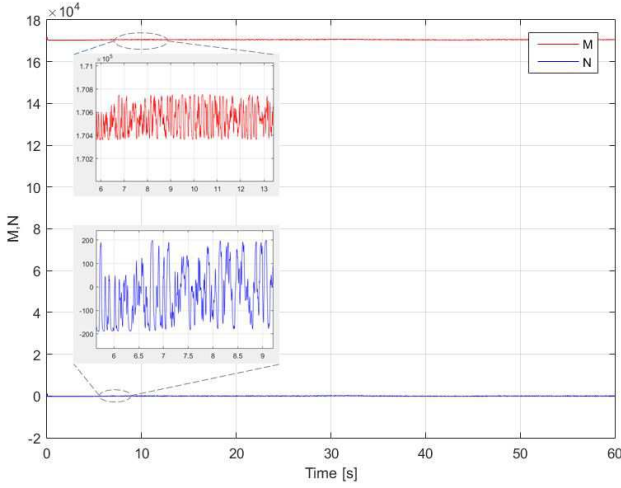


Fig. 4.25: Term in  $\ddot{x}$

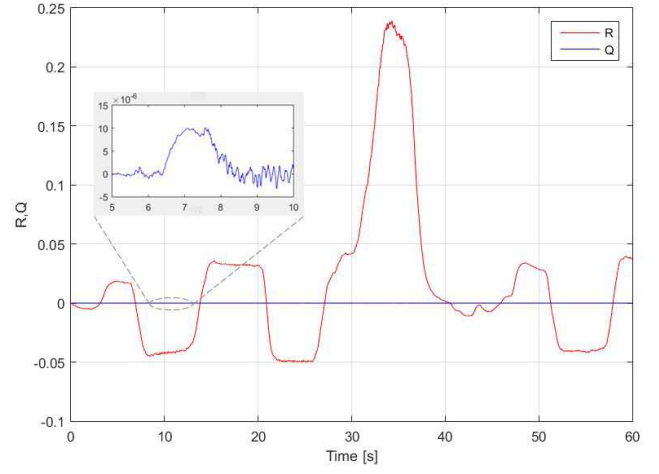


Fig. 4.26: Term in  $\ddot{\psi}$

- The lateral speed in the vehicle frame ( $\dot{y}$ ) and the vehicle yaw rate ( $\dot{\psi}$ ) are estimated by their computed values at the equilibrium from the vehicle model as:

$$\begin{aligned}\dot{\psi}_{eq} &= \rho_{ref} \dot{x} \\ \dot{y}_{eq} &= L_r \dot{\psi}_{eq} - \frac{mL_f + L_3}{(L_f + L_r)C_\alpha} \dot{\psi}_{eq} \dot{x}^2\end{aligned}\quad (4.56)$$

In fact, when replacing  $\dot{y}$  and  $\dot{\psi}$  by  $\dot{y}_{eq}$  and  $\dot{\psi}_{eq}$ , the control input  $\delta$  becomes:

$$\begin{aligned}\delta = \frac{1}{2C_{\alpha_f}} &[m\dot{x}^2\rho_{ref} - m(K_{lyy} + \lambda_y)\dot{e}_y \\ &- mK_{lyy}\lambda_y e_y + 2C_{\alpha_f} \frac{\dot{x}(\dot{y}_{eq} + L_f \dot{\psi}_{eq})}{\dot{x}^2 - (\frac{E}{2}\dot{\psi}_{eq})^2} + 2C_{\alpha_r} \frac{\dot{x}(\dot{y}_{eq} - L_r \dot{\psi}_{eq})}{\dot{x}^2 - (\frac{E}{2}\dot{\psi}_{eq})^2}],\end{aligned}\quad (4.57)$$

In order to study the effects of these changes on the convergence of the lateral error, we derive, using (4.57), the dynamics of  $\dot{s}_1$  as follows:

Using  $\ddot{e}_y = a_y - \dot{x}^2\rho_{ref}$  ((4.14)), (4.57) becomes:

$$\begin{aligned}\delta = \frac{1}{2C_{\alpha_f}} &[ma_y - m\ddot{e}_y - m(K_{lyy} + \lambda_y)\dot{e}_y \\ &- mK_{lyy}\lambda_y e_y + 2C_{\alpha_f} \frac{\dot{x}(\dot{y}_{eq} + L_f \dot{\psi}_{eq})}{\dot{x}^2 - (\frac{E}{2}\dot{\psi}_{eq})^2} + 2C_{\alpha_r} \frac{\dot{x}(\dot{y}_{eq} - L_r \dot{\psi}_{eq})}{\dot{x}^2 - (\frac{E}{2}\dot{\psi}_{eq})^2}],\end{aligned}\quad (4.58)$$

Now, replacing  $a_y$  by its value using the second equation of (4.9), we find:

$$\begin{aligned}\delta = \frac{1}{2C_{\alpha_f}} &[-2C_{\alpha_f} \frac{\dot{x}(\dot{y} + L_f \dot{\psi})}{\dot{x}^2 - (\frac{E}{2}\dot{\psi})^2} - 2C_{\alpha_r} \frac{\dot{x}(\dot{y} - L_r \dot{\psi})}{\dot{x}^2 - (\frac{E}{2}\dot{\psi})^2} + 2C_{\alpha_f} \delta - m\ddot{e}_y - m(K_{lyy} + \lambda_y)\dot{e}_y \\ &- mK_{lyy}\lambda_y e_y + 2C_{\alpha_f} \frac{\dot{x}(\dot{y}_{eq} + L_f \dot{\psi}_{eq})}{\dot{x}^2 - (\frac{E}{2}\dot{\psi}_{eq})^2} + 2C_{\alpha_r} \frac{\dot{x}(\dot{y}_{eq} - L_r \dot{\psi}_{eq})}{\dot{x}^2 - (\frac{E}{2}\dot{\psi}_{eq})^2}],\end{aligned}\quad (4.59)$$

So, by reducing (4.59), and replacing  $\dot{e}_y + \lambda_y e_y$  by  $s_1$ , we find:

$$\dot{s}_1 = \frac{1}{m} \left( 2C_{\alpha_f} \frac{\dot{x}(\dot{y}_{eq} + L_f \dot{\psi}_{eq})}{\dot{x}^2 - (\frac{E}{2} \dot{\psi}_{eq})^2} + 2C_{\alpha_r} \frac{\dot{x}(\dot{y}_{eq} - L_r \dot{\psi}_{eq})}{\dot{x}^2 - (\frac{E}{2} \dot{\psi}_{eq})^2} - 2C_{\alpha_f} \frac{\dot{x}(\dot{y} + L_f \dot{\psi})}{\dot{x}^2 - (\frac{E}{2} \dot{\psi})^2} - 2C_{\alpha_r} \frac{\dot{x}(\dot{y} - L_r \dot{\psi})}{\dot{x}^2 - (\frac{E}{2} \dot{\psi})^2} \right) - K_{lyy} s_1. \quad (4.60)$$

Knowing that  $2C_{\alpha_f} \frac{\dot{x}(\dot{y}_{eq} + L_f \dot{\psi}_{eq})}{\dot{x}^2 - (\frac{E}{2} \dot{\psi}_{eq})^2} = F_{yfl} + F_{yfr}$  and  $2C_{\alpha_r} \frac{\dot{x}(\dot{y}_{eq} - L_r \dot{\psi}_{eq})}{\dot{x}^2 - (\frac{E}{2} \dot{\psi}_{eq})^2} = F_{yrl} + F_{yrr}$ , (4.60) becomes:

$$\dot{s}_1 = \frac{1}{m} [(F_{yfl}^* + F_{yfr}^* - F_{yrl}^* - F_{yrr}^*) - (F_{yfl} + F_{yfr} - F_{yrl} - F_{yrr})] - K_{lyy} s_1, \quad (4.61)$$

where  $F_{yij}^*$  are the equivalent of the lateral forces at the equilibrium point.

At this point, two hypotheses were made:

- The lateral stability is not lost, which means that  $F_{yij}^* - F_{yij}$  is small.
- we assume that  $F_{yij}^* - F_{yij}$  is bounded and converges to zero.

By assuming that, the behavior of  $s_1$  in a neighborhood of the equilibrium can be assimilated to:

$$\dot{s}_1 \simeq -K_{lyy} s_1, \quad (4.62)$$

and this guaranty the convergence of  $s_1$  and by consequence the convergence of  $e_y$  and  $\dot{e}_y$ .

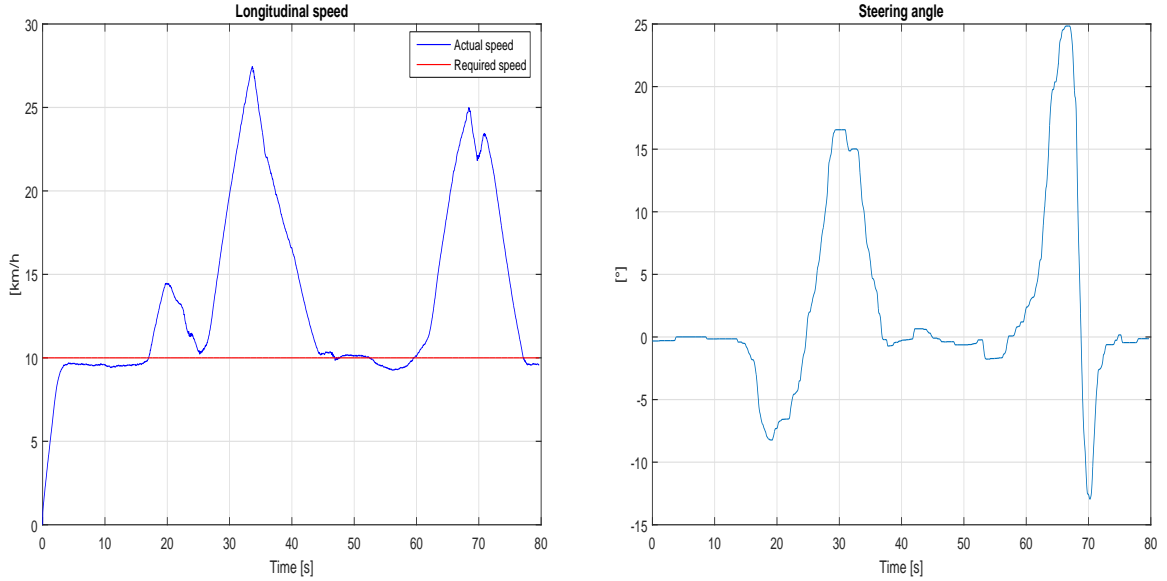
- Using the same assumptions as above, the variables  $\dot{y}$  and  $\dot{\psi}$  were replaced by  $\dot{y}_{eq}$  and  $\dot{\psi}_{eq}$  in the control input  $\tau_w$ .

Besides, after many experiments on the track Seville located near the Heudiasyc laboratory (this track will be presented in the next subsection), we found that the term in  $\delta$  in the control input  $\tau_w$  prevents the convergence of the longitudinal speed towards its desired value.

We present in Fig. 4.27 and Fig. 4.28 two scenarios. In these two scenarios, the steering angle is manual (the human driver in the vehicle is controlling the steering wheel) and the longitudinal speed is controlled using the Lyapunov controller. In the first scenario, Fig. 4.27a presents the speed tracking with a desired speed of 10km/h. Fig. 4.27b presents the steering wheel angle executed by the driver. In this scenario, the control input  $\tau_w$  is:

$$\begin{aligned} \tau_w = R_{eff} & [m_e \ddot{x}^* - m_e (K_{lyx} + \lambda_x) e_{vx} - m_e K_{lyx} \lambda_x \int e_{vx} - m \dot{y} \dot{\psi} \\ & + L_3 \dot{\psi}^2 + \underbrace{\delta (2C_{\alpha_f} \delta - 2C_{\alpha_f} \frac{\dot{x}(\dot{y} + L_f \dot{\psi})}{\dot{x}^2 - (\frac{E}{2} \dot{\psi})^2}) + F_{aero}}_{term \delta}] \end{aligned} \quad (4.63)$$

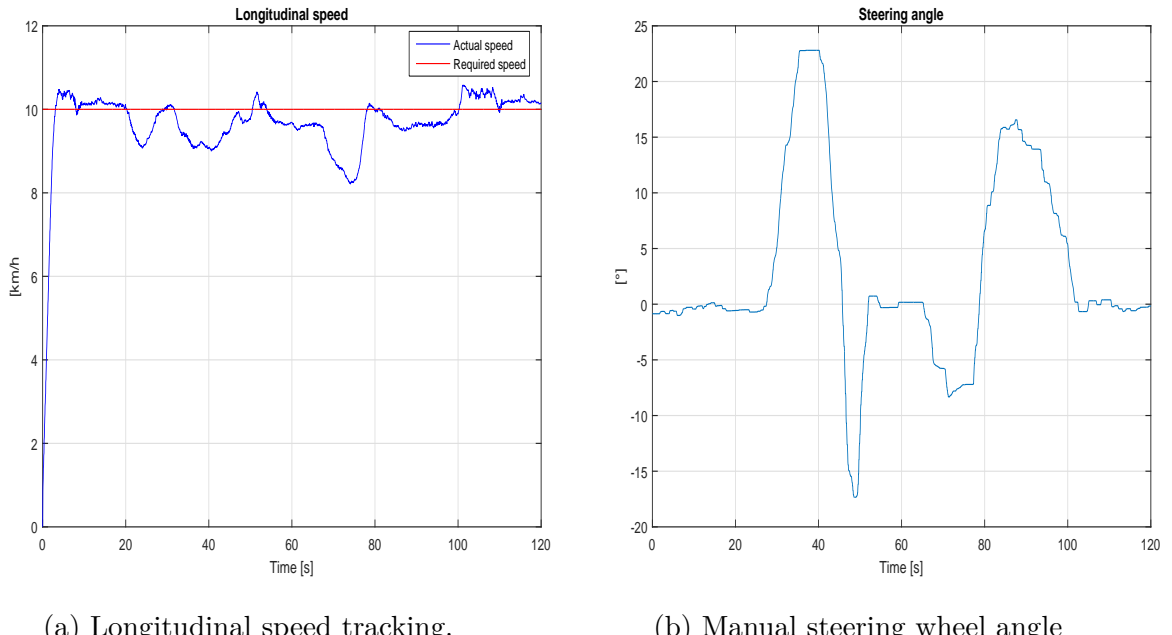
The controller gains are  $K_{lyx} = 1$  and  $\lambda_x = 0$ .



(a) Longitudinal speed tracking.

(b) Manual steering wheel angle

Fig. 4.27: Experimental test: Tracking desired speed of  $10\text{km}/\text{h}$  where the control input  $\tau_w$  contains the term in  $\delta$



(a) Longitudinal speed tracking.

(b) Manual steering wheel angle

Fig. 4.28: Experimental test: Tracking desired speed of  $10\text{km}/\text{h}$  where the control input  $\tau_w$  doesn't contain the term in  $\delta$

As we can observe in Fig. 4.27a, the vehicle speed increases to exceed the desired speed by over than  $15\text{km}/\text{h}$  in the roundabouts when the term in  $\delta$  is included in the computation of the control input  $\tau_w$ . However, in the second scenario presented in Fig. 4.28, the term in  $\delta$  is excluded from the computation of  $\tau_w$ . The result can be seen in Fig. 4.28a: The vehicle speed tracks the desired speed with only some oscillations. Fig. 4.28b shows the steering wheel angle executed by the driver during this test.

The presented tests (Fig. 4.27 and Fig. 4.28) show that there is a problem in the term in  $\delta$  when computing the control input  $\tau_w$ .

In fact, the term in  $\delta$  is:

$$term_\delta = \delta(2C_{\alpha_f}\delta - 2C_{\alpha_f} \frac{\dot{x}(\dot{y} + L_f \dot{\psi})}{\dot{x}^2 - (\frac{E}{2}\dot{\psi})^2}) \quad (4.64)$$

This term is only:

$$term_\delta = (F_{y_{fl}} + F_{y_{fr}})\delta. \quad (4.65)$$

And since the lateral forces are modeled with the linear tire model in the controller design, we have:

$$term_\delta = 2C_{\alpha_f}(\alpha_{fl} + \alpha_{fr})\delta. \quad (4.66)$$

So, the term in  $\delta$  contains an estimation of the sideslip angles  $\alpha_{fl}$  and  $\alpha_{fr}$ . As known in the automotive modeling, the estimation of the sideslip angles at low speed is not accurate. And since, in  $term_\delta$ , the sideslip angles are multiplied by the cornering stiffness which is in the order of  $10^4$ , the less of precision in estimating the sideslip angles leads to big errors in the computation of the control input  $\tau_w$ .

Now, in order to confirm that the problem is really in the estimation of the sideslip angles at low speed, we executed some tests where the desired speed was set to  $15km/h$ ,  $20km/h$  and  $25km/h$  and we computed the control input  $\tau_w$  by keeping the term in  $\delta$ . During all of these tests, the steering wheel is controlled manually. The tests at  $15km/h$  and  $20km/h$  presented the same behavior of the speed tracking but with a smaller error in the roundabouts. The scenario where the desired speed was set to  $25km/h$  shows better results as shown in Fig. 4.29. As can be seen in Fig. 4.29a, the vehicle speed is tracking the desired speed in a good way. This means that the estimation of the sideslip angles at this speed is much better.

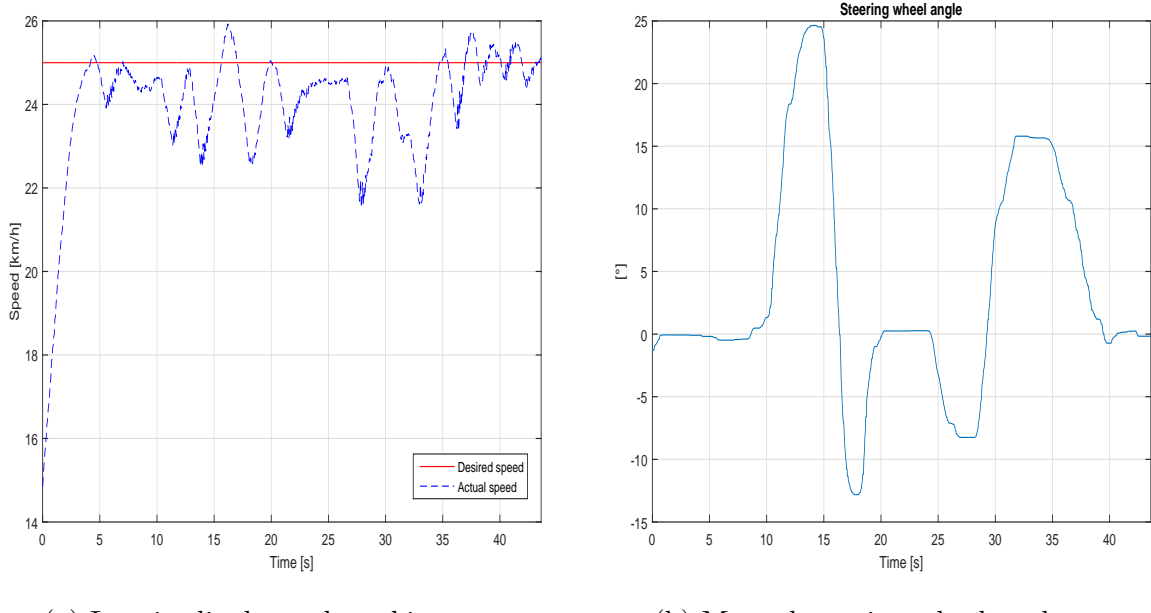


Fig. 4.29: Experimental test: Tracking desired speed of  $25km/h$  where the control input  $\tau_w$  contains the term in  $\delta$ .

Unfortunately, the validation of the Lyapunov controller is done only at  $10\text{km}/\text{h}$  and  $15\text{km}/\text{h}$ . And this is because the experiments were done on the track "Seville" and another track "Technology Park" (presented in the next subsection). The track Seville presents two roundabouts with important curvatures, which constraints the maximum speed of the vehicle in order to maintain the vehicle stability (The test done at  $25\text{km}/\text{h}$  was really on the stability limits but we did it just to prove the reason of the problem of the term in  $\delta$ ). The track "Technology Park" may be a good track to test our controllers at high speeds and this will be a part of the short-term perspectives of the work presented in this thesis.

As a result, since the experimental tests were done under low speeds, we chose to drop the term in  $\delta$  from the computation of the control input  $\tau_w$ .

In order to visualize how much this term is important, some simulations were done under Matlab/Simulink. In these simulations, we present the speed tracking errors when the term in  $\delta$  is included to the computation of  $\tau_w$  and when it's excluded from this computation. Fig. 4.30a shows the speed tracking with and without considering the term in  $\delta$  when the desired speed is  $10\text{km}/\text{h}$ . The steering wheel executed in this test is shown in Fig. 4.30b. Note that here the steering wheel is controlled using the Lyapunov controller. As can be seen, when traversing the roundabouts, the speed error is almost null when considering the term in  $\delta$  in the computation of  $\tau_w$  while it reaches almost  $1.5\text{km}/\text{h}$  when neglecting the term in  $\delta$ . Identically, Fig. 4.31a shows the speed tracking with and without considering the term in  $\delta$  but with a desired speed of  $15\text{km}/\text{h}$ . The steering wheel executed in this test is shown in Fig. 4.31b. Again, we find that the speed error in the roundabouts is almost null when considering the term in  $\delta$  while it's almost  $2.5\text{km}/\text{h}$  when neglecting this term. Consequently, we consider that the speed error of  $2.5\text{km}/\text{h} = 0.69\text{m}/\text{s}$  is not very important and then we decide to neglect the term in  $\delta$  in the experimental tests.

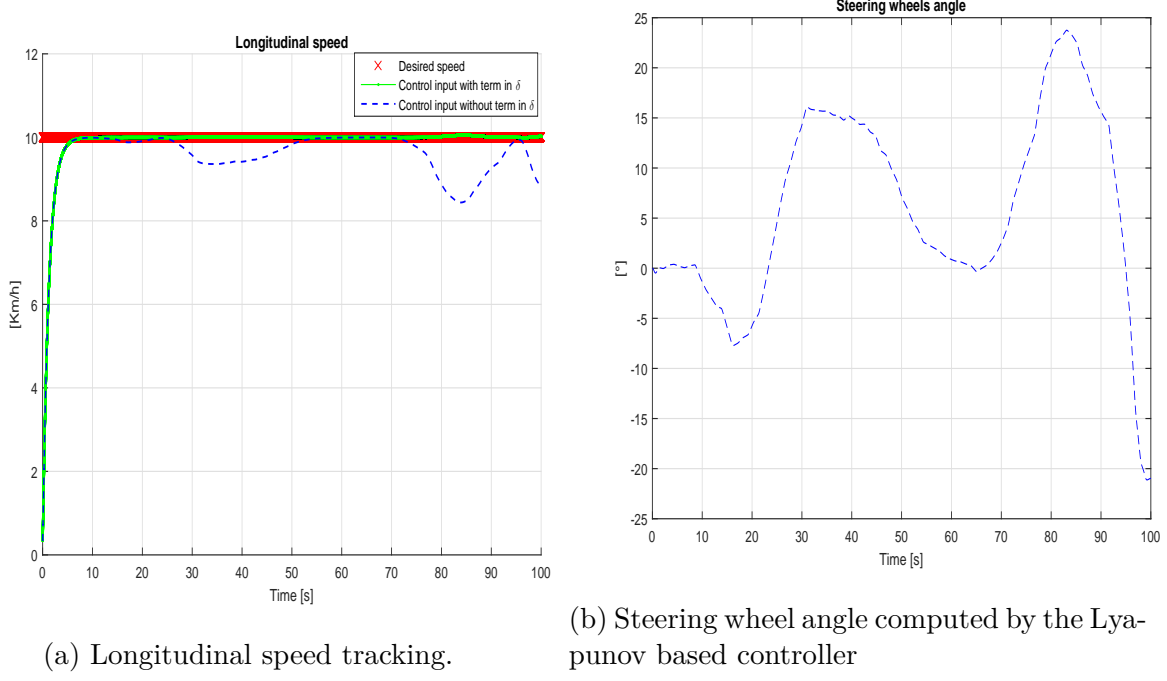


Fig. 4.30: Simulation test: Tracking desired speed of  $10\text{km}/\text{h}$  with and without considering the term in  $\delta$  in the computation of  $\tau_w$

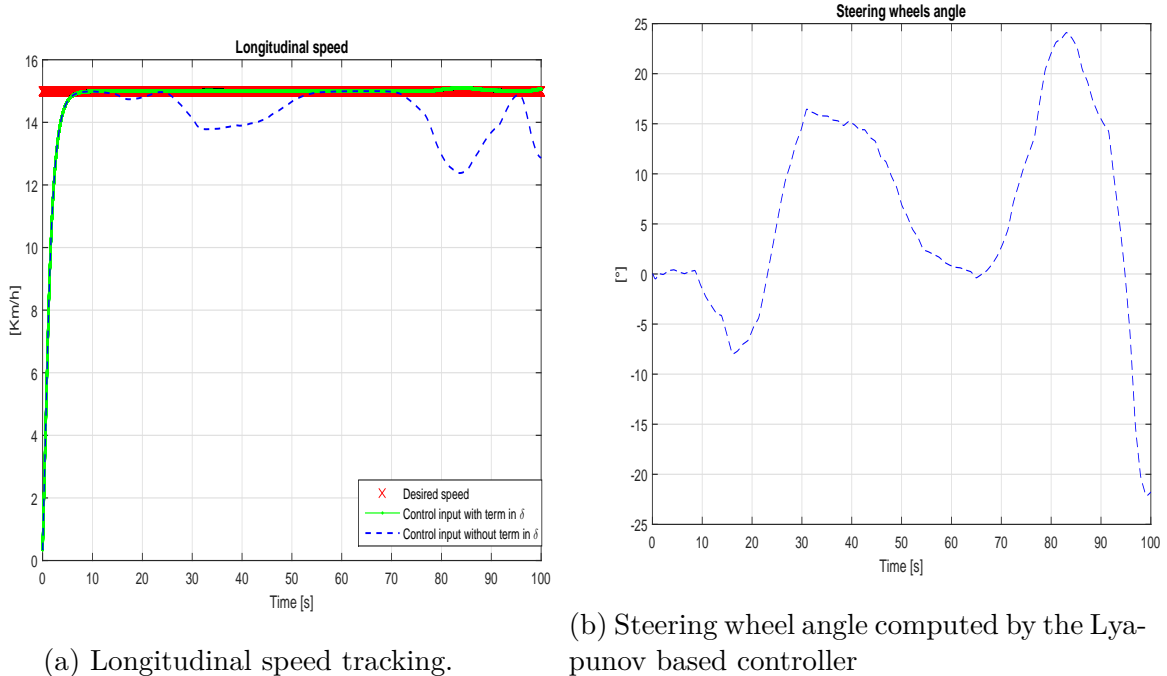


Fig. 4.31: Simulation test: Tracking desired speed of  $15\text{km}/\text{h}$  with and without considering the term in  $\delta$  in the computation of  $\tau_w$

As a result, the control laws used to control the experimental vehicle are as follows:

$$\begin{aligned} \tau_w = R_{eff} &[m_e \ddot{x}^* - m_e (K_{lyx} + \lambda_x) e_{vx} - m_e K_{lyx} \lambda_x \int e_{vx} - m \dot{y}_{eq} \dot{\psi}_{eq} \\ &+ L_3 \dot{\psi}_{eq}^2 + F_{aero}] \end{aligned} \quad (4.67)$$

$$\begin{aligned}\delta = \frac{1}{2C_{\alpha_f}} & [m\dot{x}^2\rho_{ref} - m(K_{lyy} + \lambda_y)\dot{e}_y \\ & - mK_{lyy}\lambda_y e_y + 2C_{\alpha_f} \frac{\dot{x}(\dot{y}_{eq} + L_f\dot{\psi}_{eq})}{\dot{x}^2 - (\frac{E}{2}\dot{\psi}_{eq})^2} + 2C_{\alpha_r} \frac{\dot{x}(\dot{y}_{eq} - L_r\dot{\psi}_{eq})}{\dot{x}^2 - (\frac{E}{2}\dot{\psi}_{eq})^2}],\end{aligned}\quad (4.68)$$

**4.5.1.4.2 Immersion and Invariance Based Controller** We recall here the control inputs computed using the Immersion and Invariance based controller:

$$\begin{aligned}\tau_w = R_{eff} & [m_e\ddot{x}^* - m_e(K_{imx} + \lambda_x)e_{vx} - m_eK_{imx}\lambda_x \int e_{vx} - m\dot{y}_{eq}\dot{\psi}_{eq} \\ & + L_3\dot{\psi}_{eq}^2 + \delta_{eq}(2C_{\alpha_f}\delta_{eq} - 2C_{\alpha_f} \frac{\dot{x}(\dot{y}_{eq} + L_f\dot{\psi}_{eq})}{\dot{x}^2 - (\frac{E}{2}\dot{\psi}_{eq})^2}) + F_{aero}]\end{aligned}\quad (4.69)$$

$$\delta = u_1 + u_2 + \delta^* \quad (4.70)$$

where  $u_1$ ,  $u_2$  and  $\delta^*$  are given by:

$$\begin{aligned}u_1 &= -\alpha|s_1|^{0.5}sign(s_1) \\ \dot{u}_2 &= -\beta sign(s_1)\end{aligned}\quad (4.71)$$

$$\delta^* = \frac{(2L_fC_{\alpha_f} - 2L_rC_{\alpha_r})\dot{y}_{eq} + (2L_f^2C_{\alpha_f} + 2L_r^2C_{\alpha_r})\dot{\psi}_{eq} - L_3\dot{x}^2\dot{\psi}_{eq}}{(2L_fC_{\alpha_f} - 2L_f\frac{I_w}{R_{eff}^2}\ddot{x})\dot{x}} \quad (4.72)$$

In fact, the lateral control needs only the measure of the variable  $s_1$  and the estimation of  $\delta^*$ . The variables required are then  $e_y$ ,  $\dot{e}_y$ ,  $\dot{y}_{eq}$ ,  $\dot{\psi}_{eq}$ ,  $\dot{x}$  and  $\ddot{x}$ . For the longitudinal control, besides the mentioned variables, we need  $\dot{x}^*$  and  $\ddot{x}^*$ . The measure of all these variables are already presented in the previous paragraph.

As explained for the Lyapunov controller, the term in  $\delta$  present in the computation of the Driving/Braking torque  $\tau_w$  will be neglected in the experimental tests executed at low speeds. Therefore the control inputs tested experimentally for the *I&I* controller are as follows:

$$\begin{aligned}\tau_w = R_{eff} & [m_e\ddot{x}^* - m_e(K_{imx} + \lambda_x)e_{vx} - m_eK_{imx}\lambda_x \int e_{vx} - m\dot{y}_{eq}\dot{\psi}_{eq} \\ & + L_3\dot{\psi}_{eq}^2 + F_{aero}]\end{aligned}\quad (4.73)$$

$$\delta = u_1 + u_2 + \delta^* \quad (4.74)$$

where  $u_1$ ,  $u_2$  and  $\delta^*$  are given by (4.85) and (4.86).

## 4.5.2 Results of Validation of the Lyapunov based controller

### 4.5.2.1 Results on the Track Seville

#### 4.5.2.1.1 Presentation of the Track Seville

Seville is a test track located near the Heudiasyc laboratory (see Fig. 4.33). The track curvature is computed using a map of trajectory coordinates (X,Y) provided in the ENU frame. For each point A on the map, we note B and C the next two points. Then, we proceed by searching the point O, which corresponds to the contact point of the mediators of the segments AB and BC

(see Fig.4.32). The trajectory radius at the point A is then set to the norm of the segment OA. Consequently, the trajectory curvature is the inverse of the computed radius. The curvature is then considered positive when a right turn is executed (the yaw angle of the segment BC is smaller than the one of AB) and negative otherwise. The computed curvature of the test track Seville is then filtered using a Mobile Average Filter (MA) of order 5:

$$\rho_n = \frac{1}{\sum_{i=-2}^2 a_i} \sum_{i=-2}^2 a_i \rho_{n+i}, \quad (4.75)$$

where n is the index of the considered trajectory point in the map and the parameters  $a_i$  are set to 1.

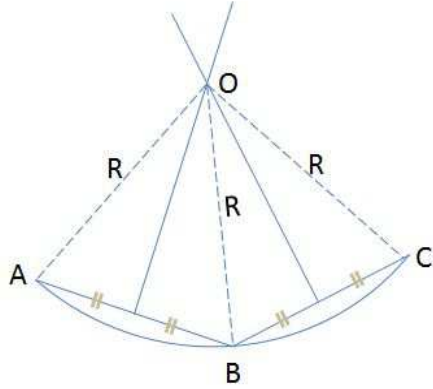


Fig. 4.32: Computing the curvature of an arc using three points from the map.

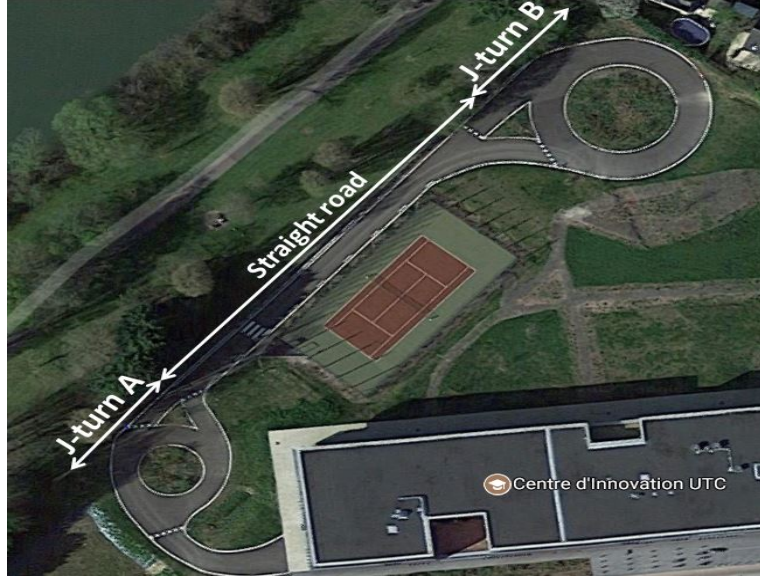


Fig. 4.33: Experimental test track: Seville.

Fig. 4.34 shows the computed curvature of the test track Seville. The curvature reaches  $0.13m^{-1}$  in the J-turn A and  $0.1m^{-1}$  in the J-turn B. Then, when leaving the J-turn A, a curve having a curvature of almost  $0.08m^{-1}$  and an arc length of almost  $25m$  must be tracked.

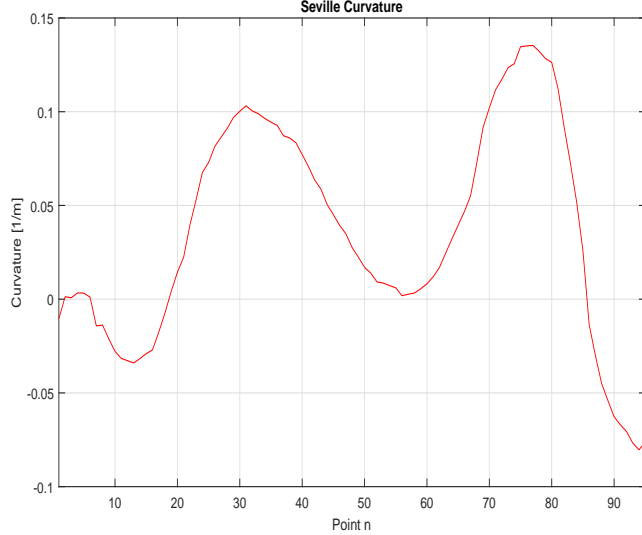


Fig. 4.34: Seville curvature.

#### 4.5.2.1.2 Results of Validation on Seville

We present below two driving scenarios conducted at  $10\text{km}/\text{h}$  and  $15\text{km}/\text{h}$  respectively. The controller gains are set to:  $K_{lyy} = 5$ ,  $\lambda_y = 3.5$  and  $K_{lyx} = 1$ . The parameter  $L_s$  is set to  $3\text{m}$ . This parameter should be adapted to the vehicle speed and the trajectory curvature as follows: When the vehicle speed increases,  $L_s$  should increase. And when the trajectory curvature increases,  $L_s$  should decrease. This adaptation will be a part of our short-term future works. The parameter  $\lambda_x$  is set to zero in this test. Using these parameters (that reflects the integrator in the speed error in the control input  $\tau_w$ ) will also be treated in the future works.

##### Test 1: Navigation on Seville Track with $10\text{km}/\text{h}$

In this scenario, we aim to track the trajectory of Seville with  $10\text{km}/\text{h}$  using the developed Lyapunov based controller for coupled longitudinal and lateral dynamics of the vehicle. The reference trajectory tracking is shown in Fig. 4.37 while the longitudinal speed tracking is shown in Fig. 4.35.

The initial speed of the vehicle is  $0\text{km}/\text{h}$  while the target speed is  $10\text{km}/\text{h}$ . As can be seen, the vehicle tracks the desired speed with a response time of almost  $3\text{s}$ . The speed tracking error in the steady state varies between  $-1.74\text{km}/\text{h}$  and  $0.74\text{km}/\text{h}$ . This error may be reduced by the use of the integrator, by setting  $\lambda_x \neq 0$ . This tuning wasn't done in this work by lack of time. The Driving/Braking wheels torque generated by the Lyapunov based controller is shown in Fig. 4.36. Note that this torque corresponds to the torque on the driving wheels, so each wheel receives half of the torque presented in Fig. 4.36. Note also that this torque is equivalent to  $9.3$  times the motor torque with a bias of  $46.5\text{ N.m}$  (equation (4.50)). This means that the motor torque required to track the desired speed is of  $145.5\text{N.m}$  at  $t = 0$ . This value then decreases to stay smaller than  $28.27\text{N.m}$  in the steady state. Nevertheless, the vehicle ZOE is equipped with a safety system that imposes the maximal motor torque to  $50\text{N.m}$ . This yields that the required motor torque is always saturated by  $50\text{N.m}$ .

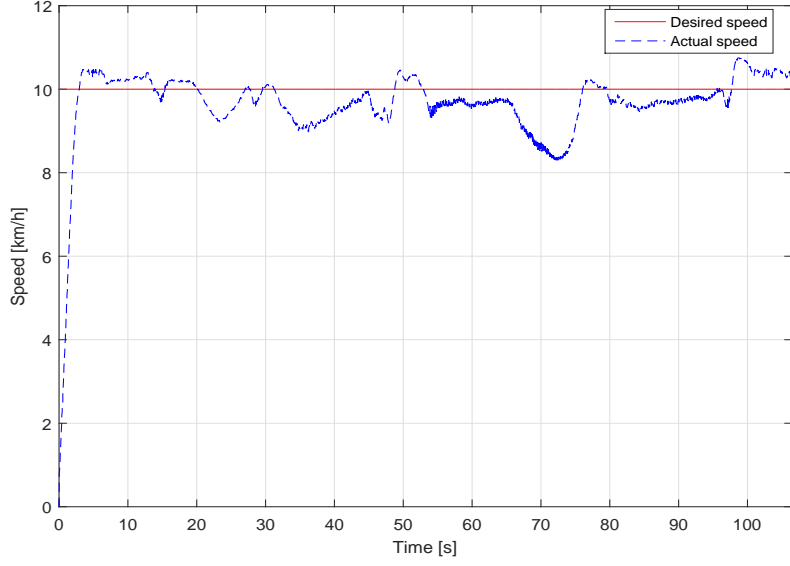


Fig. 4.35: Test 1 on Seville using Lyapunov controller: Desired longitudinal speed tracking.

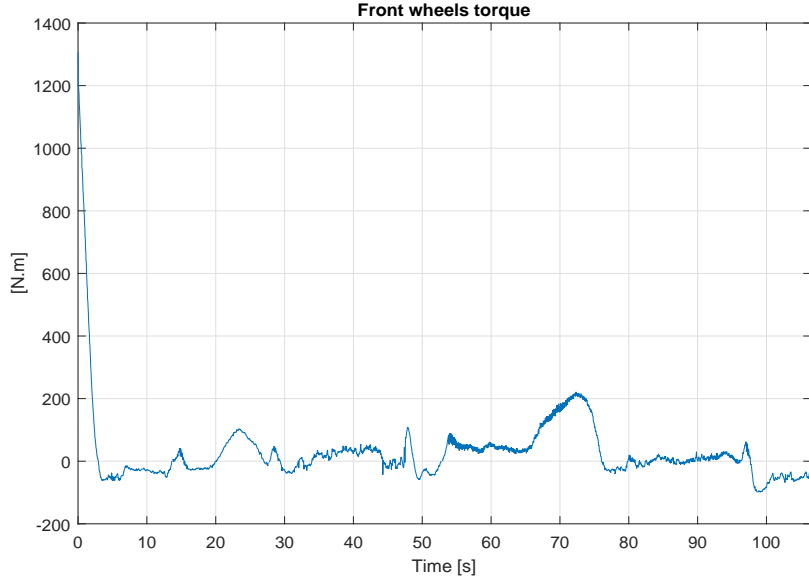


Fig. 4.36: Test 1 on Seville using Lyapunov controller: Front wheels torque.

Besides, Fig. 4.37 shows the vehicle trajectory and the reference trajectory. The corresponding lateral displacement error at the COG of the vehicle is shown in Fig. 4.38 while the steering wheel angle required at the wheel level is shown in Fig. 4.39. As we can observe, the lateral error is greater than  $0.5m$  only when executing the J-turn A (see Fig. 4.33). Actually, the road curvature in the J-turn A is important and when leaving this J-turn a very important curvature is traversed. Besides the road curvature when leaving the J-turn A changes fast from an important value to a null value (when leaving th J-turn A, we traverse a straight road segment). Note also that the map used to compute the road curvatures contains only a few

points in the J-turns. This may cause a lack of accuracy and smoothness when computing the road curvature and this lack can explain the lateral error induced by our controller.

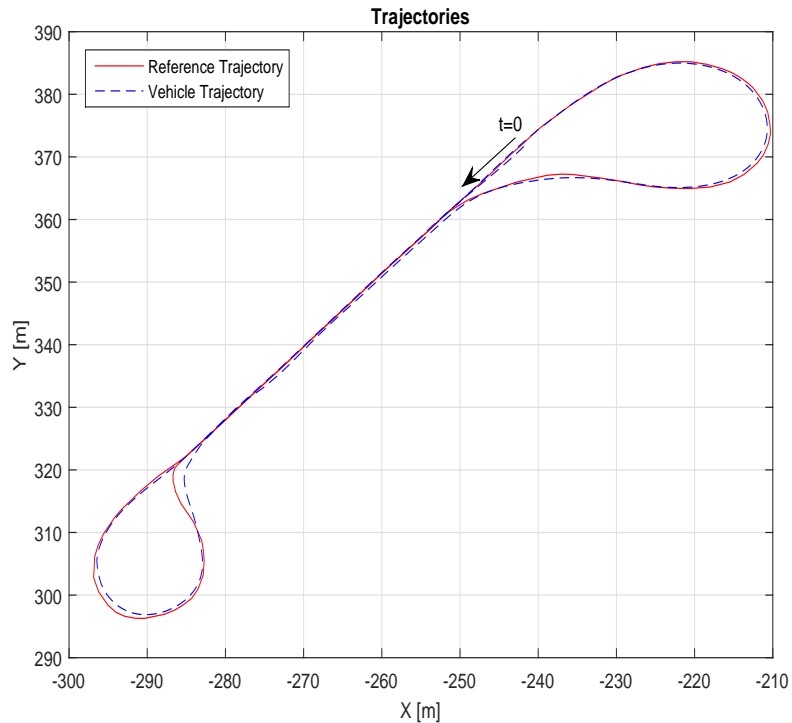


Fig. 4.37: Test 1 on Seville using Lyapunov controller: Reference trajectory tracking.

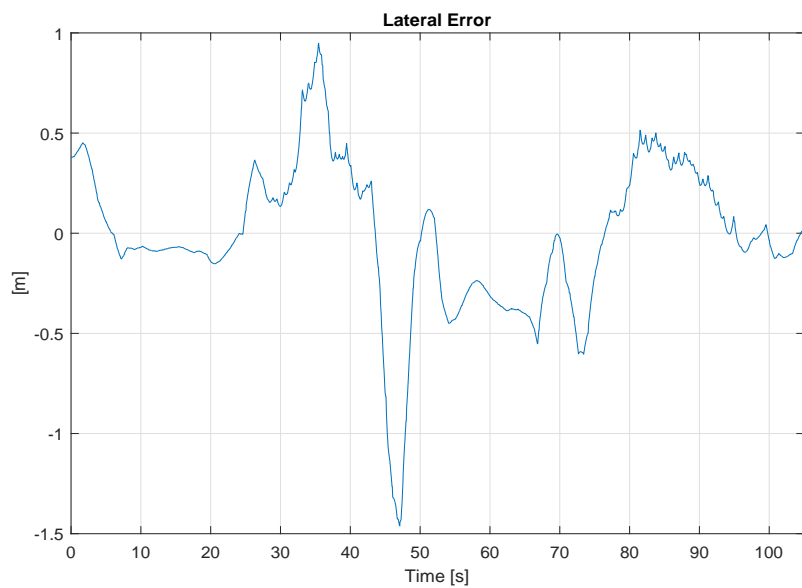


Fig. 4.38: Test 1 on Seville using Lyapunov controller: Lateral displacement error at the COG of the vehicle.

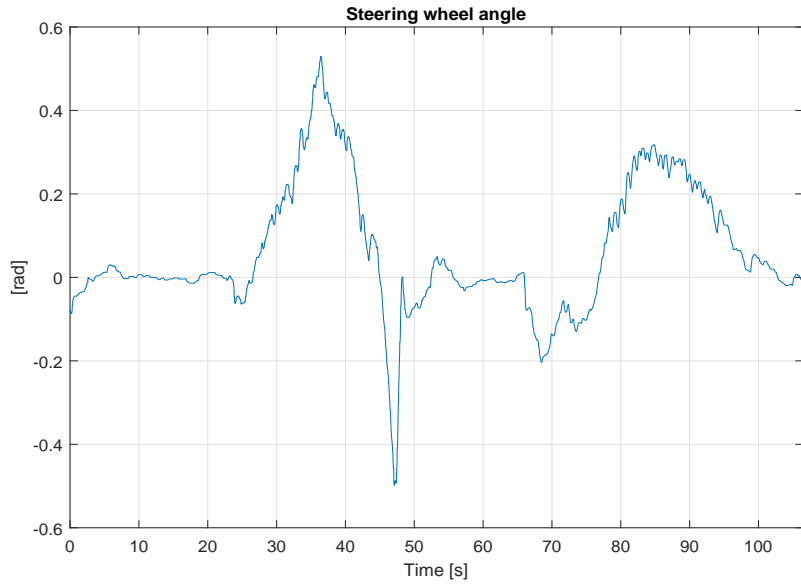


Fig. 4.39: Test 1 on Seville using Lyapunov controller: Steering wheel angle.

### Test 2: Navigation on Seville Track with $15km/h$

This test was also executed on the track Seville but with a desired speed of  $15km/h$ . The same gain controllers defined in the Test 1 are used here. The longitudinal speed tracking is shown in Fig. 4.40. The vehicle speed is initially  $0km/h$ . It then reaches the desired speed within almost  $4.2s$ . The Driving/Braking wheels torque recommended by the Lyapunov controller is shown in Fig. 4.41. Again, we note that the motor torque executed by the vehicle ZOE doesn't exceed  $50N.m$  for safety reasons. At the steady state, the behavior of the vehicle speed is very close to its behavior in the Test 1. The vehicle speed error in the steady state varies between  $-2.24km/h$  and  $0.59km/h$ .

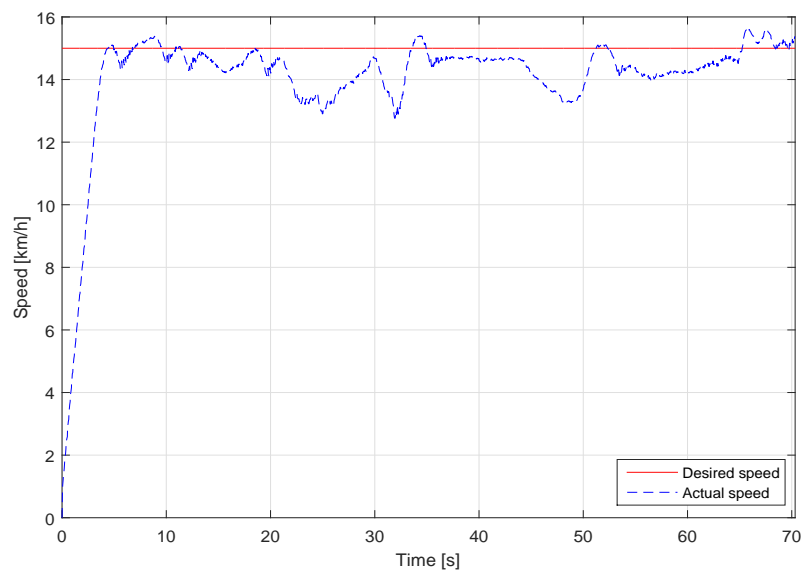


Fig. 4.40: Test 2 on Seville using Lyapunov controller: Desired longitudinal speed tracking.

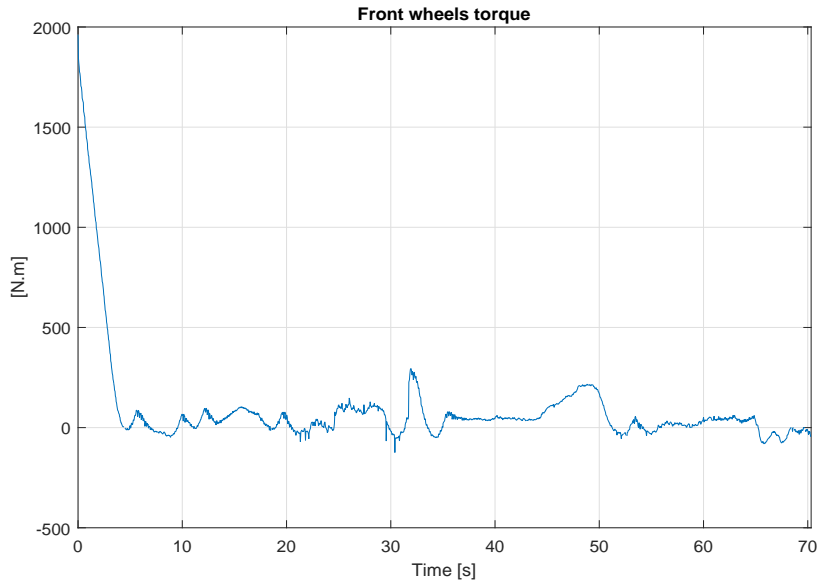


Fig. 4.41: Test 2 on Seville using Lyapunov controller: Front wheels torque.

The reference trajectory tracking is shown in Fig. 4.42. The corresponding lateral error at the COG of the vehicle is shown in Fig. 4.43 while the steering wheel angle commanded by the controller is shown in Fig. 4.44. The behavior of the controller is similar to Test 1. The lateral error exceeds  $0.5m$  only when executing the J-turn A. The steering wheel angle represents some small oscillations and this is caused, as mentioned above, by the lack of smoothness in the used road map.

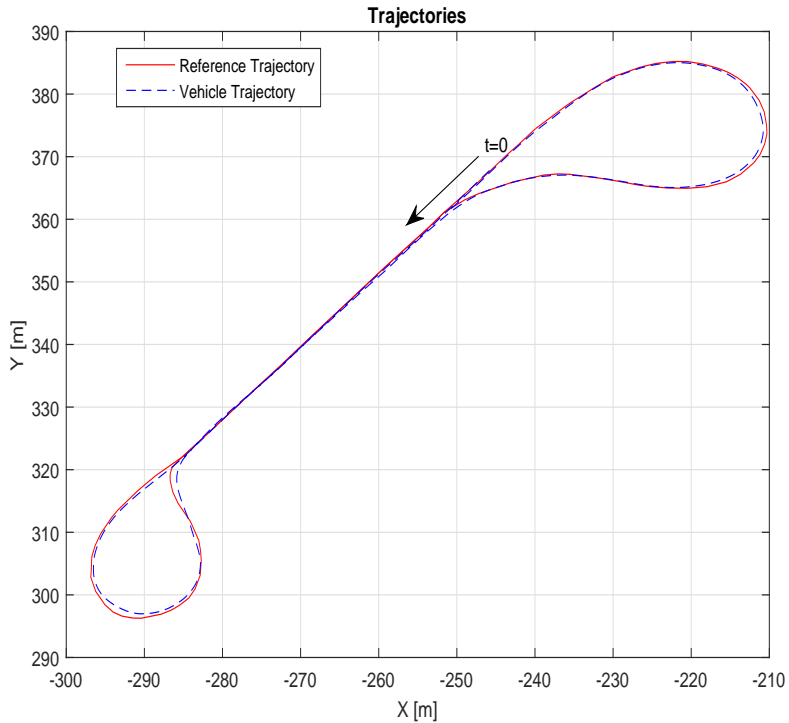


Fig. 4.42: Test 2 on Seville using Lyapunov controller: Reference trajectory tracking.

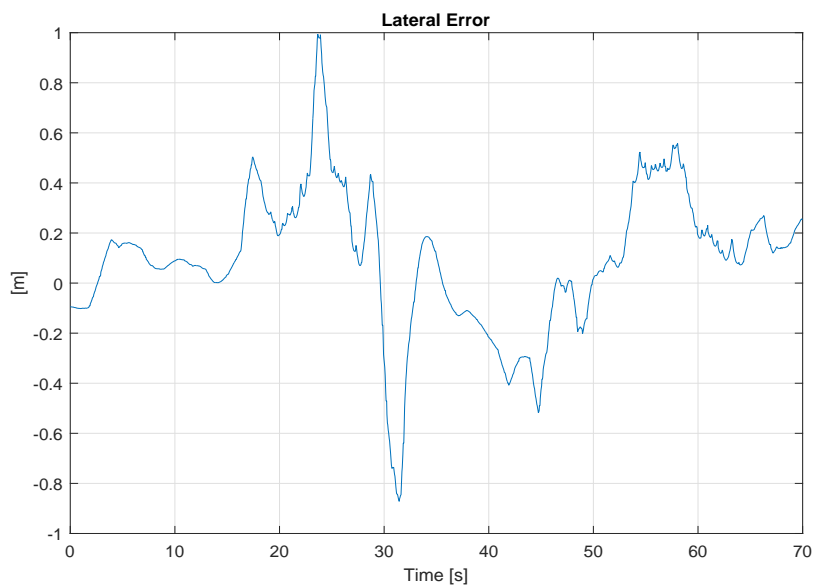


Fig. 4.43: Test 2 on Seville using Lyapunov controller: Lateral displacement error.

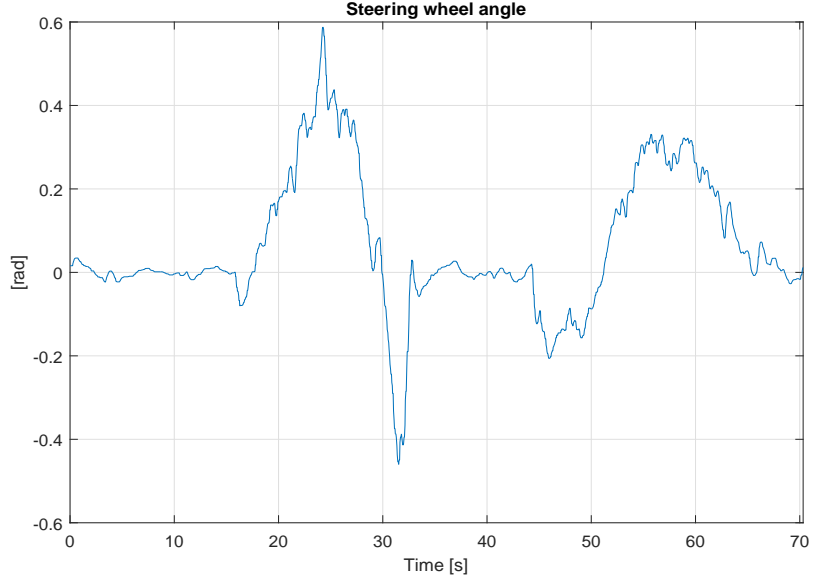


Fig. 4.44: Test 2 on Seville using Lyapunov controller: Steering wheel angle.

However, despite the non null lateral error on the J-turn A, the validation results presented for the above tests are very promising. The controller performance can be improved by using a smoother map of the track Seville and maybe by adapting the term  $L_s$  to the road curvature and the vehicle speed. We can also improve the speed tracking by adding the integral term (by tuning  $\lambda_x$ ) to the computation of the Driving/Braking wheels torque. A better estimation of the term in  $\delta$  will be also implemented and some scenarios validating the controller at high speed will be conducted.

#### 4.5.2.2 Results on the Track Technology Park

##### 4.5.2.2.1 Presentation of the Track Technology Park

The second track used to validate experimentally the Lyapunov based controller is the Technology Park, located in Compiègne (the track marked in red in Fig. 4.45 is used). The objective of using this track was initially to test the controllers performances with relatively high speeds. For the moment, only the Lyapunov based controller was tested using this track with a desired speed reaching  $20\text{km}/\text{h}$ .

The curvature of this track was computed by interpolating the coordinates ( $X, Y$ ) in the round about by a polynomial of order 5 (the curvature of the straight segment is set to zero). Then, an analytical computation of the curvature is conducted using [Cas12]:

$$\rho_{ref} = \frac{\ddot{y}}{(1 + \dot{y}^2)^{3/2}}, \quad (4.76)$$

where  $y = f(x)$  is the polynomial that fits the points ( $X, Y$ ) of the map on a round about. The computed curvature is shown in Fig. 4.46. Note that the curvature reaches a maximum value of about  $0.124\text{m}^{-1}$ .

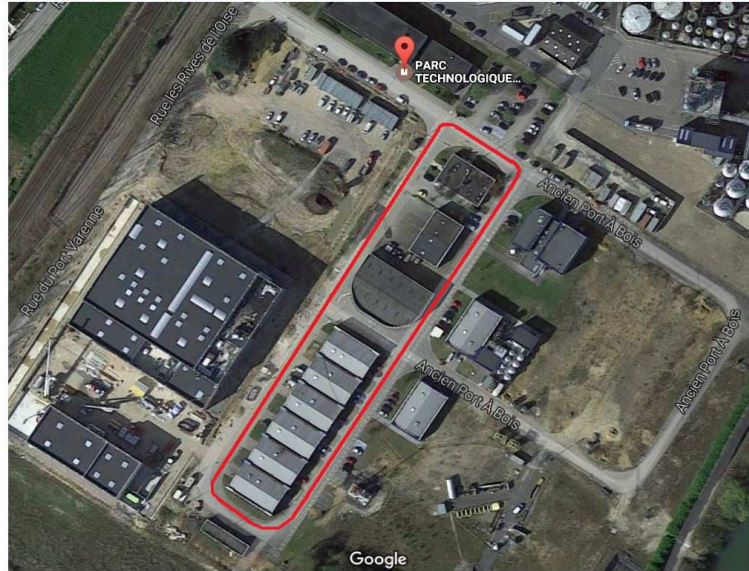


Fig. 4.45: Experimental test track: Technology Park in Compiègne.

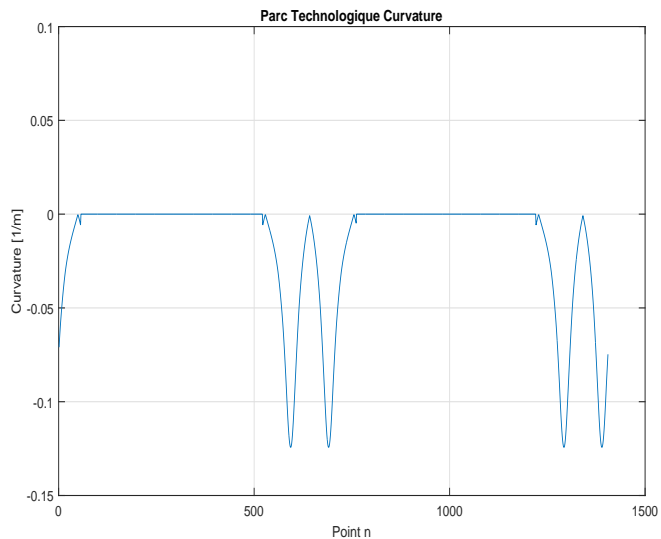


Fig. 4.46: Computed curvature of the test track Technology Park.

#### 4.5.2.2.2 Results of Validation on the Technology Park

The Lyapunov based controller was validated in many driving scenarios (at low speeds). We present below a scenario where the desired speed is 20km/h on the straight segments and decreases to 15km/h in the roundabouts. During this test, the controller gains are set to:  $K_{lyy} = 5$ ,  $\lambda_y = 3.5$  and  $K_{lyx} = 1$ . The parameter  $L_s$  is set to 3m.

The reference trajectory tracking is shown in Fig. 4.47, where we can observe that the vehicle closely tracks the centerline of the road. Note that, at t=0, the lateral displacement error is almost 0.6m. The controller succeeds to cancel this lateral error within a few seconds. Note also that at a given portion of the trajectory shown in Fig. 4.47, the driver had to brake the vehicle manually since the road presents there a bump. The lateral control, however, is always automated. The lateral displacement error with respect to the reference trajectory is shown

in Fig. 4.48 and the steering wheel angle commanded by the controller and executed by the vehicle is shown in Fig 4.49. The lateral error in this scenario is acceptable. Note that, the map used for this track contains sufficient points which make the road curvature smooth and accurate.

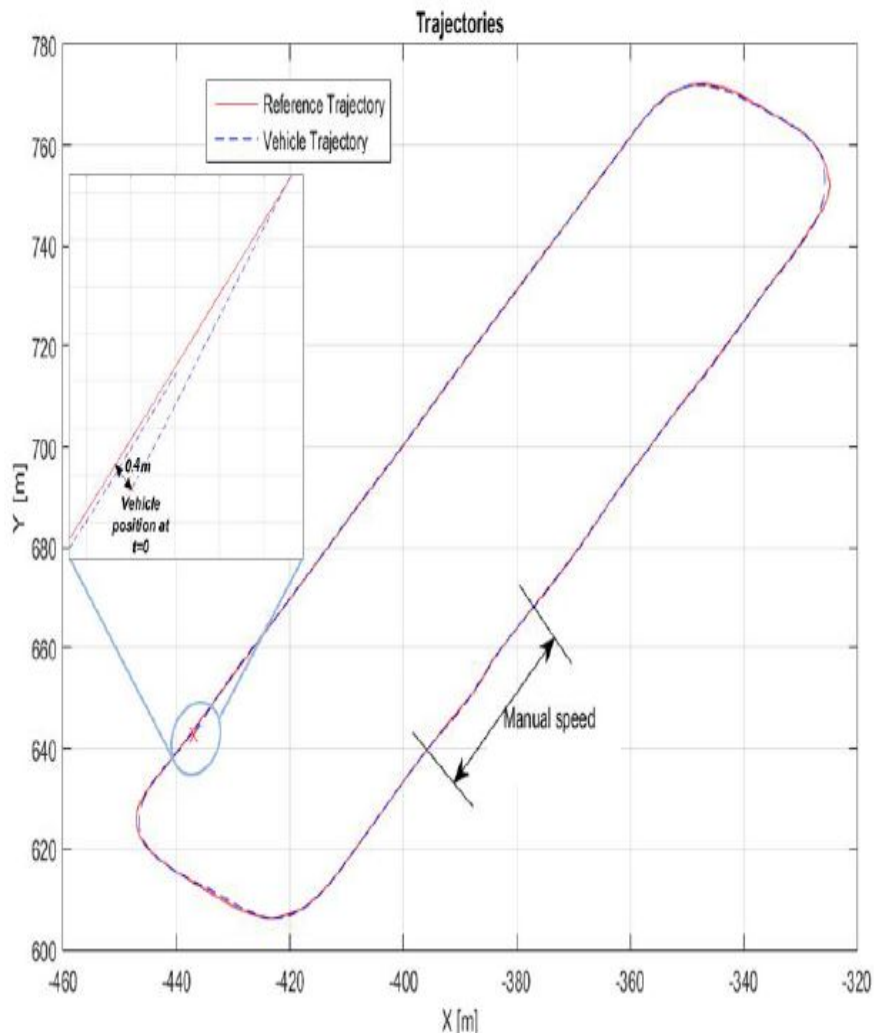


Fig. 4.47: Test on Technology Park using Lyapunov based controller: Reference trajectory tracking.

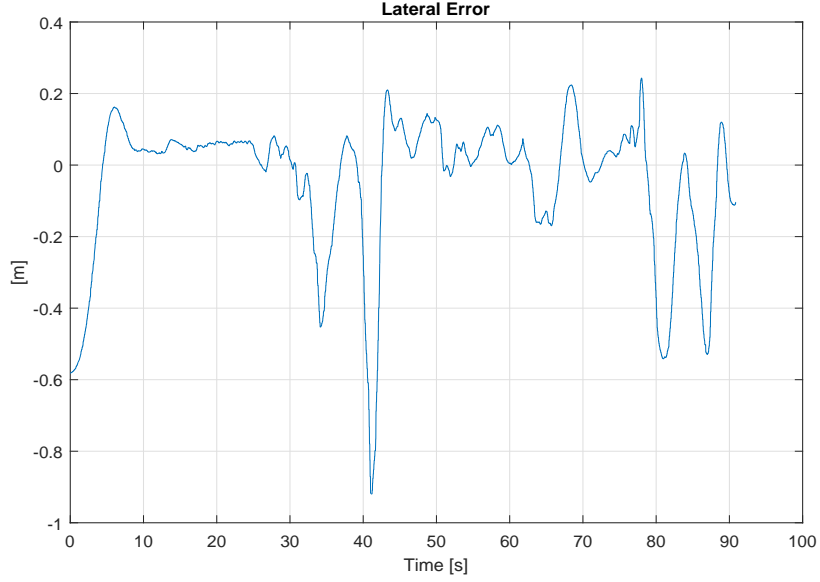


Fig. 4.48: Test on Technology Park using Lyapunov based controller: Lateral displacement error at the vehicle's COG.

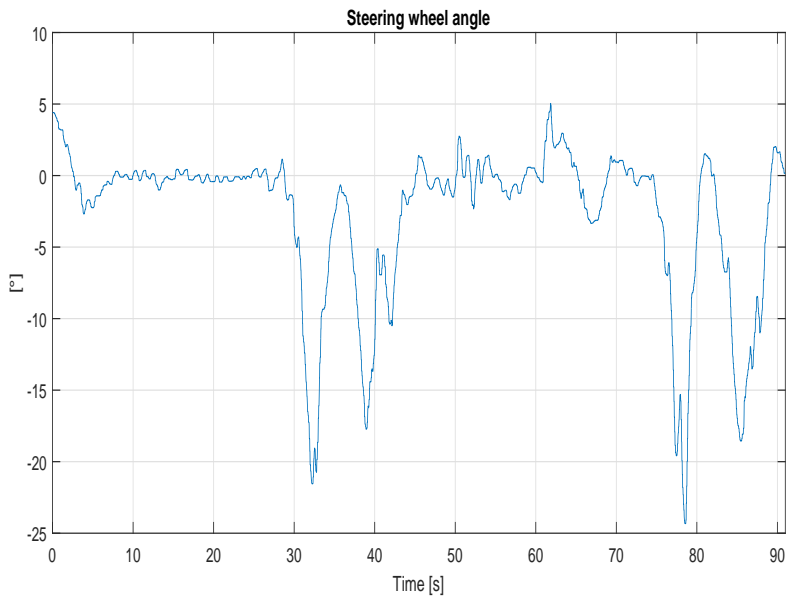


Fig. 4.49: Test on Technology Park using Lyapunov based controller: Steering wheel angle.

The vehicle speed tracking is shown in Fig. 4.50 while the Driving /Braking wheels torque is shown in Fig. 4.51. These two figures present the speed tracking on only a part of the track Technology Park, because, as mentioned above, the vehicle speed was manually controlled for a certain time. The initial speed of the vehicle is  $0\text{km}/\text{h}$ . It reaches the desired speed of  $20\text{km}/\text{h}$  in almost  $8.2\text{s}$ . As can be seen in Fig. 4.50, the vehicle speed tracks the desired speed with acceptable errors.

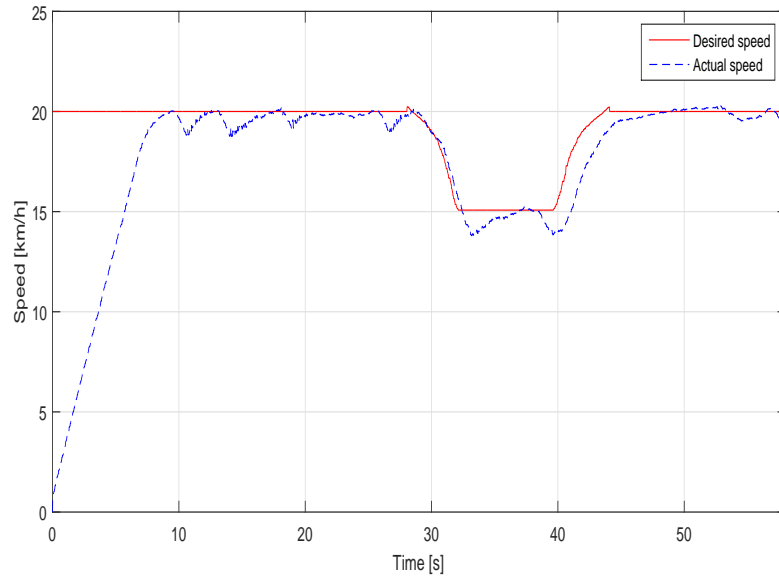


Fig. 4.50: Test on Technology Park using Lyapunov based controller: Desired longitudinal speed tracking.

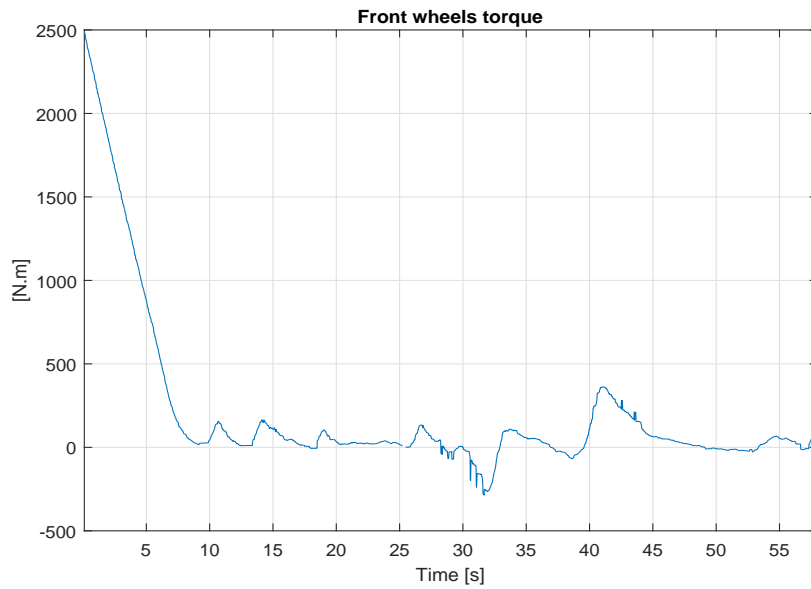


Fig. 4.51: Test on Technology Park using Lyapunov based controller: Front wheels torque.

#### 4.5.3 Results of validation of the Immersion and Invariance based controller

The Immersion and Invariance controller was validated on the Seville track presented in the previous subsection.

#### 4.5.3.1 Test 1: Navigating in Seville with 10km/h

In this test, the *I&I* controller is validated on the track Seville with a desired speed of 10km/h. As a first step, the controller was tested using these parameters:  $K_{imx} = 1$ ,  $\lambda_x = 0$ ,  $\alpha = 0.2$ ,  $\beta = 0.0001$ . The vehicle was able to track the reference trajectory but with many oscillations around it. This is actually the main drawback of the SMC technique: The chattering. In order to reduce the chattering, we used adaptive gains for  $\alpha$  and  $\beta$ , as follows:

$$\alpha = \alpha_0 \frac{s_1}{s_1 + 1} \quad (4.77)$$

$$\beta = \beta_0 \frac{s_1}{s_1 + 1} \quad (4.78)$$

where  $\alpha_0$  and  $\beta_0$  were set to 0.2 and 0.0001 respectively. The parameter  $L_s$  is also set to 3m in this test.

The speed tracking is shown in Fig. 4.52 and the Driving/Braking wheels torque is shown in Fig. 4.53. The initial speed of the vehicle is 7.85km/h. Therefore, the wheels torque necessary to reach the desired speed is of 281N.m at  $t = 0$ . This is equivalent to a motor torque of 35.21N.m. At the steady state, the speed error varies between 1.66km/h and 0.84km/h. As mentioned above, this error can be reduced by introducing the integral term to the computation of  $\tau_w$ .

Note that, in the experimental tests, the longitudinal control law is the same in the Lyapunov controller and the *I&I* controller (see 4.5.1.4). This similarity is not problematic, since in the simulation results shown in Section 4.4, we have seen that the longitudinal behavior of the Lyapunov based controller and the *I&I* controller was almost the same.

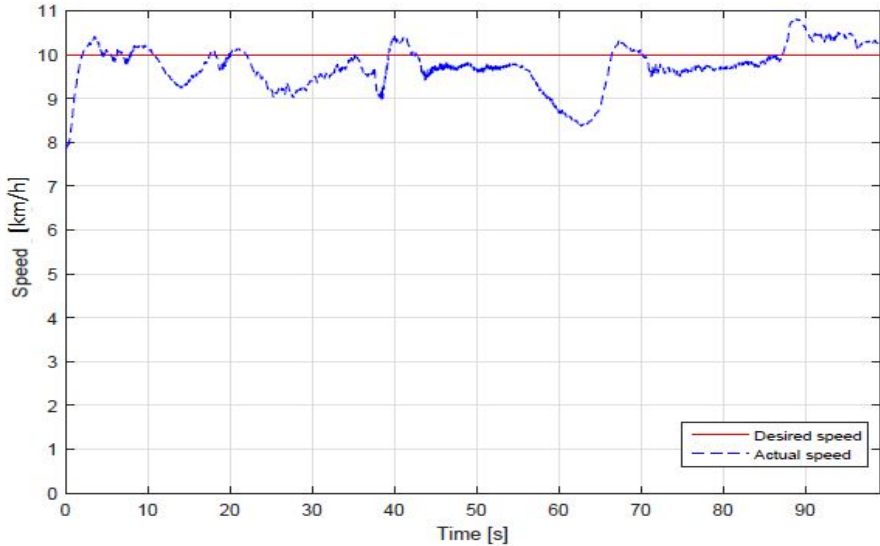


Fig. 4.52: Test 1 on Seville using I & I based controller: Desired longitudinal speed tracking.

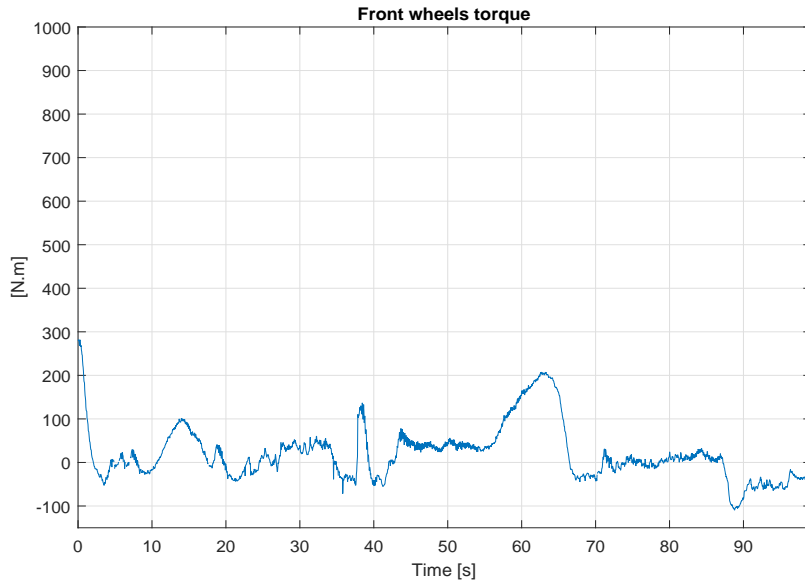


Fig. 4.53: Test 1 on Seville using I & I based controller: Front wheels torque.

The main difference between the controllers is the lateral dynamics control and the method of the controller design. Fig. 4.54 shows the vehicle trajectory when the *I&I* controller is used and the reference trajectory. We can also see the lateral displacement error at the COG of the vehicle in Fig. 4.56. The steering wheels angle computed by the controller is presented in Fig. 4.55. We can observe that the vehicle succeeds in tracking the reference trajectory with acceptable lateral error. The same points can be recalled here: the map representing Seville and used to compute the road curvature is not smooth and this leads to some oscillations in the steering wheel angle and to a non-accurate road curvature.

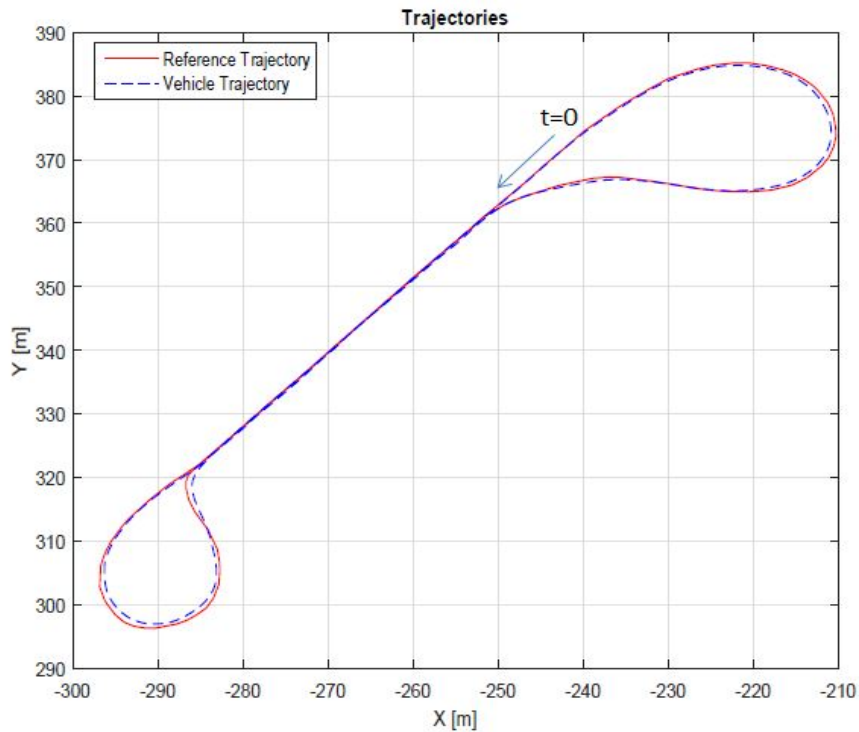


Fig. 4.54: Test 1 on Seville using I & I based controller: Reference trajectory tracking.

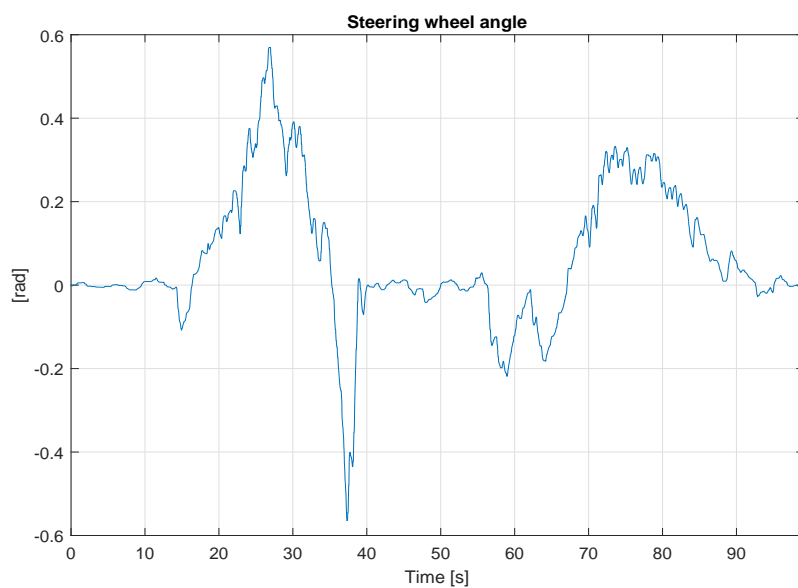


Fig. 4.55: Test 1 on Seville using I & I based controller: Steering wheel angle.

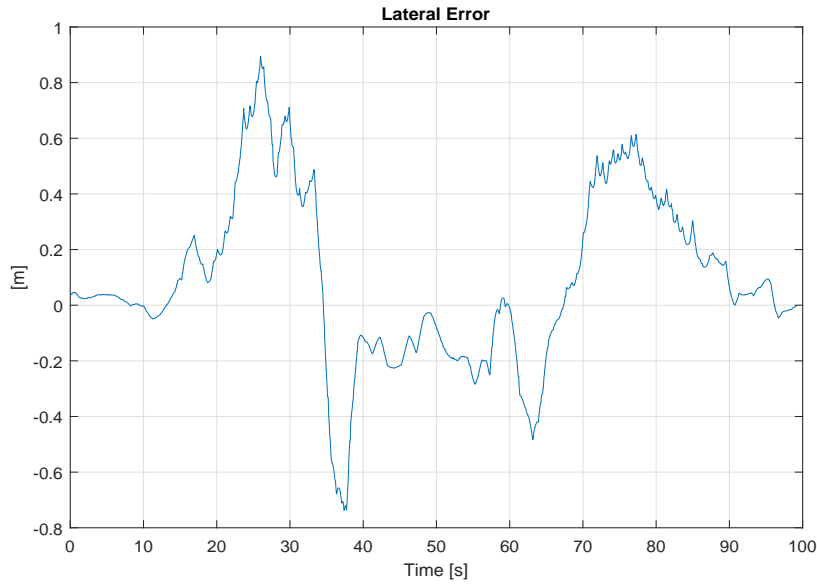


Fig. 4.56: Test 1 on Seville using I & I based controller: Lateral displacement error.

#### 4.5.3.2 Test 2: Navigating in Seville with 15km/h

In this test, the  $I\&I$  controller is also used on the track Seville but with a desired speed of  $15km/h$ . The controller gains are set as in Test 1. The speed tracking is given in Fig. 4.57 and the commanded Driving/Braking wheels torque is given in Fig. 4.58. The vehicle is initially stopped. It takes  $4.2s$  to reach the desired speed of  $15km/h$ . Its behavior in the steady state is similar to the behavior of the speed when the Lyapunov controller was used.

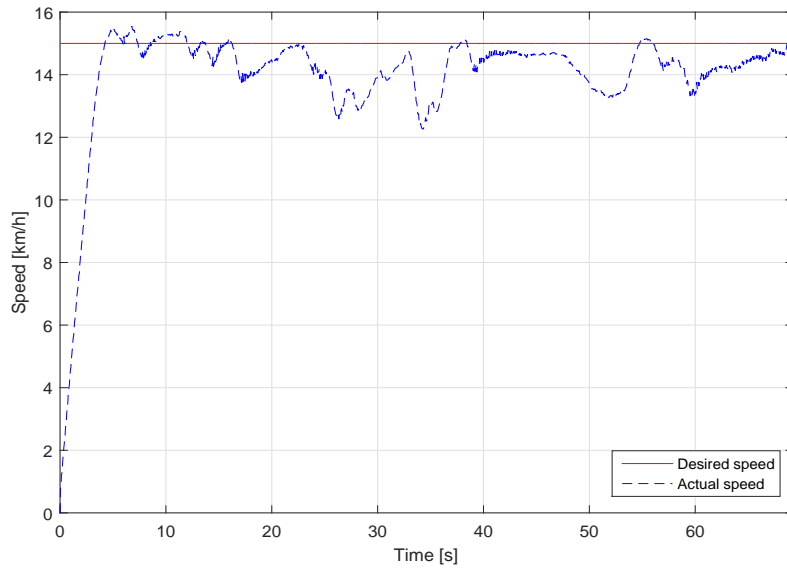


Fig. 4.57: Test 2 on Seville using I & I based controller: Desired longitudinal speed tracking.

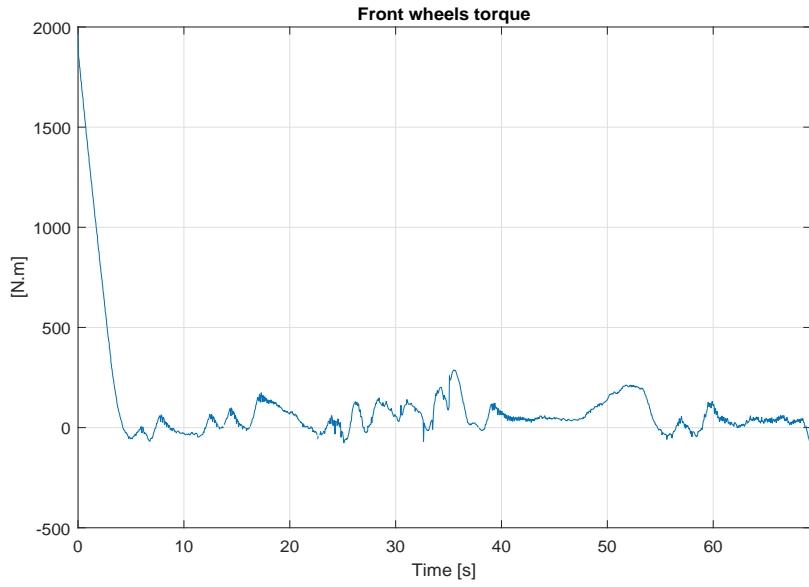


Fig. 4.58: Test 2 on Seville using I & I based controller: Front wheels torque.

The reference trajectory tracking is presented in Fig. 4.59. The lateral displacement error computed at the COG of the vehicle is shown in Fig. 4.60 and the control input which is the steering wheel angle at the wheels level is shown in Fig. 4.61. As can be seen, the vehicle can track the reference trajectory with acceptable lateral error.

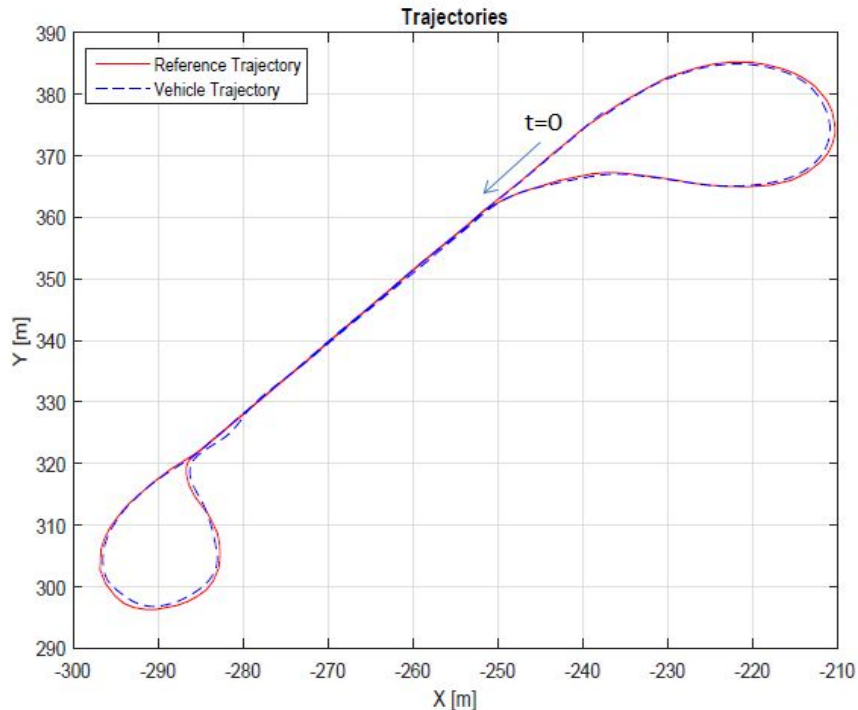


Fig. 4.59: Test 2 on Seville using I & I based controller: Reference trajectory tracking.

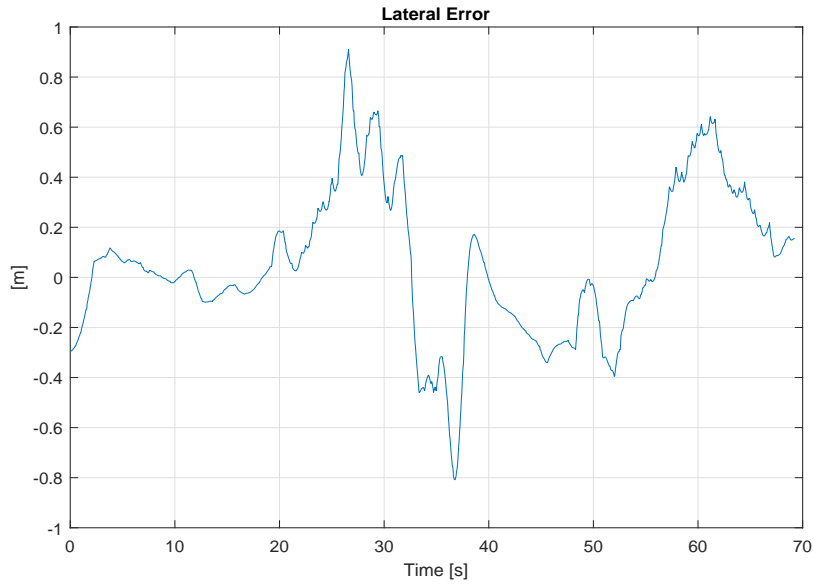


Fig. 4.60: Test 2 on Seville using I & I based controller: Lateral displacement error.

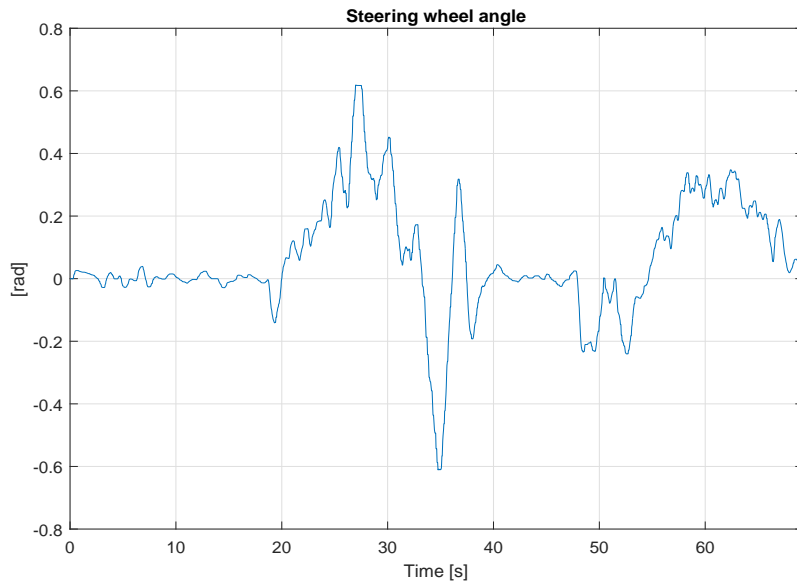


Fig. 4.61: Test 2 on Seville using I & I based controller: Steering wheel angle.

In the following, a comparison between the Lyapunov based controller and the *I&I* controller and a classical *PD/P* controller is presented. Preliminary results are shown and some conclusions are made.

#### 4.5.4 Some comparison results: Lyapunov vs I & I vs classical PD/P controller

Some comparisons were made between the developed Lyapunov based controller, the *I&I* based controller and a classical *PD/P* controller.

The PD/P controller used for the experimental comparison is composed of a PD controller for lateral control and a Proportional (P) controller for speed control. It is given by:

$$\delta = -K_{dy}\dot{e}_y - K_{py}e_y. \quad (4.79)$$

$$\tau_w = -K_{px}e_{vx}. \quad (4.80)$$

For convenience of the reader, we recall here the control inputs of the Lyapunov controller used in the experimental tests:

$$\begin{aligned} \tau_w = R_{eff}[m_e\ddot{x}^* - m_e(K_{lyx} + \lambda_x)e_{vx} - m_eK_{lyx}\lambda_x \int e_{vx} - m\dot{y}_{eq}\dot{\psi}_{eq} \\ + L_3\dot{\psi}_{eq}^2 + F_{aero}] \end{aligned} \quad (4.81)$$

$$\begin{aligned} \delta = \frac{1}{2C_{\alpha_f}}[m\dot{x}^2\rho_{ref} - m(K_{lyy} + \lambda_y)\dot{e}_y \\ - mK_{lyy}\lambda_ye_y + 2C_{\alpha_f}\frac{\dot{x}(\dot{y}_{eq} + L_f\dot{\psi}_{eq})}{\dot{x}^2 - (\frac{E}{2}\dot{\psi}_{eq})^2} + 2C_{\alpha_r}\frac{\dot{x}(\dot{y}_{eq} - L_r\dot{\psi}_{eq})}{\dot{x}^2 - (\frac{E}{2}\dot{\psi}_{eq})^2}], \end{aligned} \quad (4.82)$$

We also recall the control inputs of the *I&I* controller:

$$\begin{aligned} \tau_w = R_{eff}[m_e\ddot{x}^* - m_e(K_{imx} + \lambda_x)e_{vx} - m_eK_{imx}\lambda_x \int e_{vx} - m\dot{y}_{eq}\dot{\psi}_{eq} \\ + L_3\dot{\psi}_{eq}^2 + F_{aero}] \end{aligned} \quad (4.83)$$

$$\delta = u_1 + u_2 + \delta^* \quad (4.84)$$

where  $u_1$ ,  $u_2$  and  $\delta^*$  are given by:

$$\begin{aligned} u_1 &= -\alpha|s_1|^{0.5}sign(s_1) \\ u_2 &= -\beta sign(s_1) \end{aligned} \quad (4.85)$$

$$\delta^* = \frac{1}{m(2C_{\alpha_f} - 2\frac{I_w}{R_{eff}^2}\ddot{x})}(L_3\ddot{\psi} - 2C_{\alpha_f}\frac{\dot{x}(\dot{y} + L_f\dot{\psi})}{\dot{x}^2 - (\frac{E}{2}\dot{\psi})^2} - 2C_{\alpha_r}\frac{\dot{x}(\dot{y} - L_r\dot{\psi})}{\dot{x}^2 - (\frac{E}{2}\dot{\psi})^2} - \dot{x}^2\rho_{ref} + \lambda\dot{e}_y). \quad (4.86)$$

The comparisons were done on the track Seville with two different desired speed: 10km/h and 15km/h.

#### 4.5.4.1 Test 1: Navigating on Seville with 10km/h

In this test, the gains of the controllers are set as:

- Lyapunov controller:  $K_{lyx} = 1$  and  $K_{lyy} = 5$
- *I&I* controller:  $\alpha_0 = 0.2$ ,  $\beta_0 = 0.0001$  and  $K_{imx} = 1$   
( $\alpha$  and  $\beta$  are adapted as in (4.77) and (4.78))

- PD/P controller:  $K_{dy} = 0.7$ ,  $K_{py} = 4$  and  $K_{px} = 436$
- $\lambda_x$  and  $\lambda_y$  are respectively set to 0 and 3.5
- The parameter  $L_s$  is set to 3m.

The results of this comparison are shown below. Fig. 4.62 shows the desired speed compared to the vehicle speed when using each of the three controllers. The Driving/Braking wheels torque commanded by the three controllers are shown in Fig. 4.63. As mentioned in the previous subsection, the control laws used to track the desired speed are the same in the Lyapunov based controller and the *I&I* based one. That's why no difference could be observed between the longitudinal behaviors of these two controllers. However, we can observe some differences with the PD/P controller.

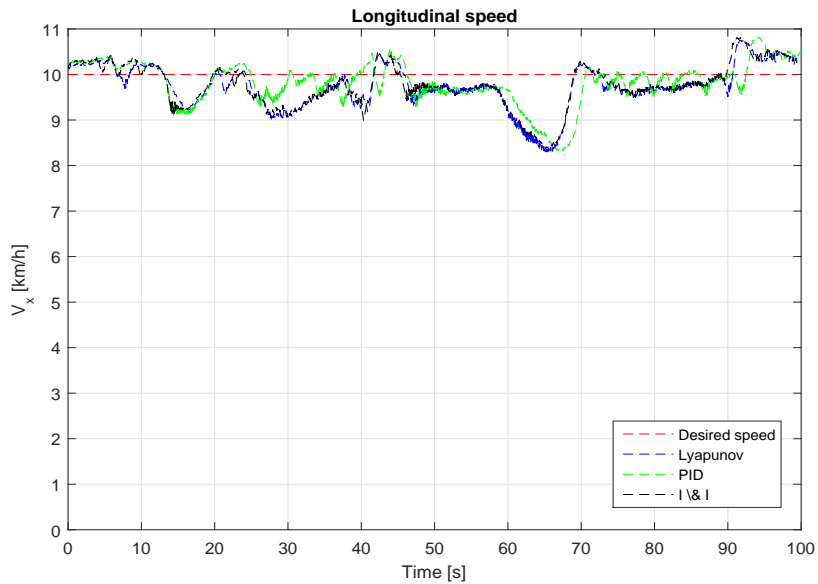


Fig. 4.62: Test 1 on Seville, controllers comparison: Desired longitudinal speed tracking.

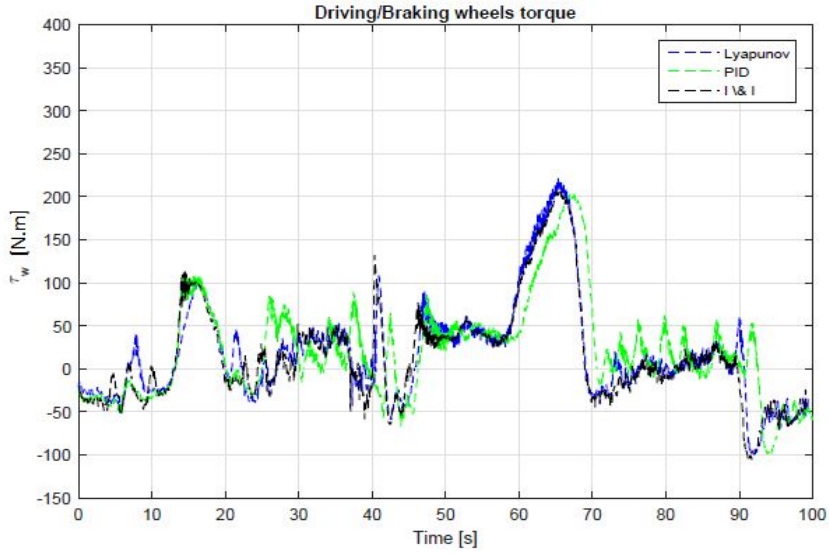


Fig. 4.63: Test 1 on Seville, controllers comparison: Front wheels torque.

Fig. 4.64 shows the reference trajectory and the trajectory executed by the vehicle when using each of the three controllers. The lateral displacement errors at the COG are given in Fig. 4.66 and the steering wheels angle provided by each of the three controllers are shown in Fig. 4.65. We can observe that all the controllers succeed in tracking the reference trajectory with acceptable errors. However, as can be seen in Fig. 4.66, when the Lyapunov and the *I&I* controllers guide the vehicle to navigate towards the interior side of the J-turns ( $e_y > 0$ ), the PD/P controller guides the vehicle to navigate towards the exterior of the J-turns ( $e_y < 0$ ). Besides, when leaving the J-turn A, the vehicle oscillates around the reference trajectory when using the PD/P controller (see Fig. 4.64), although the lateral error it provides has almost the same value as that provided by the *I&I* controller. Contrariwise, the Lyapunov based controller and the *I&I* based one leave the J-turn A with almost the same way but with different lateral errors (the lateral error given by the Lyapunov based controller is greater than that given by the *I&I* controller at this point). The behavior of the three controllers on the rest of the track Seville is almost the same.

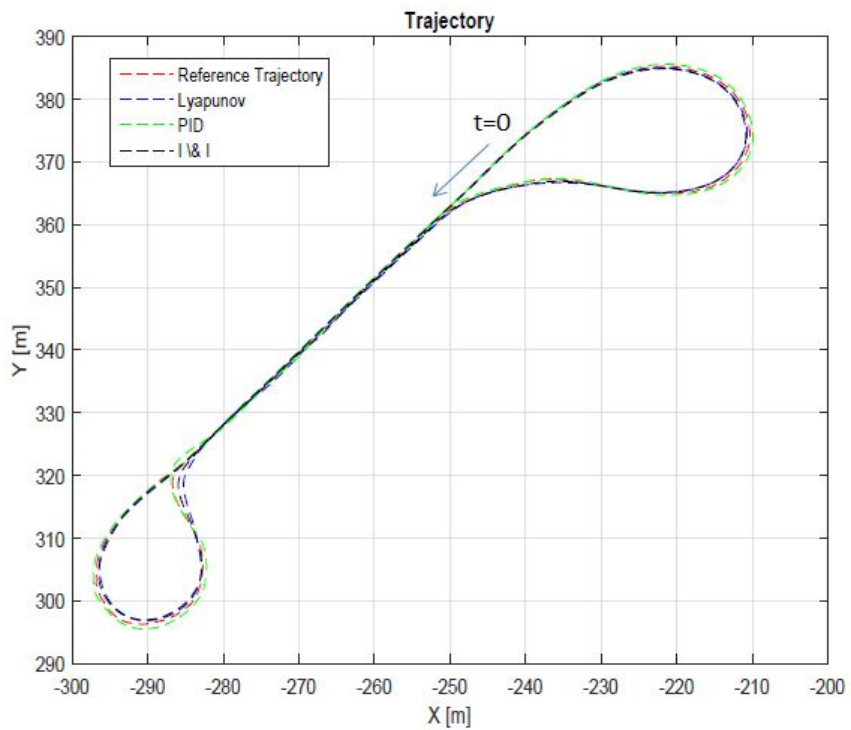


Fig. 4.64: Test 1 on Seville, controllers comparison: Reference trajectory tracking.

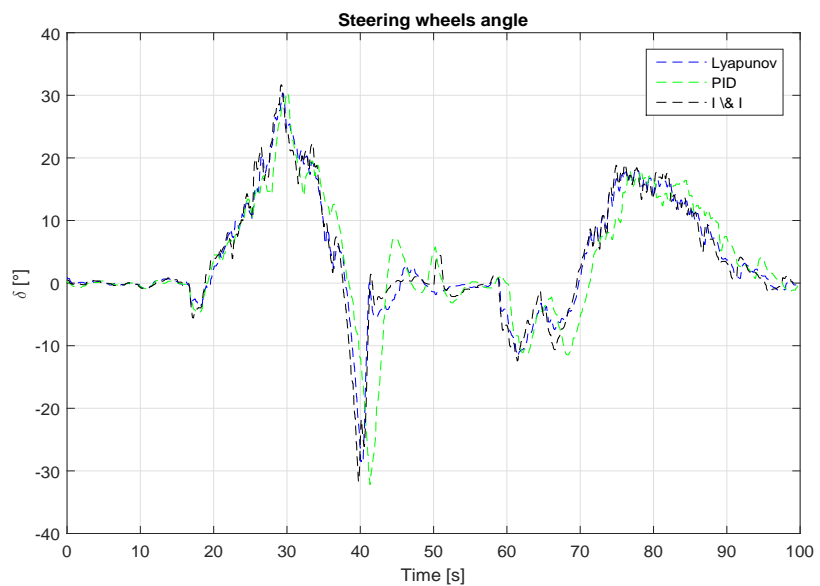


Fig. 4.65: Test 1 on Seville, controllers comparison: Steering wheel angle.

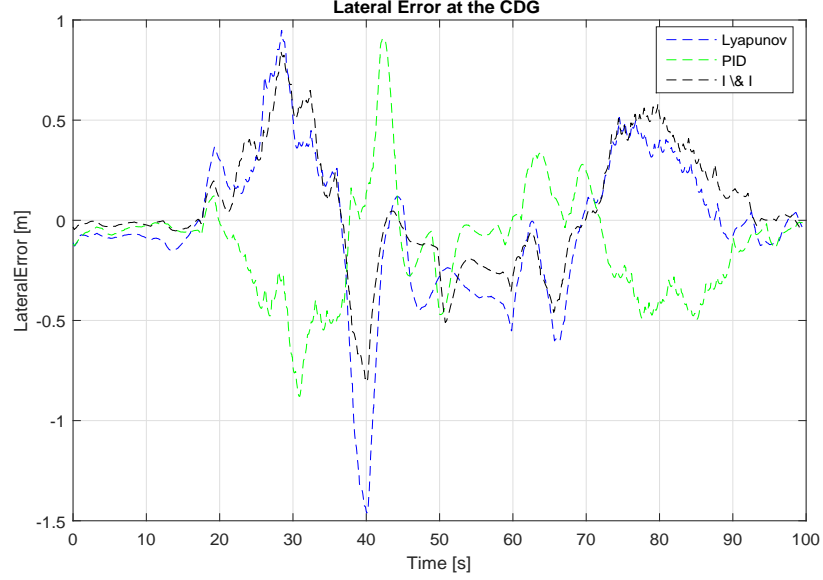


Fig. 4.66: Test 1 on Seville, controllers comparison: Lateral displacement error.

#### 4.5.4.2 Test 2: Navigating in Seville with $15km/h$

Another test was also used to compare the controllers. This test was also done on the track Seville but with a desired speed of  $15km/h$ . The controller gains and  $L_s$  are set as in the first test.

The speed tracking with the different controllers is shown in Fig. 4.67 while the Driving/Braking wheels torque generated by the different controllers are shown in Fig. 4.68. Again, the Lyapunov and the  $I\&I$  based controllers behave the same way since they are using the same control law for the longitudinal dynamics. And also again, the PD/P controller shows some differences with the coupled controllers.

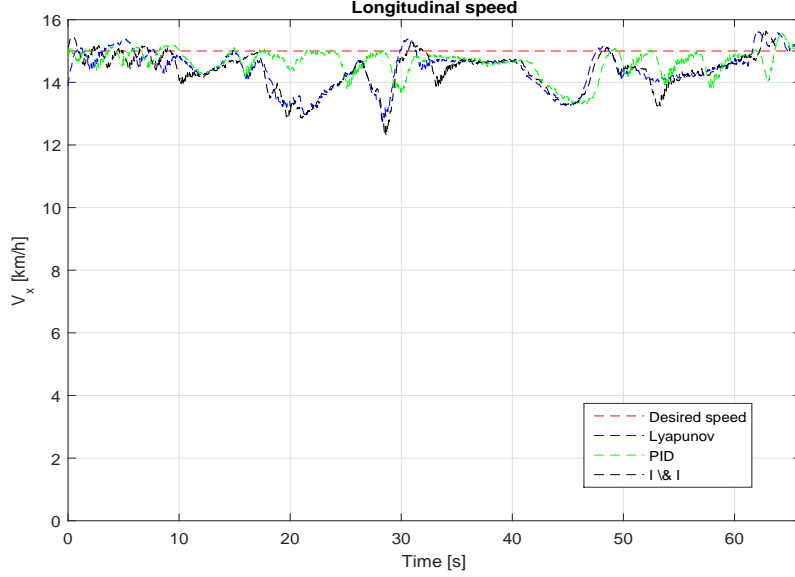


Fig. 4.67: Test 2 on Seville, controllers comparison: Desired longitudinal speed tracking.

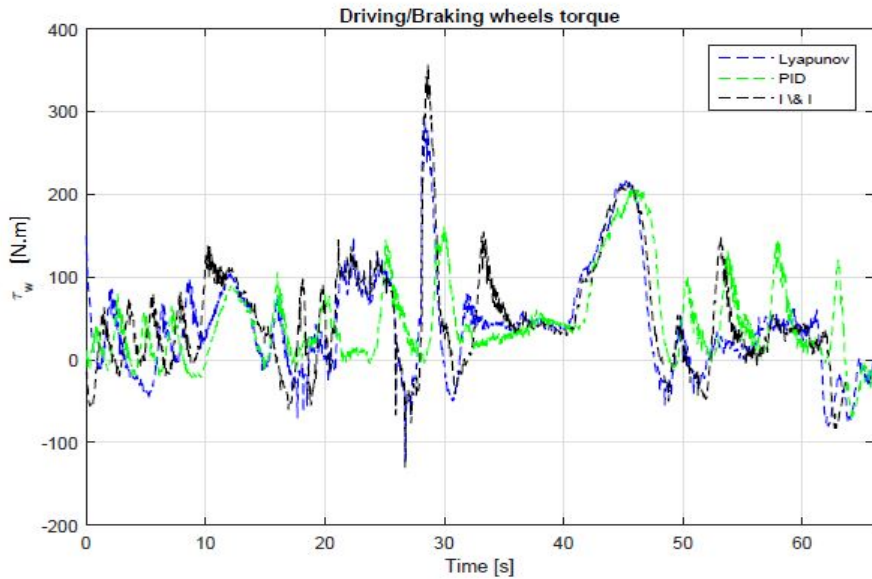


Fig. 4.68: Test 2 on Seville, controllers comparison: Front wheels torque.

Fig. 4.69 shows the reference trajectory and the trajectory executed by the vehicle when using each of the three controllers. The lateral displacement errors at the COG are given in Fig. 4.70 and the steering wheels angle provided by each of the three controllers are shown in Fig. 4.71. Again, we can observe that all the controllers succeed in tracking the reference trajectory with acceptable errors.

Once again, the PD/P controller lateral error when leaving the J-turn A is almost the same as that of the *I&I* controller. At this point, the lateral error provided by the Lyapunov controller is smaller than that provided by the *I&I* and the PD/P controllers. However, when using

the PD/P controller, the vehicle oscillates around the reference trajectory (see Fig. 4.69). Contrariwise, the Lyapunov based controller and the *I&I* based one leave the J-turn A with almost the same way (a smooth navigation) although the lateral error given by the Lyapunov based controller is smaller than that given by the *I&I* controller at this point. The behavior of the three controllers on the rest of the track Seville is almost the same. Another important point to mention is the delay the PD/P controller presents in its reaction to the given driving situation. This delay was clearly felt during the experimental tests and can be seen in Fig. 4.71 as well as in Fig. 4.65 for the previous test. For example, in this test, when leaving the J-turn A, at  $t = 27.7\text{s}$  the coupled controllers are commanding a steering wheel angle of about  $-35^\circ$  while the PD/P controller is commanding a steering wheel angle of about  $-12^\circ$ . This explains the oscillations of the vehicle trajectory provided by the PD/P controller. The reason for this delay is that both of the coupled controllers include an adaptive part in their control inputs and another part of the regulation while the PD/P controller includes only a regulation of the output. The presence of these adaptive parts of the coupled controllers made the task of the controller easier since they permit to approach to the desired value of the output and the regulation is then done in a domain near the desired output value.

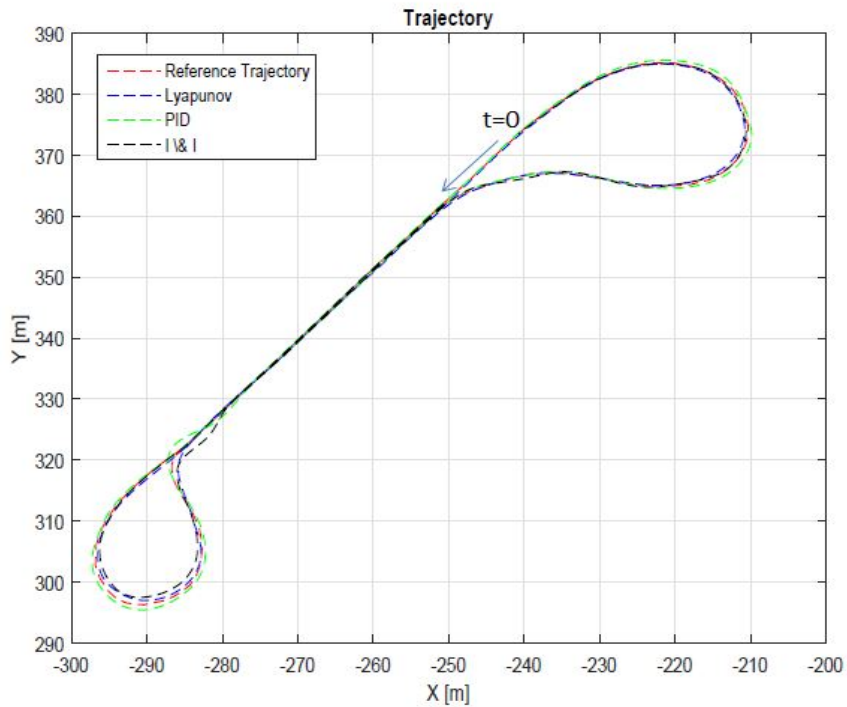


Fig. 4.69: Test 2 on Seville, controllers comparison: Reference trajectory tracking.

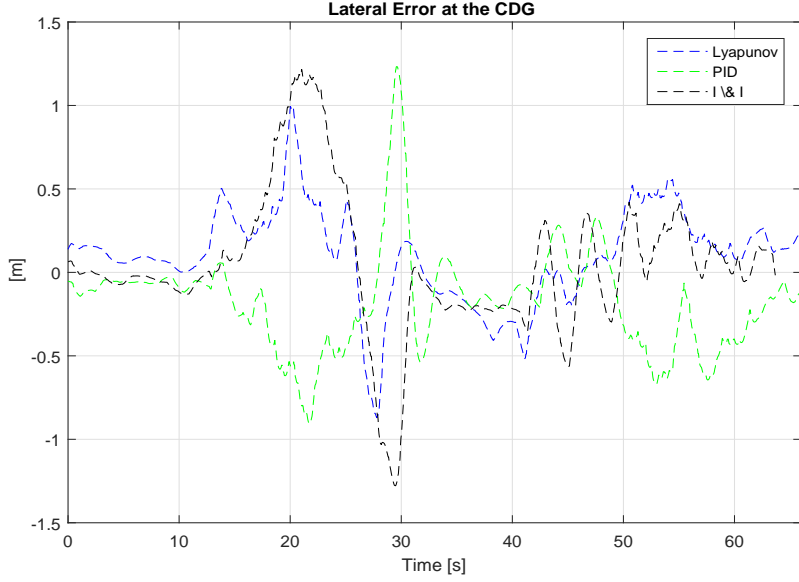


Fig. 4.70: Test 2 on Seville, controllers comparison: Lateral displacement error.

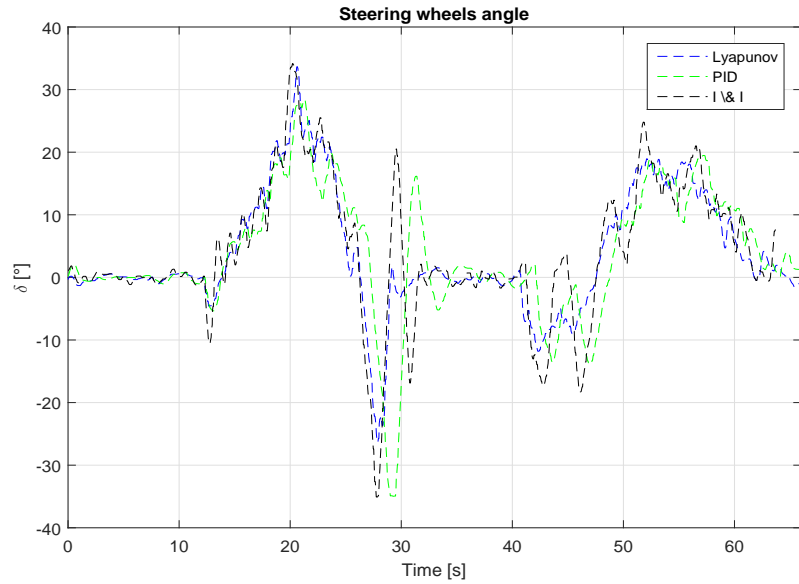


Fig. 4.71: Test 2 on Seville, controllers comparison: Steering wheel angle.

#### 4.5.4.3 Test 3: Navigating in Seville with $15km/h$ with different control parameters

This test is presented here in order to show the importance of the parameter  $L_s$ . We recall here the definition of the parameter  $L_s$  just for convenience. In fact,  $L_s$  is the distance in front of the vehicle where the lateral error with respect to the reference trajectory is computed. This parameter has the role of compensating the time delay introduced by the steering actuators in the vehicle. Indeed, after many experiments, we found that the tuning of this parameter is not at all a simple task. In fact, when this parameter is over-tuned (its value is greater than

necessary), the vehicle starts oscillating strongly; and when this parameter is under-tuned the reference trajectory tracking could fail.

In this test, all the controllers gains are set as previously. Only the parameter  $L_s$  is set to  $4m$  instead of  $3m$ . This test was also done on the track Seville with a desired speed of  $15km/h$ . The speed tracking with the different controllers is shown in Fig. 4.72 while the Driving/Braking wheels torque generated by the different controllers are shown in Fig. 4.73. Again, the Lyapunov and the  $I\&I$  based controllers behave the same way and the PD/P controller provides a speed error smaller than that provided by the coupled controllers. However, as can be seen in Fig. 4.72, the vehicle driver was forced to manually decelerate when leaving the J-turn A, when the PD/P controller was used in order to prevent any accident.

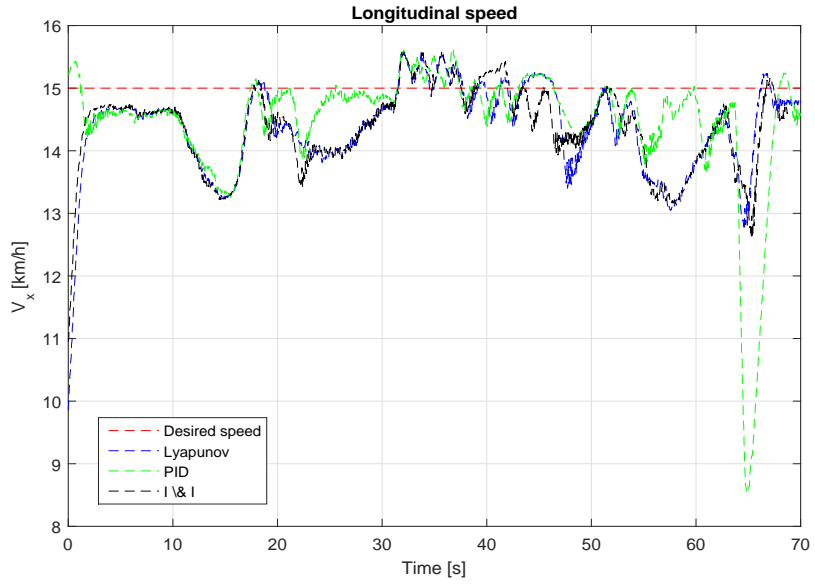


Fig. 4.72: Test 3 on Seville, controllers comparison: Desired longitudinal speed tracking at  $V_x = 15km/h$  and  $L_s = 4m$ .

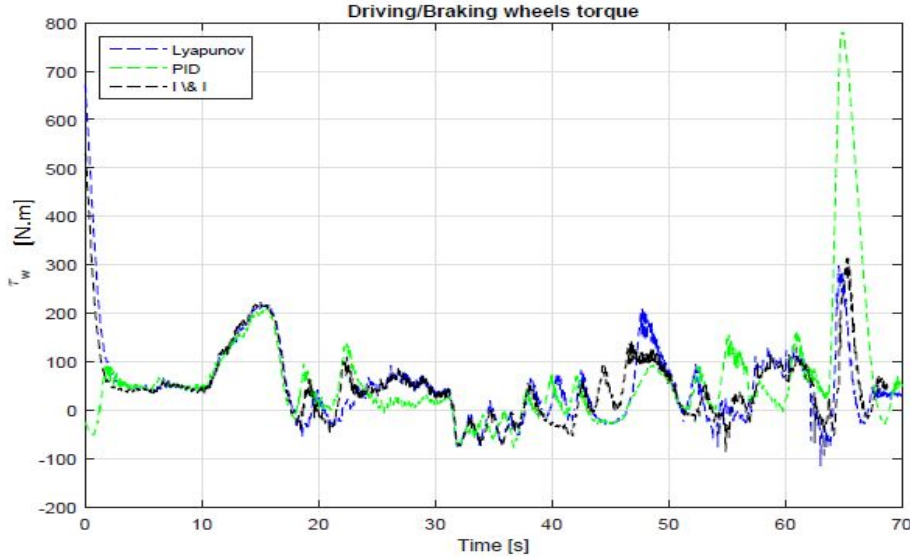


Fig. 4.73: Test 3 on Seville, controllers comparison: Front wheels torque.

Fig. 4.74 shows the reference trajectory and the trajectory executed by the vehicle when using each of the three controllers. The lateral displacement errors at the COG are given in Fig. 4.75 and the steering wheels angle provided by each of the three controllers are shown in Fig. 4.76. In this test, only the coupled controllers were able to safely track the reference trajectory with acceptable errors. However, the PD/P controller perform well on the whole track except when leaving the J-turn A. As mentioned above, the driver was forced to decelerate at this point in order to maintain the vehicle and the passenger's safety. Indeed, this part of the track is the most critical part since the road curvature changes fast and reaches high values for a few seconds. This result shows that the performance of the PD/P controller becomes worse when using a greater value for the parameter  $L_s$ .

Concerning the coupled controllers, in this test, both of the controllers perform well with almost the same behavior and the same lateral error. Once again, the delay that the PD/P controller presents in its reaction to the given driving situation can be seen in Fig. 4.76.

Now, comparing the behaviors of the Lyapunov and the *I&I* controllers in this test and the previous test, we can observe a difference that cannot be neglected. In fact, the performance of the Lyapunov controller became worse with a greater value of  $L_s$  while the performance of the *I&I* controller is not really affected. This behavior may be related to the fact that the Lyapunov controller depends on the road curvature more than the *I&I* controller. Indeed, the *I&I* controller needs to know the road curvature only for the computation of  $\delta_{eq}$ . However, the Lyapunov controller uses the road curvature more than once in the computation of the control inputs. And when  $L_s$  is over-tuned, the Lyapunov controller performance decreases faster than the *I&I* controller.

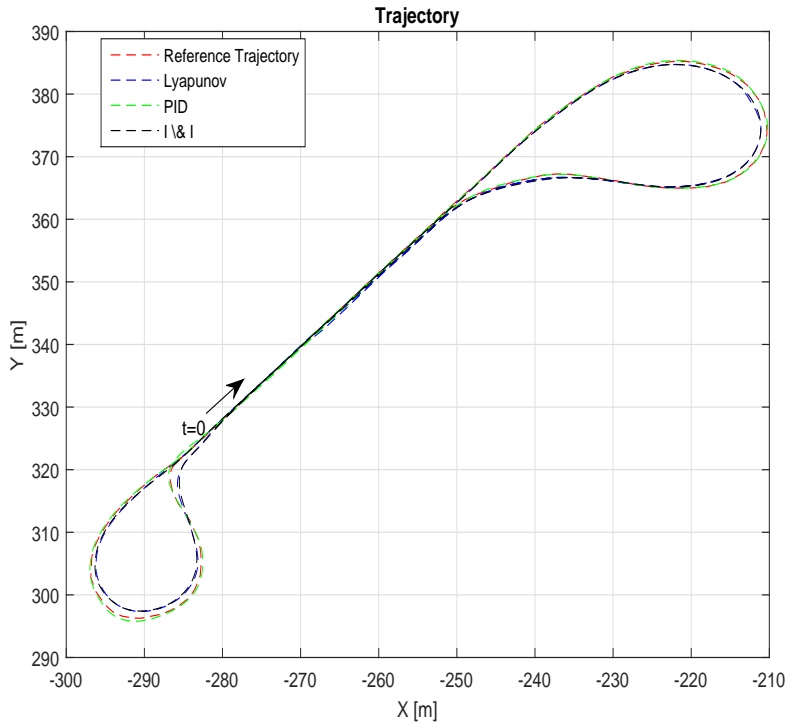


Fig. 4.74: Test 3 on Seville, controllers comparison: Reference trajectory tracking.

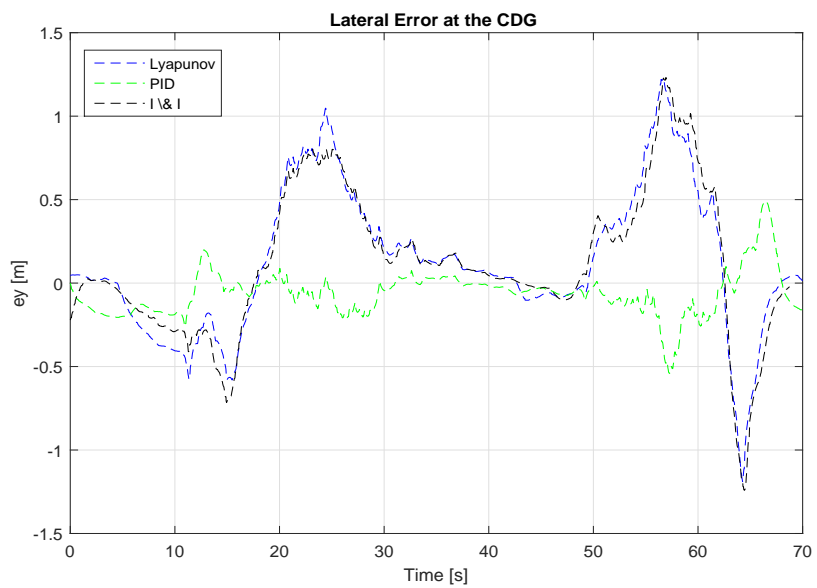


Fig. 4.75: Test 3 on Seville, controllers comparison: Lateral displacement error.

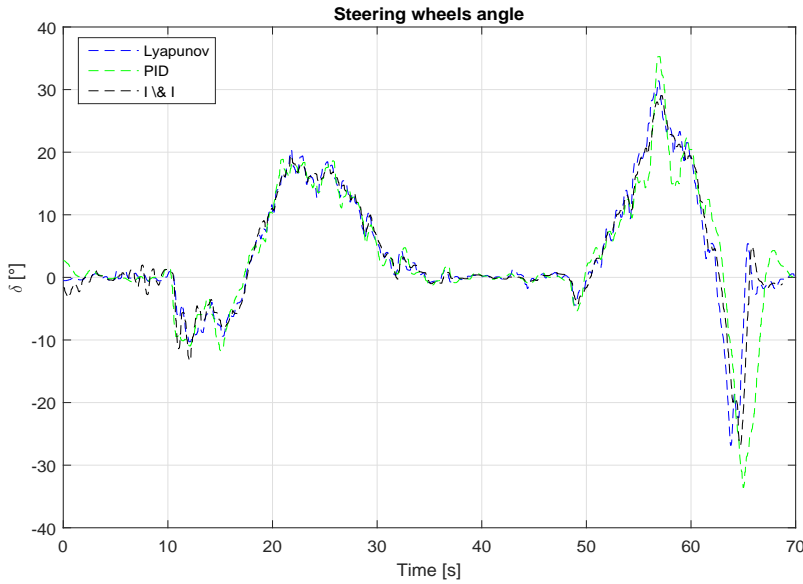


Fig. 4.76: Test 3 on Seville, controllers comparison: Steering wheel angle.

In conclusion for this section, we can claim that there is not an important difference between the developed controllers and a classical PD/P controller in normal driving scenarios. However, in critical driving scenarios, the classical PD/P controller proved to be less performant than the coupled controllers, even when navigating at low speeds.

Besides, the developed controllers, the Lyapunov based one and the *I&I* based one proved to be performant even in critical driving scenarios. Concerning the comparison between the coupled controllers, we cannot make a clear conclusion about the difference between their performances since the tests were done only for a given set of controllers gains. Further comparisons must take place in order to be able to objectively compare the developed controllers. Some scenarios with different gains for the controllers and different speeds (especially high speeds) must be done to compare the robustness of the controllers between them and their robustness with respect to a classical PD/P controller.

## 4.6 Conclusion

In this chapter, a state of the art dealing with the lateral control of the vehicle was first presented. The control of the vehicle longitudinal dynamics was also addressed and existing control techniques were presented. Afterwards, we discussed the coupled control of the lateral and the longitudinal vehicle dynamics by exposing existing solutions in the literature.

Then, two coupled controllers that take into account the strong coupling between the lateral and the longitudinal vehicle dynamics have been designed. The first controller is designed using Lyapunov control technique while the second one is based on Immersion and Invariance and Sliding Mode control techniques. The developed controllers are then validated under Matlab/Simulink using experimental data collected on an experimental vehicle DYNA in the Heudisyc laboratory. The controllers were validated under normal driving conditions, and then, a robustness study for both of the controllers against strongly nonlinear maneuvers and against parameters uncertainties were conducted.

The controllers behaviors are then compared between them and with a classical PD/PI controller. We have found out that both of the coupled controllers are valid and robust, with a certain limitation for the Lyapunov based controller against the strongly nonlinear maneuvers. Concerning the robustness against the vehicle parameters uncertainties, all of the controllers proved to be robust even with an uncertainty of  $\pm 30\%$ . However, the Lyapunov based controller is the most sensitive controller against these uncertainties. Besides, the coupled controllers showed a better performance than the PD/PI controller, especially in highly curves road segments.

Finally, an experimental validation for both of the controllers is presented. The experimental environment is firstly presented, then some scenarios validating the developed controllers are shown. In order to highlight the contribution provided by the development of the coupled controllers, a comparison between the controllers and a classical PD/P controller was conducted experimentally. The controllers were also compared between them. The comparison results prove that the coupled controllers were more performant than the classical PD/P controller in critical driving scenarios. Further experimental tests are needed to study the robustness of the coupled controllers with respect to strongly nonlinear maneuvers (high speeds on roundabouts scenarios) and their behavior with different gains and parameters values. Concerning the Lyapunov based controller, some improvements in the estimation of the sideslip angle are needed. The future works should also focus on the adaptation of the parameter  $L_s$  with respect to the vehicle speed and the road curvature. This parameter is in fact introduced in order to compensate the actuators delay and during the experimental tests, we have proven that the controllers behavior are very sensitive to its value. If  $L_s$  is over-tuned, the vehicle oscillates strongly around the reference trajectory, and if it is under-tuned, the vehicle may not be able to track the desired trajectory.

# Chapter 5

## Validation of the Navigation Strategy

### 5.1 Combined Navigation Strategy

We recall in this section the combined navigation strategy that includes the maneuver planning level and the local planning level. The vehicle dynamics are modeled using the developed model presented in Chapter 3 and the vehicle control is provided by the Lyapunov based coupled controller developed in Chapter 4.

Fig. 5.1 shows the developed navigation strategy. In the maneuver planning level, the surrounding situation is interpreted and a decision about the best maneuver to execute is made. The planned maneuver, represented as a reference trajectory and a speed profile, is transmitted to the local planner. This latter plans the local trajectory that permits the vehicle to track the desired reference trajectory while avoiding the possible obstacles.

As a last step, the local desired trajectory defined by the local planner and the speed profile defined by the maneuver planner are transmitted to the coupled controller that derives the control laws necessary to track the given trajectory with the desired speed.

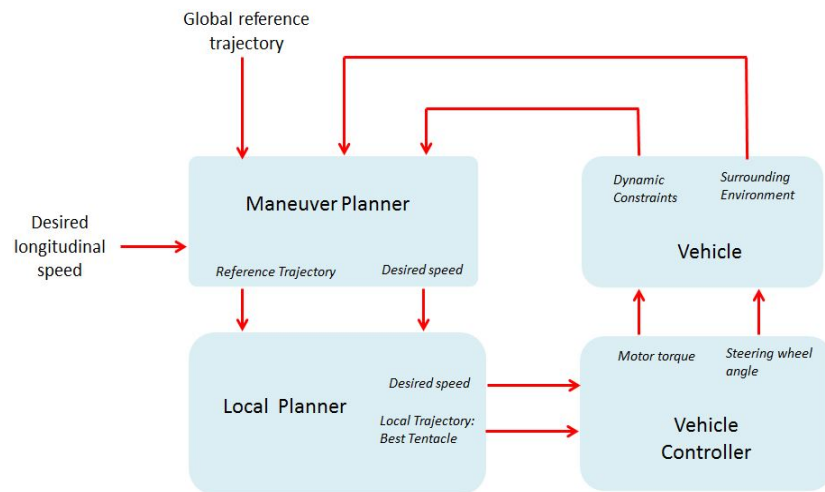


Fig. 5.1: Combined navigation strategy

## 5.2 Validation of the Navigation Strategy without the maneuver planner level

In this section, the local planner is validated while using the vehicle model developed in Chapter 3 and the Lyapunov based controller developed in Chapter 4. The maneuver planning level is omitted (see Fig. 5.2) in order to show the limitations of the clothoid method when applied alone to plan the vehicle trajectory.

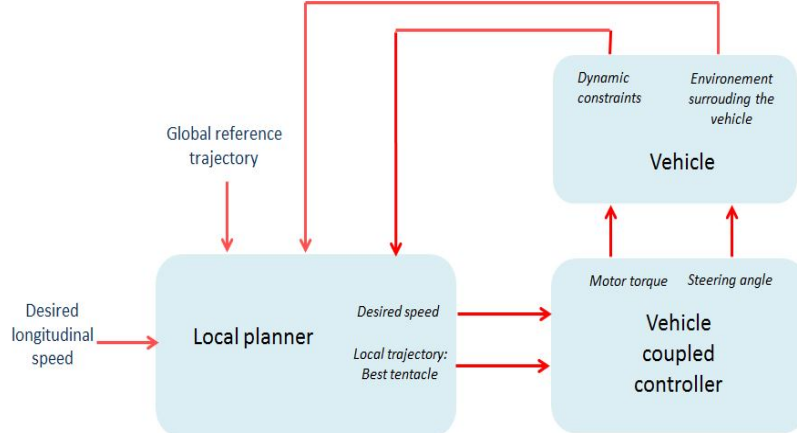


Fig. 5.2: Navigation strategy with only the local planner.

A moving obstacle is considered. The ego vehicle speed is set to  $10m/s$  while the obstacle is moving with  $5m/s$ . The vehicle motions are modeled using the robotic model developed in **Chapter 3** and the vehicle dynamics are controlled using the Lyapunov based coupled controller developed in **Chapter 4**. The scenario of the dynamic obstacle avoidance is shown in Fig. 5.3.

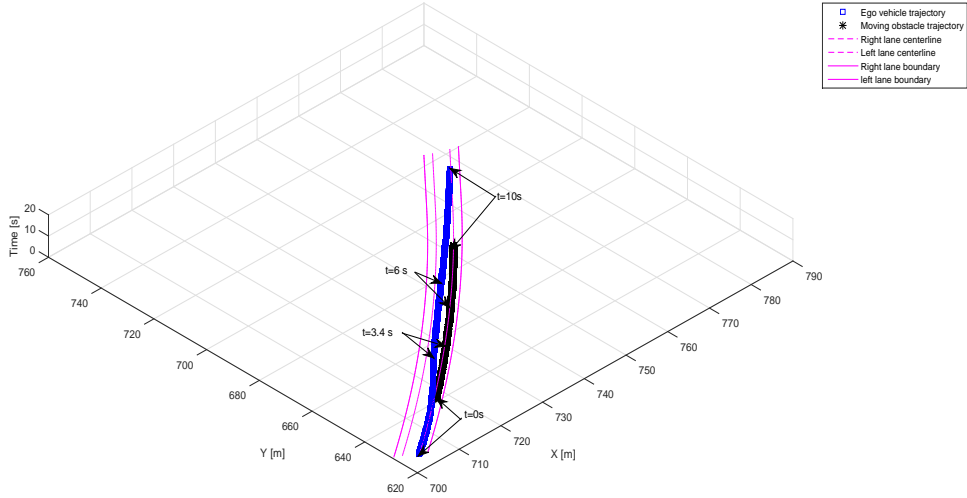


Fig. 5.3: Dynamic obstacle overtaking with clothoid tentacles.

The clothoid tentacles method outputs the best clothoid to be executed as a reference trajectory for the next time step (100 ms). The trajectory planner outputs are then a vector of desired curvatures to execute. The desired curvature is then transmitted to the coupled controller that derives the control laws necessary to track the desired local trajectory. In case no navigable tentacle can be found, the trajectory planner asks the vehicle controller to stop the vehicle. The controller outputs are shown in Fig. 5.4. The initial vehicle speed is set to  $8.5m/s$ , while the desired speed is  $10m/s$ . The desired speed is well tracked and the lateral error displacement with respect to the desired trajectory each time step is almost zero. Note that we assume a constant desired speed for the whole scenario and the clothoids method didn't request the vehicle to brake during this scenario. The corresponding control laws computed by the Lyapunov based controller are shown in Fig. 5.5. These results validate not only the tentacles method that executes the overtaking safely, but also the developed robotics model for the vehicle and the developed coupled controller.

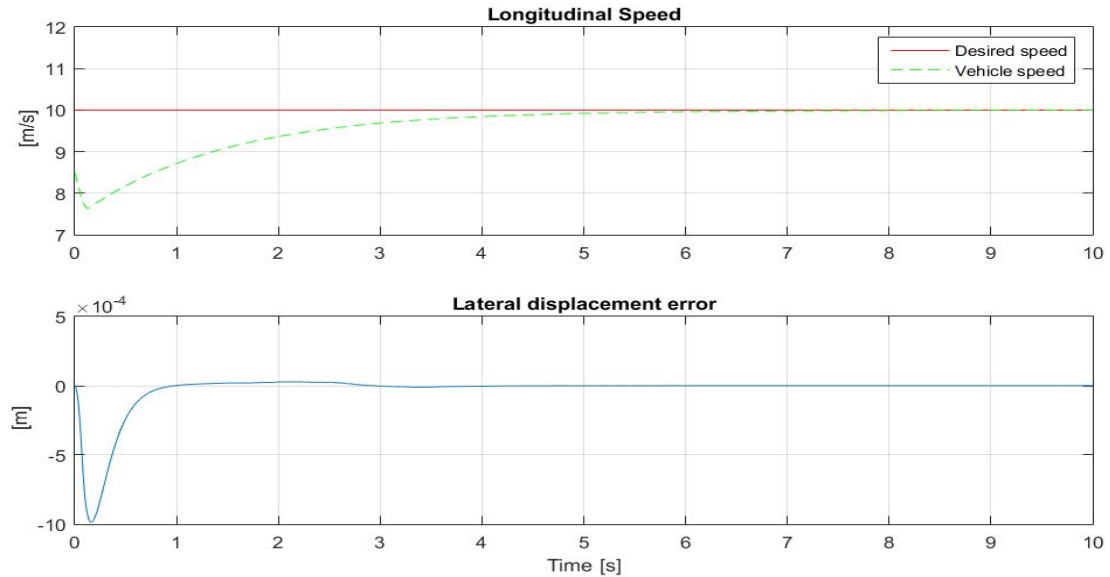


Fig. 5.4: Longitudinal speed tracking and lateral displacement error with respect to the chosen tentacle in the dynamic obstacle avoidance scenario.

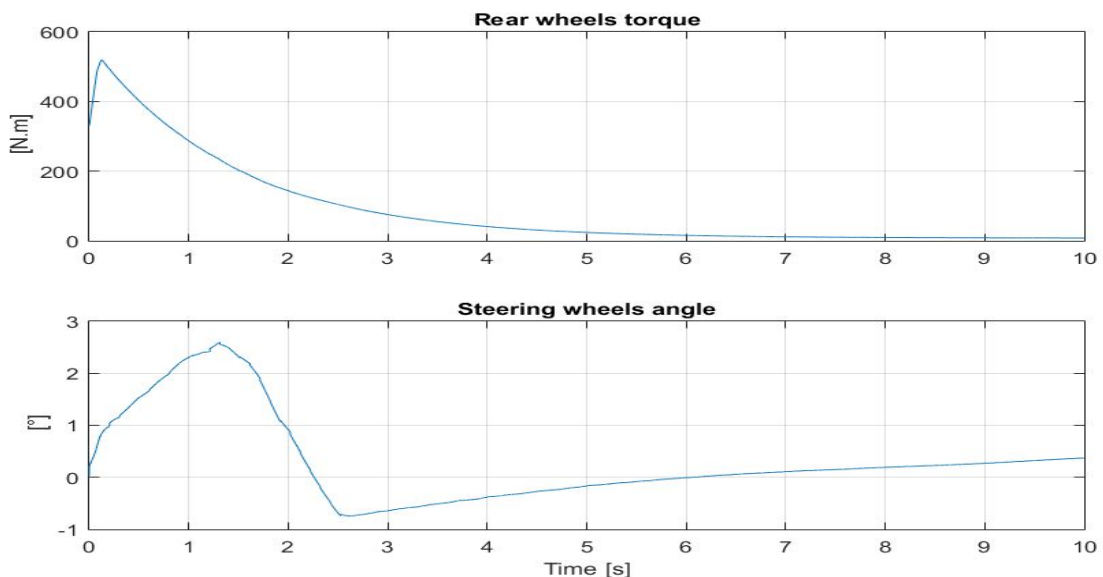


Fig. 5.5: Control laws computed by the coupled controller in the dynamic obstacle avoidance scenario.

Although the clothoid method succeeds in overtaking the moving obstacles, the overtaking maneuver is not controllable. The road rules are not necessarily respected and the behavior of the vehicle is not predictable. For example, we can not estimate the position of the ego vehicle with respect to the overtaken vehicle, on the right lane, after the end of the overtaking maneuver. This fact can threaten the vehicles safety.

According to that, a higher planning level is needed. The next section presents the combined Local/Maneuver planner validated with the consideration of the vehicle dynamics. The instructions of the combined planner are executed using a coupled controller.

### 5.3 Validation of the Combined Navigation Strategy

The combined Local/Maneuver planner presented in Fig. 5.1 is now validated using the vehicle model and the coupled controller developed in the previous chapters. The validation of the combined navigation strategy is done under Matlab/Simulink, where the desired speed of the vehicle A is set to  $11m/s$  and the speed of the vehicle B is set to  $5m/s$ .

The maximum admissible accelerations and the maximum speeds allowed on the right and the left lane are set identically to scenario 1 of the Section 2.3.3.1. The lane width, the safety distances  $m_s$  and  $m_{s2}$ , and the vehicles length are also set identically to scenario 1 of the Section 2.3.3.1.

The vehicle A starts its navigation on the right lane. When it detects the vehicle B, the Adaptive Cruise Control is activated.

The speeds of the vehicle A and B during this ACC phase are shown in Fig. 5.6 and the inter-vehicle distance between A and B is shown in Fig. 5.7. The initial distance between A and B is of  $57.5m$ .

In this scenario, we chose to start the overtaking maneuver at  $t = t_0 = 7s$ .

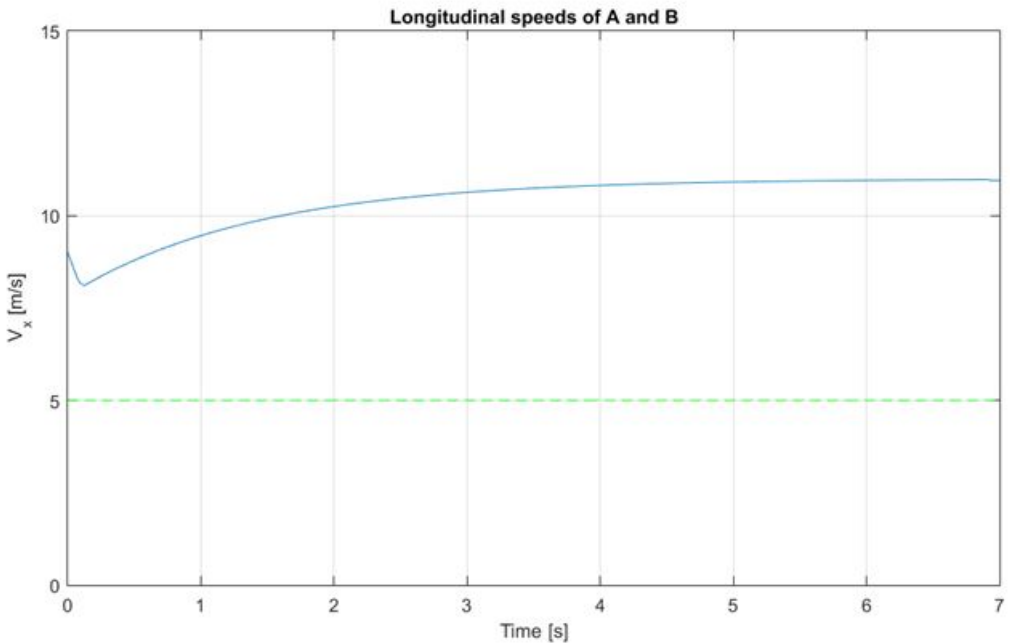


Fig. 5.6: Combined navigation: Vehicle A and B speeds during the ACC phase.

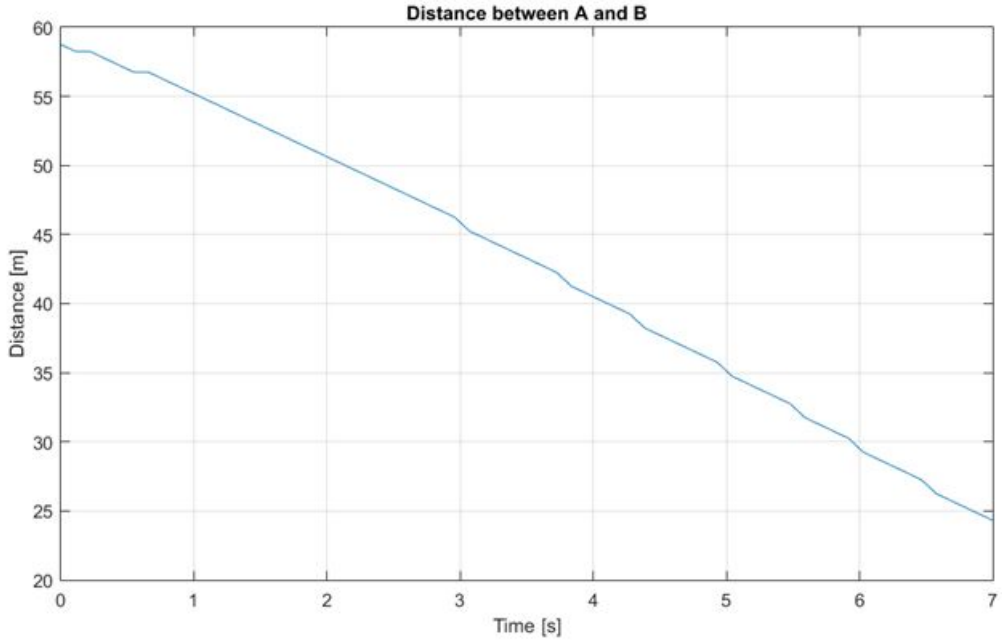


Fig. 5.7: Combined navigation: Inter-vehicles distance between A and B during the ACC phase.

As can be seen in Fig. 5.7 and Fig. 5.6, the vehicle A starts with  $8.5m/s$  at  $t = 0$  while the vehicle B navigates with  $5m/s$ . Therefore, the vehicle A speed increases in order to reach the desired speed of  $11m/s$ . The distance between the vehicles A and B remains greater than  $2V_A$  all over this ACC phase, and the vehicle A starts the overtaking maneuver with its desired speed ( $\simeq 11m/s$ )

Now, the condition (2.32) is satisfied here, as the desired speed of the vehicle A is  $V_{A_{des}} = 11m/s = 39.6km/h$  and  $V_B = 5m/s = 18km/h$ . We have then  $V_{A_{des}} > V_B + 20km/h$ .

Besides, as mentioned above, we suppose in this scenario that the left lane is free from  $t = t_0 = 7s$  (we suppose that the left lane was occupied by a vehicle C during the Adaptive Cruise Control phase, and then it becomes free at  $t = 7s$ ).

As a result, the vehicle A is allowed to overtake B from  $t = t_0 = 7s$ . Once  $t = 7s$ , the maneuver planner starts searching for a suitable lane changing trajectory that satisfies the vehicle dynamic constraints, the vehicle safety constraints and the road rules resumed by (2.32) and (2.37).

The overtaking maneuver then starts when  $t = t_0 = 7s$ ,  $d_{AB} = 24.4m$  and  $V_{A_i} = 10.9m/s$ . The target speed of the vehicle A at the end of the lane changing maneuver is then found using (2.32), that yields:

$$V_{A_f} = \max(\min(38km/h, 100.8km/h), 39.24km/h) = 39.24km/h \simeq 10.9m/s.$$

Now, the maneuver planner has to check if the condition (2.37) can be satisfied with the current situation (depending on  $V_{A_i}$ ,  $V_{A_f}$ ,  $d_{AB}$  and the other parameters).

In the current situation, the condition (2.37) is as follows:

$$\max(T_{min1}, T_{min2}) \leq T_1 \leq T_{max}$$

$$\max(2.27s, 0s) \leq T_1 \leq 2.96s$$

This means that, by choosing  $T_1$  in  $[2.27s, 2.96s]$ , we can satisfy(2.37) and then we can declare that the overtaking maneuver is feasible.

Therefore, we choose to set  $T_1$  to  $2.96s$  and the lane changing maneuver is safely executed using the generated trajectory. With  $T_1$  fixed to its maximum admissible value, the longitudinal position of the vehicle A when it reaches the left lane is of  $3m$  behind the longitudinal position of the vehicle B on the right lane. Fig 5.8 shows the ACC phase and the phase 1 of the overtaking maneuver when  $t = t_0 + 5s = 12s$ . The generated tentacles at  $t = t_0 + 5s$  are shown in this figure, where we can see the navigable tentacles and the best tentacle chosen as local trajectory to be tracked by the vehicle. Note that, for reasons of simplicity, we have supposed here that the road boundaries don't constitute an obstacle for the clothoid method. In order to surpass this hypothesis, some improvements to the clothoid method are necessary, e.g. redefine the collision distance or the tentacle's length or may be other parameters.

The longitudinal and the lateral speed and acceleration profiles executed by the vehicle A during the lane changing maneuver are shown in Fig. 5.9. We can observe that the dynamic constraints are respected since the longitudinal acceleration is less than  $a_{x_{max}}$  and the lateral acceleration is also less than its limit  $a_{y_{max}}$ .

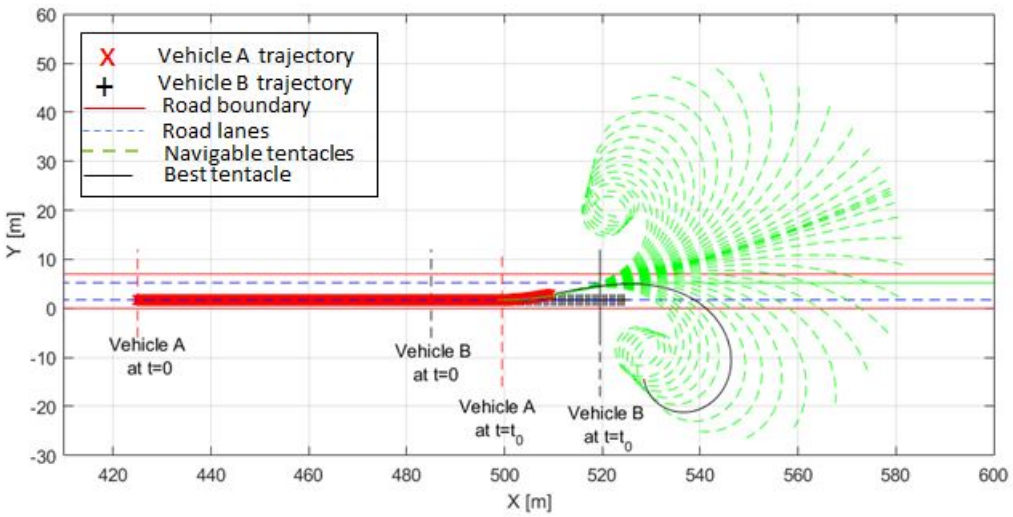


Fig. 5.8: Combined navigation: ACC phase and Phase 1 of the overtaking maneuver until  $t = t_0 = 12s$ .

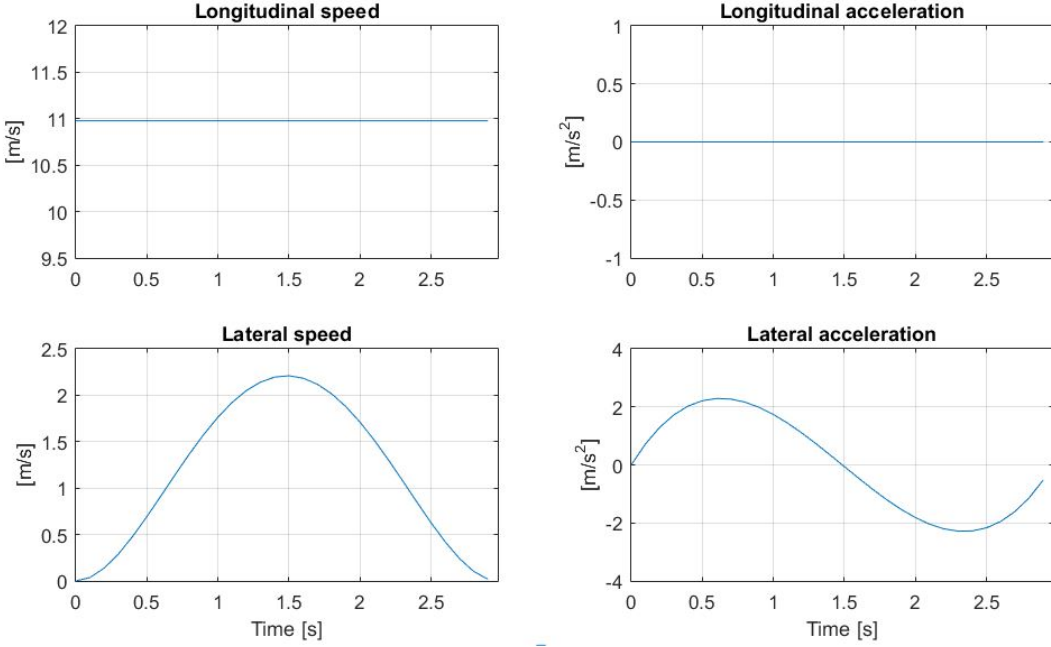


Fig. 5.9: Combined navigation: Speed and acceleration profiles of vehicle A during the phase 1 of the overtaking maneuver

During the phase 2 of the overtaking maneuver, the tentacles method is supposed to track the left lane center line with  $V_A = V_{A_f} = 10.9m/s$ . This phase lasts  $T_2 = 2.4s$ . At the end of this phase, the longitudinal distance between the vehicles A and B is of  $3m$ .

Once the second phase is over, the vehicle will return to the right lane. First, the time duration of the third phase (returning to the right lane) is specified by (2.64). In this scenario, (2.64) becomes:

$$\begin{aligned} T_3 &\geq \max(T_{min1}, T_{min2}, T_{min3}) \\ T_3 &\geq \max(2.27s, 1.50s, 0.66s) \\ T_3 &\geq 2.27s \end{aligned} \quad (5.1)$$

$T_3$  is then chosen as  $T_3 = 2.27 + 2s = 4.27s$ . Consequently, the target speed of the vehicle A once it reaches the right lane,  $V_{A_{f2}}$ , is chosen correspondingly to (2.53):

$$\begin{aligned} \max(5, 2.39) &\leq V_{A_{f2}} \leq \min(15.17, 20) \\ 5m/s &\leq V_{A_{f2}} \leq 15.17m/s \end{aligned} \quad (5.2)$$

This means that the vehicle A can either accelerate, or decelerate or stay with the same speed, in this phase in order to satisfy all the imposed constraints. We have chosen to stay at the same speed  $V_{A_{f2}} = V_{A_{i2}} = 10.9m/s$ . Note that the choice of  $V_{A_{f2}}$  fulfills the safety condition (2.53), that guarantees a safety distance greater than two seconds of reaction between the vehicles A and B once this third phase is finished, that is at  $t = t_0 + T_1 + T_2 + T_3$ . This distance is of  $D_{obs2} = 28.19m$ .

A capture of the third phase of the overtaking maneuver, when the clothoids should track the right lane again, is shown in Fig.5.10.

The speed and the acceleration profiles, generated by the maneuver planner in this phase are shown in Fig. 5.11.

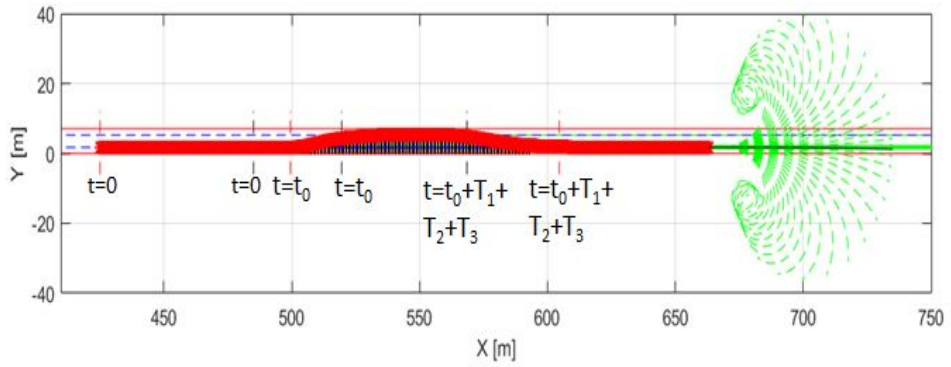


Fig. 5.10: Combined navigation: Phase 3 of the overtaking maneuver

The desired speed profile for the whole navigation is shown in Fig.5.12 and compared to the speed executed by the vehicle. The lateral displacement error with respect to the desired local trajectory at each time step is also shown in this figure.

The navigation strategy is validated in closed-loop with the developed Lyapunov based coupled controller and robotics vehicle model. Note that the safety measurement, the vehicle dynamics and the road rules are always respected.

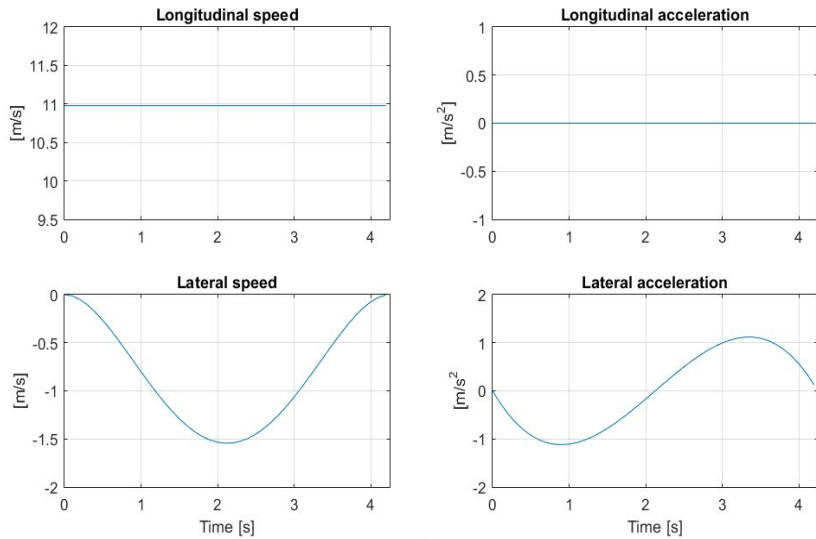


Fig. 5.11: Combined navigation: Speed and accelerations profiles to execute the phase 3 of the overtaking maneuver

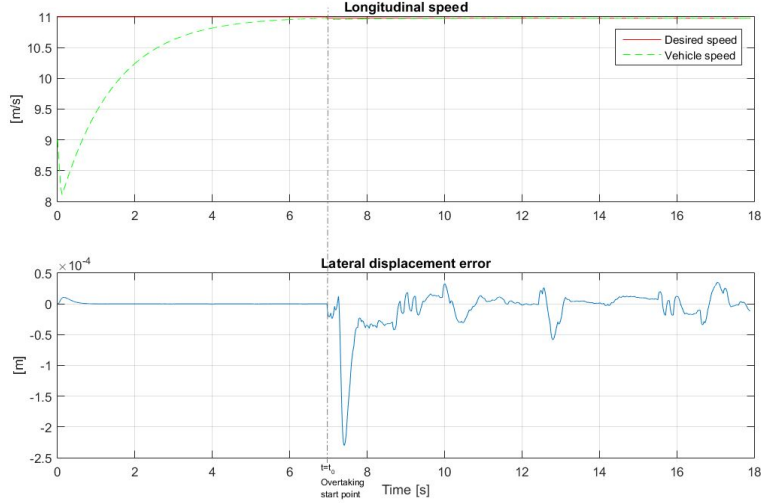


Fig. 5.12: Combined navigation: Speed profile tracking and desired reference tracking with the coupled Lyapunov controller

## 5.4 Conclusion

The combined navigation strategy includes a local planner and a maneuver planner. The local trajectory planner is based on the clothoid tentacles method. The goal of this planner is to guarantee a secure navigation on a given reference trajectory while avoiding obstacles. The maneuver planner is then added to complete the tentacles method and to adapt the navigation to an on-road navigation. This level treats essentially the overtaking maneuver and provides the local planner with the desired trajectory to execute the overtaking. The planned maneuver has to respect the vehicle dynamic constraints, the security measurements and the road rules. The combined navigation strategy is then validated using the robotics model developed in this work to represent the vehicle's dynamics and the Lyapunov based coupled controller also developed in this work. Different scenarios have been tested in simulation, representing an overtaking in different driving conditions. The simulation results validate the strategy and are very promising.

Future works include the validation of the strategy at higher vehicle speeds. Besides, the navigation strategy was tested only on a straight road. We claim that the consideration of the road curvature is very important for a better illustration of the real environment. Moreover, we look forward to validate the whole navigation strategy on a robotized vehicle in order to validate the work experimentally.

# Chapter 6

## Conclusion and Perspectives

This thesis studies the autonomous vehicles navigation topic, mainly the trajectory planning and the vehicle control.

Concerning the vehicle control, the design of the control laws is based on a vehicle planar model which is developed using robotics formalism. This formalism considers the vehicle as a robot, wherein the chassis is the vehicle base and the four wheels are the terminals. The vehicle is then represented using the geometric modified description of Denavit-Hartenberg. The dynamic model of the vehicle is then derived by applying the Newton-Euler recursive method [Maa11]. The importance of this modeling strategy is that it permits to model the interactions between the different subsystems composing the vehicle system. This fact renders this modeling strategy more accurate and representative than the classical modeling techniques.

A four wheeled planar model is then developed based on this formalism. Afterwards, the developed model was validated using Scaner-Studio simulator. The validation was done under Matlab/Simulink using data from Scaner-Studio simulator: the vehicle model inputs collected from the simulator are fed to the developed model, then, the vehicle model outputs were compared to the data collected from the simulator. The validation showed good results validating thus the modeling step.

Based on the developed vehicle model, two coupled controllers dealing with the coupled lateral and longitudinal vehicle dynamics control are proposed. Indeed, many vehicle control approaches were developed in the literature, but most of them treat the lateral and the longitudinal vehicle dynamics separately. Besides, many of them consider a constant speed while treating the lateral control of the vehicle dynamics. The separate control cannot guarantee the vehicle safety when executing coupled maneuvers such as obstacle avoidance maneuvers or when driving under critical situations. This limitation can be explained by the existence of a strong coupling between the lateral and the longitudinal dynamics of the vehicle and can be overpassed by using coupled controllers. In that context, we developed two coupled controllers: The first one is based on Lyapunov control techniques while the second is based on Immersion and Invariance (*I&I*) approach.

In fact, the solution based on Lyapunov allows the design in one step of a multivariable nonlinear controller dealing with both the longitudinal and the lateral dynamics of the vehicle. The second coupled controller is based on the Immersion and Invariance Sliding Mode approach. Indeed, the immersion and invariance (*I&I*) theory consists in defining a target dynamics (manifold) and to design a control law that makes the target dynamics attractive and invariant. In

the design of our controller, we used the fact that the lateral dynamics converge faster than the longitudinal dynamics of the vehicle. So, the manifold was defined as the equilibrium surface of the lateral dynamics. Then, in order to reach this target, a sliding mode control (SMC) approach is used. Once the manifold is reached, the stabilization of the longitudinal dynamics inside the manifold is assured by the use of a Lyapunov function where the lateral variables are substituted by their equilibrium values.

The developed controllers are then validated by simulation under Matlab/Simulink using experimental data that was collected on a vehicle (DYNA) in the Heudiasyc laboratory. The behavior of the controllers was studied and compared especially in a strongly nonlinear maneuver. A robustness study was also done and the controllers robustness was compared. In addition, the behavior of the coupled controllers was compared to that of a classical PD/PI based controller. The simulation results showed good performances of the coupled controllers and the PD/PI controller in normal driving situations, yet the PD/PI controller always showed a bigger lateral error especially in curved roads. When testing the controllers against strongly nonlinear maneuvers, the *I&I* and the PD/PI controllers showed better results than the Lyapunov based one. This means that the Lyapunov based controller robustness decreases when we attain the limits of stability of the vehicle. The robustness of the controllers was also tested against parameters uncertainty, namely the vehicle mass and the wheels cornering stiffness. All of the controllers were able to track the desired trajectory and the desired speed with acceptable errors even with a variation of  $\pm 30\%$ . However, the Lyapunov based controller was shown the most sensitive controller among the tested ones against the parameters uncertainties.

Moreover, to proceed to a further validation of the controllers, an experimental validation has been established using a robotized vehicle ZOE also in the Heudiasyc laboratory. The controllers were validated on two experimental tracks: Seville near the Heudiasyc laboratory in Compiègne and the Technology Park also situated in Compiègne. The validation was conducted for some scenarios with a desired speed of 10, 15 and 20km/h. The controllers behaviors were also compared between them and with a classical PD/P controller. The preliminary results show a better performance of the coupled controllers compared to the PD/P controller, especially in the critical driving conditions.

Concerning the trajectory planning topic, a local planner based on the clothoids tentacles method was developed. This method is a fast reactive motion planning method that consists of using virtual antennas called tentacles to discover the environment, avoid obstacles and track a given reference trajectory. However, the tentacles method behavior is not fully predictable, which constraints the application of this method for on-road driving scenarios. This fact motivated us to develop a maneuver planning approach that completes the tentacles method and serves as a higher level that defines the reference trajectory to track depending on the chosen maneuver. In the maneuver planning, we focus on the overtaking maneuver and we propose a new strategy to plan this maneuver. The local and the maneuver planners were validated under Matlab/Simulink and showed promising results.

Finally, a combined local/maneuver planning approach was proposed and then validated using the developed robotics vehicle model and the coupled controller based on Lyapunov, also under Matlab/Simulink. The simulation results are very promising.

Among the perspectives of this work, we look forward to improving and enriching the experimental study of the controllers behavior. First, we look forward to study the impact of all

the assumptions that had made to simplify the controllers and to respond to the experimental limitations (see section 4.5.1.4). In addition, the robustness of the coupled controllers should be compared with more scenarios, with higher speeds and stronger non-linearity conditions in order to be able to conclude about the controllers robustness at the limits of stability of the vehicle.

Another important point that we believe can improve the controller's performances is the use of an adaptive formulation for the parameter  $L_s$ . This parameter is in fact the distance in front of the vehicle where the lateral error with respect to the reference trajectory is computed. Its role is to compensate for the delay of the vehicle steering angle actuator. This distance should be adapted to the vehicle speed and the road curvature in order to increase with the speed and decrease with the road curvature. Actually, the executed tests have shown the sensitivity to this parameter, especially for the Lyapunov based controller. If  $L_s$  is over-tuned the vehicle can not maintain its stability, and it starts oscillating around the reference trajectory. And if  $L_s$  is under-tuned, the trajectory tracking becomes a complex task.

Besides, the speed tracking should be improved for all the controllers, by adding an integrator to the design of the control laws as done in the simulations. Concerning the Lyapunov based controller, some improvements are necessary in order to evaluate the complete control law without dropping the term in  $\delta$ . This improvement can be done by ameliorating the estimation of the sideslip angles of the wheels. Finally, we can proceed with more comparisons, with existing coupled controllers, in order to evaluate the real contribution of the developed solutions for the coupled control.

Concerning the trajectory planning, it will be important to validate the developed navigation strategy in more complicated scenarios (for ex. the left and the right lane are occupied and the ego-vehicle has to execute a secure overtaking maneuver). Besides, in our work, we have supposed that the vehicle preceding the ego-vehicle navigates with the same speed during the overall overtaking maneuver. In future works, we can include the trajectory prediction tools, to be able to predict the motion of the other vehicles surrounding the ego-vehicle. We may also take into consideration the road shape when generating the trajectory of the lane changing maneuver (for the instant, we have considered a straight road). Finally, we look forward to implementing the complete navigation strategy on a robotized vehicle in order to validate our work and define the limitations and the challenges in a real world scenario.



# Abbreviations and Notations

ABS Anti-lock Brake System

ACC Adaptive Cruise Control

ASIRT Association for Safe International Road Travel

AVC Autonomous Vehicle Competition

CC Cruise Control

COG Center of Gravity

DARPA Defense Advanced Research Projects Agency

DHM Denavit-Hartenberg Modified notation

ESC Electronic Stability Control

FSLQ Frequency-Shaped Linear Quadratic

GCDC Grand Cooperative Driving Challenge

GNSS Global Navigation Satellite System

GPS Global Positioning System

IMU Inertial Measurement Unit

INS Inertial Naviagation System

LPV Linear Parameter-Varying

LQR Linear Quadratic Regulator

LTI Linear Time Invariant

LTV Linear Time-varying

MPC Model Predictive Control

PD Proportional Derivative

PI Proportional Integral

PID Proportional Integral Derivative

RTK Real Time Kinematic

SMC Sliding Mode Control

VIAC VisLab Intercontinental Autonomous Challenge

$i, j$	Indexes of the vehicle's wheels: i stands for front or rear, j for left or right
$F_{x_{ij}}$	Longitudinal force generated in the contact between the ground and the wheel
$F_{y_{ij}}$	Lateral force generated in the contact between the ground and the wheel
$F_{z_{ij}}$	Vertical force generated in the contact between the ground and the wheel
$m_{ij}$	Mass of the wheel
$V_{wx_{ij}}$	Linear velocity of the wheel
$\alpha_{ij}$	Sideslip angle of the wheel
$\sigma_{x_{ij}}$	Longitudinal slip ratio of the tire
$\omega_{ij}$	Angular velocity of the wheel
$C_{\sigma_{ij}}$	Longitudinal stiffness of the wheel
$C_{\alpha_{ij}}$	Lateral (or cornering) stiffness of the wheel
$\tau_{w_{ij}}$	Driving/Braking torque of the wheel
$T$	Kinetic energy
$V$	Potential energy
$A$	Inertial matrix
$H$	Vector of centrifugal, coriolis and gravity
$J$	Jacobian matrix
$f_e$	Vector of external forces
$k$	Index of a body in the topology of the robot
$C_k$	The body with index $k$ in the robot's topology
${}^k\omega_k$	Angular velocity of the body $C_k$ of the robot
${}^kV_k$	Linear velocity of the body $C_k$ of the robot
$R_k$	Frame related to the body $C_k$ of the robot
${}^kT_u$	Transformation matrix between the frame $R_u$ and the frame $R_k$

${}^k Mo_k$	Resulting torque applied to the body $C_k$ of the robot
${}^k m o_k$	Resulting torque applied on the body $C_k$ of the robot by its predecessors
${}^k F_k$	Resulting force applied to the body $C_k$ of the robot
${}^k f_k$	Resulting force applied to the body $C_k$ of the robot by its predecessors
${}^k f e_k$	External forces applied to the body $C_k$ of the robot
${}^k m e_k$	External tprques applied to the body $C_k$ of the robot
$X$	Longitudinal position of the vehicle in the inertial frame
$Y$	Lateral position of the vehicle in the inertial frame
$\psi$	Vehicle's yaw angle
$V_x$	Vehicle's longitudinal speed in the vehicle frame
$\delta$	Vehicle's steering wheel angle
$L$	Vehicle's wheelbase
$m$	Vehicle's total mass
$V_g$	Vehicle's speed vector in the vehicle frame
$\beta$	Slip angle of the wheel at the vehicle's center of gravity
$I_z$	Moment of inertia around the z axis
$L_f$	Distance between the vehicle's center of gravity and the front axle
$L_r$	Distance between the vehicle's center of gravity and the rear axle
$I_\omega$	Rotational inertia of a wheel
$x$	Vehicle's longitudinal position in the vehicle frame
$y$	Vehicle's lateral position in the vehicle frame
$a_x$	Longitudinal acceleration of the vehicle with respect to the inertial frame expressed in the vehicle frame
$a_y$	Lateral acceleration of the vehicle with respect to the inertial frame expressed in the vehicle frame
$m_s$	Vehicle suspended mass
$h$	Height of the vehicle's center of gravity
$\phi_v$	roll angle of the vehicle
$F_{aero}$	Aerodynamic force applied to the vehicle

$E$	Vehicle's track
$I_{xz}$	Moment of inertia with respect to the roll and the yaw motions
$I_{xx}$	Moment of inertia with respect to the roll motion
$g$	Gravity constant
$\rho_a$	Air density
$s$	Vehicle's frontal surface
$R_{eff}$	Effective radius of the tire
$\mu$	Friction coefficient

# Bibliography

- [AAAO11] Y. Abbassi, Y. Ait-Amirat, and R. Outbib. Nonlinear feedback control of vehicle speed. *IFAC Proceedings Volumes*, 44(1):6279–6284, 2011.
- [ADL<sup>+</sup>12] R. Attia, J. Daniel, J. Lauffenburger, R. Orjuela, and M. Basset. Reference generation and control strategy for automated vehicle guidance. In *Intelligent Vehicles Symposium (IV), 2012 IEEE*, pages 389–394. IEEE, 2012.
- [AGS<sup>+</sup>95a] J. Ackermann, J. Guldner, W. Sienel, R. Steinhauser, and VI. Utkin. Linear and nonlinear controller design for robust automatic steering. *IEEE Transactions on Control Systems Technology*, 3(1):132–143, 1995.
- [AGS<sup>+</sup>95b] J. Ackermann, J. Guldner, W. Sienel, R. Steinhauser, and VI. Utkin. Linear and nonlinear controller design for robust automatic steering. *IEEE Transactions on Control Systems Technology*, 3(1):132–143, 1995.
- [AKO07] A. Astolfi, D. Karagiannis, and R. Ortega. *Nonlinear and adaptive control with applications*. Springer Science & Business Media, 2007.
- [AOB14] R. Attia, R. Orjuela, and M. Basset. Combined longitudinal and lateral control for automated vehicle guidance. *Vehicle Systems Dynamics*, 52(2):261–279, 2014.
- [APM<sup>+</sup>05] F. Aparicio, J. Paez, F. Moreno, F. Jimenez, and A. Lopez. Discussion of a new adaptive speed control system incorporating the geometric characteristics of the roadway. *International journal of vehicle autonomous systems*, 3(1):47–64, 2005.
- [AWB11] D. Althoff, D. Wollherr, and M. Buss. Safety assessment of trajectories for navigation in uncertain and dynamic environments. In *IEEE International Conference on Robotics and Automation (ICRA)*, 2011.
- [Baf07] G. Baffet. *Développement et validation expérimentale d'observateurs des forces du contact pneumatique/chaussée d'une automobile*. PhD thesis, Compiègne, 2007.
- [Bau05] J. Bauer. *Rules of the Road*. Penguin, 2005.
- [BBF<sup>+</sup>99] A. Broggi, M. Bertozzi, A. Fascioli, C. Bianco, L. Guarino, and A. Piazzi. The argo autonomous vehicle's vision and control systems. *International Journal of Intelligent Control and Systems*, 3(4):409–441, 1999.
- [BF13] E. Bertolazzi and M. Frego.  $g^1$  fitting with clothoids. *Mathematical Methods in the Applied Sciences*, 2013.

- [BFPU07] I. Boiko, L. Fridman, A. Pisano, and E. Usai. Analysis of chattering in systems with second-order sliding modes. *IEEE transactions on Automatic control*, 52(11):2085–2102, 2007.
- [BIS09] M. Buehler, K. Iagnemma, and S. Singh. *The DARPA urban challenge: autonomous vehicles in city traffic*, volume 56. Springer, 2009.
- [BK89] J. Borenstein and Y. Koren. Real-time obstacle avoidance for fast mobile robots. *IEEE Transactions on Systems, Man, and Cybernetics*, 19(5):1179–1187, 1989.
- [BK91] J. Borenstein and Y. Koren. The vector field histogram-fast obstacle avoidance for mobile robots. *IEEE Journal of Robotics and Automation*, 7(3):278–288, 1991.
- [BK99] O. Brock and O. Khatib. High-speed navigation using the global dynamic window approach. In *Robotics and Automation, 1999. Proceedings. 1999 IEEE International Conference on*, volume 1, pages 341–346. IEEE, 1999.
- [BL96] E. Bayo and R. Ledesma. Augmented lagrangian and mass-orthogonal projection methods for constrained multibody dynamics. *Nonlinear Dynamics*, 9(1):113–130, 1996.
- [BM09] T. Besselmann and M. Morari. Autonomous vehicle steering using explicit lpv-mpc. In *Control Conference (ECC), 2009 European*, pages 2628–2633. IEEE, 2009.
- [BMZ<sup>+</sup>12] A. Broggi, P. Medici, P. Zani, A. Coati, and M. Panciroli. Autonomous vehicles control in the vislab intercontinental autonomous challenge. *Annual Reviews in Control*, 36(1):161–171, 2012.
- [BNM11] A. Benine-Neto and S. Mammar. Piecewise affine state feedback controller for lane departure avoidance. In *Intelligent Vehicles Symposium (IV), 2011 IEEE*, pages 839–844. IEEE, 2011.
- [Bos00] Bosch. *Bosch Automotive handbook*. Society of Automotive Engineers, 2000.
- [BPFP06] R. Benenson, S. Petti, T. Fraichard, and M. Parent. Integrating perception and planning for autonomous navigation of urban vehicles. In *Intelligent Robots and Systems, 2006 IEEE/RSJ International Conference on*, pages 98–104. IEEE, 2006.
- [Cas12] J. Casey. *Exploring curvature*. Springer Science & Business Media, 2012.
- [CCB97] J. Cuadrado, J. Cardenal, and E. Bayo. Modeling and solution methods for efficient real-time simulation of multibody dynamics. *Multibody System Dynamics*, 1(3):259–280, 1997.
- [CDBD09] J. Cuadrado, D. Dopico, A. Barreiro, and E. Delgado. Real-time state observers based on multibody models and the extended kalman filter. *Journal of mechanical science and technology*, 23(4):894–900, 2009.
- [CDNG04] J. Cuadrado, D. Dopico, MA. Naya, and M. González. Penalty, semi-recursive and hybrid methods for mbs real-time dynamics in the context of structural integrators. *Multibody System Dynamics*, 12(2):117–132, 2004.

- [CFJCSH14] L. Ching-Fu, J. Jyh-Ching, and C. Shun-Hung. Robust Lane-Changing Maneuver, 2014.
- [CL02] V. Cossalter and R. Lot. A motorcycle multi-body model for real time simulations based on the natural coordinates approach. Vehicle system dynamics, 37(6):423–447, 2002.
- [CLS12] K. Chu, M. Lee, and M. Sunwoo. Local path planning for off-road autonomous driving with avoidance of static obstacles. IEEE Transactions On Intelligent Transportation Systems, 13(4):1599 – 1616, December 2012.
- [CNM04] S. Chaib, M. Netto, and S. Mammar.  $h_\infty$ , adaptive, pid and fuzzy control: a comparison of controllers for vehicle lane keeping. In Intelligent Vehicles Symposium, 2004 IEEE, pages 139–144. IEEE, 2004.
- [CSC<sup>+</sup>10] Y. Cong, O. Sawodny, H. Chen, J. Zimmermann, and A. Lutz. Motion planning for an autonomous vehicle driving on motorways by using flatness properties. In Control Applications (CCA), 2010 IEEE International Conference on, pages 908–913. IEEE, 2010.
- [CT95] W. Chee and M. Tomizuka. Lane change maneuver for ahs applications. JSAE Review, 2(16):219, 1995.
- [DBS<sup>+</sup>15] V. Duggal, K. Bipin, AK. Singh, B. Gopalakrishnan, BK. Bharti, A. Khiat, and KM. Krishna. Overtaking maneuvers by non linear time scaling over reduced set of learned motion primitives. In Intelligent Vehicles Symposium (IV), 2015 IEEE, pages 115–120. IEEE, 2015.
- [DFM09] V. Delsart, T. Fraichard, and L. Martinez. Real-time trajectory generation for car-like vehicles navigating dynamic environments. In Robotics and Automation, 2009. ICRA'09. IEEE International Conference on, pages 3401–3406. IEEE, 2009.
- [DFS69] H. Dugoff, P.S. Fancher, and L. Segal. Tire performance characteristics affecting vehicle response to steering and braking control inputs. Technical report, Office of Vehicle Systems Research, US National Bureau of Standards, 1969.
- [DFS70] H. Dugoff, PS. Fancher, and L. Segel. An analysis of tire traction properties and their influence on vehicle dynamic performance. Technical report, SAE Technical Paper, 1970.
- [DGCK14] D. Dopico, F. González, J. Cuadrado, and J. Kövecses. Determination of holonomic and nonholonomic constraint reactions in an index-3 augmented lagrangian formulation with velocity and acceleration projections. Journal of Computational and Nonlinear Dynamics, 9(4):041006, 2014.
- [DNBF<sup>+</sup>10] B. D’Andréa-Novel, C. Boussard, M. Fliess, O. El Hamzaoui, H. Mounier, and B. Steux. Commande sans modèle de la vitesse longitudinale d’un véhicule électrique. In Sixième Conférence Internationale Francophone d’Automatique (CIFA 2010), 2010.

- [DTMD10] D. Dolgov, S. Thrun, M. Montemerlo, and J. Diebel. Path planning for autonomous vehicles in unknown semi-structured environments. *The International Journal of Robotics Research*, 29(5):485–501, 2010.
- [EM11] M. Eilers and C. Möbus. Learning the human longitudinal control behavior with a modular hierarchical bayesian mixture-of-behaviors model. In *Intelligent Vehicles Symposium (IV), 2011 IEEE*, pages 540–545. IEEE, 2011.
- [FBT97] D. Fox, W. Burgard, and S. Thrun. The dynamic window approach to collision avoidance. *IEEE Robotics & Automation Magazine*, 4(1):23–33, 1997.
- [FBT<sup>+</sup>08] P. Falcone, F. Borrelli, HE. Tseng, J. Asgari, and D. Hrovat. Linear time-varying model predictive control and its application to active steering systems: Stability analysis and experimental validation. *International journal of robust and nonlinear control*, 18(8):862–875, 2008.
- [Fia54] E. Fiala. Lateral forces on rolling pneumatic tires. *Zeitschrift VDI*, 96(29):973–979, 1954.
- [FSR05] S. Fuchshumer, K. Schlacher, and T. Rittenschober. Nonlinear vehicle dynamics control-a flatness based approach. In *Decision and Control, 2005 and 2005 European Control Conference. CDC-ECC’05. 44th IEEE Conference on*, pages 6492–6497. IEEE, 2005.
- [FTA<sup>+</sup>07] P. Falcone, HE. Tseng, J. Asgari, F. Borrelli, and D. Hrovat. Integrated braking and steering model predictive control approach in autonomous vehicles. *IFAC Proceedings Volumes*, 40(10):273–278, 2007.
- [FV09] A. Ferrara and C. Vecchio. Second order sliding mode control of vehicles with distributed collision avoidance capabilities. *Mechatronics*, 19(4):471–477, 2009.
- [GD14] T. Gu and JM. Dolan. Toward human-like motion planning in urban environments. In *Intelligent Vehicles Symposium Proceedings, 2014 IEEE*, pages 350–355. IEEE, 2014.
- [GMAM06] S. Garrido, L. Moreno, M. Abderrahim, and F. Martin. Path planning for mobile robot navigation using voronoi diagram and fast marching. In *Intelligent Robots and Systems, 2006 IEEE/RSJ International Conference on*, pages 2376–2381. IEEE, 2006.
- [Goo02] MA. Goodrich. Potential fields tutorial. *Class Notes*, 157, 2002.
- [GPL<sup>+</sup>14] D. González, J. Pérez, R. Lattarulo, V. Milanés, and F. Nashashibi. Continuous curvature planning with obstacle avoidance capabilities in urban scenarios. In *Intelligent Transportation Systems (ITSC), 2014 IEEE 17th International Conference on*, pages 1430–1435. IEEE, 2014.
- [GPM89] C. Garcia, DM. Prett, and M. Morari. Model predictive control: theory and practice—A survey. *Automatica*, 25(3):335–348, 1989.

- [GTP96] J. Guldner, H. Tan, and S. Patwardhan. Analysis of automatic steering control for highway vehicles with look-down lateral reference systems. *Vehicle System Dynamics*, 26(4):243–269, 1996.
- [Gui00] E. Guillo. *Modélisation et identification dynamique des engins de construction de routes*. PhD thesis, Thèse de doctorat, IRCCyN Nantes, 2000.
- [GVM<sup>+</sup>10] S. Glaser, B. Vanholme, S. Mammar, D. Gruyer, and L. Nouveliere. Maneuver-based trajectory planning for highly autonomous vehicles on real road with traffic and driver interaction. *IEEE Transactions on Intelligent Transportation Systems*, 11(3):589–606, 2010.
- [H<sup>+</sup>97] K. Hedrick et al. Brake system modeling, control and integrated brake/throttle switching phase i. *California Partners for Advanced Transit and Highways (PATH)*, 1997.
- [HAS13] D. Heß, M. Althoff, and T. Sattel. Comparison of trajectory tracking controllers for emergency situations. In *Intelligent Vehicles Symposium (IV), 2013 IEEE*, pages 163–170. IEEE, 2013.
- [HB03] A. El Hajjaji and S. Bentalba. Fuzzy path tracking control for automatic steering of vehicles. *Robotics and Autonomous Systems*, 43(4):203–213, 2003.
- [HHH<sup>+</sup>08a] F. Von Hundelshausen, M. Himmelsbach, F. Hecker, A. Mueller, and H. Wuensche. Driving with tentacles: Integral structures for sensing and motion. *Journal of Field Robotics*, 25(9):640–673, 2008.
- [HHH<sup>+</sup>08b] FV. Hundelshausen, M. Himmelsbach, F. Hecker, A. Mueller, and H. Wuensche. Driving with tentacles: Integral structures for sensing and motion. *Journal of Field Robotics*, 25(9):640–673, 2008.
- [HLH<sup>+</sup>11] Michael Himmelsbach, Thorsten Luettel, Falk Hecker, Felix von Hundelshausen, and Hans-Joachim Wuensche. Autonomous off-road navigation for mucar-3. *KI-Künstliche Intelligenz*, 25(2):145–149, 2011.
- [HLV<sup>+</sup>11] S. Hima, B. Lusseti, B. Vanholme, S. Glaser, and S. Mammar. Trajectory tracking for highly automated passenger vehicles. *IFAC Proceedings Volumes*, 44(1):12958–12963, 2011.
- [HT97] P. Hingwe and M. Tomizuka. Experimental evaluation of a chatter free sliding mode control for lateral control in ahs. In *American Control Conference, 1997. Proceedings of the 1997*, volume 5, pages 3365–3369. IEEE, 1997.
- [HTMT07] GM. Hoffmann, CJ. Tomlin, M. Montemerlo, and S. Thrun. Autonomous automobile trajectory tracking for off-road driving: Controller design, experimental validation and racing. In *American Control Conference, 2007. ACC’07*, pages 2296–2301. IEEE, 2007.
- [Jaz13] RN. Jazar. *Vehicle dynamics: theory and application*. Springer Science & Business Media, 2013.

- [Jer12] W. Jerkovsky. The structure of multibody dynamics equations. *Journal of Guidance, Control, and Dynamics*, 2012.
- [KFB<sup>+</sup>06] T. Keviczky, P. Falcone, F. Borrelli, J. Asgari, and D. Hrovat. Predictive control approach to autonomous vehicle steering. In *American Control Conference, 2006*, pages 6–pp. IEEE, 2006.
- [Kha86] O. Khatib. Real-time obstacle avoidance for manipulators and mobile robots. In *Autonomous robot vehicles*, pages 396–404. Springer, 1986.
- [KK86] W. Khalil and J. F. Kleinfinger. A new geometric notation for open and closed-loop robots. In *IEEE International Conference on Robotics and Automation*, volume 3, 1986.
- [KK87] W. Khalil and J. Kleinfinger. Minimum operations and minimum parameters of the dynamic model of tree structure robots. *IEEE J. Robotics and Automation*, 3(6):517–526, 1987.
- [KKY11] D. Kim, J. Kang, and K. Yi. Control strategy for high-speed autonomous driving in structured road. In *Intelligent Transportation Systems (ITSC), 2011 14th International IEEE Conference on*, pages 186–191. IEEE, 2011.
- [KN00] U. Kienecke and L. Nielsen. *Automotive control systems*. Warrendale, PA: Society of Automotive Engineers, 2000. 432, 2000.
- [KN05] U. Kiencke and L. Nielsen. *Automotive control systems*, volume 2. Springer, 2005.
- [KND85] J. Kautsky, NK. Nichols, and P. Van Dooren. Robust pole assignment in linear state feedback. *International Journal of control*, 41(5):1129–1155, 1985.
- [LaV98] SM. LaValle. Rapidly-exploring random trees: A new tool for path planning. 1998.
- [Lec02] D. Lechner. *Analyse du comportement dynamique des véhicules routiers légers: développement d'une méthodologie appliquée à la sécurité primaire*. PhD thesis, Ecole Centrale de Lyon, 2002.
- [Lev93] A. Levant. Sliding order and sliding accuracy in sliding mode control. *International journal of control*, 58(6):1247–1263, 1993.
- [Lev98] A. Levant. Robust exact differentiation via sliding mode technique. *automatica*, 34(3):379–384, 1998.
- [LF09] M. Likhachev and D. Ferguson. Planning long dynamically feasible maneuvers for autonomous vehicles. *The International Journal of Robotics Research*, 28(8):933–945, 2009.
- [Lim98] EM. Lim. *Lateral and longitudinal vehicle control coupling in the automated highway system*. PhD thesis, University of California at Berkeley, 1998.
- [LJC14] C. Lin, J. Juang, and S. Chen. *Robust Lane-Changing Maneuver*, 2014.

- [LPW79] T. Lozano-Pérez and MA. Wesley. An algorithm for planning collision-free paths among polyhedral obstacles. *Communications of the ACM*, 22(10):560–570, 1979.
- [LSZL14] X. Li, Z. Sun, Q. Zhu, and D. Liu. A unified approach to local trajectory planning and control for autonomous driving along a reference path. In *Mechatronics and Automation (ICMA), 2014 IEEE International Conference on*, pages 1716–1721. IEEE, 2014.
- [LW07] L. Li and F. Wang. *Advanced motion control and sensing for intelligent vehicles*. Springer Science & Business Media, 2007.
- [LWP80] J. Luh, M. Walker, and R. Paul. On-line computational scheme for mechanical manipulators. *J. DYN. SYS. MEAS. and CONTR.*, 102:69–76, 1980.
- [Maa11] S. Maakaroun. *Modélisation et simulation dynamique d'un véhicule urbain innovant en utilisant le formalisme de la robotique*. PhD thesis, Université Nantes Angers Le Mans, 2011.
- [MCGK11] S. Maakaroun, P. Chevrel, M. Gautier, and W. Khalil. Modelling and simulation of a two wheeled vehicle with suspensions by using robotic formalism. *IFAC Proceedings Volumes*, 44(1):2156–2161, 2011.
- [MDNFM14] L. Menhour, B. D’Andréa-Novel, M. Fliess, and H. Mounier. Coupled nonlinear vehicle control: Flatness-based setting with algebraic estimation techniques. *Control Engineering Practice*, 22:135–146, 2014.
- [MEG<sup>+</sup>10] S. Mammar, NM. Enache, S. Glaser, B. Lusetti, and AB. Neto. Lane keeping automation at tire saturation. In *American Control Conference (ACC), 2010*, pages 6466–6471. IEEE, 2010.
- [Men10] L. Menhour. *Synthèse de commandes au volant d'une automobile pour le diagnostic de rupture d'un itinéraire: développement et validation expérimentale*. PhD thesis, Compiègne, 2010.
- [MKDN13] L. Menhour, D. Koenig, and B. D’Andréa-Novel. Continuous-time and discrete-time switched  $h_\infty$  state feedback controllers: Application for a robust steering vehicle control. In *Proc. IEEE ECC*, pages 986–991, 2013.
- [ML15] G. Max and B. Lantos. Modeling and control of tree-like structured vehicles and robots using appell method. In *2015 IEEE 13th International Symposium on Intelligent Systems and Informatics (SISY)*, pages 223–228. IEEE, 2015.
- [MNK<sup>+</sup>13a] D. Madås, M. Nosratinia, M. Keshavarz, P. Sundström, R. Philppsen, A. Eidehall, and K. Dahlén. On path planning methods for automotive collision avoidance. In *Intelligent Vehicles Symposium (IV), 2013 IEEE*, pages 931–937. IEEE, 2013.
- [MNK<sup>+</sup>13b] D. Madas, M. Nosratinia, M. Keshavarz, P. Sundström, R. Philppsen, A. Eidehall, and K. Dahlén. On path planning methods for automotive collision avoidance. In *Intelligent Vehicles Symposium (IV), 2013 IEEE*, pages 931–937. IEEE, 2013.

- [Mor13] J. Moras. Grilles de perception évidentielles pour la navigation robotique en milieu urbain. PhD thesis, Université de Technologie de Compiègne, 2013.
- [MSN11] R. Marino, S. Scalzi, and M. Netto. Nested pid steering control for lane keeping in autonomous vehicles. Control Engineering Practice, 19(12):1459–1467, 2011.
- [MT96] R. Marino and P. Tomei. Nonlinear control design: geometric, adaptive and robust. Prentice Hall International (UK) Ltd., 1996.
- [MUDL11] M. McNaughton, C. Urmson, JM. Dolan, and J. Lee. Motion planning for autonomous driving with a conformal spatiotemporal lattice. In Robotics and Automation (ICRA), 2011 IEEE International Conference on, pages 4889–4895. IEEE, 2011.
- [MYZ12] L. Ma, J. Yang, and M. Zhang. A two-level path planning method for on-road autonomous driving. In Intelligent System Design and Engineering Application (ISDEA), 2012 Second International Conference on, pages 661–664. IEEE, 2012.
- [N<sup>+</sup>07] L. Nouveliere et al. Experimental vehicle longitudinal control using a second order sliding mode technique. Control Engineering Practice, 15(8):943–954, 2007.
- [NBCF15] J. Nilsson, M. Bränström, E. Coelingh, and J. Fredriksson. Longitudinal and lateral control for automated lane change maneuvers. In American Control Conference (ACC), 2015, pages 1399–1404. IEEE, 2015.
- [NBCF16] J. Nilsson, M. Bränström, E. Coeling, and J. Fredriksson. Lane change maneuvers for automated vehicles. IEEE Transactions On Intelligent Transportation Systems, 2016.
- [NCM04] M. Netto, S. Chaib, and S. Mammar. Lateral adaptive control for vehicle lane keeping. In American Control Conference, 2004. Proceedings of the 2004, volume 3, pages 2693–2698. IEEE, 2004.
- [NGG<sup>+</sup>05] JE. Naranjo, C. González, R. García, T. De Pedro, and RE. Haber. Power-steering control architecture for automatic driving. IEEE Transactions on Intelligent Transportation Systems, 6(4):406–415, 2005.
- [NGGP08] JE. Naranjo, C. Gonzalez, R. Garcia, and T. De Pedro. Lane-change fuzzy control in autonomous vehicles for the overtaking maneuver. IEEE Transactions on Intelligent Transportation Systems, 9(3):438–450, 2008.
- [NGR<sup>+</sup>03] JE. Naranjo, C. González, J. Reviejo, R. García, and T. De Pedro. Adaptive fuzzy control for inter-vehicle gap keeping. IEEE Transactions on Intelligent Transportation Systems, 4(3):132–142, 2003.
- [NMN10] H. Nasser, NK. M’sirdi, and A. Naamane. Decoupled models for vehicle dynamics and estimation of coupling terms. In 18th Mediterranean Conference on Control and Automation, MED’10, 2010.
- [NN12] L. Nehaoua and L. Nouvelière. Backstepping based approach for the combined longitudinal-lateral vehicle control. In Intelligent Vehicles Symposium (IV), 2012 IEEE, pages 395–400. IEEE, 2012.

- [Okt16] Oktal. Driving simulation engine scanner. <http://www.scanersimulation.com>, 2016.
- [OS06] RP. Osborn and T. Shim. Independent control of all-wheel-drive torque distribution. Vehicle system dynamics, 44(7):529–546, 2006.
- [OW82] D. Orin and M. Walker. Efficient dynamic computer simulation of robotic mechanisms. ASME Trans. J. dynamics Systems, Measurement and Control, 104:205–211, 1982.
- [PB97] HB. Pacejka and IJM. Besselink. Magic formula tyre model with transient properties. Vehicle system dynamics, 27(S1):234–249, 1997.
- [PGM<sup>+</sup>12] J. Pérez, J. Godoy, V. Milanés, J. Villagrá, and E. Onieva. Path following with backtracking based on fuzzy controllers for forward and reverse driving. In Intelligent Vehicles Symposium (IV), 2012 IEEE, pages 1108–1113. IEEE, 2012.
- [PGVO13] J. Pérez, J. Godoy, J. Villagrá, and E. Onieva. Trajectory generator for autonomous vehicles in urban environments. In Robotics and Automation (ICRA), 2013 IEEE International Conference on, pages 409–414. IEEE, 2013.
- [Pis00] A. Pisano. Second order sliding modes: theory and applications. Elettronica (DIEE), Universita degli Studi di Cagliari, Cagliari, Italia, 2000.
- [PRCT13] R. Pastorino, D. Richiedei, J. Cuadrado, and A. Trevisani. State estimation using multibody models and non-linear kalman filters. International Journal of Non-Linear Mechanics, 53:83–90, 2013.
- [PS91] HB. Pacejka and RS. Sharp. Shear force development by pneumatic tyres in steady state conditions: a review of modelling aspects. Vehicle system dynamics, 20(3-4):121–175, 1991.
- [PT91] H. Peng and M. Tomizuka. Optimal preview control for vehicle lateral guidance. California Partners for Advanced Transit and Highways (PATH), 1991.
- [PT03] I. Papadimitriou and M. Tomizuka. Fast lane changing computations using polynomials. In American Control Conference, 2003. Proceedings of the 2003, volume 1, pages 48–53. IEEE, 2003.
- [PVSD<sup>+</sup>11] C. Poussot-Vassal, O. Sename, L. Dugard, P. Gaspar, Z. Szabo, and J. Bokor. Attitude and handling improvements through gain-scheduled suspensions and brakes control. Control Engineering Practice, 19(3):252–263, 2011.
- [Raj11] R. Rajamani. Vehicle dynamics and control. Springer Science & Business Media, 2011.
- [San16] E. Sanjurjo. State observers based on detailed multibody models applied to an automobile. PhD thesis, University of A Coruna, 2016.
- [SDZ<sup>+</sup>14] H. Sun, W. Deng, S. Zhang, S. Wang, and Y. Zhang. Trajectory planning for vehicle autonomous driving with uncertainties. In Informative and Cybernetics for Computational Social Systems (ICCSS), 2014 International Conference on, pages 34–38. IEEE, 2014.

- [SEFL14] Y. Shtessel, C. Edwards, L. Fridman, and A. Levant. Introduction: Intuitive theory of sliding mode control. In *Sliding Mode Control and Observation*, pages 1–42. Springer, 2014.
- [Sha71a] RS. Sharp. The stability and control of motorcycles. *Journal of mechanical engineering science*, 13(5):316–329, 1971.
- [Sha71b] RS. Sharp. The stability and control of motorcycles. *Mechanical Engineering Science*, 13(5):316–326, 1971.
- [Sha01] RS. Sharp. Stability, control and steering responses of motorcycles. *Vehicle system dynamics*, 35(4-5):291–318, 2001.
- [Sha04] T. Shamir. How should an autonomous vehicle overtake a slower moving vehicle: Design and analysis of an optimal trajectory. *IEEE Transactions on Automatic Control*, 49(4):607–610, 2004.
- [SN85] M. Sugeno and M. Nishida. Fuzzy control of model car. *Fuzzy sets and systems*, 16(2):103–113, 1985.
- [SOAL10] P. Shakouri, A. Ordys, M. Askari, and DS. Laila. Longitudinal vehicle dynamics using simulink/matlab. In *Control 2010, UKACC International Conference on*, pages 1–6. IET, 2010.
- [SOLA11] P. Shakouri, A. Ordys, DS. Laila, and M. Askari. Adaptive cruise control system: Comparing gain-scheduling pi and lq controllers. *IFAC Proceedings Volumes*, 44(1):12964–12969, 2011.
- [SS98] S. Sundar and Z. Shiller. Emergency lane-change maneuvers of autonomous vehicles. *Journal of Vehicle Dynamic Systems, Measurement, and Control*, 120:37–44, 1998.
- [SSPD12] B. Soualmi, C. Sentouh, J. Popieul, and S. Debernard. Fuzzy takagi-sugeno lq controller for lateral control assistance of a vehicle. In *Intelligent Vehicles Symposium (IV), 2012 IEEE*, pages 377–382. IEEE, 2012.
- [SSW10] R. Schubert, K. Schulze, and G. Wanielik. Situation assessment for automatic lane-change maneuvers. *IEEE Transactions on Intelligent Transportation Systems*, 11(3):607–616, 2010.
- [Tan80] A. Tannenbaum. Feedback stabilization of linear dynamical plants with uncertainty in the gain factor. *International Journal of Control*, 32(1):1–16, 1980.
- [TBFIG13] Z. Tao, P. Bonnifait, V. Fremont, and J. Ibanez-Guzman. Mapping and localization using gps, lane markings and proprioceptive sensors. In *Intelligent Robots and Systems (IROS), 2013 IEEE/RSJ International Conference on*, pages 406–412. IEEE, 2013.
- [TMD<sup>+</sup>06] S. Thrun, M. Montemerlo, H. Dahlkamp, D. Stavens, A. Aron, J. Diebel, P. Fong, J. Gale, M. Halpenny, G. Hoffmann, et al. Stanley: The robot that won the darpa grand challenge. *Journal of field Robotics*, 23(9):661–692, 2006.

- [TTC13] G. Tagne, R. Talj, and A. Charara. Higher-order sliding mode control for lateral dynamics of autonomous vehicles, with experimental validation. In *Intelligent Vehicles Symposium (IV), 2013 IEEE*, pages 678–683. IEEE, 2013.
- [UB98] I. Ulrich and J. Borenstein. Vfh+: Reliable obstacle avoidance for fast mobile robots. In *IEEE International Conference on Robotics and Automation*, pages 1572 – 1577, Leuven, Belgium, May 1998.
- [UB00] I. Ulrich and J. Borenstein. Vfh\*:local obstacle avoidance with look-ahead verification. In *IEEE International Conference on Robotics and Automation*, pages 2505–2511, San Francisco, April 2000.
- [Ven03] G. Venture. *Identification des paramètres dynamiques d'une voiture*. PhD thesis, Ecole Centrale de Nantes (ECN)(ECN)(ECN); Université de Nantes, 2003.
- [Wer10] M. Werling. *Ein neues Konzept fur die Trajektoriengenerierung und -stabilisierung in zeitkritischen Verkehrsszenarien*. PhD thesis, Institut fur Technologie, 2010.
- [WGR11] M. Wang, T. Ganjineh, and R. Rojas. Action annotated trajectory generation for autonomous maneuvers on structured road networks. In *Automation, Robotics and Applications (ICARA), 2011 5th International Conference on*, pages 67–72. IEEE, 2011.
- [WSK<sup>+</sup>13] J. Wei, JM. Snider, J. Kim, JM. Dolan, R. Rajkumar, and B. Litkouhi. Towards a viable autonomous driving research platform. In *Intelligent Vehicles Symposium (IV), 2013 IEEE*, pages 763–770. IEEE, 2013.
- [XDH<sup>+</sup>17] Ph. Xu, G. Dherbomez, E. Héry, A. Abidli, and Ph. Bonnifait. System architecture of a driverless electric car in the grand cooperative driving challenge. *IEEE Intelligent Transportation Systems Magazine (ITS Mag.)*, 2017.
- [XG10] L. Xiao and F. Gao. A comprehensive review of the development of adaptive cruise control systems. *Vehicle System Dynamics*, 48(10):1167–1192, 2010.
- [Zam81] G. Zames. Feedback and optimal sensitivity: Model reference transformations, multiplicative seminorms, and approximate inverses. *IEEE Transactions on automatic control*, 26(2):301–320, 1981.
- [Zan02] AT. Van Zanten. Evolution of electronic control systems for improving the vehicle dynamic behavior. In *Proceedings of the 6th International Symposium on Advanced Vehicle Control*, volume 2, page 9, 2002.
- [ZK10] J. Zhao and A. El Kamel. Coordinated throttle and brake fuzzy controller design for vehicle following. In *Intelligent Transportation Systems (ITSC), 2010 13th International IEEE Conference on*, pages 659–664. IEEE, 2010.
- [ZS09] J. Ziegler and C. Stiller. Spatiotemporal state lattices for fast trajectory planning in dynamic on-road driving scenarios. In *Intelligent Robots and Systems, 2009. IROS 2009. IEEE/RSJ International Conference on*, pages 1879–1884. IEEE, 2009.